STUDY OF MAGNETIC AND ELECTRICAL PROPERTIES OF ULTRA-FINE Ni-Zn FERRITE MATERIALS PREPARED BY NOVEL METHOD

A Thesis submitted to **Goa University** for the Award of the Degree of

DOCTOR OF PHILOSOPHY

In

PHYSICS

By

MANOJ M. KOTHAWALE

Research Guide	Research Co-Guide
Prof. R. B. Tangsali	**Prof. J. S. Budkuley**

DEPARTMENT OF PHYSICS
GOA UNIVERSITY
TALEIGAO GOA-403 206
March 2013

To my

Father

DECLARATION

I hereby declare that this thesis entitled “Study of Magnetic and Electrical Properties of Ultra-fine Ni-Zn Ferrite Materials Prepared by Novel Method” leading to the degree of Ph.D in Physics is my original work and that it has not been submitted to any other University or Institution for the award of any Degree, Diploma, Associateship and fellowship or any other similar title to the best of my knowledge.

Date: Mr. Manoj M. Kothawale

(Candidate)

CERTIFICATE

As required under the University ordinance, we certify that thesis entitled “Study of Magnetic and Electrical Properties of Ultra-fine Ni-Zn Ferrite Materials Prepared by Novel Method” submitted by Mr. Manoj M. Kothawale leading to the degree of Doctor of Philosophy in Physics is a record of research done by him during the study period under our guidance and that it has not previously formed the basis for the award of any Degree, Diploma, Associateship and fellowship or any other similar titles.

Date:	Prof. R. B. Tangsali	Prof. J. S. Budkuley
	Research guide	Research Co-guide
	Department of Physics	Department of Chemistry
	Goa University	Goa University

ACKNOWLEDGEMENTS

I wish to express my sincere thanks to my guiding teacher, Prof. Rudraji B. Tangsali for encouraging me to pursue research work, suggesting topic of research, continuous guidance during the entire research period and all the valuable advices from time to time.

I sincerely thank Prof. Jayant S. Buduley, my research Co-guide, for his encouragement, valuable suggestions and guidance especially during synthesis.

I am grateful to Prof. A. V. Salkar, Department of Chemistry, Goa University, for his constructive suggestions during the research period.

I thank Prof. J. A. E. Desa, Department of Physics, Goa University, for his valuable suggestions during research work.

I also thank

1. Management, Principal and Staff of DM'S College of Arts, Science and Commerce, Assagao-Goa for their cooperation.

2. All the teaching faculty and non teaching staff of Department of Physics, Goa University for extending necessary facilities and co-operation throughout my research work.

3. University Grants Commission for awarding Teacher Fellowship under F.I.P.XI plan to complete my Ph.D work.

I am grateful to

Dr. G. K Naik, Department of Chemistry, S. P. C. College of Arts and Science, Margao- Goa, for his cooperation during sample preparation.

Dr. V. Verenkar, Department of Chemistry, Goa University, for extending the facility of AC susceptibility measurements.

Prof: Manuel Almeida Valente, Aveiro University, Aveiro Portugal, for carrying out the low temperature magnetic measurements on VSM and SQUID.

Prof. Sabu Thomas, Polymer Technology lab, School of Chemical Sciences, Mahatma Gandhi University, Kottayam, Kerala, for extending AFM facility.

Dr. P. S. Patil and Mr. Dhanaji Dalavi, Thin Film Materials Lab, Department of Physics, Shivaji University, Kolhapur for providing SEM facilities.

Mr. Dinesh Sharma, Sophisticated Analytical Instrumentation Facility (SAIF), Panjab University, Chandigarh, for providing TEM and EDX facilities.

Mr. Sher Singh Meena, Solid State Physics Division, Bhabha Atomic Research Centre, Mumbai, for carrying out Mossbauer measurements.

I am also grateful to my colleagues and research scholars: Dr. Girish, Dr. Vikas, Jaison, Pranav, Shraddha, Kapil, Bosco, Reshma, Nelson, Wilson, Manoj Salgaonkar, Elaine, Neelima, Umesh and Lectina for their company and support. I thank all my friends for their support and cooperation during the tenure of my research work.

I owe a debt of gratitude to my parents for bringing the best in me. I have the greatest mother in the world who taught me to be tough to face the hard time in life. She is a tower of strength for me.

I have immense regards for my brothers and sister for their love, support and giving freedom to work in my own way. I am truly indebted for their support to bring me so far.

I feel a deep sense of gratitude to my father in- law for being a great friend of mine and for his constant encouragement throughout the Ph.D work. I would like to thank all my in-laws for their encouragement and best wishes.

A big thank you goes to my beloved wife for her love, affection, caring and concern. I deeply appreciate her perpetual support during the entire tenure of my research work. This arduous work would have not been done without her moral support.

Finally, tons of thanks to my loving and growing son Aaditya, for being part of our world during the tenure of my research work. He is a reason to smile every day, enjoy and happily pursue my research work especially during writing of this thesis.

Manoj M. Kothawale

TABLE OF CONTENTS

4. CHARACTERIZATION **62**

LIST OF FIGURES

LIST OF TABLES

CHAPTER 1

INTRODUCTION

1.1 General Introduction

Current trends in advanced materials are largely focused on controlled synthesis and processing of materials of nano length scales with designed properties and integration of such materials into different functional platforms. Extensive studies of nano-structured materials are being carried out due to their novel physicochemical properties. The significant interest of the scientific community for the nanomaterials is because, under nanometers scale, the materials show some new unseen characteristics that bulk solid do not usually exhibit. At nano dimensions, large number of atoms near surface triggers unique properties and large surface to volume ratio of nanomaterials plays a very vital role in determining surface magnetism and performance characteristics of magnetic nano materials. Some new magnetic phenomena such as superparamagnetism, spin canting and core-shell structure characteristic are observed only in nanosize magnetic materials. At nano range, superparamagnetic particles and spin clusters play role in variation of magnetization. These properties depend on number of factors such as composition, shape, size, surface morphology, anisotropy and inter-particle interactions.

The nano particle ferrites are showing capability of challenging applications in the field of modern medical sciences such as hyperthermia and targeted drug delivery applications [1, 2]. The recent advances in the field of magnetism have shown bright future for many nano materials to be used in advance technologies such as sensors and spintronics [2, 3,4].

The exhaustive research and development is carried out throughout the world to bring in newer methods of synthesis of nano ferrites to cater to the need of recent advancement in the science and technology. The nano particle ferrite technology is at the leading edge of the rapidly developing new areas of electronic engineering, computer technology and medicine, and at the same time they pose very interesting and rich fundamental physics probing [1,5]. It is probably this combination of applied and fundamental research that is responsible for the strong attraction that nano ferrites have developed in past fifteen years.

The immense scope of nano ferrites for technological device applications and curiosity to prepare nano magnetic materials in the laboratory motivated us to undertake present work on the study of magnetic and electrical properties of ultra-fine nickel zinc ferrite materials prepared by a novel method. The present study of magnetic and electrical properties of Ni-Zn ferrite has significance, both from the fundamental and application point of view.

This Chapter contains basics of magnetism and ferrites. Brief discussion is included on origin of magnetism, classification of magnetic materials, ferrites and their applications.

1.2 Origin of Magnetism

The term magnetism was coined when some kind of stones were found by the Greeks in 470 B C having unusual property to attract pieces of iron. These stones were called lodestones. The chemical formula for the loadstone is Fe_3O_4. In sixteenth century, William Gilbert made artificial magnets by rubbing pieces of iron against lodestones. The first electromagnet was made in 1825, after the discovery made in 1820 by Hans Christian Oersted that an electric current produces a magnetic field [6].

All matter is composed of atoms, whereas atoms are composed of protons, neutrons and electrons. Electrons are in constant motion around the nucleus. It is found that a magnetic field is produced whenever an electrical charge is in motion. Electrons carry a negative electrical charge and produce a magnetic field as they move through space. The strength of this field is called the magnetic moment. The magnetism in any material is fundamentally due to the spin and orbital motion of the electrons inside the atom. This motion of electron is associated with spin magnetic moment and orbital magnetic moment. The magnetic nature of the material is decided upon their response to magnetic field (*H*) or magnetic flux density (*B*). This response is measured in terms of magnetic quantity called magnetization (*M*). The simple relation between magnetic field, magnetic flux density and magnetization is given by Equation 1.1 and 1.2.

$$B = \mu_O (H + M) \qquad 1.1$$

$$B = \mu H \qquad 1.2$$

Where μ_o is a constant called as permeability in a free space and μ is the permeability of a material. From Equation (1.1), one can see that $\mu_o H$ is the magnetic induction generated by the field alone and $\mu_o M$ is the additional magnetic induction contributed by a material [6]. The magnetic nature of the material is also derived from quantity called as susceptibility (χ) and is defined as the ratio of magnetization to magnetic field given by Equation 1.3.

$$\chi = \frac{M}{H} \qquad 1.3$$

Also, from the above Equations, the permeability and susceptibility of a material is related to each other by Equation 1.4.

$$\mu = \mu_O(1+\chi) \qquad 1.4$$

The magnitude of the susceptibility and its temperature dependencies provide the information on the behavior of different types of magnetic materials. The magnetic materials are classified into diamagnetism, paramagnetism, ferromagnetism, antiferromagnetism and ferrimagnetism [6]. The different ways of ordering of magnetic moments in the magnetic materials are schematically shown in Fig. 1.1.

1.2.1 Diamagnetism

Diamagnetic material has a negative susceptibility with typical values of the order of 10^{-5} to 10^{-6}. If a magnetic field is applied to a diamagnetic material, the induced magnetic moment is small and opposite to the field direction. Diamagnetism obeys Lenz's law, which states that when a conducting loop is acted upon by an applied magnetic field a current is induced in the loop that counteracts the change in the field. According to Langevin theory, the susceptibility of diamagnetic material is given by Equation 1.5.

$$\chi = -\frac{NZe^2r^2}{(mc^2)} \qquad 1.5$$

Where N is the number of atoms per unit volume, Z is the number of electron, e is the charge of electron, r is the orbital radius and c is the speed of light. The characteristic of diamagnetic materials is temperature independent. Examples of some diamagnetic materials are copper, silver, gold, zinc, alumina and mercury [7].

1.2.2 Paramagnetism

Paramagnetic material possesses non-zero magnetic moments due to unpaired electrons. The magnetic moments can be oriented along an applied field to give rise to positive susceptibility, however their values of susceptibility are very small of the order of 10^{-5} to 10^{-2}. Examples of some paramagnetic elements are calcium, aluminum, sodium, titanium, magnesium, alloys of copper etc [7].

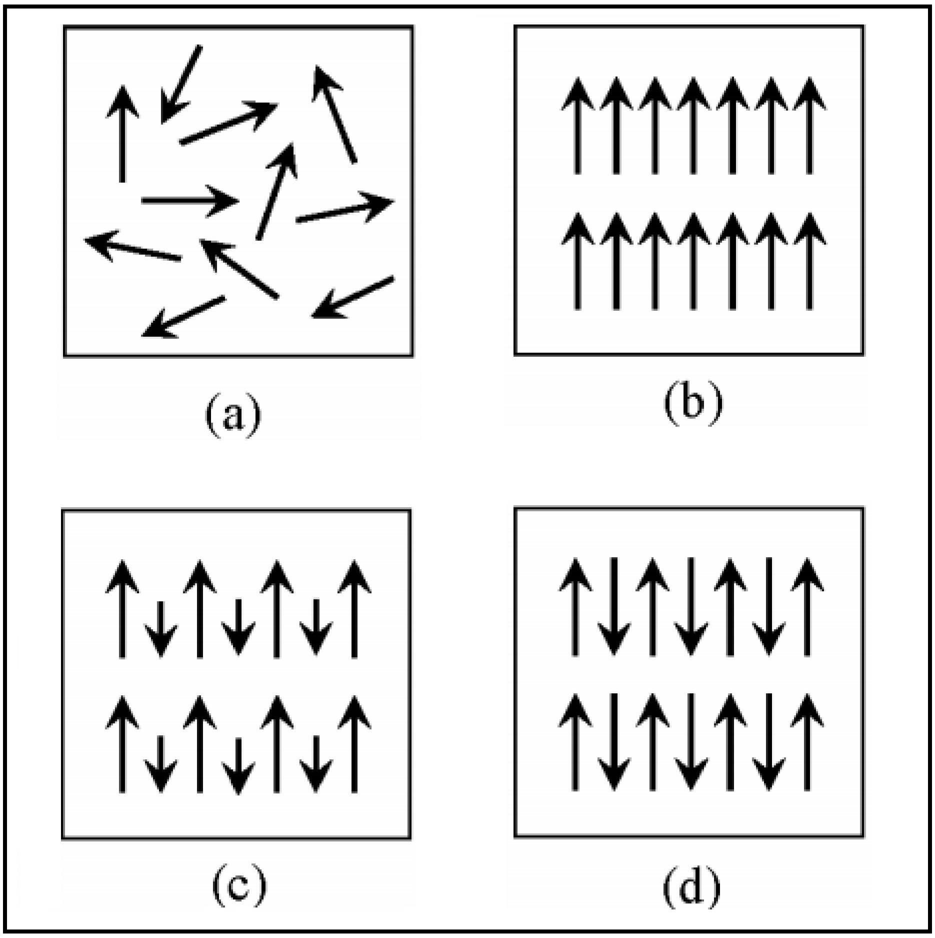

Fig. 1.1 Various types of ordering of magnetic moments in (a) paramagnetic, (b), ferromagnetic, (c) ferrimagnetic, and (d) antiferromagnetic.

The susceptibility of a paramagnetic material is inversely dependent on temperature, which is known as Curie law given by Equation 1.6. The variation of susceptibility with temperature is as shown in Fig.1.2 (a).

$$\chi = \frac{C}{T} \qquad 1.6$$

Where T is the absolute temperature and C is called the Curie constant.

1.2.3 Ferromagnetism

Ferromagnetic material differs from the diamagnetic and paramagnetic materials in many different ways. In a ferromagnetic material, the exchange coupling between neighboring moments leads the moments to align parallel with each other and, ferromagnetic materials generally can acquire a large magnetization in a relatively weak magnetic field, since all magnetic moments are easily aligned together. Also, the susceptibility of a ferromagnetic material does not follow the Curie law, but is modified by Curie-Weiss law given by Equation 1.7. The variation of susceptibility with temperature is as shown in Fig.1.2 (b).

$$\chi = \frac{C}{(T - \theta)} \qquad 1.7$$

Where C is a constant and θ is called Weiss constant. For ferromagnetic materials, the Weiss constant is almost identical to the Curie temperature (T_C). At temperature below Curie temperature, the magnetic moments are ordered, whereas above Curie temperature, material loses magnetic ordering and shows paramagnetic character [8]. Examples of ferromagnetic materials are transition metals Fe, Co and Ni. But other elements and alloys involving transition or rare-earth elements are also ferromagnetic due to their unfilled 3d and 4f shells. These materials have a large and positive magnetic susceptibility in the range of 10^6.

1.2.4 Antiferromagnetism

Antiferromagnetic material aligns the magnetic moments in a way that all moments are antiparallel to each other, which is totally opposite to ferromagnetic ordering [9]. The antiferromagnetic susceptibility is followed by the Curie-Weiss law with a negative θ as in Equation (1.7). The variation of susceptibility as a function of temperature is given in Fig. 1.2(c). Like ferromagnetic materials, these materials become paramagnetic above transition temperature, known as the Néel temperature [6]. Common examples of materials with antiferromagnetic ordering include MnO, FeO, CoO and NiO.

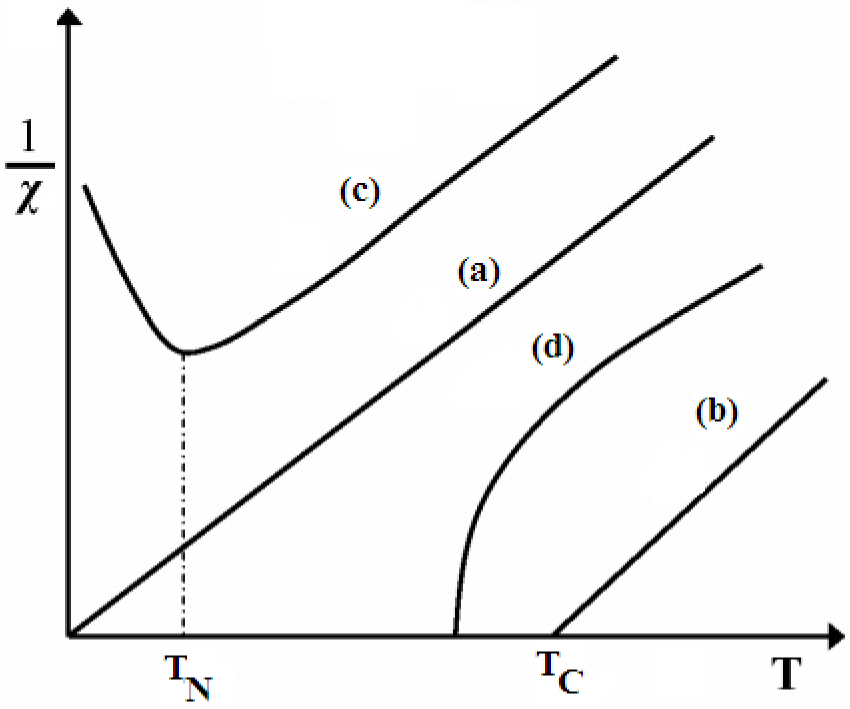

Fig. 1.2 Variation of inverse susceptibility verses temperature T for (a) paramagnetic, (b) ferromagnetic, (c) antiferromagnetic and (d) ferrimagnetic materials. T_N and T_C are Néel temperature and Curie temperature, respectively.

1.2.5 Ferrimagnetism

Ferrimagnetic material has the same antiparallel alignment of magnetic moments as an antiferromagnetic material does. However, the magnitude of magnetic moment in one direction differs from that of the opposite direction. As a result, a net magnetic moment remains in the absence of external magnetic field. The behavior of susceptibility of a ferrimagnetic material obeys Curie-Weiss law. The variation of susceptibility with temperature is as shown in Fig. 1.2(d). Cubic spinel ferrites probably are the most common ferrimagnetic materials such as Fe_3O_4, $NiFe_2O_4$, $NiZnFe_2O_4$, (MnMg) Fe_2O_4 etc.

1.3 Ferrites

Ferrites may be defined as electrically non-conductive ferrimagnetic material composed of oxides containing ferric ions as the main constituent. Ferrites are ceramic materials, dark grey or black in appearance and very hard and brittle. Magnetite (loadstone) or ferrous ferrite is an example of naturally occurring ferrite. Ferrites have been studied since 1936. Due to their low eddy current losses and high electrical resistivity, they are considered superior to other magnetic materials and have an enormous impact over the applications of magnetic materials. The magnetic materials like iron were used in early applications. They have low electric resistivity which allows induced current (eddy currents) to flow within the materials themselves, thereby producing heat. This wasted energy and heat is often a serious problem and makes them useless for applications at high frequencies. Ferrites possess high dielectric constant due to which, even though electromagnetic waves can pass through ferrites, they do not readily conduct electricity. This gives them upper hand over iron, nickel and other transition metals as these metals conduct electricity.

1.4 Classification of Ferrites

Ferrites can be classified into three different types

1. Spinel ferrites (Cubic ferrites)
2. Hexagonal ferrites
3. Garnets

Current discussion is restricted to spinel ferrites, as the present work is based on the nickel zinc ferrite which is a spinel ferrite.

1.5 Spinel Ferrites

Spinels or cubic ferrites belong to the AB_2O_4 family of oxides [10]. The general chemical formula of spinel ferrite is $A^{2+}Fe_2^{3+}O_4$ where A^{2+} usually represents one or, in mixed ferites more than one of the divalent transition metals Mn, Fe, Co, Ni, Cu and Zn or Mg and Cd. Other combinations, of equivalent valency, are possible and it is also possible to replace some or all the iron ions with other trivalent metal ions [11]. The spinel ferrite crystallizes in the cubic system [12]. The spinel ferrite has space group of O_h^7 (Fd3m) and space group number is 227. The crystal structure is best described by subdividing the unit cell into 8 octants, with edge a/2 (where ‘a’ is the lattice parameter) (see Fig. 1.3 (a)). The unit cell contains 8 formula units or each octant contains 1 formula unit and may thus be written as $M_8Fe_{16}O_{32}$.

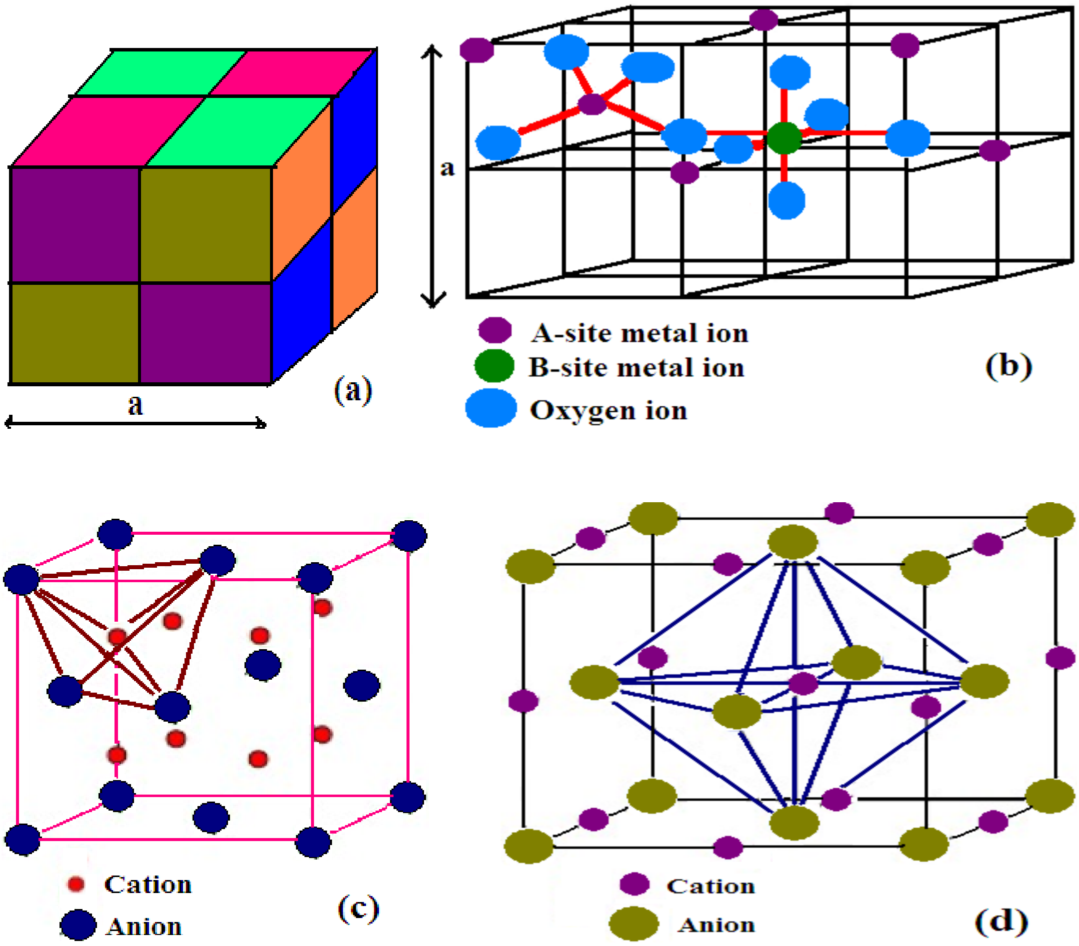

Fig. 1.3 (a) Subdivided unit cell into 8 octants, (b) Shows cubic crystal structure of spinel ferrite representing A and B sites in subdivided unit cell, (c) and (d) represents tetrahedral sites and octahedral sites in FCC lattice respectively.

The crystal structure of spinel ferrite can be regarded as an interlocking network of positively charged metal ions and negatively charged divalent oxygen ions. The oxygen anions form an ideal face-centered cubic (fcc) lattice. Within this lattice two types of interstitial positions occurs viz., tetrahedral and octahedral sites. Fig. 1.3 (b) shows cubic crystal structure of spinel ferrite representing A and B sites by subdividing the unit cell into 8 octants. Fig. 1.3 (c) and (d) represents tetrahedral and octahedral sites in FCC lattice respectively. There are 64 tetrahedral sites and 32 octahedral sites available per unit cell, and, out of these, 8 tetrahedral and 16 octahedral sites are occupied by cations. Each cation in the tetrahedral position has 4 neighboring oxygen ions and is often called an A site, while each cation in the octahedral position has 6 neighboring oxygen ions and is called as B site in the general formula AB_2O_4. Unit cell of spinel consist of 32 oxygen (O) ions, and, they have a four-fold coordination, formed by three B cations and one A cation [13].

1.5.1 Types of spinel ferrites

Based on distribution of cations on tetrahedral (A) and octahedral (B) sites, spinel ferrites have been categories into three types.

1. Normal spinel ferrites
2. Inverse spinel ferrites
3. Mixed spinel ferrites

1.5.2 Normal spinel ferrites

In these ferrites all divalent cations occupy tetrahedral (A) sites while the trivalent cations are on octahedral (B) sites. Normal spinel is represented by the formula $M^{2+}[Me^{3+}]\,O_4$. Where M represent divalent ions and Me for trivalent ions. Square brackets are used to indicate the ionic distribution of the octahedral (B) sites. An example of normal spinel ferrite is bulk $ZnFe_2O_4$.

1.5.3 Inverse spinel ferrites

In this case all divalent cations occupy octahedral (B) sites and half of the trivalent ions occupy tetrahedral (A) sites. These ferrites are represented by the formula $Me^{3+}[M^{2+}Me^{3+}]O_4$. Typical examples of inverse ferrites are Fe_3O_4 and

$NiFe_2O_4$.

1.5.4 Mixed spinel ferrites

In this all divalent metal ions and trivalent ions are uniformly distributed over the tetrahedral and octahedral sites. These ferrites are represented by the formula.

$Me^{2+}_{x}\ Me^{3+}_{1-x}\ [Me^{2+}_{1-x}\ Me^{3+}_{1+x}]$

1.6 Hexagonal Ferrites

Hexagonal ferrites are ferrimagnetic oxides with formula $MFe_{12}O_{19}$, where M is an element like Barium, Lead or Strontium. In these ferrites, oxygen ions have closed packed hexagonal crystal structure. Their hexagonal ferrite lattice is similar to the spinel structure with closely packed oxygen ions, but there are also metal ions at some layers with the same ionic radii as that of oxygen ions. They are widely used as permanent magnets.

1.7 Garnets

The general formula of the unit cell of a pure iron garnet has eight formula units of $M_3Fe_5O_{12}$, where M is the trivalent rare earth ions (Y, Gd, Dy). Their cell shape is cubic and the edge length is about 12.5 Å. They have complex crystal structure. They are largely used in applications of memory structure.

1.8 Soft and Hard Ferrites

Ferrites can be classified into two types based on their ability to be magnetized or demagnetized i.e soft and hard. Soft ferrites are easily magnetized or demagnetized whereas hard ferrites are difficult to magnetize or demagnetize. Soft magnetic materials have low coercive field and thin hysteresis loop and are used in transformer cores, inductors, recording heads and microwave devices. Examples are nickel, iron, cobalt, manganese etc. Hard ferrites have high coercive field and wide hysteresis loop. They are used as permanent magnets. Examples are alnico, rare earth metal alloys etc. [7].

1.9 Advantages of Ferrite over other Magnetic Materials

Most of the magnetic materials such as iron and metallic alloys have low dc electrical resistivity and serve no purpose at high frequencies. Their low electrical resistivity induces large eddy currents produces heat and materials become inefficient. However, ferrites can perform much better at high frequencies because of their high electrical resistivity [14]. Ferrites have high temperature stability and are cheaper than other magnetic metals and alloys [15, 16]. When one requires the combination of low cost, high quality, high stability and low volume, no other magnetic material has suitable parameters as those of ferrites [17, 18].

1.10 Applications of Ferrites

Ferrites are very important magnetic materials with wide applications in technology due to their high electric resistivity and particularly at high frequencies [19, 20]. Few of the prominent applications of the ferrites are listed below.

1. Ferrites are part of low power and high flux transformers which are used in television [13]. Small antennas are made by winding a coil on ferrite rod used in

transistor radio receiver [21]. Nano ferrite materials are useful in a variety of applications in the electronic industry due to their high permeability, high saturation magnetization, high resistivity and low loss as they help directly in miniaturization of electric circuit.

2. In computer, non volatile memories are made of ferrite materials as they are highly stable against severe shock and vibrations. Ferrites are used in computer memories i.e computer hard disk, floppy disks, credit cards, audio cassettes, video cassettes and recorder heads [22].

3. Ferrites are used to produce low frequency ultrasonic waves by magnetostriction.

4. Nickel alloys are used in high frequency equipments like high speed relays, wide band transformers and inductors. They are used to manufacture transformers, inductors, small motors and relays. They are used for precision voltage and current transformers and inductive potentiometers [23, 24]. Iron-silicon alloys are used in electrical devices and magnetic cores of transformers operating at low power line frequencies.

5. Ferrites are used in microwave devices like circulators, isolators, switches, phase shifters and in radar circuits [25, 26]. They are used as electromagnetic wave absorbers at low dielectric values.

6. Ceramic magnets are useful as medical treatment to access key acupressure points on wrist, neck and fingers to give relief from pain [27].

7. Spinel ferrites are used in the fabrication of multilayer chip inductors as surface mount devices for miniaturized electronic products such as cellular phones, digital

cameras, video camera etc. Recently, there has been a growing interest in low-temperature sintered Ni-Zn ferrite for the application in producing multilayer-type chip inductors [28].

8. The semiconductor like behavior of the resistivity shown by this material makes it a favorable material for sensor applications [29].

9. In the recent past, the targeted drug delivery or magnetic drug targeting (MDT) has gained more attention. Magnetic nanoparticles received foremost attention offering local drug delivery with reduced side effects and controlled drug release for prolonged period of time addressing problems of damage of healthy tissue and drug wastage. MNPs (magnetic nanoparticles) are commonly composed of magnetic elements, such as iron, nickel, cobalt and their oxides like magnetite [30].

1.11 Aim and Objectives of the Research Work

1. To synthesize high purity nanoparticles of $Ni_xZn_{1-x}Fe_2O_4$ of different compositions by employing novel precursor method and to investigate their structural, magnetic and transport properties.

2. To produce bulk $Ni_xZn_{1-x}Fe_2O_4$ materials on sintering nanoparticles and investigate their structural, magnetic and transport properties.

1.12 Work Plan of the Research Work

The investigations were carried out by executing the following work plan.

1. Optimization of the preparative method to synthesize nanoparticle $Ni_xZn_{1-x}Fe_2O_4$ powder of different compositions (where x=0.40, 0.50, 0.55, 0.60, 0.65 and 0.70) by

using microwave assisted combustion synthesis.

2. Characterization of freshly prepared $Ni_xZn_{1-x}Fe_2O_4$ samples for single phase formation and composition confirmation using XRD, IR and EDS respectively.

3. XRD data analysis - to calculate lattice constants, X-ray density, cation distribution and porosity of nano $Ni_xZn_{1-x}Fe_2O_4$ samples.

4. Mass density measurements of nano $Ni_xZn_{1-x}Fe_2O_4$ samples.

5. Particle size estimates, analysis and size distribution of nano $Ni_xZn_{1-x}Fe_2O_4$ samples using standard techniques such as XRD, TEM and AFM.

6. Investigations of magnetic properties such as saturation magnetization, retentivity, coercivity, AC susceptibility, Curie temperature, blocking temperature, canting angles and Mossbauer hyperfine parameters of nano $Ni_xZn_{1-x}Fe_2O_4$ samples.

7. Investigation of electrical properties such as dc resistivity, dielectric constant and dielectric loss factor of nano $Ni_xZn_{1-x}Fe_2O_4$ samples.

8. Preparation of bulk samples by sintering of nano $Ni_xZn_{1-x}Fe_2O_4$ at five different sintering temperatures of 900^oC, 1000^oC, 1100^oC, 1200^oC and 1300^oC for four hour in air by maintaining heating and cooling rate at $5^oC\ min^{-1}$.

9. Characterization of bulk $Ni_xZn_{1-x}Fe_2O_4$ samples.

10. Mass density and porosity analysis of bulk $Ni_xZn_{1-x}Fe_2O_4$ samples.

11. Microstucture and morphology investigations of bulk $Ni_xZn_{1-x}Fe_2O_4$ samples using Scanning Electron Microscope.

12. Investigations of magnetic property such as saturation magnetization, retentivity, coercivity, AC susceptibility, Curie temperature, initial permeability, permeability loss tangent and Mossbauer hyperfine parameters of bulk $Ni_xZn_{1-x}Fe_2O_4$ samples.

13. Investigations of electrical properties such as dc resistivity, thermoelectric power, dielectric constant, and dielectric loss of bulk $Ni_xZn_{1-x}Fe_2O_4$ samples.

1.13 Organization of Thesis

Systematic experiments were carried out in accordance with the requirements of the work plan as given in the Section1.12. The final report on the results and analysis of the work carried out are presented in this thesis which consists of seven Chapters, including this, and contains.

Chapter II: This Chapter contains literature survey on present status of reported research work related to Ni-Zn ferrite material. Inferences reported on the magnetic and electrical properties in the literature of the work carried out by various researchers and scholars across the world are mainly highlighted in this Chapter.

Chapter III: This Chapter describes various methods used by researchers for synthesizing magnetic materials in general and ferrite in specific. Synthesis of ultra-fine Ni-Zn ferrite samples using novel method (nitrilotriacetate precursor method) in the present investigation have been discussed in detail along with the flow chart depicting various stages of the preparation method adopted in the present work.

Chapter IV: Inscriptions on various characterization techniques used in present work for studying characteristics of Ni-Zn ferrite samples are provided in this Chapter. Sample preparation for each experimental measurement is given in this chapter. The detailed structure and composition characterization data like X-Ray diffraction patterns, IR spectrograph and EDS spectra of samples under investigation are also given in this Chapter. Calculations and numerical values of lattice parameters, X-ray density, bulk density, porosity, cation distribution and theoretical stoichiometry calculations also appear in this Chapter. Particle size characterization data like TEM micrographs, AFM micrographs and SEM images along with particle size distribution of the samples are also presented here. Analysis of microstructure, morphology and particle growth of bulk samples obtained from SEM images is also discussed in this Chapter.

Chapter V: This Chapter covers investigations of magnetic properties of nano and bulk Ni-Zn ferrite samples. Brief theoretical background of magnetic parameters, magnetic phenomenon and few models of permeability is included at the beginning of this Chapter. Investigations of room temperature magnetic properties such as saturation magnetization, retentivity and coercivity of nano and bulk samples are presented in this Chapter. Low temperature hysteresis loops of nano samples are also appearing in this Chapter along with zero field cooled (ZFC) and field cooled (FC) responses of magnetization. Variation of saturation magnetization, retentivity and coercivity are presented in the graphical form depicting their variations with composition and sintering temperature along with explanation in this Chapter. Curie temperature (T_c) obtained from A.C susceptibility measurements for nano and bulk samples are tabulated and it’s variation with composition and sintering temperature is explained in this Chapter.

Detail observations on measurements of initial permeability and loss factor as a function of frequency and temperature of sintered toroids are presented in this Chapter. This Chapter includes analysis of graphs of variation of initial permeability and loss factor as a function of composition, frequency and temperature along with values of operational frequency limit (Snoke’s limit) in the tabulated form. Discussion on the results in this Chapter includes correlation between effect of sintering temperature, microstructure, porosity, grain growth, saturation magnetization, method of preparation and observed changes in initial permeability and loss factor. At the end of this Chapter room temperature Mössbauer spectra of few nano and bulk samples are presented along with their hyperfine parameters.

Chapter VI: This Chapter includes study of electric properties such as dc resistivity, thermoelectric power, dielectric constant and loss tangent of nano and bulk samples. Brief theoretical background of parameters of electrical properties, associated phenomenon and few models of resistivity and dielectric constant is included at the beginning of this Chapter. DC electrical resistivity measurements as functions of composition and temperature of nano and bulk samples along with the effect of sintering temperature are provided in this Chapter. The variations of thermoelectric power with temperature for various bulk samples are presented here. Detailed investigation on dielectric constant and loss tangent measurement of nano and bulk samples as a function of composition, frequency and temperature forms the main component of this Chapter. The analysis of dielectric properties in this Chapter is reported by presenting various graphs such as variation of dielectric constant and dielectric loss with frequency at room temperature and variation of dielectric constant and dielectric loss with temperature at fixed frequencies.

Chapter VII: This Chapter contains summary of all the results obtained in the present investigations. Data and results obtained for various samples are co-related and logical interpretation is produced in this chapter. The scope for future work is also highlighted at the end of the Chapter.

References

1. H. Ohno, H. Munekata, T. Penny, S. Von Molnar and L. L. Chang, Phys. Rev.Lett., 68, (1992), 2664-2668.

2. G. A. Prinz, Science, 282, (1998), 1660-1667.

3. S. A. Wolf, D. D. Awschalom, R. A. Buhrman, J. M. Daughton, S. Von Molnar, M. L. Roukes, and D. M. Treger, Science, 294, (2001), 1488-1492.

4. G. A. Prinz, J. Magn. Magn. Mater., 200, (1999), 57-61.

5. J. K. Furdyna, J. Appl. Phys., 64, (1988), R 29.

6. B. D. Cullity, Introduction to Magnetic Materials, Addison Wesley publishing company, (1972).

7. M. S. Vijaya, G. Rangarajan, Materials Science, McGraw-Hill Publishing company limited, New Delhi, (1999-2000).

8. D. Jiles, Introduction to Magnetism and Magnetic Materials; Chapman & Hall, London, (1990).

9. M. A. Omar, Elementary Solid State Physics (Principles & Application Addison-Wesley publishing company, Amsterdam, (1962).

10. O. Muller and R. Roy, Crystal Chemistry of Non-Metallic Materials, Springer-Verlag, Berlin, (1974).

11. E. C Snelling “Soft Ferrites,Properties and applications”, Bitterworth and Co. (Publishers) Ltd, London (1988).

12. Vladimir Sepelak and Klara Tkacova, Acta Montanistica Slovaca, Rocnik 2, (1997), 266-272.

13. V. G. Harris, J. Magn. Magn Mater, 321, (2009), 2035-2047.

14. Woo Chul Kim, Sam Jin Kim, Seung Wha Lee and Chul Sung Kim, J. Magn.

Magn Mater, 226, (2001), 1418-1420.

15. D. A. Thompson and J. S. Best, IBM Journal of Research and Development, 44, (2000), 311-315.
16. Z. Yue, J. Zhou, L. Li, H. Zhang and Z. Gui, J. Magn. Magn Mater., 208, (2000), 55-59.
17. C. Upadhyay, H. C. Verma and S. Anand J. Appl. Phys., 95-10, (2004) 5746-5751.
18. Z. Krysicki and T. Lubanska, J. Magn. Magn Mater, 19, (1980), 107-108.
19. S. T. Mahmud, J. Magn. Magn Mater, 305, (2006), 269-274.
20. N. Sivakumar, A. Narayanasamy, N. Ponpandianb and G. Govindaraj, J. Appl. Phys. 101, (2007), 084116-21,
21. M. A. Et Hiti, J. Magn. Magn Mater, 164, (1996), 187-196.
22. M. P. Horvath, J. Magn. Magn Mater, 215, (2000)171-183.
23. A. Thakur and M. Singh, Ceramics International, 29, (2003), 505-511.
24. Noboru Ichinose, “Introduction to Fine Ceramics”, Ohmsha (Publisher) Ltd., Japan (1987).
25. N. Nanakorn, P. Jalupoom, N. Vaneesorn, A. Thanaboonsombut, Ceram. Int. 34 (2008), 779-782.
26. R. A. Islam, D. Viehland and S. Priya, J Mater Sci., 43, (2008), 1497-1501.
27. www.ferrite.com (web).
28. A. E. Virden aand K. O’Grady, J. Magn. Magn Mater, 290, (2005), 868-870.
29. P. K. Gallagher, E. M. Gyorgy, D. W. Johnson, W. David, M. Robbins and M. Vogel, J.Amer. Ceram. Soc., 66(7), (1983), C110.
30. W. Fu, H. Yang, H. Bala, S. Liu, M. Li and G. Zou, Mater. Lett., 60, (2006), 1728-1732.

CHAPTER 2

LITERATURE SURVEY

Spinel ferrites of different composition have been studied and used for a long period of time to get required products. We do not have a single ideal ferrite, which can fulfill each and every requirement, because each one has its own advantages and disadvantages. It is difficult to frame a rigid set of rules for ferrites about their properties. Since research on ferrites is vast, the discussion in the literature survey is focused and restricted to nickel zinc ferrite material only. Work on nickel zinc ferrite reported by other researchers globally is referred here.

Nanocrystalline powders of $Ni_xZn_{1-x}Fe_2O_4$, ($x = 1, 0.8, 0.6, 0.4, 0.2$, and 0), were synthesized by chemical co-precipitation technique by A. D. Sheikh and V. L. Mathe [1]. Variation of dielectric constant and loss tangent with frequency were studied at room temperature. They reported that microstructure study from SEM showed that the grain size increases with sintering temperature, % porosity and resistivity of the samples were dependent on Zn concentration. The nature of dc resistivity with temperature at different sintering temperatures clearly shows the change in conduction behavior of sample and the anomalous behavior was attributed to change in cation distribution. P. Priyadharsini et al. [2] reported structural parameters and cation distribution of $Ni_xZn_{1-x}Fe_2O_4$ ($x =0, 0.2, 0.4, 0.6, 0.8$ and 1) using novel combustion synthesis from high purity zinc nitrate, nickel nitrate, ferric nitrate and glycine. The values of crystallite size obtained using Scherer’s formula were found varying between 10 and 20 nm. The mean value of X-ray density was around 5343 Kg/m^3, which was more than experimentally observed for their bulk counterparts. The cation distribution was proposed theoretically for each concentration with reference to their respective experimental lattice constant values. Magnetization values were in the range of 4 emu/g to 26 emu/g and were lower than that of bulk particles.

Nanocrystalline powders in the range 20-40 nm of $Ni_xZn_{1-x}Fe_2O_4$ (x = 0, 0.2, 0.4, 0.6, 0.8 and 1) were synthesized by eco-friendly precursor via sol–gel auto-combustion method using tartaric acid as combustion complexing agent by Tamara Slatineanu et al. [3]. The influence of nickel content on the microstructure was investigated considering the crystallite size, distance between adjacent crystal planes, lattice parameter and porosity. They have proposed cation distribution, relative bond angles and canting angles. The highest magnetization (63 emu/g) was found for $Ni_{0.8}Zn_{0.2}Fe_2O_4$. Magnetic results were explained taking into account Neel’s two sub- lattice model, spin canting and shape anisotropy due to surface spin disorder.

C. F. M. Costa et al. [4] observed effect of heating conditions during combustion synthesis on the characteristics of $Ni_{0.5}Zn_{0.5}Fe_2O_4$ nano powders. They found that the reaction gets accomplished directly on the heating plate, resulting in the Ni-Zn ferrite powders with excellent nano-characteristics, such as particles sizes between 15-30 nm and surface area of $38.9m^2/g$ compared to combustion reaction in muffle furnace.

Highly homogeneous $Ni_{1-x}Zn_xFe_2O_4$ (x= 0.25, 0.50,0.75 and 1.0) within the range of 7-15 nm was prepared by the simple and economical chemical co-precipitation method by I.H. Gul et al. [5], and showed the decrease in crystallite size with increasing zinc concentration. DC electrical resistivity decreases with increase in temperature indicating semiconductor like behavior of the samples. The dielectric constant follows the Maxwell-Wagner interfacial polarization. The observed decrease in Tc with increase in zinc concentration was explained on the basis of distribution of cations on A and B sites.

N. Sivakumar et al [6] studied dielectric properties of nanocrystalline $Ni_{0.5}Zn_{0.5}Fe_2O_4$ sample obtained by mechanical milling in the frequency range 1 KHz to 10 MHz. The real part of dielectric constant for the 14 nm grain size sample was found to be about an order of magnitude smaller than that of the bulk nickel zinc ferrite. The anomalous frequency dependence of dielectric constant has been explained on the basis of hopping of both electrons and holes. The unusual increase in dielectric loss with grain size reduction is attributed to the increase in the electrical conductivity due to oxygen vacancies introduced upon milling.

X. Lu et al. [7] synthesized Ni-Zn ferrite nanoparticles by low temperature coprecipitation method. The highest saturation magnetization observed was 60 emu/g. Permeability showed broad peak in the frequency range of 200 MHz to 6 GHz, indicating feature of electromagnetic wave absorption in high-frequency range. The structural and magnetic properties of nanoparticles of $Ni_xZn_{1-x}Fe_2O_4$ (x = 0.20, 0.40. 0.50, 0.60, 0.65, 0.70, 0.75, 0.80, 0.90 and 1.00) were reported by Zhang et al. [8]. Ferrites samples were prepared by sol-gel auto-combustion method. Lattice parameter showed decrease with increase in Ni contents. Saturation magnetization and coercivity showed dependence on composition as well as the annealing temperature. E. Manova et al. [9] prepared nano Ni-Zn ferrite having dimensions below 10 nm using combination of chemical precipitation and mechanical milling. They claimed that it is a promising technique for a relatively large scale preparation of zinc-nickel ferrite nanoparticles.

Adriana S. Albuquerque et al. [10] synthesized nanoparticles of $Ni_{0.5}Zn_{0.5}Fe_2O_4$, at relatively low temperatures (<800°C) by co-precipitation technique followed by the heat treatment. They obtained high purity and high homogeneity in the samples with average diameter between 9 and 90 nm. Critical particle diameter for transition from mono-domain to multidomain behavior investigated was close to 40 nm. Nanocrystalline $Ni_{0.5}Zn_{0.5}Fe_2O_4$ ferrite with average grain sizes ranging from 10 to 100 nm was prepared using spraying coprecipitation method by Liu Yin et al. [11]. Specific saturation magnetization increases from 40.2 to75.6 emu/g as grain size increases from 11 to 94 nm, whereas, coercivity increases monotonically as size goes below 62 nm.

Elsa E. Sileo et al. [12] carried out synthesis of nano size $Ni_{1-x}Zn_xFe_2O_4$ (x =0.2, 0.4, 0.5, 0.6 and 0.7) at low temperatures (<300^{o}C) via combustion method using precursors obtained from metal nitrates and citric acid by a sol-process. The sintering processes showed increase in the crystallinity of solids and domain sizes. Lattice parameter also increases with the increment of x.

J. Azadmanjiri et al. [13] found that sol-gel combustion method is convenient for synthesis of nano-size $Ni_{1-x}Zn_xFe_2O_4$ (x=0, 0.1, 0.2, 0.3, 0.4) in which the gel exhibits a self-propagating behavior after ignition in air. Highest saturation magnetization value of 73 emu/g for sample sintered at 950^{o}C was obtained.

Nanoparticle $Ni_{0.65}Zn_{0.35}Fe_2O_4$ starting from Fe(III), Ni (II), Zn (II) nitrates and some polyols 1,2-propane diol, 1,3-propane diol and glycerol was prepared by

Mircea Stefanescu et al. [14]. All precursors which were synthesized thermally decompose up to 350°C to form nano particle nickel zinc ferrite with average crystallite size ranging from 20 to 50 nm. Samples had shown saturation magnetization of ~70 emu/g. Nanoparticle $Ni_{1-x}Zn_xFe_2O_4$ (x = 0.1, 0.2, 0.3, 0.4 and 0.5) was prepared by S. Nasir et al. [15] using sol-gel method. Maxwell-Wagner model was used to explain dependence of dielectric constant and loss with frequency. Samples exhibited low dielectric constant and low loss tangent in MHz frequency range and also showed composition dependency. A. M. El-Sayed and E. M. A. Hamzawy [16] synthesized nanoparticle $Ni_{0.4}Zn_{0.6}Fe_2O_4$ (28 to 120 nm) using glass crystallization method. They observed particle sizes, coercivity values and saturation magnetization were dependent on sintering time. Nanoparticles of around 10 nm of $Ni_xZn_{1-x}Fe_2O_4$ (x=0.65) was prepared via co precipitation method by B.P. Rao et al. [17]. It was found that low saturation magnetization value of 9.1 emu/g was attributed to surface disorder and modified cationic distribution in nanoparticles compared to that of the bulk.

Nanopowders with average particle size of ~35 nm of $Ni_{1-x}Zn_xFe_2O_4$ (x=0.20, 0.35, 0.50 and 0.60) were reported by P. P. Sarangi et al. [18]. Samples were synthesized at temperature of 850°C using oxalate based precursor method. Dc resistivity of nanopowder was of the order of 10^7 Ω-cm and saturation magnetization was varying between 34-49 emu/g. The microstructures of nano samples had large amount of open porosity while sintered samples (≥ 2μm) revealed densified microstructures and almost devoid of porosity.

Z. Beji et al. [19] noted effects of annealing on magnetic properties of nanocrystalline $Ni_{1-x}Zn_xFe_2O_4$ (x = 0.2 and 0.4) having size about 6 nm prepared by forced hydrolysis in polyol. Samples showed relatively low blocking temperature of about 47 to 53 K which was derived from the peak of zero-field-cooled direct current (dc) susceptibility measurements. Up to annealing temperature of 800^{o}C, blocking temperature was found to increase with increasing particle size and was attributed to progressive aggregation of particles achieved by heating accompanied by the creation of spin canted interfaces between crystallites.

A. E. Virden and K. O. Grady [20] reported core shell nanoparticles of $Ni_{1-x}Zn_xFe_2O_4$ (x= Zn=0.3 to 0.7 in steps of 0.1) prepared by wet method. They investigated non-magnetic coating layer of about 4 nm for particles having size typically of 9 nm.

R. C. Kambale et al. [21] prepared $Ni_xZn_{1-x}Fe_2O_4$ (x = 0.1, 0.2, 0.3, 0.4 and 0.5) by chemical combustion route yielding nanocrystalline product (53 nm to 71 nm) on calcination at 700^{o}C for 2h. They observed increase in saturation magnetization with increase in Ni content. Temperature dependent dc resistivity measurements showed semi-conducting behavior. The room temperature relative dielectric permittivity and dielectric loss showed usual dielectric dispersion due to Maxwell-Wagner type. Small polaron hopping conduction mechanism was suggested from the results of ac conductivity measurement.

The structural, electrical and magnetic properties of $Ni_{1-x}Zn_xFe_2O_4$ (x = 0.0 to 1.0 in step of 0.2) prepared by microwave sintering as well as by conventional sintering was reported by Yadoji et al. [22]. It was found that X-ray crystallite size decreases with the increase in Zn concentration. The dielectric constant and dielectric loss factor decreases with the increase in frequency. The variation in magnetization and coercivity has also been discussed with the increase in Zn concentration.

The structural, electrical transport and magnetic properties of $Ni_{1-x}Zn_xFe_2O_4$ (x = 0.2 and 0.4) prepared using solid state reaction technique followed by sintering at various temperatures has been investigated by Hossain et al. [23]. Bulk density of $Ni_{0.8}Zn_{0.2}Fe_2O_4$ samples were found to increase up to sintering temperature of 1300°C and minor decrease in bulk density above 1300°C was reported. DC electrical resistivity showed decrease with increase in temperature indicating semiconductor-like behavior. As Zn content increases, Curie temperature, resistivity and activation energy decreases whereas, magnetization, initial permeability and relative quality factor (Q) increases. Density and average grain sizes were correlated for variation in initial permeability and magnetization of samples.

Pradeep et al. [24] prepared $Ni_{0.5+x}Zn_{0.5}Fe_{2-x}O_4$ by conventional ceramic double sintering method and observed that lattice constant, Curie temperature and activation energy increases, whereas, magnetic moment decreases with the increase in Zn concentration. M. El-Shabasy [25] observed decrease in dc electrical resistivity, Curie temperature and activation energies for electric conduction in ferrimagnetic and in paramagnetic region as zinc ion substitution increases in $Zn_xNi_{1-x}Fe_20_4$ samples (x = 0,0.2,0.4,0.6,0.8 and 1) prepared using usual ceramic technique. The dc resistivity was found to increase as the porosity increases and an empirical formula was suggested for composition dependence of electrical resistivity. A.M Abdeen [26] reported dielectric properties as a function of frequency, temperature and composition of $Ni_xZn_{1-x}Fe_2O_4$ (where x = 0, 0.2, 0.4, 0.6, 0.8 and 1) prepared using standard ceramic method. Dielectric constant and dielectric loss were found to decrease with frequency, whereas, same were increasing with temperature. However abnormal peak for dielectric loss was observed at high temperature and is explained using Rezlescu model. Murthy et al. [27] measured lattice constant, Neel temperature, Debye temperature, magnetic moment and Yafet-Kittel angles using neutron diffraction for $Zn_xNi_{1-x}Fe_2O_4$ ($0 \leq x \leq 0.75$ with the step increment of 0.25) prepared by usual ceramic sintering process. It was noted that lattice parameter and Y-K angles increases, whereas, Neel temperature decreases with the rise in zinc concentration. Magnetic moment increased with the increase in zinc concentration up to 0.3 and was found to decrease with further increase in zinc concentration.

Wet chemical co-precipitation method was utilized for preparing $Ni_{1-x}Zn_xFe_2O_4$ (x= 0.0, 0.1, 0.2, 0.3, 0.4, 0.5, 0.6, and 0.7) by Santosh S. Jadhav et al. [28]. Magnetization results exhibit collinear ferrimagnetic structure for $x \leq 0.4$ and which changes to non-collinear for x>0.4. Curie temperature (T_C) obtained from AC susceptibility data decreases with increasing x. Islam et al. [29] prepared $Ni_{1-x}Zn_xFe_2O_4$ with (x = 0.0, 0.25, 0.5, 0.75, 1.0), by co-precipitation technique. They reported that resistivity and activation energy both increases up to x = 0.25 and then decreases with further rise in Zn concentration.

Localized canting effect in Zn-substituted Ni ferrites has been observed by Bercoff et al. [30] in a theoretical model of three sublattices (A, B and $B^{'}$) to describe their magnetic behavior. Number of Bohr magnetons per formula unit and Curie temperature were also discussed as a function of Zn content. C. Pasnic and D. Condurache [31] explained the dependence of saturation magnetization, Curie point, density and the dielectric properties on the forming pressure before sintering for Ni-Zn ferrites. Experimental results were discussed in terms of ZnO migration tendency to the frontier of bonding grains in the initial stage of sintering reaction. Verma et al. [32] reported about the dielectric properties of $Ni_{1-x}Zn_xFe_2O_4$ (x =0.2, 0.35. 0.5, 0.6) prepared by citrate precursor method. Variations of dielectric constant, with frequency at different sintering temperatures for various compositions are explained on the basis of Maxwell-Wagner interfacial polarization.

Dielectric behavior of $Ni_{1-x}Zn_xFe_2O_4$ prepared by flash combustion technique was studied by Mangalaraja et al. [33]. Dielectric constant and the dielectric loss factor decreases with the rise in frequency for various concentrations of zinc, sintered at different temperatures. Decrease in porosity and increase in bulk density was reported for sintered samples at different temperatures. Using conventional ceramic powder processing technique J. Bera and P. K. Roy [34] prepared polycrystalline $Ni_{0.7}Zn_{0.3}Fe_2O_4$ with varying grain size in the range of 1-12 μm. Initial permeability was found to increase linearly with grain size upto about 5 μm, and after that, the rate of increase was reduced which was attributed to the formation of more number of closed pores. Ferrite sintered at a temperature of 1250°C for 1 hour duration was reported as the best for high-frequency low-loss application.

Srinivasan et al. [35] measured lattice constant, theoretical density, saturation magnetization, Curie temperature, grain size and permeability of $Ni_{1-x}Zn_xFe_2O_4$ ($0 \leq x \leq 1$ with the step increment of 0.2) prepared by novel hydrazinium metal hydrazinecarboxylate precursors. The lattice constant increases, whereas the Curie temperature decreases with the rise in zinc concentration. Theoretical density, grain size and permeability were found to increase with the increase in sintering temperature.

Verma et al. [36] investigated the temperature dependence of electrical properties of $Ni_{1-x}Zn_xFe_2O_4$ (x = 0.2, 0.35. 0.5, 0.6) prepared by citrate precursor technique. Author observed high activation energy in the range 0.55eV to 0.73eV indicating low eddy current losses and high feasibility of their utility at higher frequencies. The variations in activation energy with composition and sintering temperature have been explained on the basis of site occupancy in ferrites and atomic radii of the constituent metal ions. Resistivity and activation energy decreases with the increase in temperature, whereas, the dielectric constant and dielectric loss angle both increases with the rise in temperature.

Study on lattice parameter, grain size, FTIR and morphology were reported by Bahout et al. [37] for $Zn_{1-x}Ni_xFe_2O_4$ (x= 0, 0.25, 0.50, 0.75 and 1) prepared by soft-chemistry method using citrate-ethylene glycol precursors. Ferrites were formed at a relatively low temperature of 650^oC. The lattice parameter decreased with the rise in nickel concentration, whereas, grain size increased with the increase in annealing temperature. Ghazanfar et al. [38] reported work on room temperature resistivity and activation energy of $Ni_xZn_{1-x}Fe_2O_4$ (x = 0.66, 0.77, 0.88, 0.99). Resistivity showed semiconductor like behavior, whereas, resistivity and activation energy both increases with the increase in nickel concentration.

Magnetic properties such as Curie temperature and permeability of $Ni_xZn_{1-x}Fe_2O_4$ (x=0.3 and 0.4) prepared using conventional ceramic powder methodology were reported by Rosales et al. [39]. Author used different sintering temperatures and time, and observed that Curie temperature and permeability increases with the increase in sintering time. Effect of sintering conditions on resistivity and dielectric properties of $Ni_{0.65}Zn_{0.35}Fe_2O_4$ were investigated by Rao et al. [40]. Decrease in resistivity with increasing sintering time and sintering temperature was observed. Dielectric constant showed increase with sintering temperature. The dielectric constant and dielectric loss tangent were found to be decreasing with the increase in frequency.

Sample morphology, hysteresis loss, coercivity and maximum permeability were measured, by Costa et al. [41] for $Ni_{0.5}Zn_{0.5}Fe_2O_4$ prepared by combustion synthesis, using urea as fuel. The measurements were carried out for sintering temperature in the range of 1100°C to 1400°C (step of 100°C). It was noted that average grain size, maximum flux density and maximum permeability increases whereas, coercivity, and hysteresis loss decreases with the rise in sintering temperature. Optimum grain growth was obtained for samples sintered at 1200°C and abnormal grain growth with larger trapped porosity was observed for sintering temperature above 1300°C.

El-Sayed [42] reported variation of lattice constant, bulk density, X-ray density and porosity of $Ni_{1-x}Zn_xFe_2O_4$ ferrites (x= 0.1, 0.3, 0.5, 0.7 and 0.9) prepared by ceramic method and sintered at 1250°C in static air atmosphere. It was noted that lattice constant and porosity increased whereas, bulk density and X-ray density decreased with the increase in zinc concentration. He reported exaggerated grain growth with fine pores inside the grains for sample sintered at 1250°C.

Solid state synthesis of $Ni_{1-x}Zn_xFe_2O_4$ (x=0, 0.1, 0.2, 0.3, 0.4, and 0.5) and results of structural parameters like lattice constant, jump rate, polaron radius, bond lengths and porosity obtained using XRD data were reported by A. S. Fawzi et al. [43]. Radius of octahedral sites, X-ray density, and experimental density found to decrease with increase in Zn concentration whereas, porosity and tetrahedral sites radius increases. Variation of dielectric constant and loss tangent as function of temperature were also studied and explained in terms of electron exchange between Fe^{2+} and Fe^{3+}, suggesting that polarization was due to heterogeneity of the samples. Dc resistivity variation with temperature shows two regions of conductivity and change in slope of curves beyond transition temperature indicate change in activation energy for all the samples. N. D. Chaudhari et al. [44] carried out investigation on initial permeability and loss factor for $Ni_xZn_{1-x}Fe_2O_4$ (x= 0.28 to 0.40 in step of 0.02) synthesized by oxalate precursor method. Initial permeability increases with increase in Ni up to x=0.32 and beyond which it decreases. Permeability results were explained as effect of grain size, as well as on saturation magnetization and anisotropy constant. Method of preparation and high density of samples were attributed to be responsible for resulting into low loss factor.

Mangalaraja et al. [45] investigated increase in bulk density with the increase in sintering temperature and decrease in dielectric constant and dielectric loss factor with the increase in frequency for $Ni_{0.8}Zn_{0.2}Fe_2O_4$ ferrites. Samples were prepared by microwave-assisted flash combustion technique and sintering temperatures used were 1150°C to 1350°C (with step of 100°C). N.D. Chaudhari et al. [46] reported presence of Yafet Kittel type of spin and increase in magnetic moment (n_B) and remanance (R) ratio with addition of $Ni^{2+}$for $Ni_xZn_{1-X}Fe_2O_4$ (x=0.28–0.40 step of 0.02) synthesized by an oxalate precursor route starting with acetates. The presence of multidomain grains were confirm from thermally insensitive behavior of remanance ratio and coercivity in the samples.

$Ni_{1-x}Zn_xFe_2O_4$ (x= 0.2, 0.3, 0.4 and 0.5) prepared using non-conventional flash combustion and citrate gel decomposition techniques by R. V. Mangalaraja et al. [47] reported low remanent flux density and decrease in coercivity with increasing zinc content as well as sintering temperature. Tseng et al. [48] also reported increase in sintered density, average grain size and permeability whereas, decrease in resistivity with the rise in sintering temperature for $Ni_{0.5}Zn_{0.5}Fe_2O_4$ prepared by chemically co-precipitated powders and sintering temperature ranges from 1000°C to 1200°C in step of 50°C.

A claim was made by A. Verma et al. [49] of reduction in sintering temperature by at least 100°C and reduction in sintering time from more than 3 h for conventional method to 1 h in his non-conventional citrate precursor method designed to prepare nickel zinc ferrite. Samples showed low relative loss factor $\sim 10^{-4}$ to 10^{-5} in the frequency range 100 kHz to 8 MHz and optimum properties such as Curie temperature, saturation magnetisation, hysteresis loop and permeability loss factor were obtained for samples sintered at 1200°C. Increase in sintered density, grain size, saturation magnetization, remanent flux density whereas, decrease in coercivity, activation energy and porosity with the rise in sintering temperature were observed by Mangalaraja et al. [50] for $Ni_{0.8}Zn_{0.2}Fe_2O_4$ ferrites prepared using microwave-assisted flash combustion technique and sintering temperature of 1150°C, 1250°C and 1350°C.

V. L. O. Brito et al. [51] prepared nickel zinc ferrite using conventional ceramic method sintered at 1200°C, 1300°C and 1400°C showing promising results in use of these samples for temperature sensors at the human body temperature level. They investigated the variation of the real part of complex magnetic permeability for temperature sensitivity at frequency of 100 kHz and found highest magnitudes of temperature sensitivity occurred between 30°C and 50°C.

World wide researchers are engaged in adopting new methods to synthesize ferrites and tailoring of the preparation methods are being carried out to control critical parameters such as size, composition, shape, structure, physics and chemistry of samples. The controlling of the various characteristics such as physical, chemical, electrical, magnetic etc of the samples for specific application and performances are being critically investigated by researchers across the globe. The present work has also employed new method of preparation of ultra-fine nickel zinc ferrite samples. The sintering parameters (temperature time, rate of heating and cooling) selected to obtain bulk samples also differ from reported sintering parameters. The various results of nano and bulk nickel zinc ferrite investigated in the present work are superior compared to earlier reported results. The detailed comparisons of the results are provided in the Chapter Four, Chapter Five and Chapter Six.

References

1. A. D. Sheikh and V. L. Mathe, J Mater Sci, 43, (2008), 2018-2025.
2. P. Priyadharsini, A. Pradeep and G. Chandrasekaran, J. Magn. Magn Mater, 321 (2009), 1898-1903.
3. T. Slatineanu, A. R. Iordan, M. N. Palamaru, O. F. Caltun, V. Gafton and L. Leontie, Materials Research Bulletin, 46, (2011), 1455-1460.
4. A. C. F. M. Costa, E. Tortella, M. R. Morelli, M. Kaufman and R. H. G. A. Kiminami, J. Mater. Sci., 37, (2002), 3569-3572.
5. I. H. Gul, W. Ahmed and A. Maqsood, J. Magn. Magn Mater, 320, (2008), 270-275.
6. N. Sivakumar, A. Narayanasamy, N. Ponpandian and G. Govindaraj, J. Appl. Phys. 101, (2007), 084116(1-6).
7. X. Lu, G. Liang, Q. Sun and C. Yang, Materials Letters, 65, (2011), 674-676.
8. H. E. Zhang, B. F. Zhang, G. F. Wang, X. H. Dong and Y. Gao, J. Magn. Magn. Mater., 312, (2007), 126-130.
9. E. Manova, D. Paneva, M. Kostadinova, B. Kunev and I. Mitov, Bulgarian Academy of Sciences, (2008), BT-BG-06-1-4.
10. A. S. Albuquerque, J. D. Ardisson, A. Waldemar, A. Macedoa, C. Maria and M. Alves, J. Appl. Phys., 87(9), (2000), 4352-4357.
11. L. Yin and Q. Tai, Chin. Phys. Soc., 16 (12), (2007), 3837-3842.
12. E. E. Sileo, R. Rotelo, S. E. Jacobo, Physica B, 320, (2002), 257-260.
13. J. Azadmanjiri, Materials Chemistry and Physics, 109, (2008), 109-112.
14. M. Stefanescu, M. Stoia, O. Stefanescu and P. Barvinschi, J Therm Anal Calorim, DOI 10.1007/s10973-009-0168-3, (2009).

15. S. Nasir, G. Asghar, Muhammad Ali Malik and M. Anis-ur-Rehman, J Sol-Gel Sci Technol, DOI 10.1007/s10971-011-2468-x, (2011).
16. A. M. El-Sayed, E. M. A. Hamzawy and M. Fur., Chemie, 137, (2006), 1119-1125.
17. B. P. Rao, O. Caltun, W.S. Cho, C. O. Kim and C. G. Kim, J. Magn. Magn Mater, 310, (2007), e812–e814.
18. P. P. Sarangi, S. R. Vadera, M. K. Patra and N. N. Ghosh, Powder Technology, 203, (2010), 348-353.
19. Z. Beji, L. S. Smiri, N. Yaacoub, J. M. Greneche, N. Menguy, S. Ammar and F. Fievet Chem. Mater., (2010), 22, 1350-1366.
20. A. E. Virden and K. O’Grady, J. Magn. Magn Mater, 291, (2005), 868–870.
21. R. C. Kambale, N. R. Adhate, B. K. Chougule and Y. D. Kolekar, Journal of Alloys and Compounds, 491, (2010), 372-377.
22. P. Yadoji, R. Peelamedu, D. Agrawal and R. Roy, Mater. Sci. Eng.B, 98, (2003), 269-278.
23. A. K. M. A. Hossain, S. T. Mahmud, M. Seki, T. Kawai and H. Tabata, J. Magn. Magn.Mater., 312, (2007), 210-219.
24. A. Pradeep, C. Thangasamy and G. Chandrasekaran, J. of Matr. Sci: Matrs. in Elec., 15, (2004), 797-802.
25. M. El-Shabosy, J. Magn. Magn Mater, 172, (1997), 188-192.
26. A. M. Abdeen, J. Magn. Magn Mater, 192, (1919), 121-129.
27. N. S. S. Murthy, M. G. Natera, S. I. Youssef, R. J. Begum and C. M. Srivastava, Phys.Rev., 181, (1969), 969-977.
28. S. S. Jadhav, S. E. Shirsath, B. G. Toksha, S. J. Shukla and K. M. Jadhav, Chin. J. Chem. Phys., 21(4), (2008), 381-386.

29. M. U. Islam, T. Abbas, S. B. Niazi, Z. Ahmad, S. Sabeen and M. A. Chaudhry, Solid State Commun, 130, (2004), 353-356.

30. P. G. Bercoff and H. R. Bertorello, J. Magn. Magn. Mater., 213, (2000), 56-62.

31. C. Pasnicu and D. Condurache, Tomul XL, s. I.b.fasc.2 Fizica Solidelor-Fizica Teoretica, (1994).

32. A. Verma, T. C. Goel, R. G. Mendiratta and M. I. Alam, Mater. Sci. Eng.B, 60, (1999), 156-162.

33. R. V. Mangalaraja, S. Ananthakumar, P. Manohar an F. D. Gnanam, Mater.Lett., 57, (2003), 1151-1155.

34. J. Bera and P.K. Roy, j.physb doi:10.1016.(2005).03.010

35. T. T. Srinivasan, P. Ravindranathan, L. E. Cross, R. Roy and R. E. Newnham, J. Appl.Phys., 63, (1988), 3789-3791.

36. A. Verma, O. P. Thakur, C. Prakash, T. C. Goel and R. G. Mendiratta, Mater. Sci. Eng.B, 116, (2005), 1-6.

37. M. M. Bahout, S. Bertrand and O. Pena, J. Solid State Chem., 178, (2005),1080-1086.

38. U. Ghazanfar, S. A. Siddiqi and G. Abbas, Mater. Sci. Eng.B, 118, (2005), 132-134.

39. M. I. Rosales and M. P. Cuautle, J. Mater. Sci., 33, (1998), 3665-3669.

40. B. P. Rao and K. H. Rao, J. Mater. Sci., 32, (1997), 6049-6054.

41. A. C. F. M. Costa, E. Tortella, M. R. Morelli and R. H. G. A. Kiminami, J. Magn. Magn. Mater., 256, (2003), 174-182.

42. A. M. El-Sayed, Ceram. Internal., 28, (2002), 363-367.

43. A. S. Fawzi, A. D. Sheikh and V. L. Mathe, Journal of Alloys and Compounds, 502, (2010), 231-237.

44. N. D. Chaudhari, R. C. Kambale, J. Y. Patil, S. R. Sawant and S. S. Suryavanshi, Materials Research Bulletin, 45, (2010), 1713-1719.

45. R. V. Mangalaraja, S. Ananthakumar, P. Manohar, F. D. Gnanam and M. Awano, Mater. Lett., 58, (2004), 1593-1596.

46. N. D. Chaudhari, R. C.Kambale, D. N.Bhosale, S. S. Suryavanshi and S. R. Sawant, J. Magn. Magn Mater, 322, (2010), 1999-2005.

47. R. V. Mangalaraja, S. Ananthakumar, P. Manohar and F. D. Gnanam, Materials Letters, 57, (2003), 2666-2669.

48. T. Y. Tseng and J. C. Lin, IEEE Trans. Magn., 25, (1989), 4405-4408.

49. A. Verma, T.C. Goel, R. G. Mendiratta and P. Kishan, J. Magn. Magn Mater, 208, (2000), 13-19.

50. R. V. Mangalaraja, S. Ananthakumar, P. Manohar and F. D. Gnanam, J. Magn. Magn.Mater., 253, (2002), 56-64.

51. V. L. O. Brito, L. F. A. de Almeida, A. K. Hirata and A. C. C. Migliano, Progress In Electromagnetics Research Letters, Vol. 13, (2010), 103-112.

CHAPTER 3

SAMPLE PREPARATION

3.1 Introduction

Nanotechnology manipulates matter at the scale of one billionth of a meter (10^{-9} m). The interest in nanoscale materials sparks from the fact that new properties are inherited at this length scale that bulk solid or isolated molecules do not usually exhibit. Therefore nanomaterials are important due to changes in properties with size and shape [1] .There are two fundamental approaches in fabricating nanomaterials. The first is “Bottom-up” approach wherein, construction of nanomaterial is from basic building blocks, such as atoms or molecules. The second approach, the “top-down” method, involves restructuring a bulk material in order to create a nanomaterial [2]. Bottom-up approach is much better suited to generate uniform particles, often of distinct size, shape, and structure.

Preparation of nanomaterials can be broadly classified into physical and chemical methods. The physical methods are based on subdivision of bulk metals, including mechanical crushing or pulverization of bulk metal, arc discharge between metal electrodes, etc. The common problems associated with physical methods and conventional mixed oxide method are generally contamination during milling, non stoichiometric composition, higher calcination and sintering temperatures, non uniform particle size distribution etc. All these discrepancies make the product non reproducible in terms of their electric and magnetic properties.

The chemical synthesis of nanomaterials inevitably is related to the crystallization of solid phase from a solution. Various wet chemical routes such as co-precipitation, spray pyrolysis, hydrothermal, sol-gel and sol-gel auto combustion synthesis have been adopted as an alternative option. The homogenized composition, smaller crystallite size and low processing temperature are the main advantages of wet chemical routes over conventional methods [3]. Some methods can be considered as either chemical or physical routes depending on the medium, the precursors and the operating conditions such as milling used in the sample preparation. For example, mechano-chemical synthesis involves mechanical activation of solid state displacement reactions and milling of precursor powders to form nanomaterials.

3.2 Different Methods of Synthesis of Ferrites

The synthesis of ferrite nanoparticles has been an area of study for a long time because of their potential in advanced applications. These particles are very interesting in practical applications such as magnetic recording, magnetic fluids, permanent magnets, etc. [4]. A wide variety of methods are reported for the synthesis of different spinel ferrite nanoparticles such as mechanical milling, gas condensation, aerosol, co-precipitation, sol-gel processing, hydrothermal treatment, normal or reverse/inverse microemulsion method etc. However, method of preparation decides about size control, size distribution, control on shapes and other properties [5]. Since, each method has its own advantage and disadvantage, suitability of a particular method for preparing desired sample mainly depends on the properties we are looking for. We have presented here an overview and processing steps along with some of the raw materials commonly used in few different methods used for synthesis of magnetic materials in general and ferrites in particular.

3.2.1 Solid state or Conventional ceramic method

In conventional ceramic route, metal oxides were thoroughly mixed in appropriate stoichiometric ratio and calcined at ~700-1000°C for 5 to 10 hr in air. After calcination, milling is again required to break down the agglomerates to improve compaction and thermal reactivity of powder, reduce particle sizes etc. The wet milling i.e. grinding in some alcoholic or aqueous medium is preferred rather than dry milling to improve particle size. This milled powder is pressed in pellets/torroids and final sintering is done under controlled atmosphere at ~1200°C to 1350°C. For example S. Zahi et al. [6] reported Ni-Zn ferrites prepared by conventional method given by Equation 3.1.

$$0.3NiO + 0.7ZnO + Fe_2O_3 \rightarrow Ni_{0.3}Zn_{0.7}Fe_2O_4 \qquad 3.1$$

The metal oxides were blended and homogenized in a wet ball mill for 16 h. The resultant slurry was filtered and masses obtained were dried in an oven. The mixed powder of the Ni-Zn ferrite was preheated at 1150°C for10 h. The preheated powder was milled in a planetary micro mill using ceramic balls for 5 h. Then, powder was blended with polyvinyl alcohol and was pressed at 220MPa into torroidal shapes followed by sintering in air, at 1300°C for 10 h. Similarly, Sivakumar et al. [7, 8] reported preparation of bulk $Ni_{0.5}Zn_{0.5}Fe_2O_4$ ferrite via conventional ceramic method using calcination temperature of 1173 K in air for 5 h. The pellets of ferrite were then sintered at 1473 K for 5 h in air and were further reduced to powders by milling using zirconia vials and balls at 300 rpm for 30 min. This powder was taken to be as-prepared sample. The time of milling affects size distribution, coercivity, magnetization, chemical composition and morphology of nanoparticles.

This method has disadvantages such as, it needs very high temperature, poor homogeneity, monitoring progress of reaction is difficult and completion of reaction is decided by trial and error method etc. [9, 10]. As the procedure of ceramic method is costly, time consuming and particles showing large size distribution, it was replaced by chemical and thermal methods [11]. Although it is old, it is used in producing large scale different commercial products, and is still in practice to meet the massive demand of soft ferrite industry [12].

3.2.2 Arc discharge method and Hydrogen plasma metal reaction

Most nano capsules are synthesized by arc discharge method, in which metal precursors are normally packed inside a cave drilled into a graphite electrode and then subjected to arc vaporization. Dravid and coworkers [13] modified the arc discharge method successfully to produce nanophase Ni encapsulated in graphite shells. Recently, Zhang et al. [14] have used the arc discharge method in a diborane atmosphere to prepare amorphous boron oxide encapsulated magnetic nanocapsules. This method requires temperature as high as 3500^{o}C for the cathode and over 2000^{o}C for anode. As a result, metal graphite composite evaporates while carbon and metal vapors are deposited on the cathode surface to form encapsulation structured nanoparticles. Hydrogen plasma metal reaction (HPMR) method developed by Ohno and Uda [15] is used to produce nanoparticles by dc thermal plasma in a mixture of hydrogen and argon gas at vacuum. In principle, it is similar to arc discharge method. However, there are some differences, such as HPMR is an aerosol method, and is a very promising way to produce inter-metallic compound nanoparticles with possibility to control the content of each element in nanoparticles accurately. In addition, HPMR is found suitable to prepare industrially important ultra-fine particles (UFPs) at low cost [16, 17]. Nanoparticles of several metals and alloys, such as Mg, Ni, Cu, Ag, Fe-Co, Fe-Ni, and Fe-Cr have been prepared by HPMR.

3.2.3 Spray pyrolysis method

Spray pyrolysis is an excellent technique for direct and continuous production of well defined magnetic nanoparticles under exhaustive control of the experimental condition. In this process, solid is obtained by spraying solution into a series of reactors, where, aerosol droplets undergo evaporation of the solvent and solute condensation within the droplet. There after drying and thermolysing of the precipitated particles is done at higher temperature [18]. Recently, this method has been used to prepare colloidal aggregates of superparamagnetic maghemite nanoparticles in the form of hollow or dense spheres. This method allows preparation of air-stable superparamagnetic α-Fe metallic and FeCo nanomagnets encapsulated in silica or alumina [19].

3.2.4 Spray drying process

It is a process to produce fine spherical powder particles. In this method, aqueous or organic base solution is prepared from metal precursors and sprayed in a chamber. A hot gas/air is also passed through this chamber for drying of the aerosol particles. The viscosity of solution, temperature of main chamber and flow rate of drying gas are the main controlling parameters of this process. The fine powder particles having uniform size with high yield ratio are the key features of this process. This process has been adopted for large scale production of different ceramic oxides and pigments for paints. The spray dryer setup is different from hydrothermal or co-precipitation processes. If the sol spray is composed of some reactive or flammable species then inert gas has to be supplied instead of ordinary air to get powder particles. This process has been employed by many scientists to get soft ferrite powders [20, 21, 22].

3.2.5 Laser pyrolysis

Laser driven pyrolysis of organometallic precursors is a general synthetic tool for nanoscale particles ranging from 2 nm to 20 nm [23, 24]. It involves heating of mixture of flowing gases with a continuous wave of carbon dioxide laser, which initiates and sustains a chemical reaction [18]. Above a certain pressure and laser power, a critical concentration of nuclei is reached in the reaction zone, which leads to homogeneous nucleation of particles that are further transported to a filter by an inert gas. Laser pyrolysis is based on the resonant interaction between laser photons and at least one gaseous species, reactants or sensitizer. A sensitizer is an energy transfer agent that is excited by the absorption of the CO_2 laser radiation and transfers, by collision, the absorbed energy to the reactants [25]. Biocompatible magnetic dispersions have been prepared from gamma Fe_2O_3 nanoparticles (5 nm) synthesized by continuous laser pyrolysis of $Fe(CO)_5$ vapors. Advantages of this method are small and narrow particle size distribution and also near absence of aggregation. Moreover, the use of CO_2 laser and a continuous flow reactor demands large experimental setup.

3.2.6 Micro-emulsion method

Micro-emulsion is an isotropic and thermodynamically stable single phase formed by at least three components, two of them are non miscible and a third, called surfactant, has an amphiphilic behavior. Depending on the proportion of suitable components and hydrophilic-lipophilic balance (HLB) value of the surfactant used, the formation of micro droplets can be in the form of oil-swollen micelles dispersed in aqueous phase as the oil/water (O/W) micro-emulsion or water-swollen micelles dispersed in oil as the water/oil (W/O) micro-emulsion (reverse or inverse micro-emulsion). In the intermediate phase region between O/W and W/O micro-emulsions, there may exist bi-continuous micro-emulsions with aqueous and oil domains interconnected randomly in the form of sponge-like microstructures [26]. A variety of surfactants such as sodium dodecyl sulfate (SDS), cetyltrimethylammonium bromide (CTAB), polyvinylpyrrolidone (PVP), diethyl-sulfosuccinate (DES) etc. can be used for preparing nanoparticle materials by micro-emulsion method [1].

The water-in-oil micro-emulsion has been widely used to synthesize nanoparticles iron compounds including iron oxide, iron boride, gold coated iron nanoparticles, magnetic polymeric particles, iron oxide-doped alumina nanoparticles, silica-coated iron oxide nanoparticles etc [27]. Magnetite nanoparticles around 4 nm in diameter have been prepared by the controlled hydrolysis with ammonium hydroxide of $FeCl_2$ and $FeCl_3$ aqueous solutions within the reverse micelle nano-cavities generated by using aerosol optical thickness (AOT) as surfactant and heptane as the continuous oil phase [18]. Synthesis of nanocrystalline nickel zinc ferrites <10 nm via a micro-emulsion route using low-temperature co-precipitation method within the reverse micelles of ternary CTAB/1-hexanol/water micro-emulsions was reported [5].

Some of the disadvantages of this method are lack of crystallization or poor degree of crystallization that can be improved by annealing process or working in an inert atmosphere or by using large amounts of Fe^{2+}[28,29]. This method is expensive due to the large amounts of surfactant (as much as 20-30%) added to the system. Another drawback is that the surfactant ensuring colloidal stability is adsorbed on the surface of nanoparticles, thereby decreasing their usability.

3.2.7 Hydrothermal method

Hydrothermal is a well known method to synthesize nano size crystals of complex compounds (perovskite, spinel etc.) under high temperature and pressure conditions. It involves reactions of mixed oxides or hydroxides of iron and other selected metals carried out in water under supercritical conditions, i.e. at temperatures above 200^{o}C and under a pressure higher than 14 MPa [11]. The solvent is not limited to water but includes also other polar or non polar solvents, such as benzene, and the process is more appropriately called solvo-thermal synthesis in the different solvents [1]. To synthesize any particular composition by this method, solution of water soluble salts (hydroxide, chloride, nitrate etc.) is prepared. After adjusting the pH of solution, it is put in an autoclave. A suitable pressure is built by raising the temperature of vessel. After a number of experiments, reaction time is adjusted to get nano crystallites of a particular compound. The crystals settled at the bottom of vessel are filtered out and washed with de-mineralized water/organic solvent many times, dried in air and finally calcined to obtain purified nanocrystalline powder. Low synthesis temperature, nanosize powder production, homogeneous nucleation processes, narrow particle size distribution, single phase, controlled particle morphology, high density, low porosity and high-purity powders and environment friendly are the main advantages of this method. It has been employed by numerous scientists to synthesize nanosize crystallites of soft ferrites [30, 31, 32].

3.2.8. Sol gel

In sol-gel process, sol stands for stable suspension of colloidal particles in a solvent and gel is three dimensional porous network structures of constituent elements [11]. It involves transition of a system from a liquid (“sol”) into a solid (“gel”) phase. In this case, precursor is subjected to a series of hydrolysis and polymerization reactions to form a colloidal suspension (gel) [3]. The main steps are addition of complexing agent (organic acid) to aqueous solution of metallic salts followed by evaporation in rotary evaporator at 75°C±5 to yield a highly viscous gel. The wet gel is then placed in vacuum oven and heated at 65°C±5 for 12 hours to get dry gel having an amorphous/glassy structure, there after it is calcined in air at appropriate temperature (300-700°C for ferrites) to remove the organic and volatile species to get fine crystalline oxide powder.

S. Zahi et al. [33] have reported sol–gel method used in preparing Ni-Zn ferrite. The reaction process is given by Equation 3.2 and 3.3. The metal acetates were first dissolved in acetic acid and a small amount of water under a constant stirring at the room temperature. The solutions were then mixed and stirred for about 6 h. Constant stirring was carried out and temperature was maintained at about 70^oC until gel was formed. This gel was heated at 600^oC for 4 h to form powder of Ni-Zn ferrite having narrow particle size distribution.

$$0.3Ni(CH_3C00)_2 + 0.7Zn(CH_3C00)_2 + 2Fe(CH_3C00)_3 + 8H_2O \rightarrow Ni_{0.3}Zn_{0.7}Fe_2(OH)_8 + 8CH_3C00H \tag{3.2}$$

$$Ni_{0.3}Zn_{0.7}Fe_2(OH)_8 + 8CH_3C00H \rightarrow Ni_{0.3}Zn_{0.7}Fe_2O_4 + 4H_2O \; + \; \text{Gases} \tag{3.3}$$

The high cost involved in the use of starting materials is the main disadvantages of this unconventional method. In addition, the much higher content of the organic matter associated with the metals are known to fly during the heat treatments.

3.2.9 Combustion process

The combustion process may be termed as self propagating high temperature synthesis (SHS). In order to obtain nanosized powder of ceramic oxides i.e. magnetic, semi- conducting oxides, oxides for catalysis, sensors etc. combustion method is one of the best choices. It is simple, rapid and low cost method to obtain nanosized powder of transition metal oxides. There are three most famous combustion synthesis routes such as, a) condensed phase combustion in which reactants are in solid state phase, b) solution combustion synthesis in which primary reactants are in liquid phase and c) gas phase combustion process in which initial reaction occurs in gaseous phase. Fuel is an essential ingredient of each route. It is used to activate the combustion/ignition process. Among these routes, solution combustion synthesis is very simple and versatile method to obtain nanosized oxide powder and is also called as modified form of sol gel process. In this process, particle size varies from 20-100 nm depending upon synthesis conditions. The high yield and compositional homogenization of synthesized product are remarkable advantages of solution combustion synthesis [34]. The exothermicity of ignition/

combustion reaction is controlled by the type of fuel and fuel to oxidant ratio. Citric acid, tartaric acid, urea, glycine, hydrazine etc. are most commonly used fuels. In this process, aqueous solution of desired metal salts is mixed with suitable organic fuel and a strong base is added to adjust pH and then evaporated at 70-80°C to get dry gel. This dry gel is heated until ignition gets started (200°C to 300°C) and the entire gel is converted into fine fluffy powder. Single step combustion that gives Mn-Zn ferrite powder was reported by S. Lorentzou et al. and chemical reaction is given by Equation 3.4 [35]. Where, x is the molar fraction of metal salts.

$$2Fe(NO_3)_3 + xMn(NO_3)_2 + (1-x)Zn(NO_3)_2 + 3C_6O_7H_8 + 8HNO_3 + O_2 \rightarrow Mn_xZn_{1-x}Fe_2O_4 + 18CO_2 + 8N_2 + 24H_2O \quad 3.4$$

3.2.10 Co-precipitation method

The precipitation reactions involve separation of the nucleation and growth of the nuclei. In this process the reaction species (metallic salts of alkoxide, nitrate, oxalate, sulfate etc.) are dissolved in some aqueous/organic medium in an appropriate proportion and, with the addition of an inorganic solvent (sodium hydroxide, ammonia, hexane etc.) pH of the solution is adjusted between 8 to 14 and continues stirring is carried out . Sometimes, heat is also provided to complete the reaction. Precipitates get settled at the bottom of flask. They are filtered and washed number of times with water and alcoholic solvents to remove impurities and then dried in air. In order to obtain final crystal structure, powder is calcined in air [36, 37]. The reaction principle for magnetite spherical particles reported by Guo et al. [18] is given by Equation 3.5.

$$2Fe^{3+} + Fe^{2+} + 8OH \Leftrightarrow Fe(OH)_2 + 2Fe(OH)_3 \rightarrow Fe_3O_4 + 4H_2O \quad 3.5$$

The difficulty in preparing Fe_3O_4 magnetic nanoparticles by chemical co-precipitation is the tendency of agglomeration of particles. In addition to magnetite, the other ferrites are also prepared by co-precipitation of corresponding divalent metals salts, such as Co(II), Cu(II), Ni(II), Mn(II), and Fe(III) with an alkali [38, 39, 40]. The emission of fumes and incorporation of impurities in synthesized compounds are the common problems associated with this method [3].

3.2.11 Sonochemical method

In sonochemical method molecules undergo chemical reactions due to the application of powerful ultrasound radiation (20 KHz to 10 MHz) [41]. The sonolysis technique involves passing sound waves of fixed frequency through a slurry or solution of carefully selected metal complex precursors. In a solvent with vapor pressure of a certain threshold, the alternating waves of expansion and compression cause cavities to form, grow, and implode [42]. The physical phenomenon responsible for the sonochemical process is acoustic cavitation. Ultrasound power effects the occurring chemical changes due to cavitations phenomena involving the formation, growth, and collapse of bubbles in liquid [43,44,45]. Sonochemistry has been used to prepare various kinds of amorphous magnetic nanomaterials of metal, metal alloy, oxide, ferrite, and nitride and has been extended to produce core-shell type materials [45].

3.2.12 Polyols

In polyol process, liquid polyol acts as solvent of the metallic precursor, reducing agent and in some cases as a complexing agent for metallic cations. Fine metallic particles can be obtained on reduction of dissolved metallic salts and direct metal precipitation from a solution containing a polyol. The metal precursor can be highly or only slightly soluble in the polyol. The solution is stirred and heated to a given temperature reaching the boiling point of the polyol for less reducible metals [18]. By controlling the kinetics of the precipitation, non agglomerated metal particles with well defined shape and size could be obtained. Chimie douce route is a modified polyol process reported for preparing nickel zinc ferrites. This route involves forced hydrolysis of metallic salts dissolved and heated in a polyol. Polyols plays a role of crystal growth media for the synthesis of particles with narrow size distribution and high crystallinity in nickel zinc ferrites [46, 47]. This method allows simultaneous control of the morphology and the crystalline quality of the particles which is difficult in other low temperature synthesis methods for example, reverse micelle technique, hydrothermal technique etc. Also, Fe_3O_4 magnetic nanoparticles were prepared with the co-precipitation method combining a surface decoration process, and the polyol process.

3.2.13 Thermolysis of organometallic precursors

A two-step thermal decomposition of iron pentacarbonyl in the presence of a stabilizing polymer provides 10-20 nm mono disperse magnetite nanoparticles [48]. The process is based on the formation of primary Fe nanoparticles in a non polar liquid followed by their subsequent oxidation to magnetite particles. The decomposition temperature plays the crucial role in the determination of the particle size and poly-dispersity [49]. Surfactant (e.g. oleic acid) has to be used, it can, however, hinder subsequent surface modification. The decomposition of iron precursors in the presence of hot organic surfactants has yielded markedly improved samples with good size control, narrow size distribution and good crystallinity of individual and dispersible magnetic iron oxide nanoparticles [18]. The magnetic metal oxides nanocrystals can be prepared by simply substituting different metal precursors for iron. The thermal decomposition of $(\eta C_5H_5)CoFe_2(CO)_9$ with oleic acid in octyl ether followed by oxidizing by trimethylamine N-oxide ($(CH_3)_3NO$) can form $CoFe_2O_4$ nanocrystals [50].

3.3 Synthesis of Ultra-Fine $Ni_xZn_{1-x}Fe_2O_4$ in Present Study

The various steps involved in the method of sample preparation employed in the present work are shown in the flow chart in Fig. 3.1. Calculated amount of nickel nitrate hexahydrate and zinc nitrate hexahydrate powder were taken as per the required composition and are dissolved in sufficient volume of distilled water to obtain solution mixture of two ions. Calculated amount of ferrous sulphate heptahydrate was taken such that proportion of Fe^{2+} to (Ni^{2+}+Zn^{2+}) was maintained as 2:1. This Fe^{2+} salt was dissolved in sufficient amount of distilled water and requisite amount of aqueous solution of barium nitrate was added to precipitate sulphate (SO_4^{2-}) as barium sulphate ($BaSO_4$) in the ferrous nitrate solution. Mixture was filtered to remove insoluble barium sulphate and further washed with water to remove traces of Fe^{2+} ions. This in situ prepared filtered ferrous nitrate solution was added to aqueous solution of nickel zinc nitrate followed by addition of appropriate amount of solution containing calculated amount of nitrilotriacetic acid (NTA) $N(CH_2COOH)_3$ and hydrazine hydrate $H_4N_2.H_2O$. The entire solution was heated, until mixture gets converted into a thick/fluffy paste resulting in to a solid sticky mass. The solid sticky mass was then collected in a crucible and placed in domestic microwave oven (600 W, 2.4 GHz) for 5-6 seconds to decompose resulting into the desired ultra-fine $Ni_xZn_{1-x}Fe_2O_4$ material. The powder obtained was thoroughly

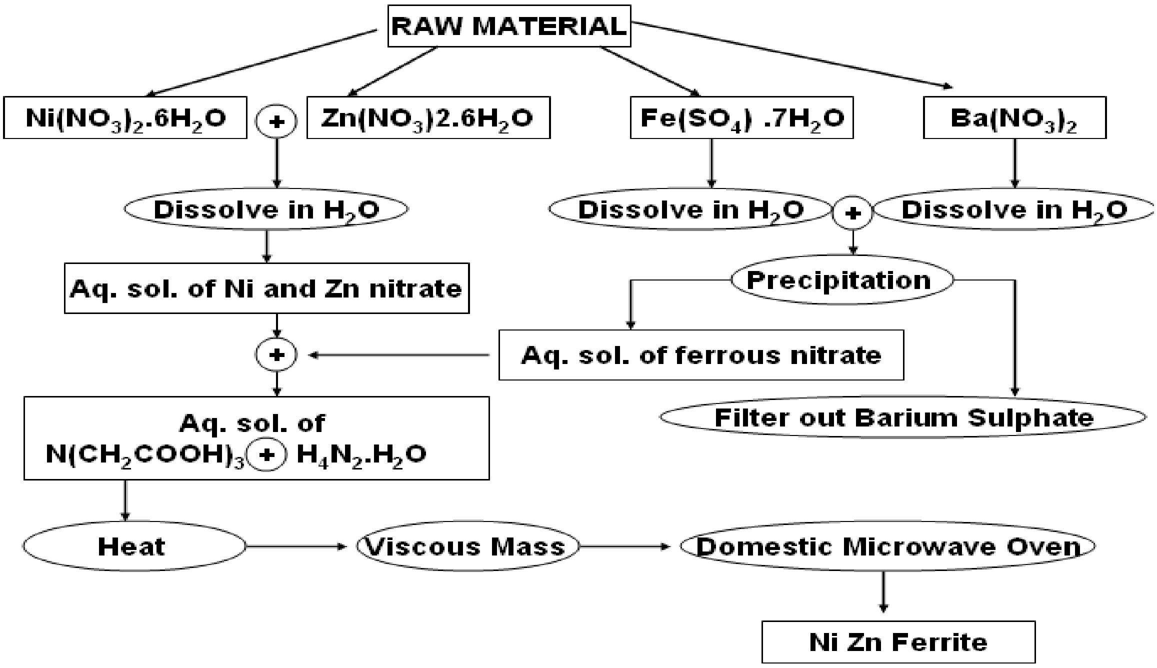

Fig. 3.1 Represents flow chart of the stages involved in process of preparation of ultra-fine Ni-Zn ferrite.

ground in an agate mortar for 10-15 minutes and was used as freshly prepared sample for characterization and other measurements. The general reactions in the process of sample preparation are given in Equation 3.7, 3.8 and 3.9. Where, x is the molar fraction of nitrate salts.

$$xNi(NO_3)_2.6H_2O + (1-x)Zn(NO_3)_2.6H_2O + H_2O \rightarrow xNi(NO_3)_2 + (1-x)Zn(NO_3)_2 + 2H_2O \quad 3.6$$

$$2FeSO_4.7H_2O + 2Ba(NO_3)_2 \rightarrow 2Fe(NO_3)_2 + 2Ba(SO_4) + 14H_2O \xrightarrow{filter\ out\ Ba(SO4)} 2Fe(NO_3)_2 + 14H_2O \quad 3.7$$

$$xNi(NO_3)_2 + (1-x)Zn(NO_3)_2 + 2H_2O + 2Fe(NO_3)_2 + 14H_2O + N(CH_2COOH)_3 + N_2H_4.H_2O \xrightarrow{\text{Heat}} \xrightarrow[\text{decomposition}]{\text{microwave}} Ni_xZn_{1-x}Fe_2O_4 + \text{Gases} \quad 3.8$$

Table 3.1 Amount of metal salts used in the synthesis of Ni-Zn ferrite samples.

Sr. No	Composition	Amount of $Ni(NO_3)_2.6H_2O$ (M.W. = 290.79) g.	Amount of $Zn(NO_3)_2.6H_2O$ (M. W. = 297.47) g.	Amount of $FeSO_4.7H_2O$ (M. W. = 278.02) g.
1	$Ni_{0.4}Zn_{0.6}Fe_2O_4$	5·8158	8·9241	27.802
2	$Ni_{0.5}Zn_{0.5}Fe_2O_4$	7.2697	7·4367	27.802
3	$Ni_{0.55}Zn_{0.45}Fe_2O_4$	7.9967	6.6931	27.802
4	$Ni_{0.6}Zn_{0.4}Fe_2O_4$	8.7237	5·9494	27.802
5	$Ni_{0.65}Zn_{0.35}Fe_2O_4$	9.4507	5·2057	27.802
6	$Ni_{0.7}Zn_{0.3}Fe_2O_4$	10.1776	4·4620	27.802

All the chemicals used in the present work are of AR grade and SD Fine make. The details of the amount of metal salts used for preparing 10 gm of Ni-Zn ferrite sample is given in Table 3.1.

3.3.1 Typical preparation of $Ni_{0.40}Zn_{0.60}Fe_2O_4$ sample

The method of sample preparations in the present work is described in detail in the Section 3.3. In a typical experiment for the preparation of $Ni_{0.4}Zn_{0.6}Fe_2O_4$, 5.8158 g of Ni $(NO_3)_2.6H_2O$ (0·4x0·05m), and 8·9241 g of $Zn(NO_3)_2{\cdot}6H_2O$ (0·6x0·05m) each dissolved in minimum quantity of distilled water and were mixed.

In situ $Fe(NO_3)_2$ solution was prepared by slow addition of aqueous solution of barium nitrate [0.1mole i.e. 29.734 g of Ba $(NO_3)_2{\cdot}2H_2O$] to aqueous solution of ferrous sulphate [0.1 mole i.e. 27.802 g of $FeSO_4{\cdot}7H_2O$]. Resultant mixture was filtered to remove white precipitate of barium sulphate. The precipitate on the filter paper was thoroughly washed and the filtrate containing ferrous nitrate was collected and kept in air tight stopper bottle.

Ferrous nitrate solution was added to the aqueous mixture of zinc nitrate and nickel nitrate. Appropriate amount of ligand solution was added to this mixture and then, resultant solution was evaporated to dryness. The dry mass was allowed to decompose by self ignition in a microwave oven to obtain Ni-Zn mixed ferrite product.

3.4 Preparation of Bulk $Ni_xZn_{1-x}Fe_2O_4$ Samples

The bulk samples of $Ni_xZn_{1-x}Fe_2O_4$ were obtained by sintering the pallets of freshly prepared nano samples at 900°C, 1000°C, 1100°C, 1200°C and 1300°C for 4 hours in air. The heating and cooling rate while sintering was fixed to 5°C min^{-1}. The pallets (10mm diameter and 2mm thickness) of nano samples were made by pressing finely grounded powder of nano samples using hydraulic press by applying pressure of 7.5 KN for 5 minutes.

References

1. C. Burda, X. Chen, R. Narayanan and M. A. El-Sayed, Chem. Rev., 105, (2005), 1025-1031.
2. R. Lane, B. Craig and W. Babcock, Amtiac, vol 6, 31, (2002).
3. A. Thakur and M. Singh, Ceram. Int., 29, (2003), 505-511.
4. J. A. Lopez Perez, M. A. Lopez Quintela, J. Mira, J. Rivas, and S.W.Charles, J. Phys. Chem., B 101, (1997), 8045-8052.
5. V. Uskokovi and M. Drofenik, Materials Science Forum, Vols. 453-454, (2004), 225-230.
6. S. Zahi A.R. Dauda and M. Hashim, Materials Chemistry and Physics, 106, (2007), 452–456.
7. R. Janot and D. Guerard, J. Alloys Compd, 333, (2002), 302-306.
8. R. J. Joseyphus, A. Narayanasamy, A. K. Nigam, and R. J. Krishnan, J. Magn. Magn. Mater., 296, (2006), 57-60.
9. N. Murillo, E. Ochoteco, Y. Alesanco and J. A. Pomposo, Nanotechnology 15, (2004), S322-S327.
10. Guozhong Cao, Nanostructures and nanomaterials, (2004).
11. D. Horak, M. Babic, H. M. Milan and J. Benes, J. Sep. Sci., 30, (2007), 1751 – 1772.
12. S. Sakurai, S. Sasaki, M. Okube, H. Ohara and T. Toyoda, Physica B, 403, (2008), 3589-3595.
13. V. P. Dravid, J. J. Host, M. H. Teng, B. Elliott, J. H. Hwang, D. L. Johnson, T.O. Mason and J. R. Weertman, Nature 374, (1995), 602-607,
14. W. Z. Wu, Z. P. Zhu, Z. Y Liu, Y. I Xie, J. Zhang and T. D. Hu, Carbon 41, (2003), 317-322.

15. S. Ohno, and M. Uda, Trans., Jpn. Inst. Met., 48, (1984), 640-644.

16. T. Liu, Y. H. Leng, and X .G. Li, Solid State Commun., 125, (2003), 391-395.

17. T. Liu, H. Y. Shao, and X. G. Li, J. Phys. Condens.Matter., 15, (2003), 2507-2511.

18. T. K. Indira, P. K. Lakshmi, International Journal of Pharmaceutical Sciences and Nanotechnology, Volume 3-3, (2010), 1035-1042.

19. P. Morales, M. P. Veintemillas Verdaguer, S. Teresita Gonzalez Carreno and T. Carlos Serna, J.Phys. D:, Appl. Phys., 36, (2003), R182–R197.

20. E. Munnier, S. C. Jonathan, C. Linassier, L. D Eyrolles, H. Marchais, S. K. Herve, P. Dubois and I. Chourpa, Int. J. Pharm., 363, (2008), 170–176.

21. L. Ning, L. Xiaojie, W. Xiaohong, Y. Honghao, M. Fei and S. Wei, Comp. Sci.Technol, 69, (2009), 2554–2558.

22. J. D. Qiu, M. Xiong, R. P. Liang, H. P. Peng, F. Liu and Biosens, Bioelectron., 24, (2009), 2649-2653.

23. C. A Grimes, D. Qian, E. C. Dickey, J. L. Allen, and P. C. Eklund, J. Appl. Phys., 87, (2000), 5642-5648.

24. B. David, N. Pizurova, O. Schneeweiss, P. Bezdicka, I. Morjan, and R. Alexandrescu, J. Alloys Compd.,378, (2004), 112-116.

25. F. Dumitrache, I. Morjan, R. Alexandrescu, V. Ciupina, G. Prodan, I. Voicu, C.Fleaca, L. Albu, M. Savoiu, I. Sandu, E. Popovici, and I. Soare, Appl. Surf.Sci., 25, (2005), 247-251.

26. I. Capek, Adv. Colloid Interface Sci., 110, (2004), 49-53.

27. S. Santra, R. Tapec, N. Theodoropoulou, J. Dobson, A. Hebard, and W.H Tan, Langmuir 17, (2001), 2900-2906.

28. P. Ayyub, M. Multari, M. Barma, V. Palkar and R. Vijayaraghavan, J. Phys. C, 210, (1988), 22-29.
29. M. Gobe, K. Kon-no, K. Kyori and A. Kitahara, J. Colloid Interface Sci., 93, (1983), 293-296.
30. C. Liu, C. Lin and Y. Fu, Jpn. J. Appl. Phys., 45, (2006), 4040-4041.
31. G. Ying-ying, S. Shang-bin, H. Ke-long and L. Jian-shen, J. Cent. South Univ. Tech., 7, (2000), 37-39.
32. H. Kumazawa, K. Oki, H. M. Cho and E. Sada, Chem. Eng. Commun., 115, (1992) 25-33.
33. S. Zahi, A. R. Daud and M. Hashim, Materials Chemistry and Physics, 106, (2007), 452–456.
34. H. Dislich, J. Non-Cryst. Solids, 80, (1986), 115-121.
35. S. Lorentzou, A. Zygogianni, K. Tousimi, C, Agrafiotisa and A.G. Konstandopoulos, J. Alloy Compd., 483, (2009), 302-305.
36. T. N. Brusentsova, N. A. Brusentsov, V. D. Kuznetsov and V. N. Nikiforov, J. Magn. Magn. Mater., 293, (2005), 298-302.
37. R. Massartan and C. R. Hebd Seances, Acad. Sci., Paris, C 291,(1980), 1-3.
38. E. Tamura and E. Matijevic, J. Colloid Interface Sci., 90, (1982),100 -109.
39. D. S. Kumar and K. C. Mouli, Int. J. Nanotech. Ap., 4, (2010), 51-59.
40. S. P. Gaikwad, S. R. Dhage, H. S. Potdar, Violet Samuel and V. Ravi, J.Electroceram., 14, (2005), 84-85.
41. K. S. Suslick, S. B. Choe, A. A. Cichowlas and M. W. Grinsta, Nature 353, (1991), 414-417.
42. H. Khalil, D. Mahajan, M. Rafailovich, M. Gelfer and K. Pandya, Langmuir, 20, (2004), 6896-6872.

43.V. G. Pol, M. Motiei, A. Gedanken, J. Calderon Moreno, and Y. Mastai, Chem. Mater., 15, (2003),1378-1382.

44. R.Vijayakumar, Y. Koltypin, I. Felner and A. Gedanken, Mater. Sci. Eng.,A 286, (2000), 101-106.

45. K.V. Shafi, A. Ulman, Z. Z. Yan, N.Yang, C. Estournes, H. White and M. Rafailovich, Langmuir 17, (2001), 5093-5097.

46. S. Chkaoundali, S. Ammar, N. Jouini, F. Fievet, M. Richard, E. Villain, J. Greneche, M. Danot and P. Molinie, J. Physics, Condens. Mater., 16, (2004), 4357-4362.

47. S. Ammar, A. Helfen, N. Jouini, F. Fievet, I. Villain, M. Rosenman, M. Danot and P. Molinie, J. Mater. Chem, 10, (2001), 186-190.

48. M. Gonzales and K. M. Krishnan, J. Magn. Magn. Mater., 293, (2005), 265-270.

49. W. Pei, H. Kumada, T. Natusme, H. Saito and S. J. Ishio, J. Magn.Magn. Mater., 310, (2007), 2375-2377.

50. T. Hyeon, Y. Chung, J. Park, S. Lee, Y. M. Kim and B. H. Park, J. Phys. Chem., B, 106, (2002), 6831-6834.

CHAPTER 4

CHARACTERIZATION

4.1 Introduction

A core foundation of useful ferrite materials lies in their properties and performances, and is the consequence of the processes used to prepare it. Characterization has the task of revealing structure in all detailed needed to make the link between processing stages, properties and performance. The structure of a material may be considered in general as atomic structure, atomic arrangement, microstructure, and macrostructure. Atomic structure influences how the atoms are bonded together, which in turn helps us to categorize materials as metals, ceramics and polymers and it permits us to draw some general conclusions concerning the mechanical properties and physical behavior of these materials. Similarly materials characterization can also describe those features of composition and structure of a material that are significant to yield information primarily related to materials properties, such as thermal, electrical, and mechanical properties. Characterization is usually achieved by allowing some form of probe to interact with sample under study. The most commonly used probes include X-ray diffraction, electron microscopy, optical microscopy and scanning probe microscopy. Thus structure determines properties, which can be changed by altering composition and/or processing. Thus one must understand “structure” and composition of materials so as to use the same for appropriate application.

The key methods of characterization employed in the present work are X-ray diffraction (XRD), Infrared Spectroscopy (IR), Transmission Electron

Microscopy (TEM), Atomic Force Microscopy (AFM), Scanning Electron Microscopy (SEM) and Energy Dispersive Spectroscopy (EDS). These methods are treated to get qualitative and quantitative information of the Ni-Zn ferrite samples prepared in present study. Experimental techniques used in this research work explores materials characterization with respect to crystal structure, phases involved, particle size, size distribution, cation distribution, density, porosity, micro-structural morphology and chemical composition.

4.2 Characterization Techniques

The experimental work such as sample preparation, the characterization techniques and parameters adopted in various techniques, and basic principle involved in the instruments used for characterization of samples is discussed in this Section.

4.2.1 X-ray diffraction spectroscopy (XRD)

XRD is nondestructive technique used to study the crystal structure of solids, phase identification, crystal parameters such as lattice constants, crystallite size, shape of unit cell, identification of unknown materials, defects, stresses, etc [1]. Each crystalline solid has its unique characteristic X-ray powder pattern, which may be used as a "fingerprint" for its identification. When X-rays interact with a crystalline substance, one gets a diffraction pattern. A crystal might be regarded as a three dimensional diffraction grating for X-rays whose wavelength is comparable with the atomic spacing and hence diffraction pattern provides information about the regular arrangements of atoms in the lattice. In context to nanocrystalline samples, the most important parameter that influences physical and chemical properties of the samples is average crystallite size. X-ray diffraction is the most convenient indirect method for the determination of average crystallite size of nanocrystalline samples [2].

4.2.1.1 Bragg's law of X-ray diffraction

The interaction of X-ray radiation with crystalline sample is governed by Bragg's Law. The X-ray diffraction can be visualized as X-rays reflecting from a series of crystallographic planes interfere constructively as shown in Fig. 4.1. This Fig. shows two parallel planes separated by a distance **d**. X-rays incident at glancing angle **θ** are reflected partially from each plane. Path difference between rays reflected from the first and second planes is the length **PB +BQ= 2d sin θ**. According to Bragg's law a diffraction peak is observed if the path difference is an integral multiple of the wavelength **λ** [3] and Bragg Equation is given by Equation 4.1.

$$n\lambda = 2d\sin\theta \qquad 4.1$$

Where, d is interplanar spacing, λ is wavelength, θ is Bragg angle and n=1, 2, 3…is order of diffraction.

The intensity of powder diffraction peaks is in principle determined by the structural factor, which in turn depends on crystal structures including relative positions of atoms in the unit cell, types of unit cells and other characteristics such as thermal motion, population parameters etc. The intensity of diffraction also depends on instruments including detector, slit and / or monochromator geometry. Besides phase identification of crystalline compound, various other parameters of the samples that can be obtained from the X-ray data are as follows.

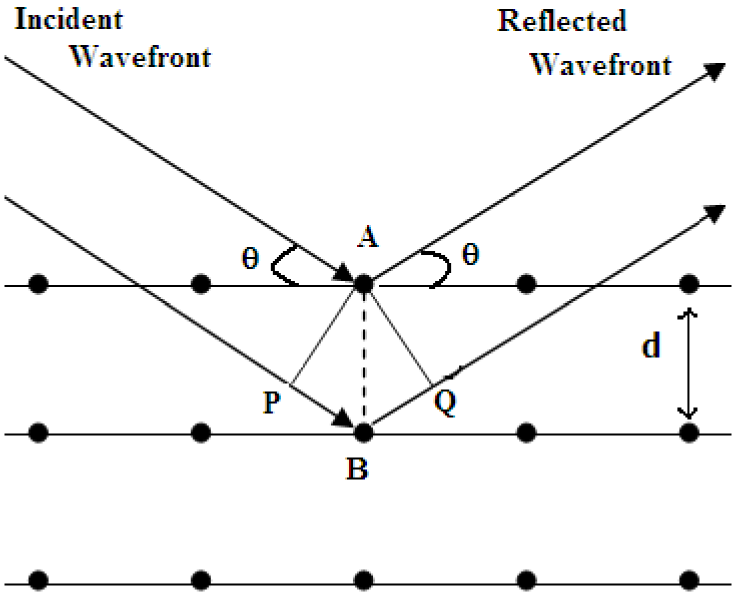

Fig. 4.1 Geometrical illustrations of crystal planes and Bragg's law.

4.2.1.2 Lattice constant (a)

The lattice constant '*a*' of each peak of the individual sample was calculated using Equation 4.2.

$$a = d\left(h^2 + k^2 + l^2\right)^{1/2} \qquad 4.2$$

Where *h*, *k* and *l* are Miller indices of crystal planes and *d* is an interplanar distance. More accurate values of '***a***' of each samples were calculated using Nelson-Riley method. The Nelson-Riley function *F(θ)* is given by Equation 4.3.

$$F(\theta) = \frac{1}{2}\left[\left(\cos^2\theta/\sin\theta\right) + \left(\cos^2\theta/\theta\right)\right] \qquad 4.3$$

In this method, values of lattice constant '*a*' of all the peaks obtained using Equation 4.2 of each sample were plotted against *F(θ).* The exact '***a***' was then determined using a least square fit method. The point where least square fit straight line cuts y-axis (i.e. at $F(\theta) = 0$) is considered as actual lattice constant of the sample [4].

4.2.1.3 Crystallite size (D)

The peak broadening in X-ray diffraction patterns of nanomaterials are due to their finite size effect. The average crystallite sizes of freshly prepared samples were calculated by substituting X-ray line broadening in Debye Scherrer formula given in Equation 4.4.

$$D = {}^{0.89\lambda}\!\big/_{\beta\cos\theta} \qquad 4.4$$

Where D is crystallite size in nm, λ is X-ray wavelength in Å, β is line broadening at full width half maxima intensity (FWHM) in radians, 0.89 is shape factor and θ is Bragg’s angle [3].

4.2.1.4 Micro-strain (ε)

It may be noted that in the above Scherrer Equation, it was considered that broadening of XRD peak was only due to the small size of the crystallites. However, there exist two other contributions to the line broadening, (i) from instrumental factors (negligible) and (ii) strain in the crystallites [5]. Thus stain broadening of the diffraction peaks must also be taken into account for an unambiguous determination of crystallite size. This strain broadening is explained by Williamson-Hall method [6]. In this method it is assumed that the size and strain contributions to the line broadening are independent of each pother and the observed line broadening (FWHM) is simply the sum of crystallite size broadening and strain induced broadening. In this method β (FWHM) is given by Equation 4.5. Here, ε is the root mean square value of the micro-strain introduced and D is crystallite size. Equation 4.6 is called as Williamson-Hall Equation.

$$\beta = \beta_D + \beta_\varepsilon \qquad 4.5$$
$$where \quad \beta_D = \frac{0.89\lambda}{D\cos\theta} \quad and \quad \beta_\varepsilon = 4\varepsilon\tan\theta$$

$$\therefore \beta\cos\theta = \frac{0.89\lambda}{D} + 4\varepsilon\sin\theta \qquad 4.6$$

By plotting Equation 4.6 the value of micro-strain ε may be estimated from the slope of the line and crystallite size D from the intersection with the y-axis. Micro-strain, i.e. strain that extends over a few lattice spacing in the crystallites is another important contribution to X-ray diffraction line broadening. Thus strain contribution may be resolved from the particle size contribution by Hall-Williamson method [7].

4.2.1.5 X-ray density (ρ_X)

The X-ray density was calculated using Equation 4.7.

$$\rho_X = \frac{8M}{Na_{ob}^3} \qquad 4.7$$

Where N is Avogadro’s number, M is molecular weight of the sample, and ‘a’ is lattice constant calculated using Nelson-Riley function.

4.2.1.6 Porosity (*P*)

The extent of porosity was calculated using Equation 4.8, where ‘ρ_B is mass density measured using Archimedes principle.

$$P = (\frac{\rho_X - \rho_B}{\rho_X}) \qquad 4.8$$

4.2.1.7 Cation distribution

In present work cation distributions were calculated using lattice constant obtained from Nelson–Riley method and site preferences of various atoms. In general cation distribution of $Ni_xZn_{1-x}Fe_2O_4$ is given by Equation 4.9 [8, 9].

$$(Ni_{\delta}Zn_{1-x-\gamma}Fe_{x+\gamma-\delta})_A[Ni_{x-\delta}Zn_{\gamma}Fe_{2-x+\delta-\gamma}]_B \qquad 4.9$$

$$\therefore r_A = \delta Ni^{2+} + (1-x-y)Zn^{2+} + \left(x+y-\delta\right)Fe^{3+} \qquad 4.10$$

$$r_B = \tfrac{1}{2}\left[\left(x-\delta\right)Ni^{2+} + \gamma Zn^{2+} + \left(2-x+\delta-\gamma\right)Fe^{3+}\right] \qquad 4.11$$

Where r_A and r_B are ionic radii of A and B sites respectively and Zn^{2+}, Ni^{2+}, Fe^{3+} represents respective ionic radii [10]. Similarly we have,

$$r_A = (u - 1/4)a\sqrt{3} - Ro \qquad 4.12$$

$$r_B = (5/8 - u)a - Ro \qquad 4.13$$

Where u is oxygen parameter (u=0.382) taken from AMCSD card 99-101-2527 and R_o is radius of oxygen ion (1.38 Å) and ionic radii of Zn^{2+}, Ni^{2+}, Fe^{3+} for A- and B sites in the above Equations were taken from literature [10]. Cation distribution is calculated by solving above Equations for δ and γ.

4.2.1.8 Sample preparation and experimental work

Freshly prepared Ni-Zn ferrite samples were individually pounded in to a very fine powder and spread as thin layer using glass slide in a groove on the quartz glass plate. This layer is placed in a sample holder attached to goniometer and exposed to X-rays. In case of bulk samples pallets of 10 mm diameter and 2mm thickness were exposed to X-rays by placing them in the sample holder. The diffraction patterns were recorded in the range $2\theta = 20°$ to $80°$, with a step size of 0.02°. All X-ray diffraction patterns presented in this research work, were obtained from Righaku XRD diffractometer using Cu Kα radiation (λ=1.5406Å) operated at voltage of 40 kV and filament current of 20 mA.

4.2.2 Energy dispersive X-ray spectroscopy (EDS or EDX)

Energy Dispersive X-ray Spectroscopy (EDX) technique is used for compositional information and elemental analysis in conjunction with Scanning Electron Microscopy (SEM). EDS identifies elements with a relative concentration of 0.1% or higher. EDS is more accurate for heavy elements and less accurate for light elements. In this technique, electron beam (energy of the beam is typically in the range of 10-20 keV) of the SEM is focused into the sample being studied. This causes X-rays to be emitted from the irradiated material. The energy of each X-ray photon is a characteristic of the element, which produced it. The EDS microanalysis system collects the X-rays and plots them by energy. The out put data displays number of X-rays emitted from a specimen as a function of X-ray energy. Thus, an X-ray spectrum can be acquired giving information on the elemental composition of the material under examination. The intensity of a peak in an EDX spectrum is proportional to the concentration of the corresponding element in the specimen.

4.2.2.1 Sample preparation and experimental work

The freshly prepared Ni-Zn ferrite powder of the samples was finely grounded and spread as thin layer on sample holder. The thin conductive gold coating on the sample was obtained using sputter coater. The samples were then exposed to electron beam from Joel Model (6380A) (SEM) and analysis of estimation of percentage content of Ni, Zn, Fe and O in samples were carried out. The EDS spectra of all the samples were also recorded.

4.2.3 Infrared spectroscopy (IR)

IR spectroscopy is one of the most common spectroscopic techniques in both organic and inorganic chemistry, research and industry. The main goal of IR spectroscopic analysis is to determine the chemical functional groups in the sample. It is a nondestructive method used in identification of compounds by matching spectrum of unknown compound with the reference spectrum. It is also used to determine local symmetry in crystalline solids, ordering phenomenon in spinels and presence/absence of Fe^{2+}ions in the samples [11].

The term infra red covers the wavelength range of the electromagnetic spectrum between 0.78 and 1000 μm. In the context of infra red spectroscopy, wavelength is measured in wave numbers, which have the unit cm^{-1}. IR radiation does not have enough energy to induce electronic transitions and its absorption is restricted to compounds with small energy differences in the possible vibrational and rotational states. The major types of molecular vibrations are stretching and bending. Stretching (change in inter-atomic distance along bond axis) can be symmetric or asymmetric. Bending (change in angle between two bonds) can be of rocking, scissoring, wagging or twisting type. In addition to these, interaction between vibrations can lead to vibrational coupling if the vibrating bonds are joined to a single, central atom. Infrared radiation is absorbed and the associated energy is converted into these types of motions. The absorption involves discrete and quantized energy levels. However, the individual vibrational motion is usually accompanied by other rotational motions. These combinations lead to the absorption bands and not the discrete lines in IR spectrum.

The infrared spectrum of a sample is recorded by passing a beam of infrared light through the sample. When the frequency of the IR is the same as the vibrational frequency of a bond, absorption occurs. For a molecule to absorb IR, the vibrations or rotations within a molecule must cause a net change in the dipole moment of the molecule. The alternating electrical field of the radiation interacts with fluctuations in the dipole moment of the molecule. If the frequency of the radiation matches the vibrational frequency of the molecule then radiation will be absorbed, causing a change in the amplitude of molecular vibration. Analysis of the position, shape and intensity of peaks in this spectrum reveals details about the molecular structure of the sample.

4.2.3.1 Sample preparation and experimental work

The freshly prepared powder of Ni-Zn ferrite sample was grounded with pure dry KBr in the ratio of 1:100. The mixture was then pressed into pellet by applying a pressure of 3 ton for 5 minutes using hydraulic press. Pallet was placed in sample holder and exposed to IR radiation. IR transmittance spectra of all the compositions were recorded at room temperature using Shimatzu FTIR 8900 spectrometer (resolution of 0.25 cm^{-1} and wave number accuracy of 0.01cm^{-1}) in frequency range from 400 cm^{-1} to 4000 cm^{-1} at the rate of 100 scans per second. Similarly, spectra were also recorded by slow scanning rate (50 scans per second) for all the samples in frequency range of 300 cm^{-1} to 1000 cm^{-1} to get closer view of the ferrites related absorption bands.

4.2.4 Transmission electron microscopy (TEM)

The TEM is useful to get information about the morphology, crystal structure and defects. It is highly useful in resolving crystal phases, grain boundaries, interfaces, etc with atomic scale resolution. The TEM is also capable of forming a focused electron probe, as small as 20 Å, which can be positioned on very fine features in the sample for micro diffraction information or analysis of X-rays for compositional information. In addition, the instrument can be used to produce electron-diffraction patterns, useful for analyzing the properties of a crystalline specimen. The TEM has been equally useful in the life sciences, for example for examining plant and animal tissue, bacteria, and viruses. The greatest advantage is that it provides very high magnification ranging from 50 to 10^6 and its ability to provide both image and diffraction information from single sample.

In transmission electron microscopy technique, electrons are accelerated beyond 90 to 100 KeV and are projected onto the thin specimen by means of electromagnetic lenses. The transmitted beam after interaction with specimen is used to form magnified image on photographic film or on a fluorescent screen or is detected by a sensor such as a CCD camera. The four main parts of TEM system are electron source, electromagnetic lens system, sample holder, and imaging system. The electron source is normally a tungsten filament which emits electrons when being heated. After leaving the electron source, the beam is then accelerated and is tightly focused using electromagnetic lens and metal apertures to pass through the specimen. The transmitted electrons are refocused using electromagnetic lens and enlarged image is projected onto a screen for the user to see.

4.2.4.1 Sample preparation and experimental work

To obtain the TEM images of the samples, the finely grounded powder of freshly prepared Ni-Zn ferrite was dispersed in the ethanol by ultrasonic machine and placed in sample holder for exposure of electron beam. In present work Hitachi model H-7500 (TEM) (resolution of 0.204 nm, operated at 100KeV) with CCD camera was used for investigation of particle size and morphology of the Ni-Zn ferrite powder. Detailed calculations of particle size and size distribution from TEM images were carried out using Image J software.

4.2.5 Atomic force microscopy (AFM)

An AFM is one of the novel tools for imaging, measuring, and manipulating matter at the nanoscale. A great advantage of AFM compared to TEM or SEM, is that it is simple to operate in almost any environment, such as aqueous solutions, also other solvents, in air, vacuum, or other gases. This property makes it very attractive as a tool for biological applications for live cell imaging and single molecule force spectroscopy. In some variations, electric potentials can also be scanned using conducting cantilevers. In newer more advanced versions, currents can even be passed through the tip to probe the electrical conductivity or transport of the underlying surface [12]. AFM provides a 3-D surface profile and not 2-D image as in SEM and also not require any special treatments (such as metal/carbon coatings) to the sample.

The principle of operation of the AFM is very similar with that of a stylus phonograph i.e. a sharp cantilever tip interacts with the sample surface sensing the local forces between the molecules of the tip and sample surface. The cantilever is typically silicon or silicon nitride with a tip radius of curvature of the order of nanometers. When the tip is brought into proximity of a sample surface, forces between the tip and the sample lead to a deflection of the cantilever according to Hooke's law. Depending on the situation, forces that are measured in AFM include mechanical contact force, Van-der Waals forces, capillary forces, chemical bonding, electrostatic forces etc.

The deflection in the cantilever due to the forces acting on the tip is detected by a laser focused on the back of the cantilever. The laser is reflected by the cantilever onto a distant photo detector. The movement of the laser spot on the photo detector gives a greatly exaggerated measurement of the movement of the probe. This setup is known as an optical lever. The probe is moved over the sample by a scanner, typically a piezoelectric element, which can make extremely precise movements. The combination of the sharp tip, the very sensitive optical lever, and the highly precise movements by the scanner, combined with the careful control of probe-sample forces allow the extremely high resolution image [13].

The AFM can be operated in static (also called contact) mode and dynamic (non-contact or “tapping”) mode. In static mode, the cantilever is “dragged” across the surface of the sample and the contours of the surface are measured directly using the deflection of the cantilever. In the dynamic mode, the cantilever is externally oscillated at or close to its fundamental resonance frequency or a harmonic. The oscillation amplitude, phase and resonance frequency are modified by tip-sample interaction forces. These changes in oscillation with respect to the external reference oscillation provide information about the sample's characteristics.

4.2.5.1 Sample preparation and experimental work

The fine powder of freshly prepared Ni-Zn ferrite was dispersed uniformly on a glass plate and scanned using scan2 Flex AFM in dynamic (tapping mode, constant amplitude mode) mode at room temperature. Measurement was also done on sample in solution method. In solution method, small amount of sample material was introduced into a vial containing 1ml of ethanol. A sonication treatment of about 20 to 30 min in a commercial ultrasonic cleaner was carried out, resulting in a gray solution. The solution was then deposited to obtain a suitable density on graphite surface glass pipette. This step was done shortly after the end of the sonication treatment to avoid a possible exaggeration of the sample. Once the solution is evaporated from the surface, the sample was scanned with an AFM.

4.2.6 Scanning electron microscopy (SEM)

The SEM is widely used to generate high-resolution images of the shapes of objects, show spatial variations in chemical compositions, acquire spot chemical analyses using EDS and identify phases based on qualitative chemical analysis and/or crystalline structure. It is used in materials evaluation such as grain size, surface roughness, porosity, particle size distributions, mechanical damages etc. The SEM has a large depth of field, which allows a large amount of the sample to be in focus at one time. Even though image resolution of an SEM is about an order of magnitude poorer than that of a TEM, its images rely on surface processes rather than transmission [14].

In (SEM), a source of electrons is focused in vacuum into a fine probe that is raster over the surface of the specimen. The electron beam passes through scan coils and objective lens that deflect horizontally and vertically so that the beam scans the surface of the sample. As the electrons penetrate the surface, a number of interactions occur that can result in the emission of X-rays, Auger electrons, backscattered electrons and secondary electrons from the sample or through the surface. These signals are collected by detectors to form images of the sample displayed on the CRT monitor or the images can be printed. Secondary electron imaging shows the topography of surface features whereas backscattered electron imaging shows the spatial distribution of elements or compounds within the top micron of the sample. These characteristic X-rays are used to identify the composition and measure the abundance of elements in the sample using EDS [15,16].

4.2.6.1 Sample preparation and experimental work

The pallets of bulk samples were polished and placed in a sputter coater to apply conductive gold coating on it and were then exposed to electron beam from Joel Model JSM (6360) (SEM). Analysis of morphology, particle size and size distribution were done from the obtained images.

4.3 Results and Discussion

4.3.1 XRD analysis of freshly prepared $Ni_xZn_{1-x}Fe_2O_4$ samples

The X-ray spectrum of the freshly prepared $Ni_xZn_{1-x}Fe_2O_4$ samples were used to calculate lattice constant, crystallite size, micro strain, X-ray density, porosity and cation distributions of the samples in addition to its phase identification.

4.3.1.1 X-ray diffraction spectrum and phase identification

The X-ray diffraction (XRD) patterns of the freshly prepared $Ni_xZn_{1-x}Fe_2O_4$ samples (x=0.40, 0.50, 0.55, 0.60, 0.65 and 0.70) are shown in Fig. 4.2. The strongest reflection coming from (311) plane for all the samples denotes spinel phase. The positions of the peaks of all the freshly prepared samples are in agreement with those reported in JCPDS file no 8-234 and AMCSD card 99-101-2527.

All the peaks indexed to (220), (311), (222), (400), (422), (511), (440), (620), (533) and (622) planes are corresponding to cubic spinel structure. This confirms that all the samples prepared in the present work are having single phase cubic spinel structure. Thus method of sample preparation employed in the present work, produces mono phasic Ni-Zn ferrite material.

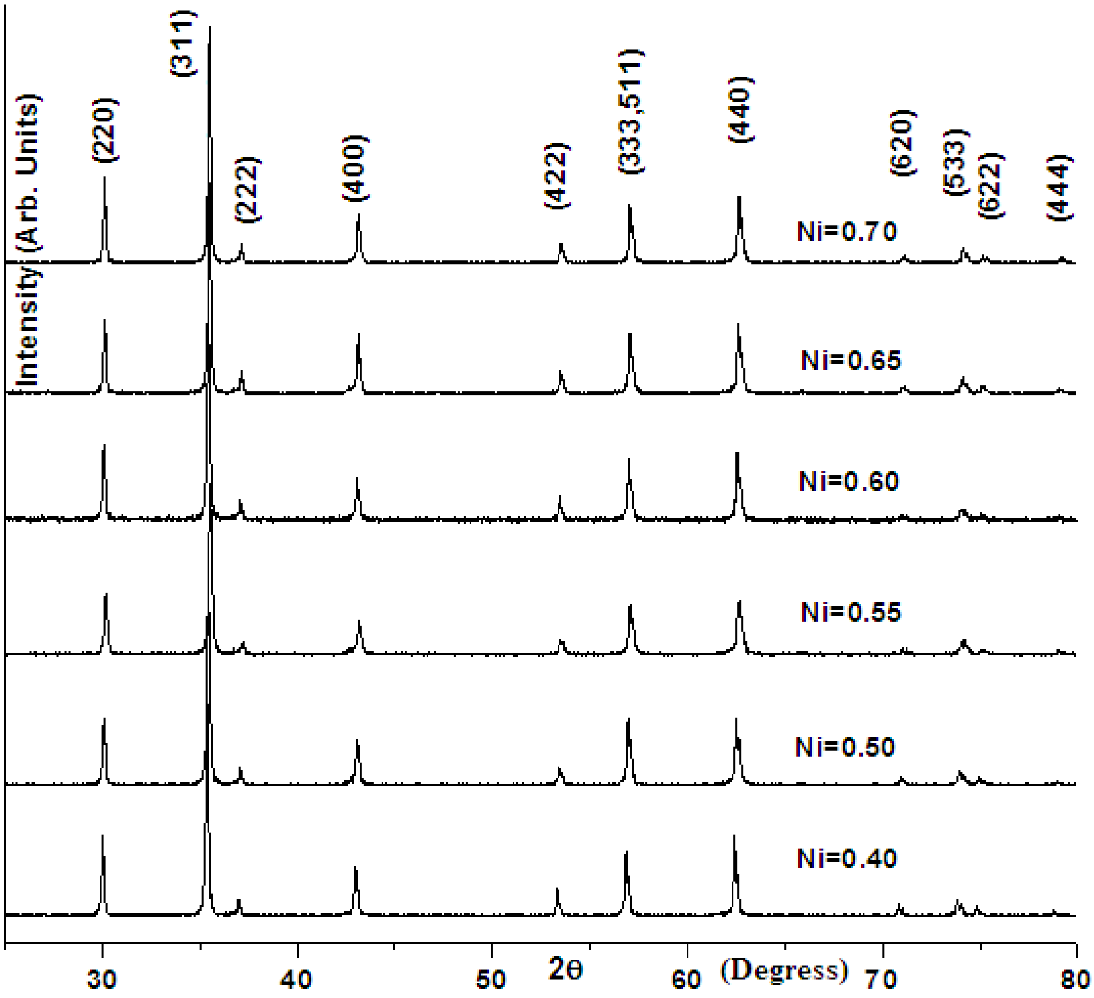

Fig. 4.2 XRD patterns of freshly prepared $Ni_xZn_{1-x}Fe_2O_4$ samples.

4.3.1.2 Lattice constant (*a*) and Nelson-Riley function *F (θ)*

Fig. 4.3 show plots of Nelson–Riley function F(θ) of freshly prepared samples with Ni=0.60 and 0.70. The values of lattice constant '***a***' of all the freshly prepared samples obtained from this method are given in Table 4.1. Fig. 4.4 shows that '***a***' decrease with increasing Ni concentration. The '***a***' values decreases from 8.4168 Å to 8.3867 Å as Ni concentration increases from 0.4 to 0.70. This decrease can be explained on the basis of difference in ionic radii, i.e., Ni^{2+} (0.69 Å) < Zn^{2+} (0.74 Å). Decrease in '***a***' is essentially attributed to the substitution of large sized

Zn^{2+}cation by small sized Ni^{2+}cation. Continuous decrease in '***a***' with increasing Ni content is also an indication of formation of compositionally homogeneous samples [4, 17]. The values of '***a***' obtained in the present work are also in good agreement with reported values in literature [8].

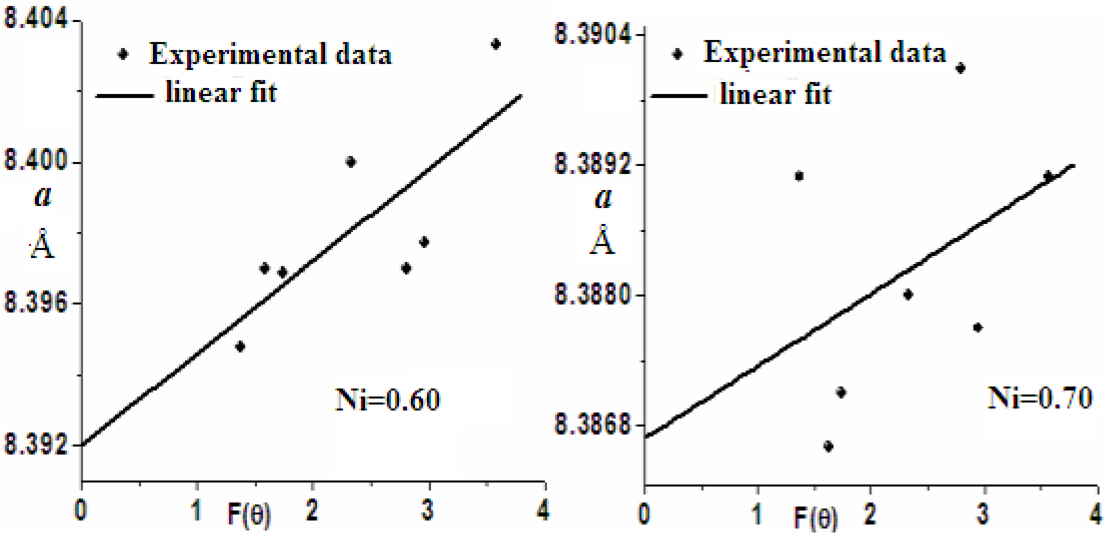

Fig. 4.3 Nelson-Riley functions of freshly prepared $Ni_xZn_{1-x}Fe_2O_4$ samples.

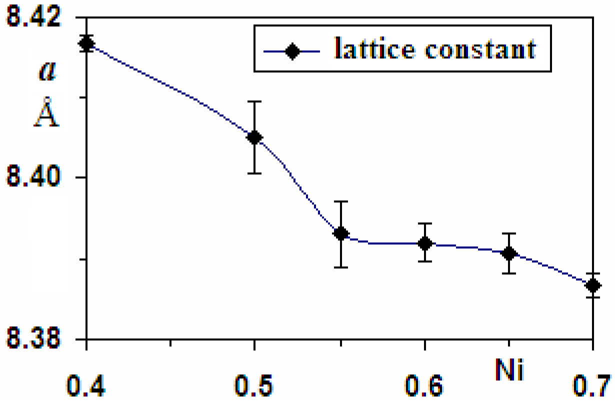

Fig. 4.4 Variation of lattice constant with Ni content of freshly prepared $Ni_xZn_{1-x}Fe_2O_4$ samples.

4.3.1.3 Williamson-Hall plot, crystallite size (D) and micro strain (ε)

Fig. 4.5 show Williamson Hall plots of freshly prepared samples with Ni=0.50 and 0.70 and are used to calculate strain contribution to line broadening in XRD peak. The values of crystallite sizes and micro strain of freshly prepared samples are given in Table 4.1. The crystallite sizes were found to be varying in the range of 51 nm to 69 nm. Thus the method of synthesis employed in the present work yields nanoparticle Ni-Zn ferrite samples at low temperature. The maximum strain of 9.4 x 10^{-4} was found for Ni=0.60, whereas minimum of 3.0 x 10^{-4} for Ni=0.50 and Ni=0.70. The strain may arise from number of factors such as lattice defects, presence of impurities, large surface energy, thermal history etc. [18, 19, 20]. In the context of nanocrystalline materials, microstrain arises primarily from the large surface energy associated with the large surface area to volume ratio of the samples [6, 7]. It was also observed that all the nano samples did not exhibit identical crystallite sizes. This was probably due to different rate of ferrite formation for different compositions, favoring variation of crystallite sizes [21].

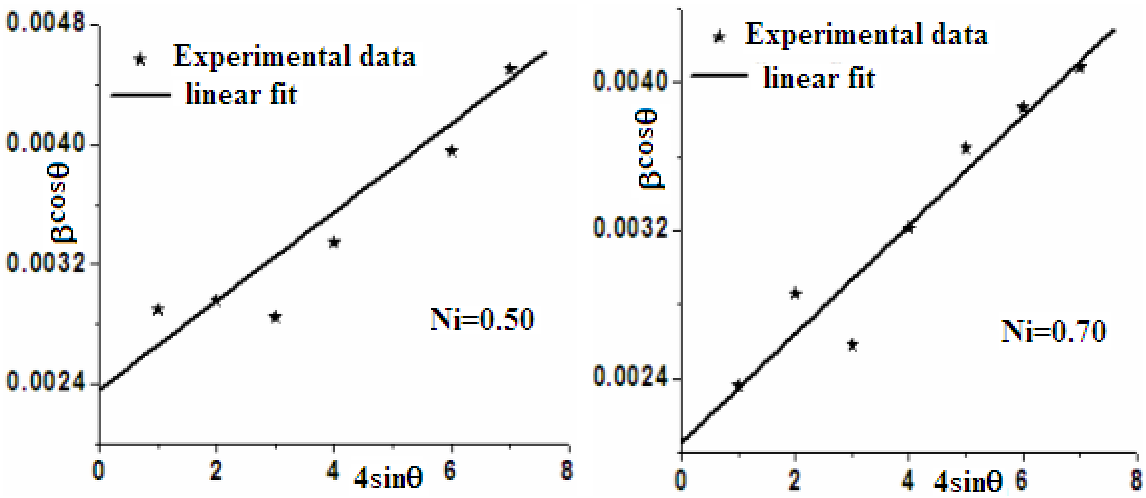

Fig. 4.5 Williamson-Hall plot of freshly prepared Ni_xZn_{1-x} Fe_2O_4 samples.

Table 4.1 Lattice parameter (a) using Nelson–Riley method, crystallite sizes and micro strain (ε) of freshly prepared $Ni_{1-x}Zn_xFe_2O_4$ samples.

Ni=x	(a) Å	Crystallite size D (nm)	Micro strain ε x10^{-4}
0.40	8.4168 ±0.0009	67 ±9	5.9 ±0.7
0.50	8.4050 ±0.0045	58 ±7	3.0 ±0.6
0.55	8.3931 ±0.0041	51 ±5	3.0 ±0.6
0.60	8.3920 ±0.0024	69 ±11	9.4 ±0.3
0.65	8.3907 ±0.0025	59 ±4	3.2 ±0.4
0.70	8.3867 ±0.0015	67 ±5	3.0 ±0.4

4.3.1.4 X-ray density (ρ_x) and porosity (P)

It can be seen from Fig. 4.6(a) that X-ray density (**ρ_x)** of nano samples increases as Ni concentration increases from 0.40 to 0.55, whereas, for Ni >0.55, **ρ_x** decreases. This initial increase up to Ni=0.55 may be attributed to sharp decrease in lattice parameter '***a***'. For Ni>0.55, the decrease in '***a***' is slow and observed decrease in **ρ_x** for these samples may be attributed to predominance of their decreasing molecular weights over decreasing '***a***' with increasing Ni content (see Equation 4.7). Similar trend was also observed for mass density (**ρ_B**). The **ρ_B** of samples were measured pyknometrically under CCl_4 medium using Archimedes principle [22]. The **ρ_B** of all compositions were found to be smaller than their corresponding **ρ_x**. This can be related to pores formed leading to porosity (**P**) during the sample preparation. The variation of **ρ_B** and **P** of nano samples with Ni concentration are shown in Fig. 4.6(b). The **P** of the nano samples varies in the range of 22% to 30%. The lowest **P** of 22% was observed for Ni=0.55 and it has also highest density (**ρ_x**= 5.3360 gm/cm^3 and **ρ_B**= 4.16 gm/cm^3) as expected. The **ρ_x** of samples with Ni=0.70

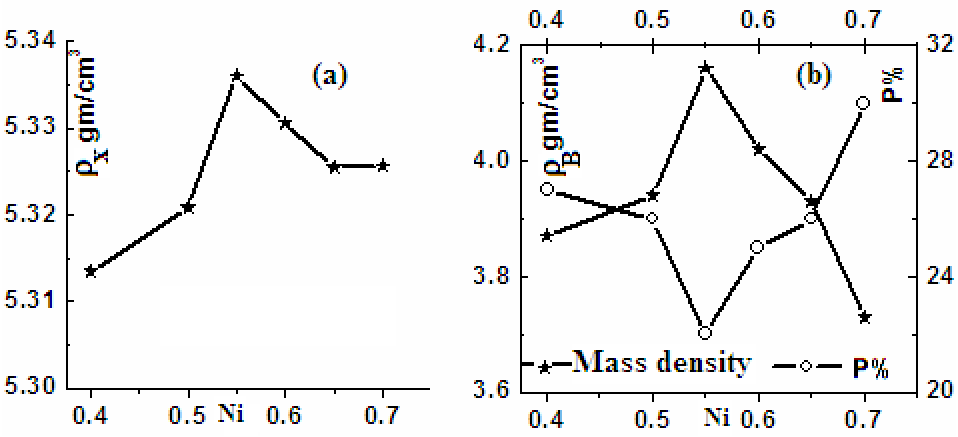

Fig. 4.6 Variation of (a) X ray density, (b) mass density (left scale) and porosity (right scale) of nano $Ni_xZn_{1-x}Fe_2O_4$ samples with Ni concentration.

and 0.60 in the present work are higher than compared to those reported by Santosh S. Jadhav et al [8].

4.3.1.5 Cation distributions

The cation distributions of nano samples were calculated using site preferences of various atoms and XRD data as explained in Section 4.2.1.7 and are listed in Table 4.2. It was found that all the zinc atoms prefer to reside only on A site for all the compositions as expected, except small fractions of zinc, 0.006 and 0.003 were found on B site for sample with Ni=0.40 and 0.50 respectively. Also, most of Ni ions prefer to reside at B site and Fe atoms are distributed over A and B site. The calculated cation distributions were also in agreement with earlier reported results [8, 23].

Table 4.2 Cation distributions at A and B site of nano $Ni_xZn_{1-x}Fe_2O_4$ samples.

Ni =X		at A Site			at B Site	
	Ni	Zn	Fe	Ni	Zn	Fe
0.40	0.012 ±0.002	0.594 ±0.001	0.394 ±0.001	0.388 ±0.002	0.006 ±0.001	1.606 ±0.001
0.50	0.007 ±0.004	0.497 ±0.005	0.496 ±0.004	0.493 ±0.009	0.003 ±0.005	1.504 ±0.004
0.55	0.004 ±0.003	0.449 ±0.004	0.547 ±0.004	0.546 ±0.008	0.001 ±0.004	1.453 ±0.004
0.60	0.004 ±0.005	0.399 ±0.002	0.597 ±0.002	0.596 ±0.005	0.001 ±0.002	1.403 ±0.002
0.65	0.004 ±0.005	0.350 ±0.003	0.646 ±0.002	0.646 ±0.005	0.000 ±0.003	1.354 ±0.002
0.70	0.004 ±0.003	0.300 ±0.002	0.696 ±0.001	0.696 ±0.003	0.000 ±0.002	1.304 ±0.001

4.3.2 Elemental analysis using (EDS or EDX)

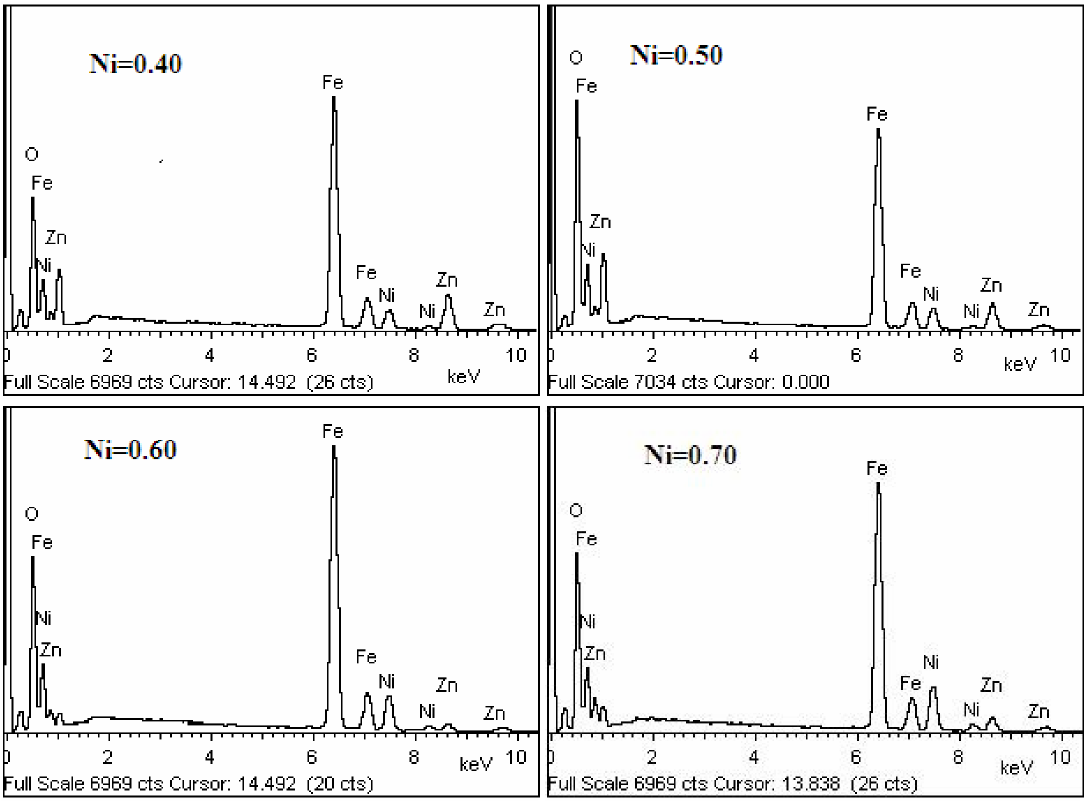

Fig. 4.7 EDS spectrum of nano $Ni_xZn_{1-x}Fe_2O_4$ samples.

Table 4.3 Atomic and weight percentages of Ni, Zn, Fe and O elements of nano $Ni_xZn_{1-x}Fe_2O_4$ samples.

Sample Ni =X	Element	Observed		Totals of weight	Theoretical Weight %
		Atomic %	Weight %		
0.40	Ni	4.92	9.64	100%	9.85 ±2.10
	Zn	8.01	16.72		16.46 ±1.60
	Fe	25.12	45.61		46.85 ±2.65
	O	61.95	28.03		26.84 ±4.42
0.50	Ni	7.24	12.10	100%	12.34 ±1.97
	Zn	6.42	13.49		13.75 ±1.91
	Fe	26.54	46.47		46.98 ±1.09
	O	59.80	27.94		26.92 ±3.79
0.60	Ni	8.31	14.38	100%	14.85 ±3.19
	Zn	5.11	11.23		11.03 ±1.79
	Fe	26.86	46.76		47.12 ±0.76
	O	59.72	27.63		27.00 ±2.35
0.70	Ni	10.12	16.93	100%	17.38 ±2.58
	Zn	4.07	8.63		8.30 ±4.00
	Fe	27.98	46.91		47.25 ±0.72
	O	57.83	27.53		27.07 ±1.69

Energy dispersive X-ray spectra of nano samples with Ni=0.40, 0.50, 0.60 and 0.70 are as shown in Fig. 4.7. It can be seen that EDS spectra of all the samples have only Ni, Zn, Fe and O peaks without any impurity peak. The details about observed and theoretical elemental weight percentage of each composition are given in Table 4.3. It was found that observed composition is in good agreement (within 5% error) with that of the theoretical stoichiometric calculations. Thus the method of sample preparation employed in the present work preserves stoichiometry.

4.3.3 Infrared spectroscopy

Fig. 4.8 shows IR absorption spectra of nano samples. Presence of two main absorption bands for all samples reveals that they are having single phase spinel structure with two sub lattices [17]. In case of ferrites, higher absorption band ν_1 is normally observed between 610-550 cm^{-1} whereas, lower absorption band ν_2 lies between 450-375cm^{-1}. The highest band 'ν_1' corresponds to intrinsic stretching vibrations of metal at the tetrahedral site, M_{tetra}---O and whereas, the lower band 'ν_2' is assigned to octahedral metal stretching, (M_{octa}---O).

The positions of infrared absorption band ν_1 (corresponding center frequency on tetrahedral site) and ν_2 (corresponding center frequency on octahedral site) are represented by arrows in Fig. 4.8 and corresponding values of $\nu_1$and ν_2 are reported in Table 4.4. Since minor observed splitting at lower band was observed, the accuracy in reported ν_2 values is low compared to values of ν_1. The observed band values of ν_1 at tetrahedral site are more than ν_2 at octahedral site. As tetrahedral site dimension is less compared to that of octahedral site, and, as resonant frequency has inverse relation with bond length, band values of ν_1 at tetrahedral site is more than ν_2

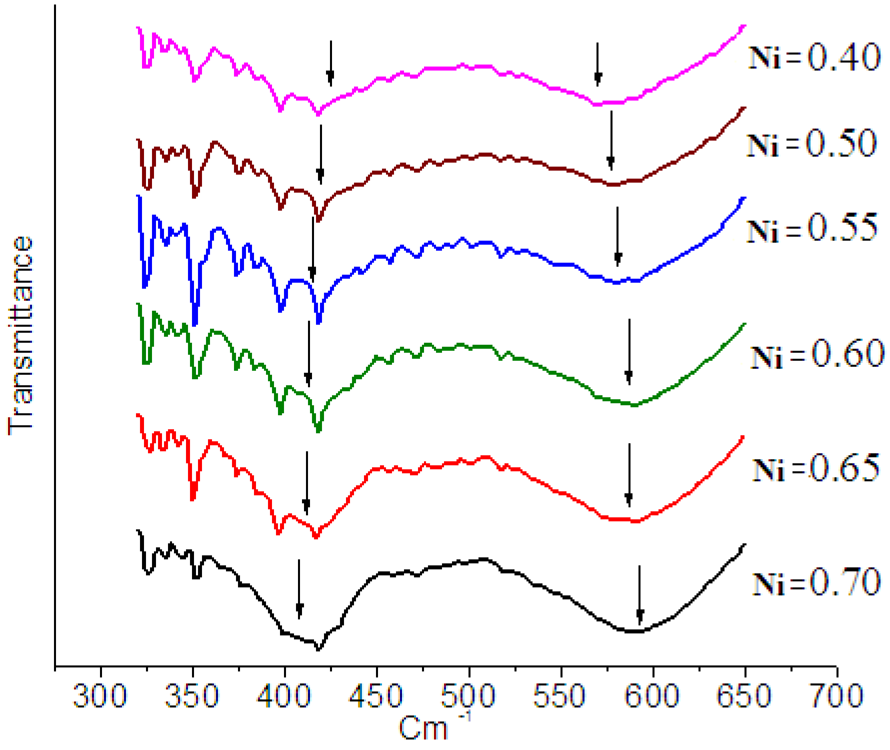

Fig. 4.8 IR spectra of nano $Ni_xZn_{1-x}Fe_2O_4$ samples.

at octahedral site. Also, the shift or displacement in ν_2 band with variation of Ni concentration is so light that it can be noticed only when composition difference is large (for example comparing Ni=0.40 and 0.70). However, shift in higher band ν_1 is clearly noticeable.

It is observed that wave number ν_1 increases with increase in Ni concentration from 0.40 to 0.70. This can be explained on the basis of decrease in tetrahedral bond length due to replacement of bigger Zn^{2+} ion by smaller Fe^{3+} ion at A site as Ni concentrations increases. Linear decrease in tetrahedral bond length or linear increase in wave number ν_1 as Ni concentration increases from 0.40 to 0.70 shows that substituted Ni ion prefers to resides only on B site and displaces proportional amount of Fe^{3+}ion from B site to A site. Similarly, shifting of ν_2 band to lower values with increase in Ni concentration from 0.40 to 0.70 can be explain on the basis of increase in bond length R_B of B site on replacement of smaller Fe^{3+} ion (0.645 Å) by bigger Ni^{2+}ion (0.69 Å) [17]. Thus, IR spectroscopy shows linear variation in wave number $\nu_1$and ν_2 that clearly ruled out the possibility of occupying B site by appreciable amount of Zn^{2+}ions [24]. Hence, IR spectroscopic results support the cation distributions calculated using XRD data.

The splitting of lower band (see Fig. 4.8) for Ni = 0.40 to 0.65 at around 410 cm^{-1} to 420 cm^{-1} may be due to the presence of Fe^{2+}ions in these compositions. This is attributed to Jan-Tellar distortion produced by Fe^{2+}ions. This effect produces local deformation in crystal field potential and leads to splitting of the absorption band [25]. However for Ni=0.70 the splitting of band almost vanishes indicating absence of Fe^{2+}ions at B site for this composition. The disappearance of splitting of ν_2 band for Ni=0.70 suggest that the Fe^{2+}ion formation has been hampered with

Table 4.4 Wave numbers of IR absorption bands of nano $Ni_xZn_{1-x}Fe_2O_4$ samples at tetrahedral (ν_1) and octahedral (ν_2) site.

Ni (x)	Zn (1-x)	ν_1 cm_{-1}	ν_2 cm^{-1}
0.40	0.60	575	421
0.50	0.50	580	419
0.55	0.45	581	416
0.60	0.40	586	416
0.65	0.35	586	413
0.70	0.30	590	412

decrease in Zn concentration in the sample [26]. Third band at around 350 cm^{-1} is observed for all the samples. The frequency of this band depends mainly upon mass of the tetrahedral metal ion complexes and hence it is attributed to vibrations of ions at tetrahedral site. However exact absorption values and other details of these bands observed below 400 cm^{-1} cannot be explain as we have recorded IR spectrum using KBr medium which is transparent till 400 cm^{-1}.

4.3.4 TEM micrographs and particle size distribution

The TEM micrographs and corresponding histogram of particle size distribution of all the nano samples are shown in Fig. 4.9 to Fig. 4.14. Some of the TEM images were taken by scanning the same samples at different locations with different magnification power for better understanding of size distribution. The TEM micrographs showed that samples are having different and irregular shapes, except for Ni=0.55, which shows partly spherical shape nano particles (see TEM image of Ni=0.55 (b) and (e) in Fig. 4.10). The histogram of particle size distribution was obtained by measuring particle sizes of 20 to 400 individual particles from TEM image using Image J software.

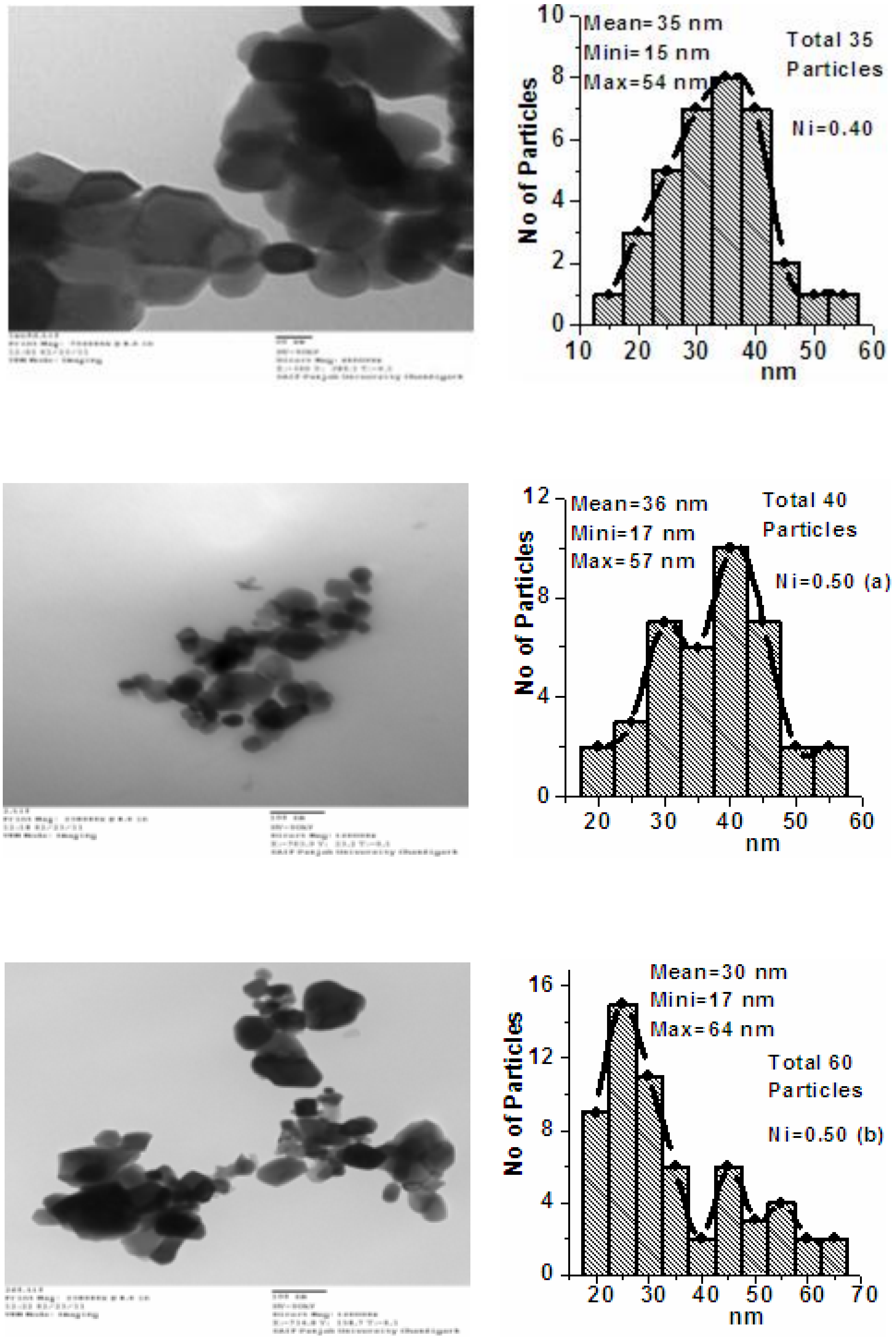

Fig. 4.9 (Left) TEM images of nano $Ni_xZn_{1-x}Fe_2O_4$ samples (x=0.40 and 0.50) and (right) corresponding histograms of particle size distribution.

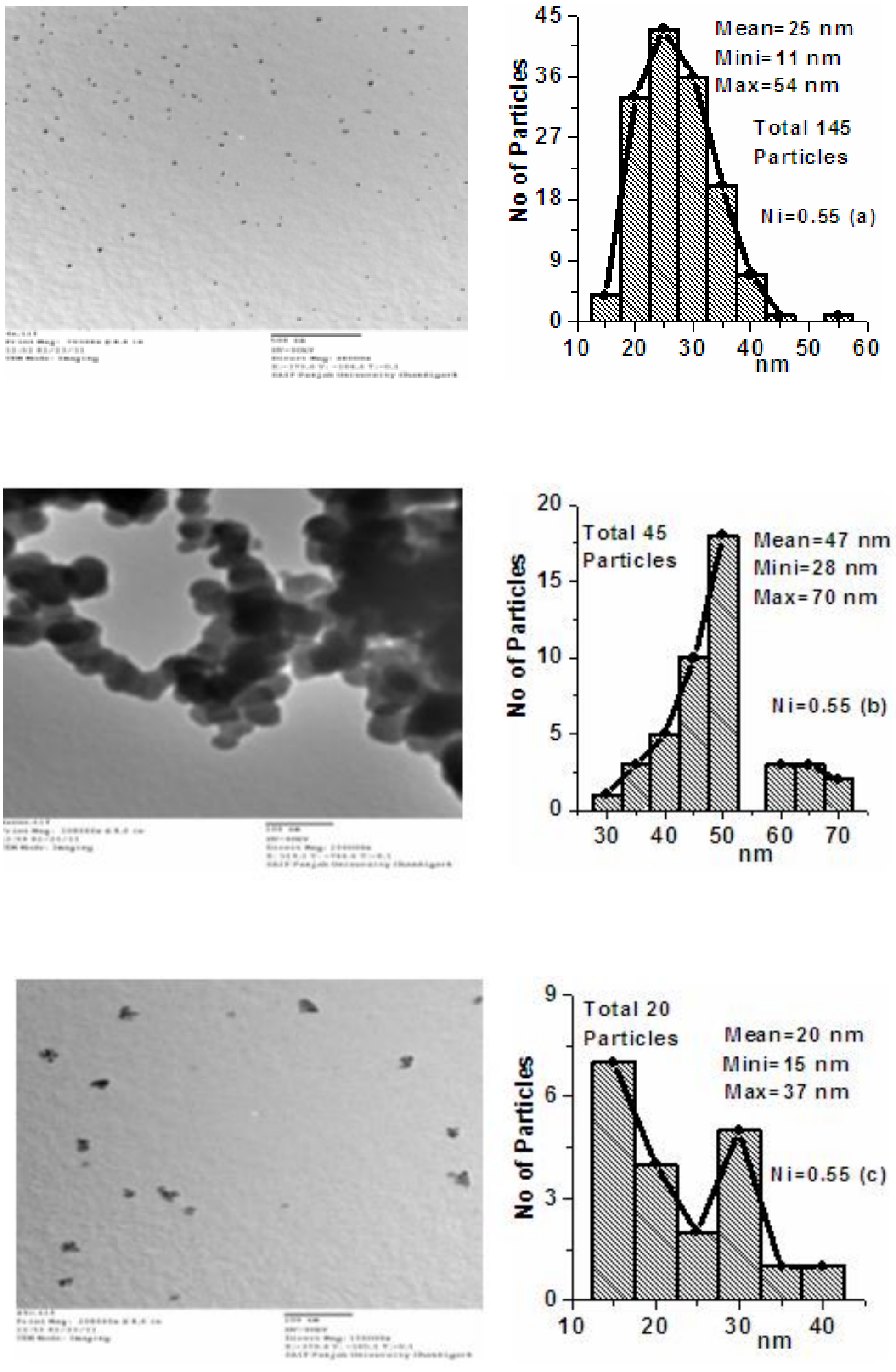

Fig. 4.10 (left) TEM images of nano $Ni_xZn_{1-x}Fe_2O_4$ samples (x=0.55) and (right) corresponding histograms of particle size distribution.

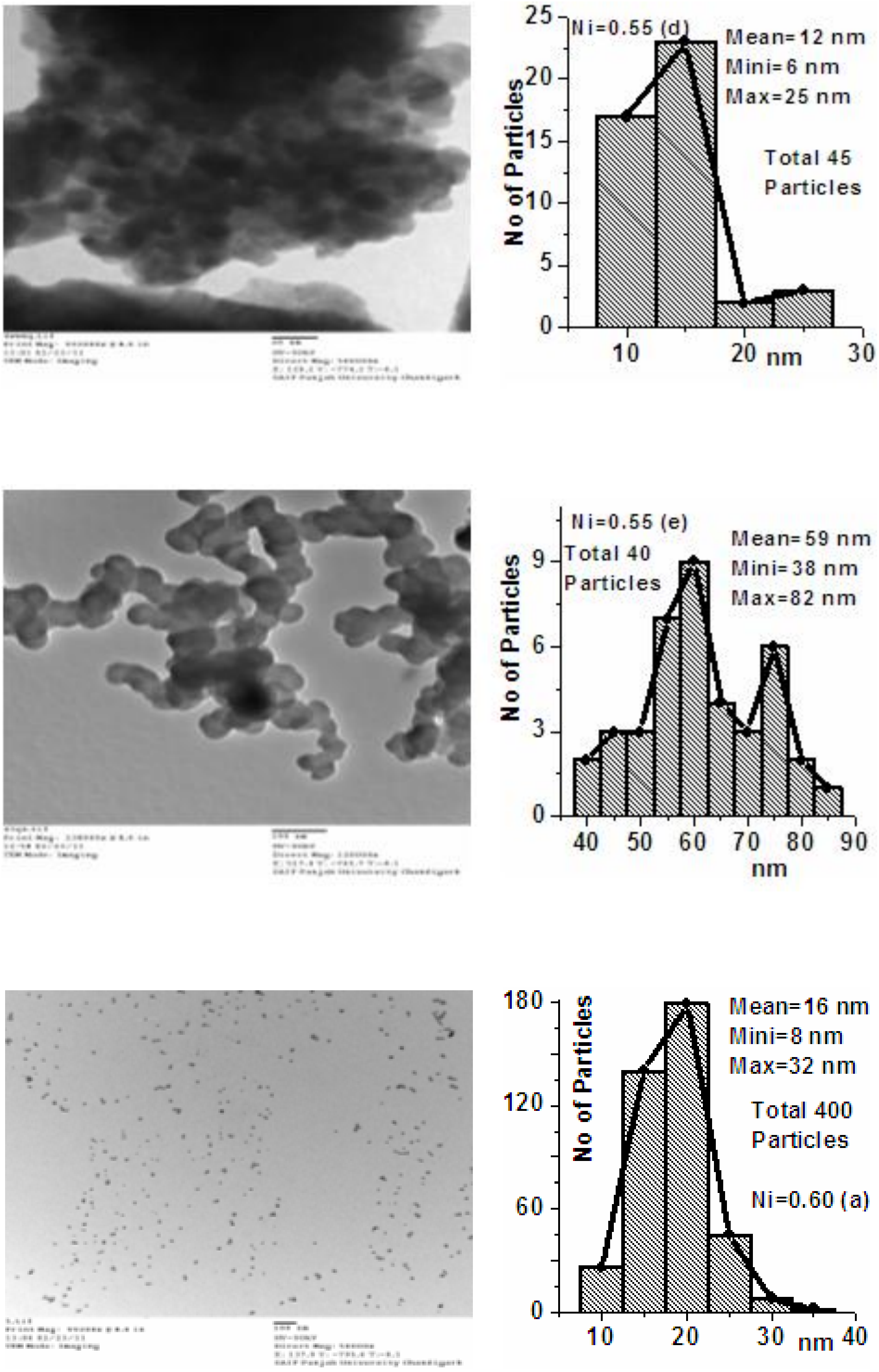

Fig. 4.11 (left) TEM images of nano $Ni_xZn_{1-x}Fe_2O_4$ samples (x=0.55 and 0.60) and (right) corresponding histograms of particle size distribution.

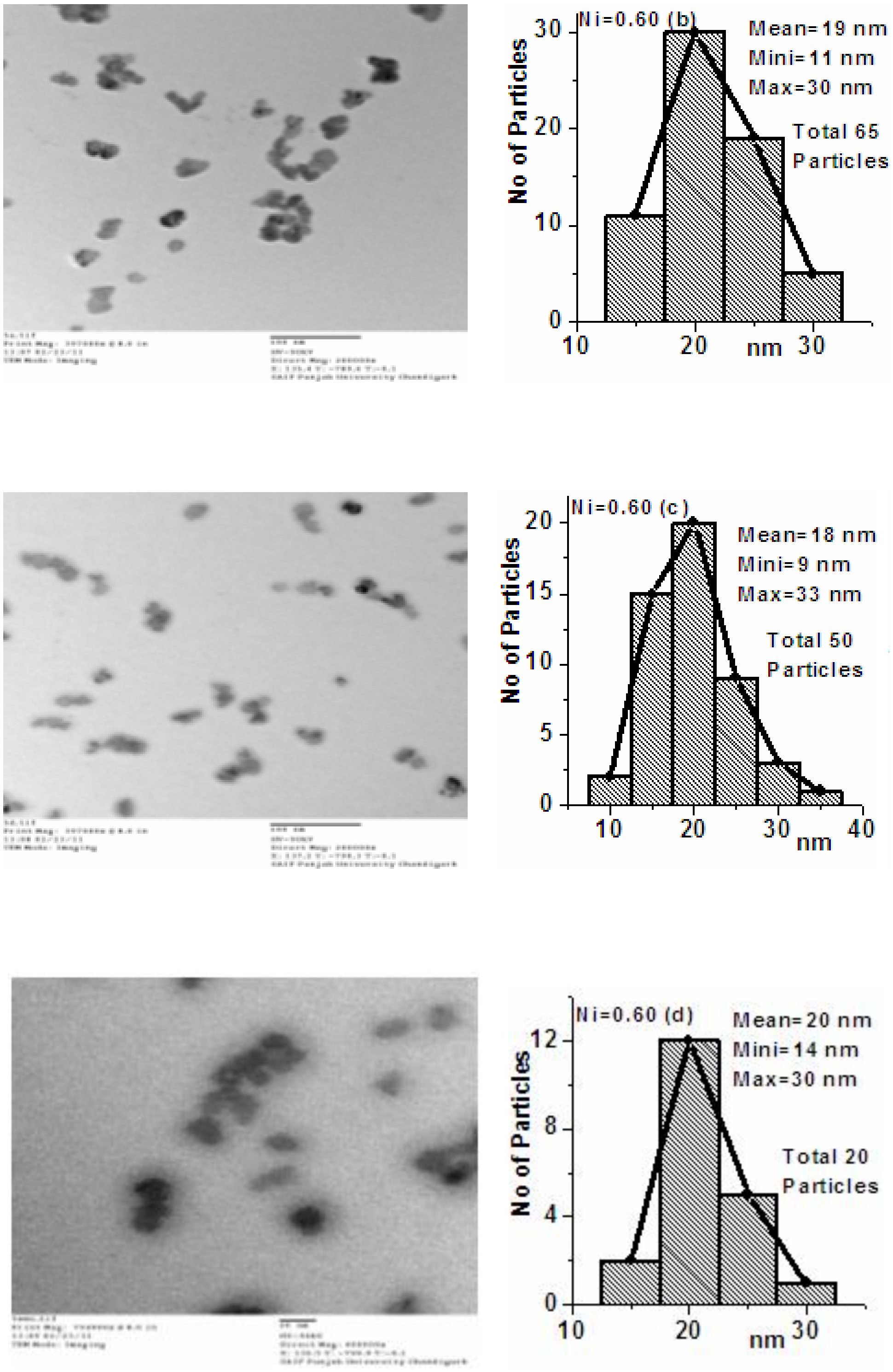

Fig. 4.12 (left) TEM images of nano $Ni_xZn_{1-x}Fe_2O_4$ samples (x=0.60) and (right) corresponding histograms of particle size distribution.

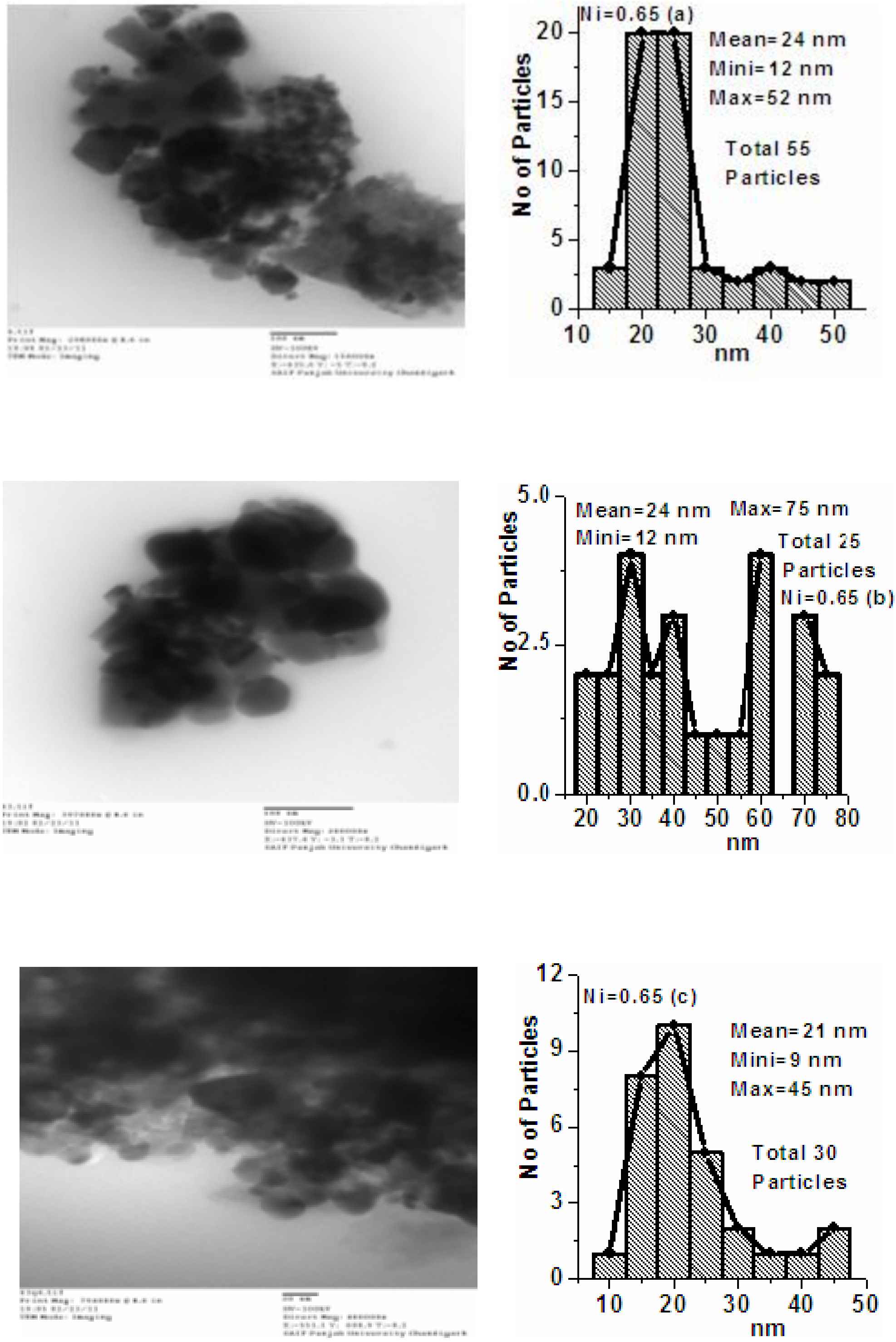

Fig. 4.13 (left) TEM images of nano $Ni_xZn_{1-x}Fe_2O_4$ samples (x=0.65) and (right) corresponding histograms of particle size distribution.

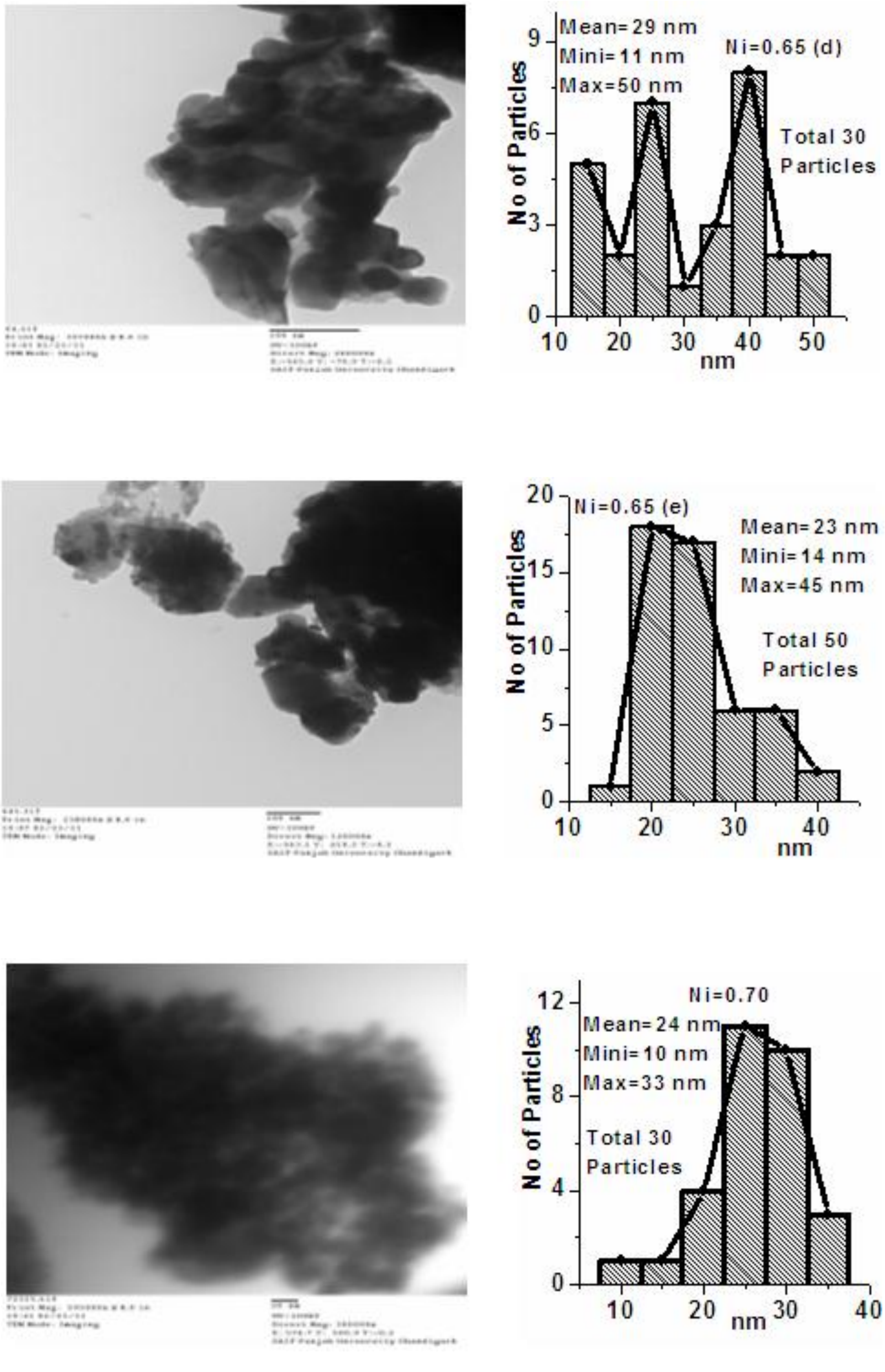

Fig. 4.14 (left) TEM images of nano $Ni_xZn_{1-x}Fe_2O_4$ samples (x=0.65 and 0.70) and (right) corresponding histograms of particle size distribution.

The histogram data of particle size distribution shows that sample with Ni=0.55 has wider particle size distribution between 10 nm to 60 nm (average 73% of particles). Whereas, narrow particle size distribution 15 nm to 25 nm (average 76% of particles) was observed for Ni=0.60. The particle size histogram for Ni=0.70 has maxima ranging between 25 nm to 30 nm, whereas, from 30 nm to 40 nm for Ni=0.40.

In general, the average particle sizes of the nano samples were found to be in the range of 6 nm to 75 nm. TEM results of particle sizes were in good agreement with crystallite sizes obtained from XRD data.

4.3.5 AFM images and particle size distribution

An AFM measures locally an individual cluster or several clusters on the surface up to the level of atomic resolution and provides a three-dimensional surface profile while TEM or SEM providing a tow dimensional image of a sample. The AFM investigation of nano $Ni_{0.70}Zn_{0.30}Fe_2O_4$ sample was carried out by solution (depositing ferrite solution on graphite) and powder method (depositing powder on glass surface).

The results of AFM scanning for solution and powder deposition method are shown in Fig. 4.15 and 4.16 respectively. It can be seen that a large-scale AFM image (Fig. 4.15 (a)) shows the presence of small and randomly distributed islands. Fig. 4.15(b) shows small-scale AFM images of many island types, revealing that all islands have different size and height. Fig. 4.15(c) shows (height and size of 4 individual clusters from Fig. 4.15 (a) marked in blue arrow) that smaller islands have an apparent height of 4 nm and a size of ~ 0.140 μm while, the bigger islands have an apparent height of 40 nm and a size of 0.350 µm. Fig. 4.15(d) provides mean and average parameters of clusters in image (a). Mean diameter of grains was found to be 71 nm.

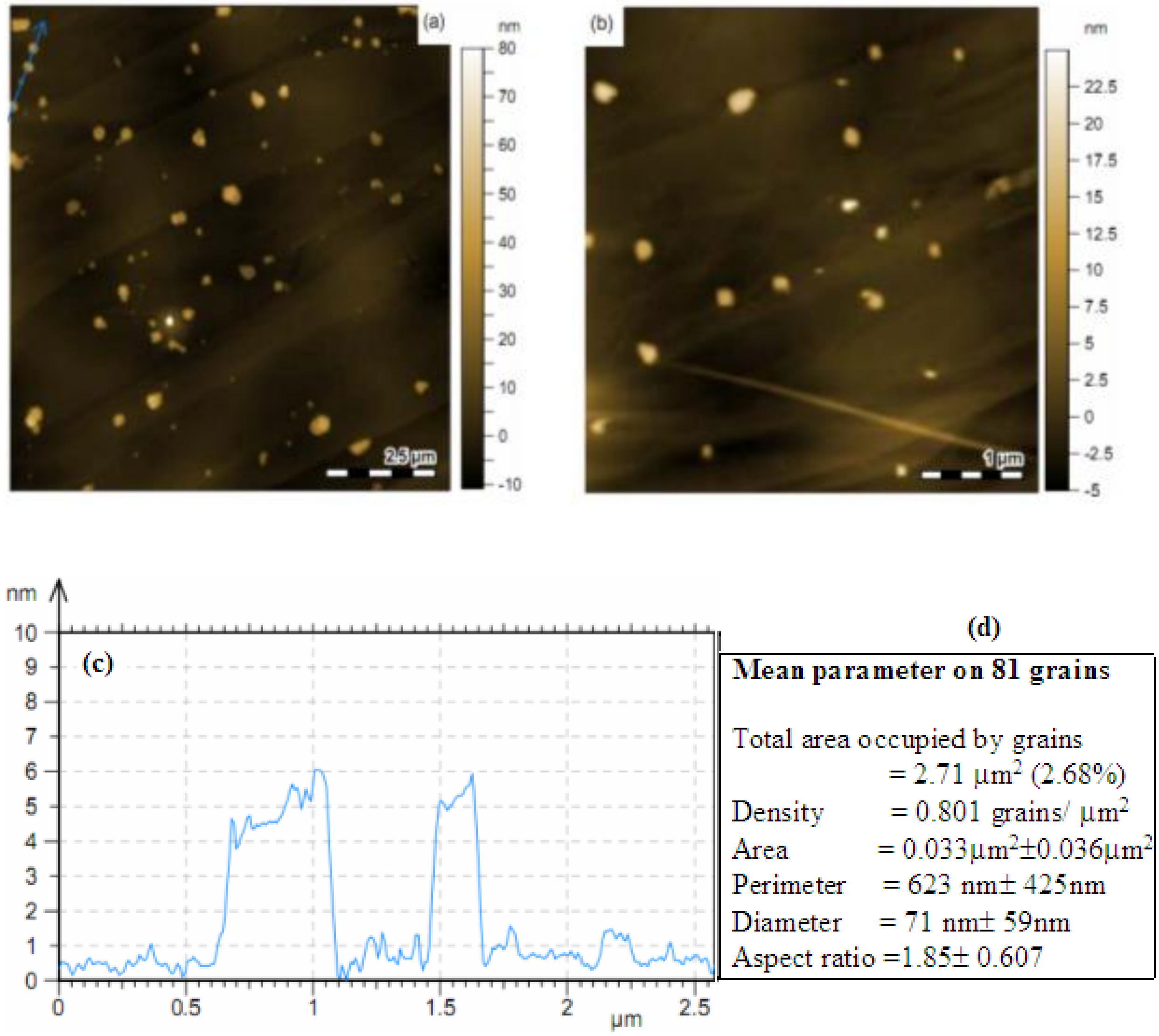

Mean parameter on 81 grains

Total area occupied by grains
= 2.71 μm^2 (2.68%)

Density = 0.801 grains/ μm^2

Area = $0.033\mu m^2 \pm 0.036\mu m^2$

Perimeter = 623 nm± 425nm

Diameter = 71 nm± 59nm

Aspect ratio =1.85± 0.607

Fig. 4.15 AFM images (a) large scale, (b) small scale, of nano $Ni_{0.70}Zn_{0.30}Fe_2O_4$ ferrite solution deposited on graphite. (c) A line profile through few clusters (shown in blue colour in image a), indicates their apparent height and their size and (d) a statistical analysis of the image (a) showing the mean area, the mean parameter, the mean diameter and the aspect ratio of the grains.

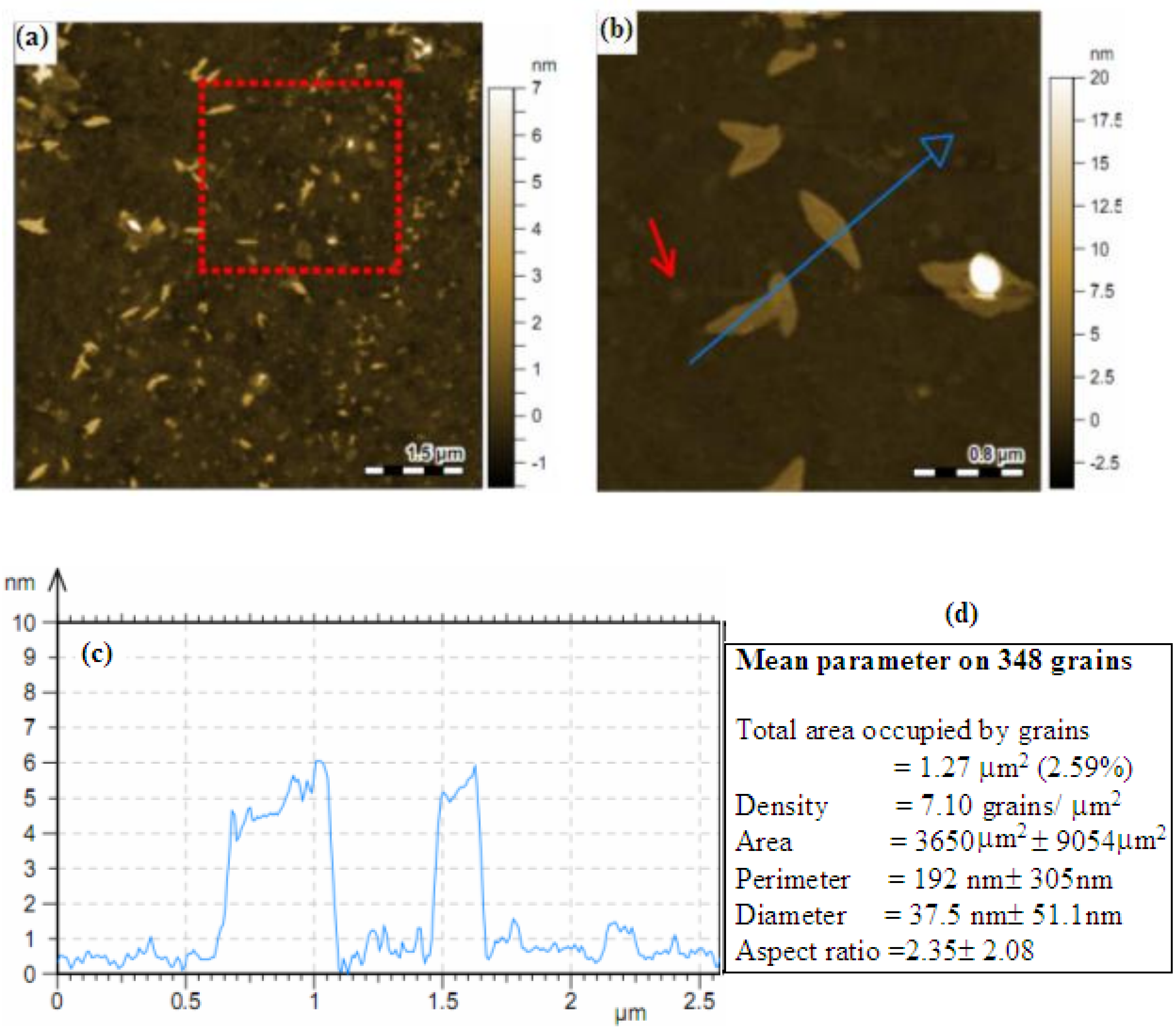

Mean parameter on 348 grains

Total area occupied by grains
= 1.27 μm² (2.59%)

Density = 7.10 grains/ μm²

Area = 3650μm² ± 9054μm²

Perimeter = 192 nm± 305nm

Diameter = 37.5 nm± 51.1nm

Aspect ratio =2.35± 2.08

Fig. 4.16 (a) Large scale AFM image of nano $Ni_{0.70}Zn_{0.30}Fe_2O_4$ ferrite powder deposited on glass. (b) Zoom of image (a) showing more characteristics of the cluster. (c) A line profile through few clusters (shown in blue colour in image b), indicates their apparent height and their size and (d) a statistical analysis of the image (a) showing the mean area, the mean parameter, the mean diameter and the aspect ratio of the grains.

In the second case (Fig. 4.16 (a) powder deposited directly on glass), we find randomly distributed islands on the surface. With this preparation, some islands appear flat and larger (about 500 nm) than the solution method. However, we also observe a very small island having an apparent height of around 1 nm and 6 nm as indicated by red and blue arrow respectively in Fig. 4.16 (b). Fig. 4.16 (d) provides the statistical analysis of image (a). It was found that the mean diameter of grains was found to be 37 nm. The TEM results of particle size distribution of Ni=0.70 shows maxima ranging between 25 nm to 30 nm and overall particle size ranges from 10 nm to 33 nm. Hence, the AFM result of grain diameter from powder deposition method is in good agreement with TEM particle size analysis.

4.3.6 XRD analysis of bulk samples

The XRD patterns of bulk $Ni_xZn_{1-x}Fe_2O_4$ samples (x=0.40, 0.50, 0.60, and 0.70) at various sintering temperatures are shown in Fig. 4.17. It can be seen that all the peaks in XRD patterns of bulk samples are corresponding to cubic spinel structure. It is also seen that, intensity of the peaks of all the samples increases with the increase in sintering temperature. The increase in sharpness and intensity of XRD peaks with increasing sintering temperature depicts the improvement in crystallinity of the bulk samples [8].

Fig. 4.18 show the effect of sintering temperature on the peaks of XRD pattern of bulk $Ni_{0.55}Zn_{0.45}Fe_2O_4$ samples at (a) 1100^oC, (b) 1200^oC and (c) 1300^oC. The increase in sharpness and intensity of peaks with increase in sintering temperature can be seen clearly indicating improvement in crystallinity of samples. The inset of the Fig. shows the shifting of (311) peaks towards higher Bragg’s angle with the increase in sintering temperature. This shifting of peaks indicates lattice contraction of the sample after sintering and may be attributed to change in cation distribution in the samples due to sintering process.

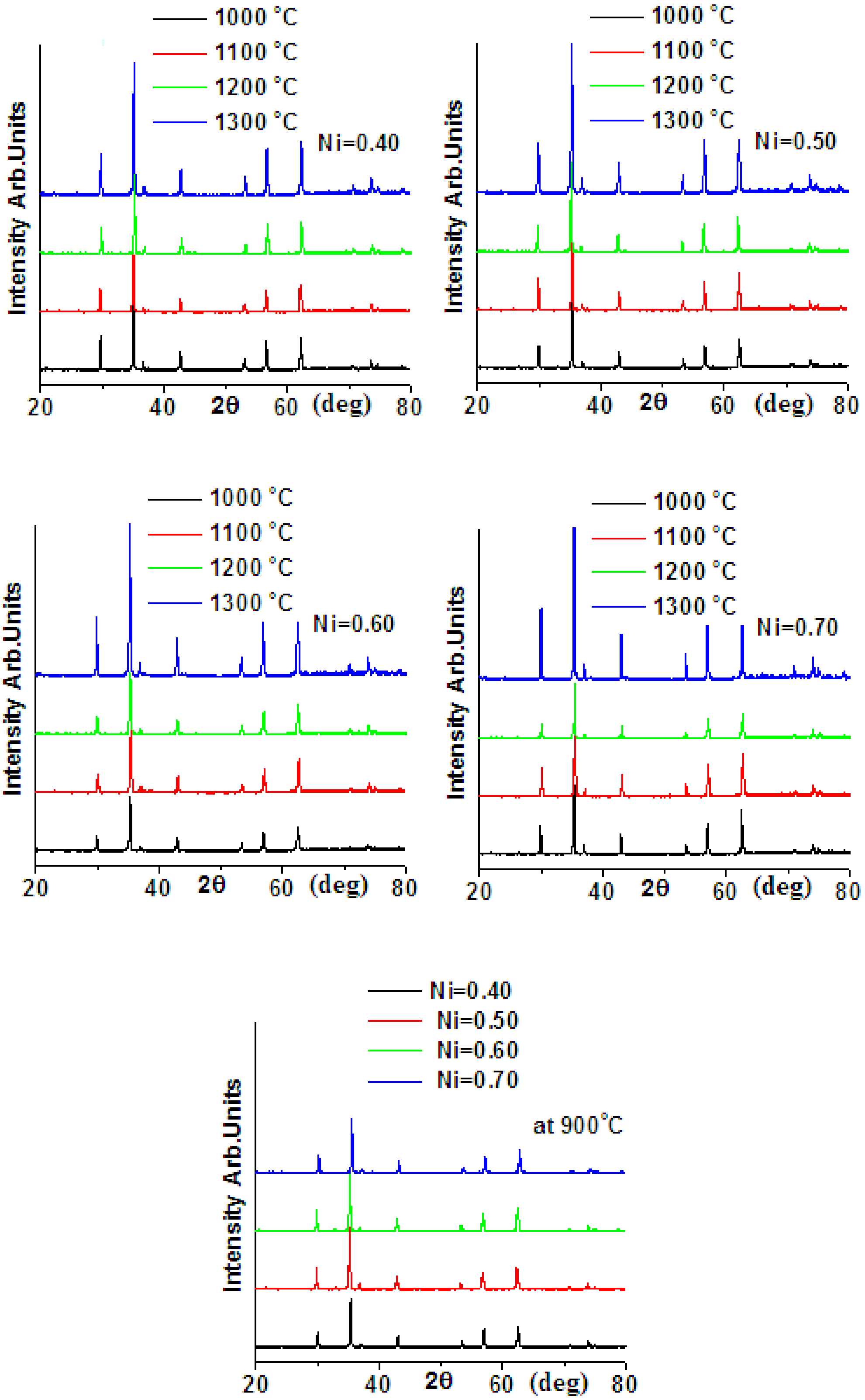

Fig. 4.17 XRD patterns of bulk $Ni_xZn_{1-x}Fe_2O_4$ samples.

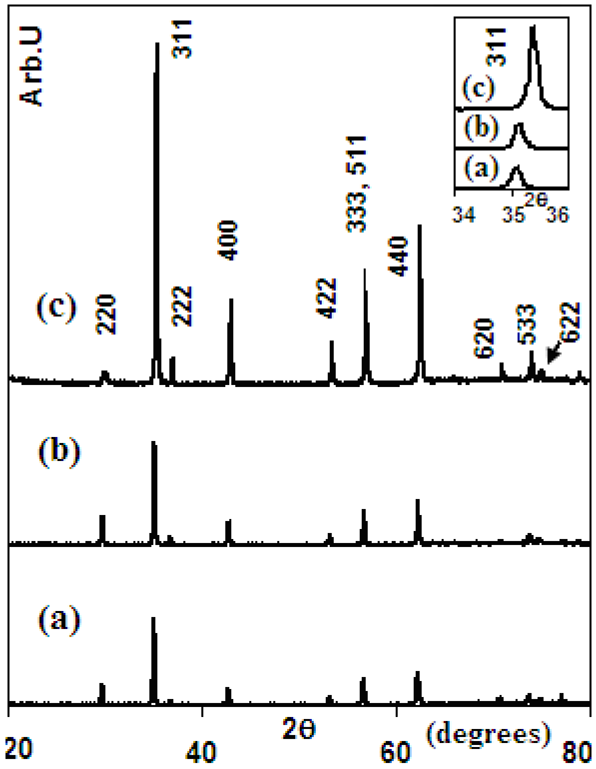

Fig. 4.18 XRD patterns of bulk $Ni_{0.55}Zn_{0.45}Fe_2O_4$ samples at (a) 1100°C, (b) 1200°C and (c) 1300°C. Inset shows shifting of (311) peaks with sintering temperature.

4.3.7 Density (ρ) and porosity (P) of bulk samples

Fig. 4.19(a) shows variation in density of bulk samples at 900°C, 1000°C, 1100°C, 1200°C and 1300°C with Ni concentration along with that of corresponding densities of nano-samples for comparison. It was observed that density increases for most of the compositions with increasing sintering temperature with some exceptional decrease in between for some compositions at specific sintering temperatures.

In exceptional cases it was found that for Ni=0.40 (ρ_B at 1100°C < ρ_B at 1000°C), Ni=0.55 (ρ_B at 1300°C < ρ_B at 1200°C) and Ni=0.70 (ρ_B at 1100°C < ρ_B at 1000°C). The increase in density with sintering temperature is attributed to increase in crystallite sizes and decrease in porosity. Although, density depends on Ni concentration (as observed in case of nano samples), variation in density of bulk samples with Ni concentration in the present work was found to be arbitrary and did not show any specific trend. Such variation in densities indicates that the compacting was not homogeneous in all samples. Also, effect of sintering temperature on density of bulk samples was more pronounced compared to variation in Ni concentrations in the samples. In case of bulk samples, the highest density of 4.99 gm/cm^3 for Ni=0.65 at 1300°C was obtained, whereas lowest of 4.26 for Ni=0.40 gm/cm^3 at 900°C. The observed density of 4.89 gm/cm^3 for Ni=0.60 at 1300°C is closely matching with that of 4.9072 gm/cm^3 for same composition and same sintering temperature reported by A.K.M Akther Hossain et al.[4].

Fig. 4.19(b) shows variation of porosity of bulk samples with Ni concentration along with that of nano-samples for comparison. As expected, it was

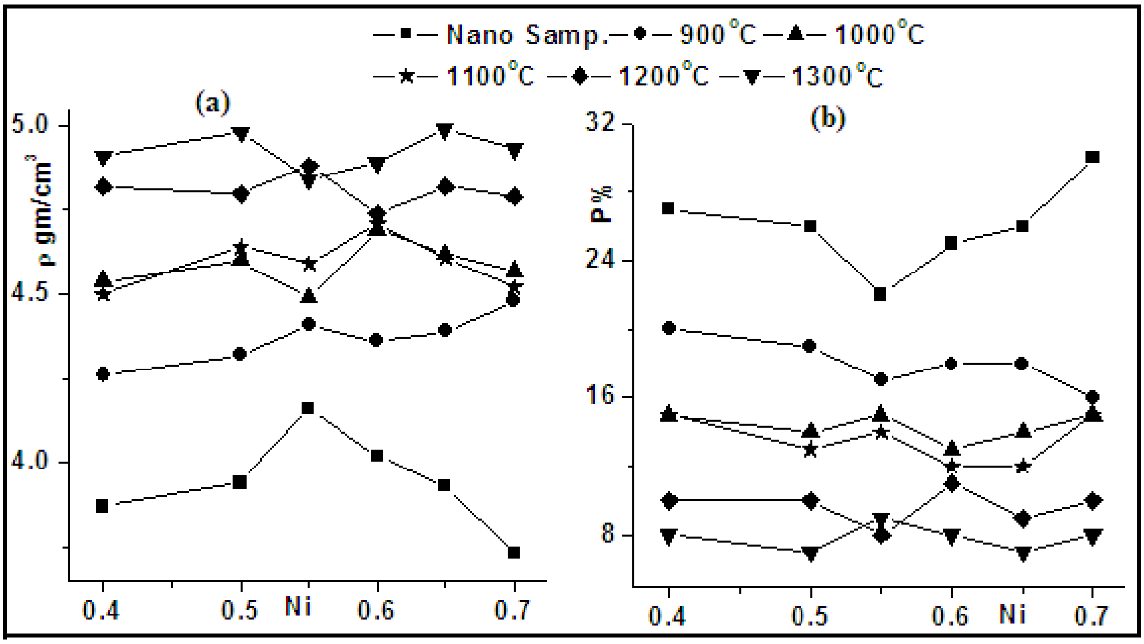

Fig. 4.19 Variations of (a) density and (b) porosity with Ni concentration of nano and bulk $Ni_xZn_{1-x}Fe_2O_4$ samples.

observed that porosity of samples for all the compositions decreases with increase in sintering temperature except for Ni=0.55 (P% at 1300°C < P% at 1200°C). The decrease in porosity with sintering temperature is mainly due to grain growth leading to less pores and improvement in crystallinity. In case of bulk samples, the lowest porosity of 7% for Ni=0.50 and 0.65 at 1300°C was obtained, whereas highest of 20% for Ni=0.40 at 900°C. As like, bulk density, variation of porosity with Ni concentration for a given sintering temperature was found to be arbitrary and did not show any specific trend.

4.3.8 SEM analysis of bulk samples

The SEM micrographs of the bulk samples were recorded to carry out analysis of their morphology, micro structural evolution, particle size distribution, changes in porosity and densification process during sintering process. The SEM micrograph images of bulk $Ni_{0.50}Zn_{0.50}Fe_2O_4$ samples at various sintering temperatures are shown in Fig. 4.20 and Fig. 4.21. Images with higher magnification of 10000 are provided in each case for better view of variation in porosity level.

From the point of view of morphology, the bulk samples sintered at 900°C and 1000°C (see Fig. 4.20 (a) and (b)) show large number of unresolved fine and small powdery grains may be having sizes in the range of few hundred nanometers (unable to resolve them clearly in SEM images even at higher magnification of 10000). They show uneven porous patches/regions and also formation of big clusters on agglomeration of ultra-fine particles especially can be seen in Fig. 4.20 (b).

The bulk sample at 1100°C (see Fig. 4.20(c)) shows increase in compactness in microstructure with small developed grains without clear grain boundaries and large number of open and interconnected pores of different sizes. Clear grains can be observed at 1200°C along with inter particle pores or voids and at 1300°C, well resolved micrometer size grains can be noticed. Thus increase in grain sizes of bulk $Ni_{0.50}Zn_{0.50}Fe_2O_4$ sample from submicron dimensions to micrometer order as sintering temperature increases from 1100°C to 1300°C can be noticed (see Fig. 4.20 and Fig. 4.21). The micro-structure of the samples shows polycrystalline grains.

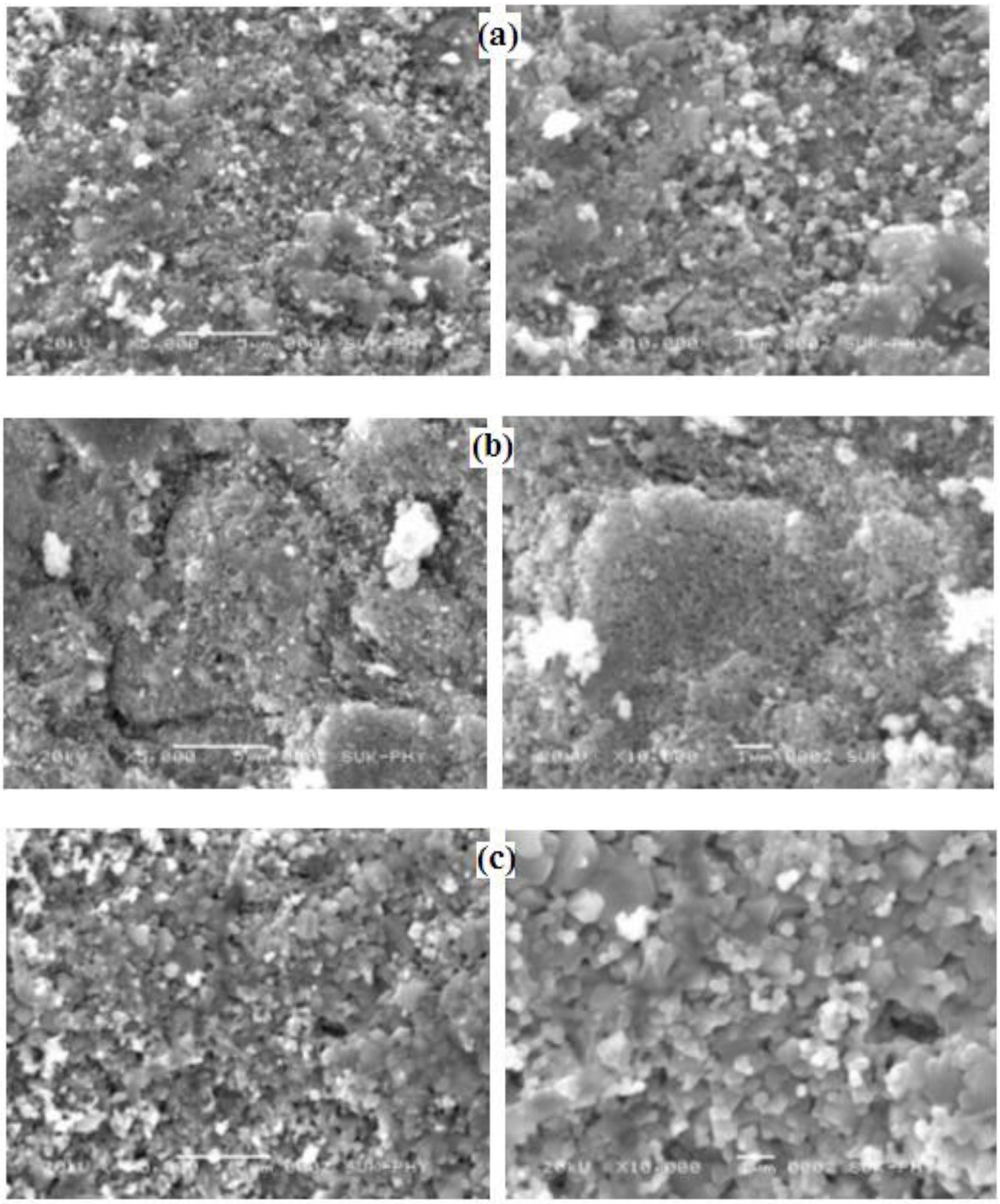

Fig. 4.20 SEM images of bulk $Ni_{0.50}Zn_{0.50}Fe_2O_4$ samples at sintering temperature of (a) 900°C, (b) 1000°C, and (c) 1100°C. Magnification of image [5000 (left) and 10000 (right)].

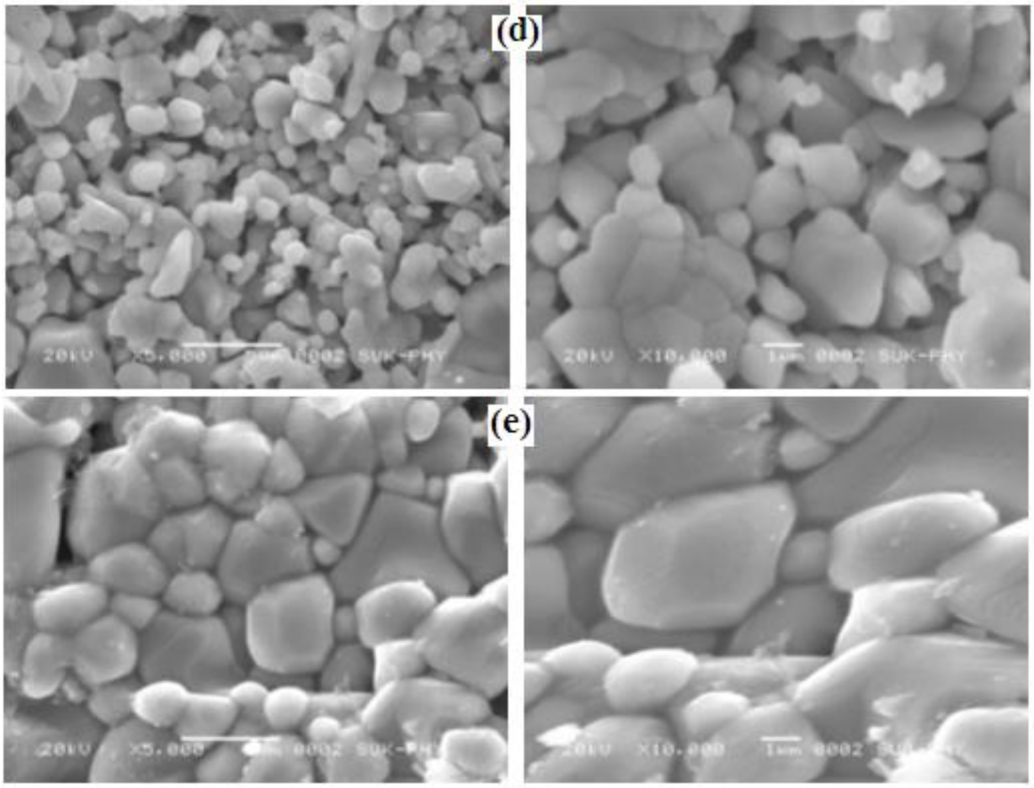

Fig. 4.21 SEM images of bulk $Ni_{0.50}Zn_{0.50}Fe_2O_4$ samples at sintering temperature of (d) 1200^{o}C and (e) 1300^{o}C. Magnification of image [(left) 5000 and (right) 10000)].

Fig. 4.20 (a) and (b) show improvement in the densification process without grain growth at 900°C and 1000°C. Fig. 4.20 (c) shows slow grain growth at 1100^{o}C and Fig. 4.21 (d) and (e) clearly indicates high grain growth along with densification. The density of bulk $Ni_{0.50}Zn_{0.50}Fe_2O_4$ sample was found to vary from 4.32 g/cm^3 to 4.60 g/cm^3 as sintering temperature increases from 900°C to 1000°C. Also, same was varying from 4.80 g/cm^3 to 4.98 g/cm^3 for further increase in sintering temperature from 1200^{o}C to 1300^{o}C. It was found that the grains and grain boundaries could not be observed clearly at sintering temperature of 900°C and 1000°C due to lack in grain growth. However, grain sizes vary in the range 0.9 μm to 2.8 μm for 1200^{o}C and 1.2 μm to 7.2 μm for 1300^{o}C. Thus in the sintering process, the rate of densification was higher at lower sintering temperature from 900°C to 1000°C compared to rate of grain growth. On the other hand, rate of grain growth was higher than rate of densification at higher sintering temperature of 1200°C and 1300°C. Bulk sample at 1100°C has density of 4.64 g/cm^3 which is slightly higher than 4.60 g/cm^3 for 1000°C, but appreciably lower compared to 4.80 g/cm^3 for 1200°C. Thus at sintering temperature of 1100°C, sample shows negligible increase in density and, heating energy is mostly utilized by sample for grain growth. At sintering temperature of 1300°C, the highest density of 94% for Ni=0.65 was obtained and lowest of 91% for Ni=0.55.

4.3.8.1 Grain growth and particle size distribution at 1300°C

The SEM images of bulk $Ni_xZn_{1-x}Fe_2O_4$ samples at sintering temperature of 1300°C along with the histogram representing respective particle size distribution are shown in Fig. 4.22 and Fig. 4.23. The particle size distribution of the bulk samples at 1300°C showed composition dependence.

The maxima in the histogram was observed at size of 5 μm for Ni=0.55 and at the size of 2 μm for Ni=0.70. The maxima in histogram corresponding to three compositions Ni=0.40, 0.50 and 0.60 were found to be at size of 3 μm. Thus Ni=0.55 has maximum grain growth and minimum was observed for Ni=0.70. As far as compromise with density and grain growth is concern, sample with Ni=0.65 show best results (maximum density of 4.99 gm/cm^3 at 1300°C and maxima of histogram at grain size of 4 μm) among all other samples studied in the present work. Since densification and grain growth are competitive and simultaneous processes, the variation in density and grain growth largely depends on method of sample preparation and sintering conditions.

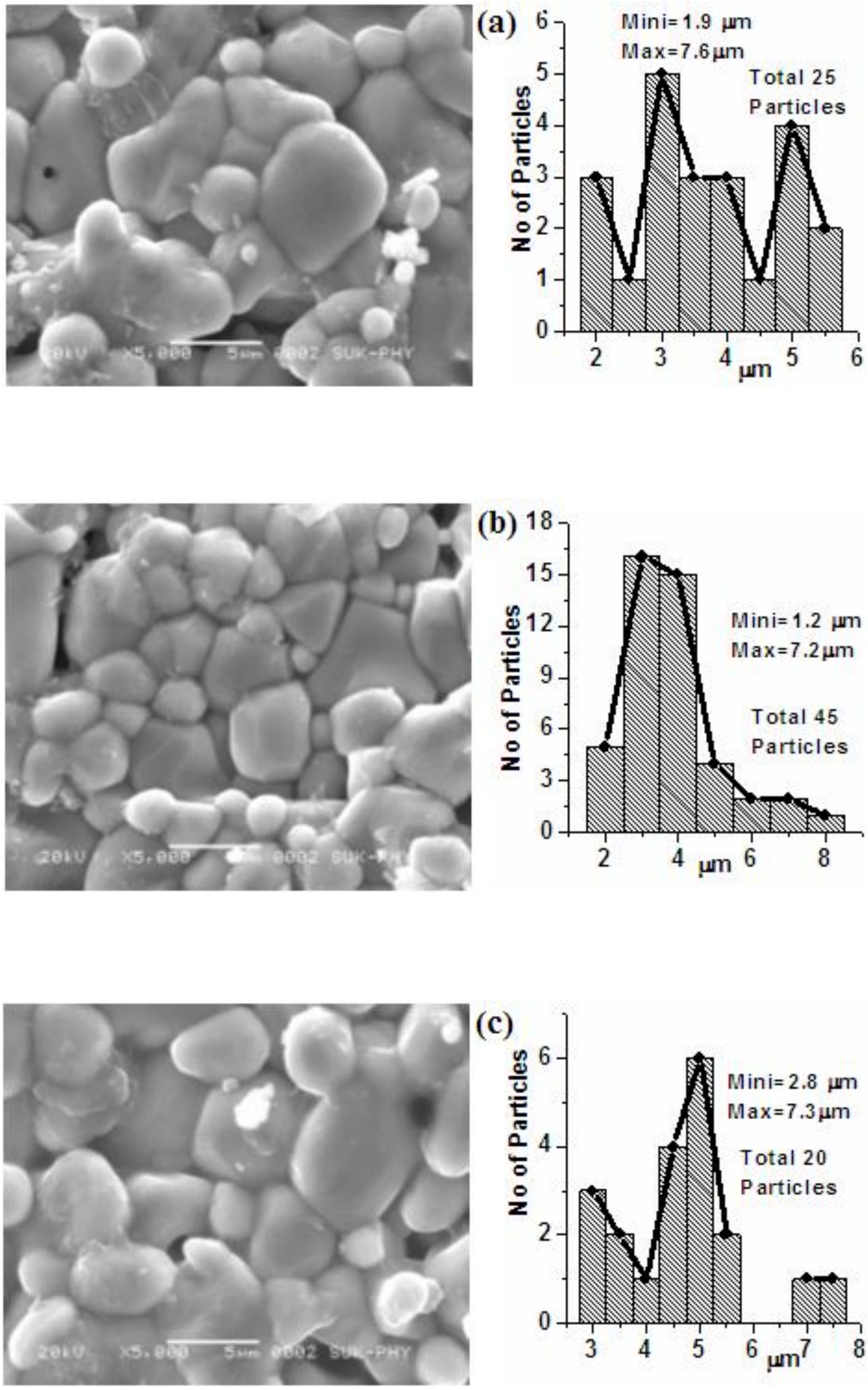

Fig. 4.22 SEM images (left) of bulk $Ni_xZn_{1-x}Fe_2O_4$ samples at sintering temperature of 1300°C for (a) x=0.40, (b) x=0.50 and (c) x=0.55 and (right) corresponding histograms of particle size distribution.

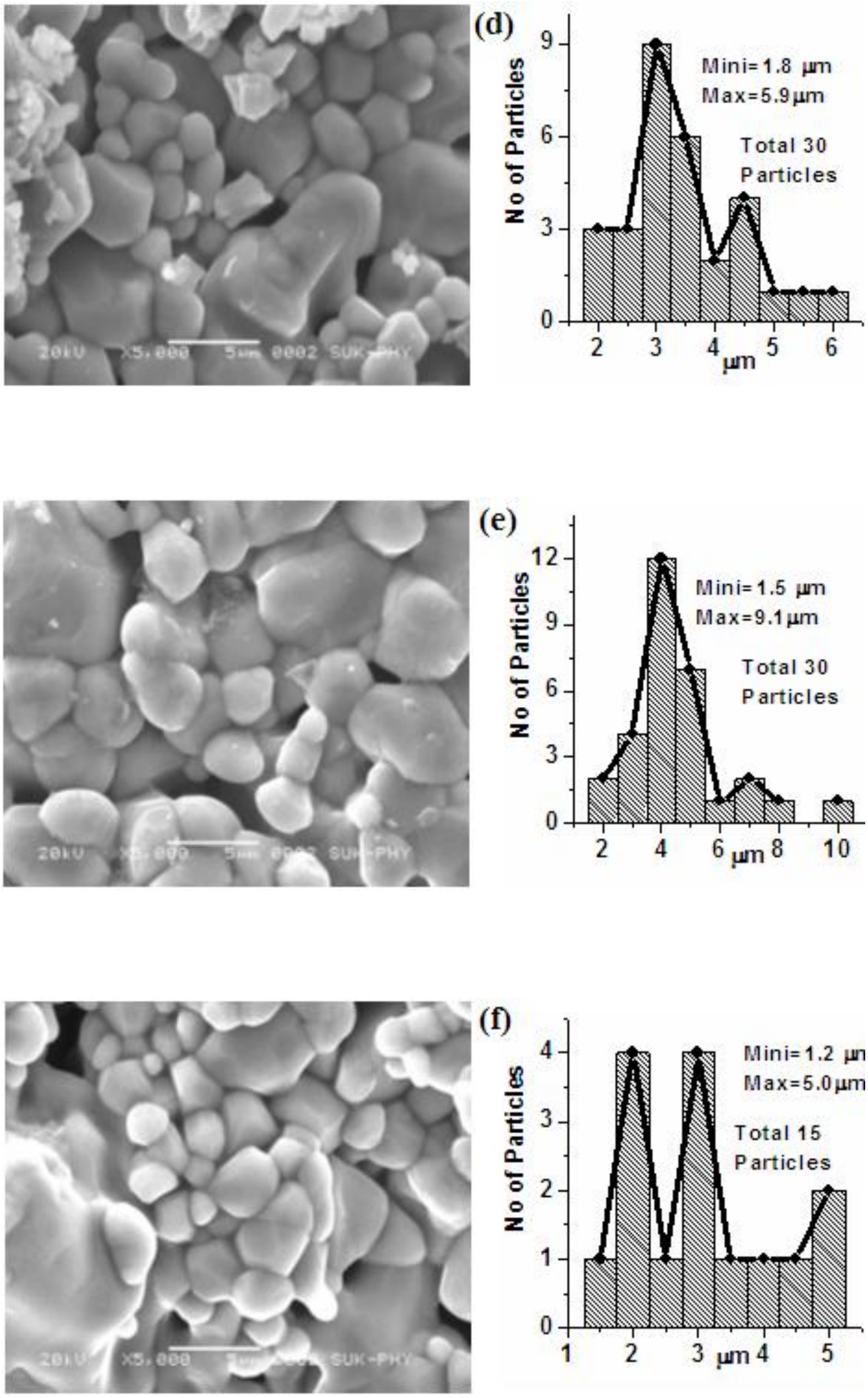

Fig. 4.23 SEM images (left) of bulk $Ni_xZn_{1-x}Fe_2O_4$ samples at sintering temperature of 1300°C for (d) x=0.60, (e) x=0.65 and (f) x=0.70 and (right) corresponding histograms of particle size distribution.

The observed non uniform grain growth and particle size distribution for different compositions at fixed sintering temperature of 1300^oC may be attributed to the observed multi size or poly size dispersion in starting nano samples. Multi size or poly size dispersion influences results of shrinkages during sintering. Monosized particles are easier to process into homogeneous microstructures with respect to size and distribution of the voids/pores and also results in easier control of the microstructure during densification [27].

It can be seen that, the grain growth has not saturated at sintering temperature of 1300^oC and, further grain growth can be expected for higher sintering temperature. However, due to system constraints sintering process could not be extended beyond 1300^oC. However, process of diffusion of many small grains to form single big grain for some samples was taking place at 1300^oC as seen from micrographs in Fig. 4.22 (a), (c) and Fig. 4.23(e) and (f). Few truncated hexagonal shape grains can be observed in some samples at 1300^oC indicating sintering is close to a transitional phase. However, uniform specific shape of the grains was not observed till 1300^oC, as the same may be observed at higher sintering temperature. In general, uniformly packed microstructures must be obtained to achieve reliability and reproducibility in sample processing. Thus the sintering time and rate of heating can be adjusted to get desired grain size and densification. Hence, there is scope for undertaking further investigation to restrict the range of particle size distribution of nano as well as bulk samples.

References

1. J. P. Srivastava, Elements of Solid State Physics, Prentice - Hall India, New Delhi (2001).
2. C. B. Murray, C. R. Kagan, and M. G. Bawendi, Annu. Rev. Mater. Sci., 30, (2000), 545-550.
3. C. Kittel, Introducion to Solid State Physics, Seventh Edition, John Wiley & Sons Inc., Singapore, (1995).
4. A. K. M. Akther Hossaina, S.T. Mahmuda, M. Seki, T. Kawai and H. Tabata, J. Magn. Magn Mater, 312, (2007), 210-219.
5. Yu. Rosenberg, V. S. Machavariani, A. Voronel, S. Garber, A. Rubshtein, A. I. Frenkel and E. A. Stern, J. Phys. Condens. Matter., 12, (2000), 8081-8084.
6. J. A. Eastman, M. R. Fitzsimmons, L. J. Thompson, A. C. Lawson and R. A. Robinson, Nanostruct. Mater., 1, (1992), 465-470.
7. D. Oleszak and P. H. Shingu, J. Appl. Phys., 79, (1996), 2975-2980.
8. S. S. Jadhav, S. E. Shirsath, B. G. Toksha, S. J. Shukla and K. M. Jadhav, Chinese journal of chemical physics, 21, (2008), 381-386.
9. R. L. Dhiman, S. P. Taneja and V. R. Reddy, Ad. Cond. Matt. Phy. (2008), 1-7.
10. S. Hugh, C. O’Neill and A. Navrotsky, American mineralogist, 68, (1983), 181-194.
11. M. A. Amer, A. Samy, T. M. Meaz, S. Ata-Allah and S. Aboul-Enein, Turk J. Phys 29, (2005), 163-177.
12. N. Yao and Z. L. Wang, Handbook of Microscopy for Nanotechnology (2005).
13. R. N. Jagpat and A. H. Ambre, Indian J. Eng. Mater. Sci., 13, (2006), 368-384.
14. J. Goldstein, Scanning electron microscopy and x-ray microanalysis, Kluwer Adacemic/Plenum Publishers, (2003), 689.

15. B. Voutou and E. C. Stefanaki, Physics of Advanced Materials Winter School, (2008).
16. E. Suzuki, Journal of Microscopy, 208 (3), (2002), 153-157.
17. M. B. Mona, B. Sarah and P. Octavio, J. Solid State Chem., 178, (2005), 1080-1086.
18. G. Mathew, A. M. John, S. Nair, P. A Joy and M. R. Anantharaman, J. Magn. Magn Mater, 302, (2006), 190-195.
19. S. Chipera and D. L. Bish, Advances in X-ray Analysis, 34, (1991) 473-476.
20. G. K. Williamson and W. H Hall, Acta. Metall., 1, (1953), 22-25.
21. K. Velmurugan, V. S .K. Venkatachalapathy and S. Sendhilnathan, Materials research, 12, (2009), 529-534.
22. A. A. Pandit, S. S. More, R. G. Dorik and K. M. Jadhav, Bull. Mater. Sci., 26, (2003), 517-521.
23. B. P. Ladgaonkar and A. S. Vaingankar, Bull. Mater. Sci., 25, (2002), 351-354.
24. R. Iyer, R. Desai and Upadhyay, Bull. Mater. Sci., 32, (2009), 141-147.
25. B. K. Labde, M. C. Sable and N. R. Shamkuwar, Mat. Lett. 57, (2003), 1651-1655.
26. M. A. Amer, T. M. Meaz, S. Ata-Allah, S. Aboul-Enein and M. O. Abd- El-Hamid, Egypt. J. Solids, 28, (2005), 275-293.
27. A. Dias, R. L. Moreira and N. D. S. Mohallem, J. Phys. Chem Solids, 58, 4, (1997), 543-549.

CHAPTER 5

MAGNETIC PROPERTIES

5.1 Introduction

The origin of magnetism lies in the orbital and spin motions of electrons and their interactions with each other. The magnetic properties of any given material can be understood by studying its response to external magnetic fields. However, it is also found that magnetic properties of ferrites are strongly dependent on grain sizes [1, 2]. The nano particles show interestingly different magnetic properties owing to their small grain sizes [3, 4].

The size dependent magnetic properties is highly important in new technological applications such as ultrahigh density magnetic data storage, ferrofluids, giant magneto resistance (GMR) sensor, magneto caloric refrigerator, magneto electrics, magnetic resonance imaging (MRI) contrast enhancement agents, magnetically guided target-specific drug delivery systems, DNAs and genes sorting etc. [5, 6,7].

Ni-Zn ferrites are one of the most versatile magnetic materials for general use in both low and high-frequency devices because of their high resistivity, low dielectric losses and high Curie temperature [8]. Ni-Zn ferrites is highly promising candidate for above mentioned applications. It is also useful in transponders i.e. devices used to transmit or respond to RF signals and its ferrite core is popularly used for low frequency application (below 500 KHz). Due to their high permeability they are also used for antennas in frequency range of few hundred KHz to few MHz.

The magnetic property of ferrite depends on the relative position of the ions in the lattice. In Ni-Zn ferrites Ni^{2+}ions prefer to occupy the octahedral sites and Zn^{2+} prefer tetrahedral sites. The Fe^{3+} ions are distributed on both sites. Depending on the composition, method of preparation and processing conditions such as sintering temperature and atmosphere, the lattice site occupancy changes leading to the change in magnetic and electrical properties. This shows that, the critical problem in the physics of solid state and magnetism is to select proper method of synthesis, composition and processing conditions to get the required results.

In the present work, the magnetic properties such as saturation magnetization, retentivity, coercivity, blocking temperature, Curie temperature, initial permeability and permeability loss of nano and bulk Ni-Zn ferrite are investigated. Basics theory of various magnetic parameters and corresponding phenomenon in ferrites are also briefly described at the beginning of this Chapter.

5.2 Domains

In magnetic materials, small regions with a particular overall spin orientation are termed as domains. The size of the domain is of the order of 0.05μm to 0.5μm and is property of each material [9]. The boundary between two neighboring domains is called domain (or block) wall. In the natural state, magnetic materials has no net magnetic moment, because the domains are randomly oriented as shown in Fig. 5.1(a). When a magnetic field is applied, the domains align in the direction of field and a strong magnetization results as shown in Fig. 5.1(b). An applied field results in shifts and rotation of the domains in the direction of field such that the large volume of domains is aligned with field. Domain (or Block) wall is a narrow

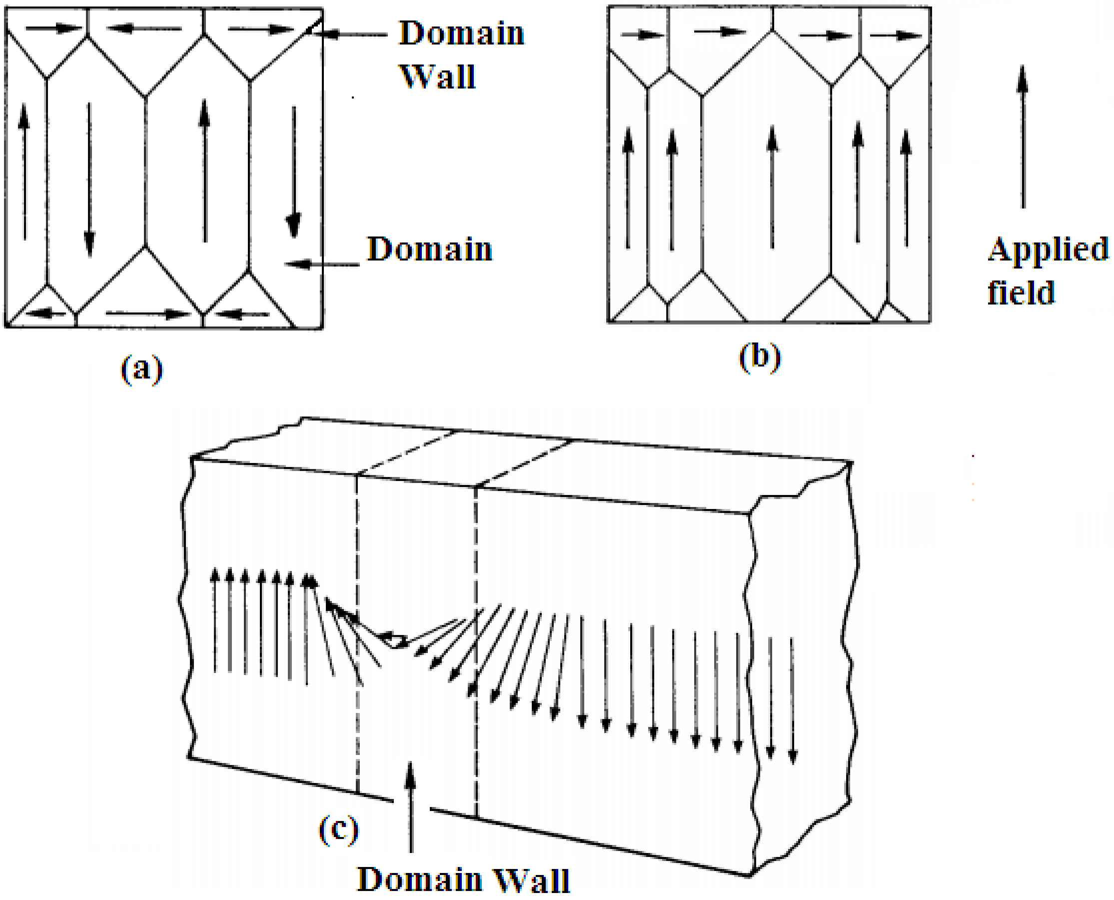

Fig. 5.1 (a) Domain structure with random orientation, (b) domain growth and alignment in the direction of applied field and (c) reorientation of spins in domain wall.

region in which atomic moments changes orientation by 180^{o}C as shown in Fig. 5.1(c). If small magnetic fields are applied, only domain wall movements are possible and the magnetization process is reversible. For higher applied fields, the domain rotation are achieved which are irreversible.

5.3 B-H curve

B-H curve is the characteristic curve for a magnetic material, which represents the magnetic response (soft/hard) of that material under an applied field. It is commonly called as Hysterisis loop or B-H curve of magnetic materials. Where *B* is magnetic induction measured in gauss, *M* is magnetization or magnetic moment per unit volume measured in emu/cm^3 and *H* is the applied field measured in (Oe). *B*, *M* and *H* are related according to Equations 5.1 and 5.2.

$$B = \mu_o (H + M) \qquad in \ (SI) \tag{5.1}$$

$$B = H + 4\pi M \qquad in \ (CGS) \tag{5.2}$$

Where μ_o (i.e. permeability of free space) having a value of 4π x10^{-7} H/m. The measure of effectiveness of an applied field for inducing magnetic dipole in the material is given by magnetic susceptibility (χ) and the ratio of magnetic induction to magnetic field strength is called as magnetic permeability (μ) as given by Equation 5.3 and 5.4 respectively.

$$\chi = M / H \tag{5.3}$$

$$\mu = B / H \tag{5.4}$$

Fig. 5.2 shows M-H hysteresis loop and orientation of domain microstructure at various stages. Proceeding from H=0 and M=0, so-called initial magnetization curve is first obtained. At low field strength, domains that are favorably oriented to the magnetic field direction grow at the expense of those that are not. This gives rise to wall displacements and is reversible. At higher field strength, whole domains overturn magnetically which are irreversible. This is the steepest part of the curve. Finally the magnetic moments are moved out of the preferred states given by the crystal lattice into the direction of the field until saturation is obtained, i.e. all elementary spins in the material are in the direction of the field. If H is now reduced again, the magnetization curve takes different path and produces hysteresis loop.

The important parameters those can be extracted from this loop are as mentioned below.

5.3.1 Saturation magnetization (M_s)

The maximum value of magnetization, which can be obtained from a particular type of ferrite under the applied field, is called saturation magnetization. At this point, almost all the magnetic domains align along the direction of applied field.

5.3.2 Remanence magnetization or retentivity (M_r)

When the applied field approaches to zero, magnetic material still retains some of its magnetization called as remanence magnetization or retentivity. It is mainly due to the resistance offered by domain walls against the direction of applied field.

5.3.3 Coercive field or force (H_c)

The amount of applied field required to fully demagnetize the material is termed as coercive field or force.

5.3.4 Hysteresis loss

As discussed above, due to magnetic anisotropy the second reversal does not coincide with its first reversal and causes hysteresis. This loss is proportional to the total area trapped inside the loop.

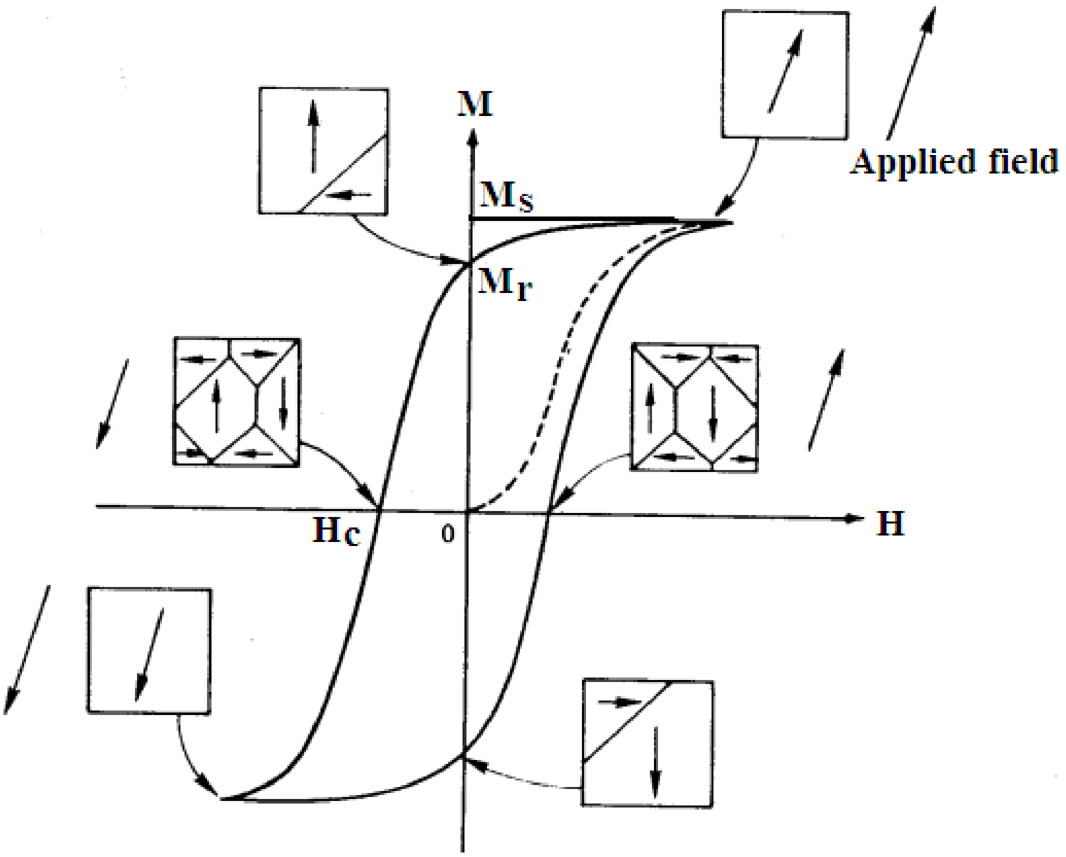

Fig. 5.2 M-H hysteresis loop showing orientation of domain microstructure at various stages.

5.4 Single Domain Theory and Superparamagnetism

When dimensions of a magnetic material are reduced, the size of the domains is accordingly decreased and their structures may change in terms of domain wall width. When the size reaches a critical value, the magnetic material only possesses a single domain. Below critical size, magnetic anisotropy energy may become as low as to be comparable to or even lower than the thermal energy. As a result, the energy barrier for magnetization reversal may be thermally overcome, and the magnetic moment is thermally fluctuated, like a single spin in a paramagnetic material. This phenomenon is called superparamagnetism.

Superparamagnetism is also characterized by a relaxation time (T_N) and thus the actual magnetic behavior depends on the value of measuring time (t_m) in a particular experimental technique. At given temperature, if the measurement time is much longer than relaxation time, the moment is rapidly relaxed by thermal fluctuation, and consequently the entire system is in superparamagnetic state. On the contrary, as the measurement time is much shorter than the relaxation time, the moment relaxes so slow that it seems to be blocked. The blocking temperature is thus defined as the temperature at which the magnetic moment relaxation time is equal to the measurement time ($T_N = t_m$), or the temperature where the moment is able to overcome the energy barrier into the superparamagnetic state at a certain measurement time. The mean time between two flips is called the Néel relaxation time T_N and is given by the Neel-Arrhenius Equation 5.5 [10].

$$T_N = T_o \exp(\frac{KV}{K_B T}) \qquad 5.5$$

Where, T_N is the average length of time that it takes for the nanoparticle’s magnetization to randomly flip as a result of thermal fluctuations, T_o is called the attempt time or attempt period, and is characteristic of the material (its typical value is 10^{-9}–10^{-10} second), K is the nanoparticle’s magnetic anisotropy energy density, V is its volume, k_B is the Boltzmann constant and T is the temperature. The amount KV is the energy barrier associated with the magnetization moving from its initial easy axis direction, through a “hard plane”, to the other easy axis direction.

5.5 Magnetic Anisotropy

The phenomenon of dependence of macroscopic behavior or extent of magnetization on the spatial direction in which it is measured is called magnetic anisotropy. There are several causes from which the magnetic anisotropy may occur, including magnetostriction and stress, magnetocrystalline anisotropy, shape anisotropy and surface anisotropy. Three important magnetic anisotropies responsible for the magnetic properties of nanomaterials are given below.

5.5.1 Magnetocrystalline anisotropy

The magnetocrystalline anisotropy is intrinsic and depends on spin orbital coupling. Material with large magnetocrystalline anisotropy energy is called hard magnetic material and shows a large coercivity in hysteresis measurement. A magnetic material with small magnetocrystalline anisotropy energy is referred to soft magnetic material and has a small value of coercivity.

5.5.2 Shape anisotropy

Shape anisotropy is induced from magnetostatic energy and is an extrinsic property. For nonspherical magnetic materials such as a long rod, the shape anisotropy can be very predominant.

5.5.3 Surface anisotropy

Surface anisotropy is caused by the existence of a surface that represents a discontinuity for magnetic interactions. Such surface effects become more significant as the size of magnetic nanomaterials decrease, due to increasing numbers of atoms on the surface layer of a particle. Surface anisotropy generally leads the surface to be magnetically harder than the core of the particle. In case of nano particles, effective anisotropy constant (K_{eff}) for a spherical shape particle is given by Equation 5.6 [11].

$$K_{eff} = K + (6/d)K_s \qquad 5.6$$

Where K_s is surface anisotropy constant, K is magnetocrystalline anisotropy constant, and d is diameter of the particle.

5.6 Permeability

In ferromagnetic and ferrimagnetic materials, permeability is very important parameter. It deals with the ratio of flux density (B) attained by a ferromagnetic material under an applied field (H). Actually, it is the slope of line, which connects the origin and any point of B-H curve. It is dimensionless quantity and is given by Equation 5.4.

Permeability depends upon composition, sintered density and working temperature. Under the applied field, permeability initially increases and reaches its maximum value i.e. saturation point of B-H curve and after that it decreases with further increase of magnetic field (H). In general, permeability can be classified in three different categories such as maximum permeability, differential permeability and initial permeability.

5.6.1 Maximum permeability

It is the ratio of maximum flux density and applied magnetic field given by Equation 5.7. In B-H curve, the slope of line starting from origin to the point of saturation flux density represented the value of maximum permeability.

$$\mu_{\max} = B_{\max} / H \tag{5.7}$$

5.6.2 Differential permeability

It is the slope of the line at any point on B-H curve and given by Equation 5.8. Differential type permeability helps to understand the variation in permeability from one point to other point and whole trend of the B-H curve can be analyzed in detail.

$$d\mu = dB / dH \tag{5.8}$$

5.6.3 Initial permeability

It is the property, which defines how quickly the domains of magnetic material align along the direction of applied field. It is denoted by μ_i. The slope of linear portion of B-H curve represents initial permeability. According to Goldman [12] if the applied field is very low (approaches towards zero) then the ratio of magnetic induction to applied field is called initial permeability and is given by Equation 5.9.

$$\mu_i = \lim_{H \to 0} \left(\frac{B}{H}\right) \tag{5.9}$$

The initial permeability [13] in present work on the toroid type core can be calculated by using formula given by Equation 5.10.

$$\mu_i = \frac{2\pi L}{N^2 h \ln\left(\frac{OD}{ID}\right)\mu_o} \qquad 5.10$$

Where L is inductance in Henry, N is number of turns on toroid, h is height of core in meters, OD and ID is outer and inner diameter of toroid in meters and μ_O is permeability of free space (1.25x10^{-6} Hm^{-1}).

It is well known that permeability of polycrystalline ferrite is related to two different magnetizing mechanisms; spin rotation and domain wall motion [14] which can be describe by Equation 5.11 to 5.13.

$$\mu_i = 1 + \chi_w + \chi_s \qquad 5.11$$

$$\chi_w = (3\pi M_s^2 D)/4\gamma \qquad 5.12$$

$$\chi_s = (2\pi M_s^2)/K \qquad 5.13$$

Where, χ_w is domain wall susceptibility, χ_s is intrinsic rotational susceptibility, M_s is saturation magnetization, K is total anisotropy, D is grain diameter and γ is domain wall energy. It is generally assumed that the initial permeability is due to reversible displacement of the domain walls and the contribution from the rotation of spin inside each domain is small due to high crystal anisotropy.

5.7 Models of Permeability

5.7.1 Globus model

According to Globus model initial permeability is mainly due to reversible motion of domain walls under very small magnetic field [15]. As per this model, domain wall is pinned at the grain boundaries and they get bulged till critical applied field is reached at which walls get unpinned and growth of domain volume stops. According Globus model initial permeability is given by Equation 5.14.

$$(\mu_i - 1) = 3M_s^2 D/16\gamma \qquad 5.14$$

Where, M_s is saturation magnetization, D is grain diameter and γ is domain wall energy.

5.7.2 Non magnetic grain boundary model

This model accounts for grain size dependence of initial permeability and was developed by Johnson [16]. According to this model permeability has almost linear dependence on grain size and is given by Equation 5.15.

$$\mu_e = \frac{\mu_i D}{(\mu_i \delta + D)} \qquad 5.15$$

Where, μ_e is effective permeability, μ_i is initial permeability, D is grain size and δ is grain boundary thickness. For larger grains $D >> (\mu_i\ \delta)$, this model predicts that effective permeability is equivalent to initial permeability of single crystal of the same material.

5.8 Snoek's Law

Snoek stated that, ferrites having high initial permeability (μ_i) showed low resonance frequency (F_r) [17]. The loss of inductive component at resonance frequency indicates that ferrite have lost its magnetic nature i.e. initial permeability approaches towards zero. In order to measure the variation in magnetic behavior with rise of frequency, a relationship between resonance frequency and permeability was firstly suggested by Snoek and is given by Equation 5.16.

$$\mu_i F_r = constant. \qquad 5.16$$

From Equation 5.16 it is clear that higher the value of initial permeability (μ_i), lower will be the resonance frequency **(**F_r).

5.9 Loss Tangent (tanδ)

The ratio of resistive to inductive component of magnetic impedance is called loss tangent and is denoted by tanδ. Alternatively, it can also be expressed by taking the [18] ratio of imaginary to real part of the complex permeability as given by Equation 5.17.

$$\tan\delta = \frac{\mu''}{\mu'} \qquad 5.17$$

The loss tangent is frequency dependent property and increases with the rise of frequency. It is used to determine the efficiency of a ferrite core to suppress the electromagnetic interference at a particular frequency. The reciprocal of loss tangent is termed as quality factor Q.

5.10 Mössbauer Spectroscopy

Mössbauer spectroscopy is widely used in mineralogy to examine the valence state of iron and type of coordination polyhedron occupied by iron atoms (trigonal, tetrahedral, octahedral, etc.) in a given sample. Additional information in the form of a value of magnetic field can help in identification of magnetically ordered phases. Mössbauer spectroscopy technique is based on the recoil-free, resonant absorption and emission of gamma rays in solids. The Mössbauer effect relies on the fact that ^{57}Fe, which is a decay product of ^{57}Co, is unstable. The ^{57}Fe decays by giving off a gamma ray (γ-ray), along with other types of energy. This γ-ray may be absorbed without recoil by a nearby ^{57}Fe, which happens to have just the right splitting between the energy levels in its nucleus to absorb it. This scenario will only happen if the decaying Co atom is surrounded by the same atoms as the absorbing Fe. If the receiving Fe atoms are in a different matrix than in the emitter, then no absorption can occur. When source and absorber atoms are in different local environments, their nuclear energy levels are different and appears in the transmission spectrum as a shift of the minimum away from zero velocity. This shift is generally called isomer shift (IS). Interaction of the nuclear quadrupole moment with the electric field gradient leads to splitting of the nuclear energy levels. For ^{57}Fe, this causes individual peaks in the transmission spectrum to split into doublets having a quadrupole splitting of QS. When a magnetic field is present at the nucleus, Zeeman splitting takes place, yielding a sextet pattern. The areas of the lines vary in the ratio of 3:2:1:1:2:3 [19, 20].

5.11 Sample Preparation and Experimental Work

The experimental work such as sample preparation and the various parameters selected in different experimental techniques to characterize the magnetic properties of the nano and bulk samples is discussed in this Section.

5.11.1 High field hysteresis loop tracer

Room temperature magnetic properties of nano and bulk samples were investigated using pulse field hysteresis loop tracer describe by Likhite et. al [21]. The fine powder of nano samples was pressed into pallets of 10 mm diameter by applying pressure of 7.5 KN for 5 minutes. These pallets were then placed in a sample holder of high field hysteresis loop tracer and variation of magnetic moment with applied field up to 6 KOe was measured. Similar experimental measurements were repeated for all the bulk samples. Hysteresis loops of all the nano and bulk samples were also recorded.

5.11.2 Vibrating sample magnetometer (VSM)

Magnetic properties of nano samples at low temperatures (5K, 10K, 50K, 100K, 200K and 300K) were obtained using VSM (Lakeshore model 7404). The fine powder of the nano samples was directly placed in the sample holder of the device and variation of magnetic moment with applied field up to 2T was measured. Corresponding hysteresis loops were also recorded.

5.11.3 Superconducting quantum interference device (SQUID)

Zero field cooled (ZFC) and field cooled (FC) response of magnetization as a function of temperature (5 K to 300 K) were recorded at field of 0.1T and 0.05T for nano $Ni_xZn_{1-x}Fe_2O_4$ samples (x=0.40, 0.55, 0.65 and 0.70) using (SQUID). The fine powder of the nano samples was directly place in the sample holder of the device to obtain the required magnetic profiles.

5.11.4 AC susceptibility

The variation of magnetic moment with temperature of nano samples were investigated using automated low field AC susceptibility apparatus describe by Likhite et. al [22]. Samples in the powder form were directly placed in the sample holder of the instrument and variation of magnetic moment with temperature up to Curie temperature was recorded. The plots of normalized susceptibility and Curie temperatures of the samples were obtained. The experiments were repeated for bulk samples to obtain their Curie temperature.

5.11.5 Permeability measurements

Room temperature variation of initial permeability (μ_i) and magnetic loss factor (tanδ) as a function of frequency (in the range of 20 Hz to 3 MHz) and temperature in the range of 30^oC to 495^oC for few selected frequencies of bulk samples were obtained by measuring inductance value of toroids using LCR-Q meter (Wayne Kerr 6440B precision component analyzer setup). The fine powder of nano particle Ni-Zn ferrite samples was pressed into toroids of height 2 mm to 3 mm and, inner and outer diameter of 1 cm and 2 cm respectively by applying pressure of 75 KN for 5 minutes. These toroids were then sintered at 900^{o}C, 1000^{o}C, 1100^{o}C, 1200^{o}C and 1300^{o}C for 4hr in air in a progressive manner using a programmable Carbolite furnace by setting heating and cooling rate of 5^{o}C min^{-1}. A winding of 100 turns of super enameled doubly insulated copper wire of gauge 33 was wound on each toroid and connected to the leads of the precision component analyzer to measure inductance and loss. Initial permeability was calculated using formula given in Equation 5.10.

5.11.6 Mössbauer spectroscopy

The fine powder of nano samples (0.25 grams to 0.30 grams) was spread across the sample holder and exposed to γ-rays. Spectra of samples were recorded using a Mössbauer spectrometer (Nucleonix Systems Pvt. Ltd., Hyderabad, India) operated in constant acceleration mode (triangular wave) in transmission geometry at room temperature. The source employed was ^{57}Coin Rh matrix. The calibration of the velocity scale is done by using an enriched ^{57}Fe metal foil. The line width (inner) of calibration spectra is 0.23 mm/s. Mössbauer spectra were fitted by using a Win-Normos fit program.

5.12 Results and Discussion

5.12.1 Saturation magnetization (M_s) of nano samples

The M-H loops of nano samples at room temperature are shown in Fig. 5.3 and 5.4. The loops show clear ferrimagnetic behavior for all the samples. The narrow loops obtained for all the nano samples indicate that samples in the present work are soft magnetic materials. The magnetization increases with increasing applied magnetic field and reach near saturation for fields above 0.50 T (5 KOe). The hysteresis loops were found to deviate from rectangular nature, reflecting the magnetic behavior of soft ferrite materials [2].

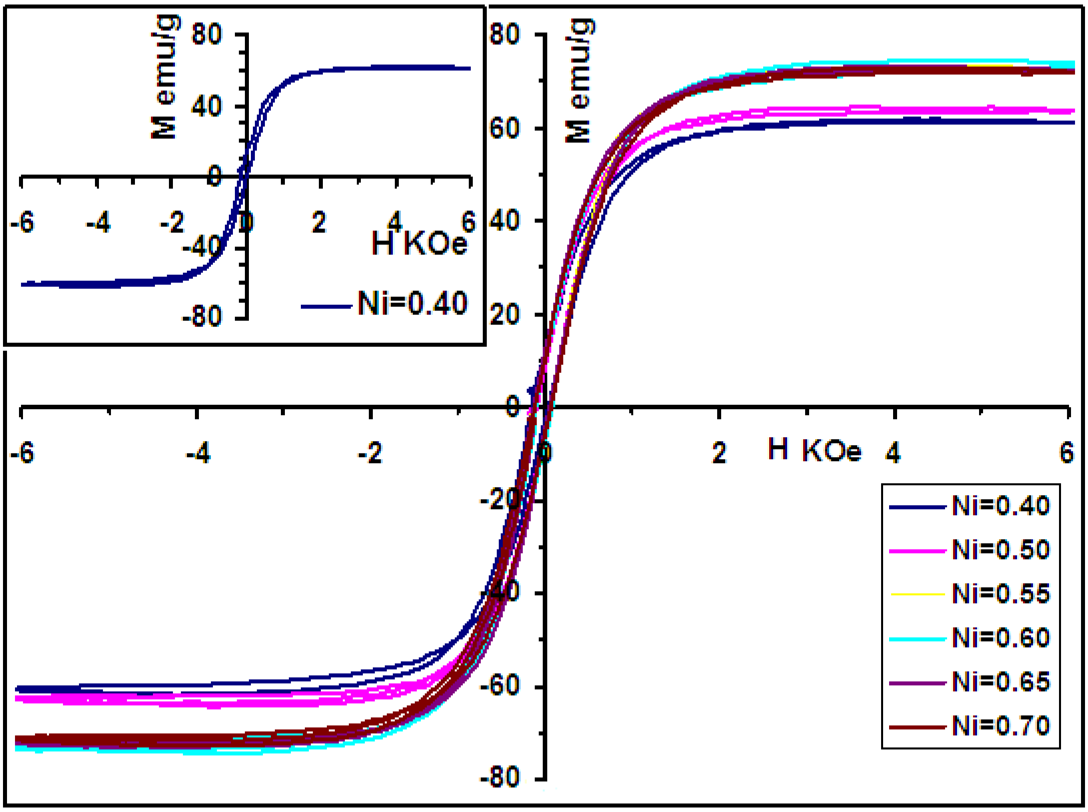

Fig. 5.3 The M-H loops of nano $Ni_xZn_{1-x}Fe_2O_4$ samples measured at room temperature using pulse field hysteresis loop tracer. Inset shows M-H loop for Ni=0.40.

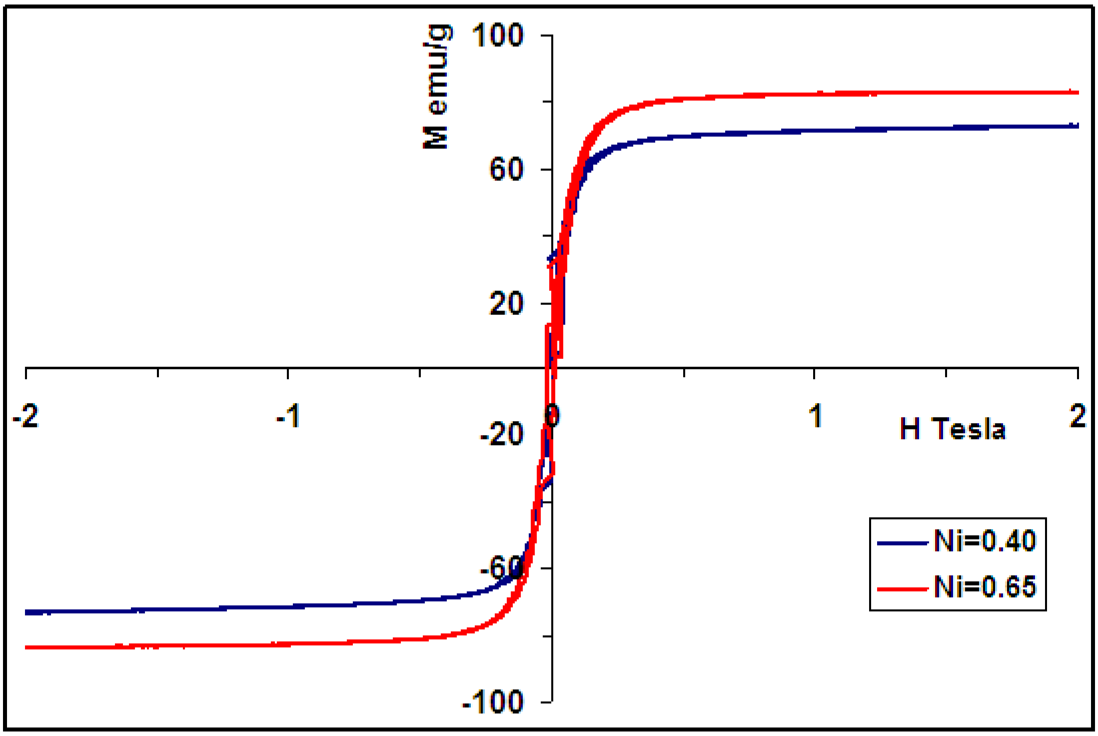

Fig. 5.4 The M-H loops of nano $Ni_xZn_{1-x}Fe_2O_4$ samples measured at room temperature using VSM.

The variation of $\mathbf{M_s}$ of nano samples with Ni content is shown in Fig. 5.5. It can be seen that $\mathbf{M_s}$ increases much rapidly as the Ni concentration increases till $x \leq 0.60$, however the same is seen to show a slow fall as x goes beyond 0.60 thereby showing a broad hump. The initial rise in $\mathbf{M_s}$ is essentially due to strengthening of A-B exchange interaction due to replacement of nonmagnetic Zn ions by Ni ions. The decrease in $\mathbf{M_s}$ for $x>0.60$ can be explained on the basis of magnetic moment of A and B sites. The net magnetization of the sample is given by $M = M_B - M_A$, where M_A and M_B are the magnetic moments of A and B sites, respectively. As Ni is added (with an affinity to B site), proportionate Fe^{3+} ions are transfer from B site to A site. This results in a marginal decrease and marginal increase in magnetic moment of B site and A site respectively, hence there is a net decrease in over all $\mathbf{M_s}$ of the

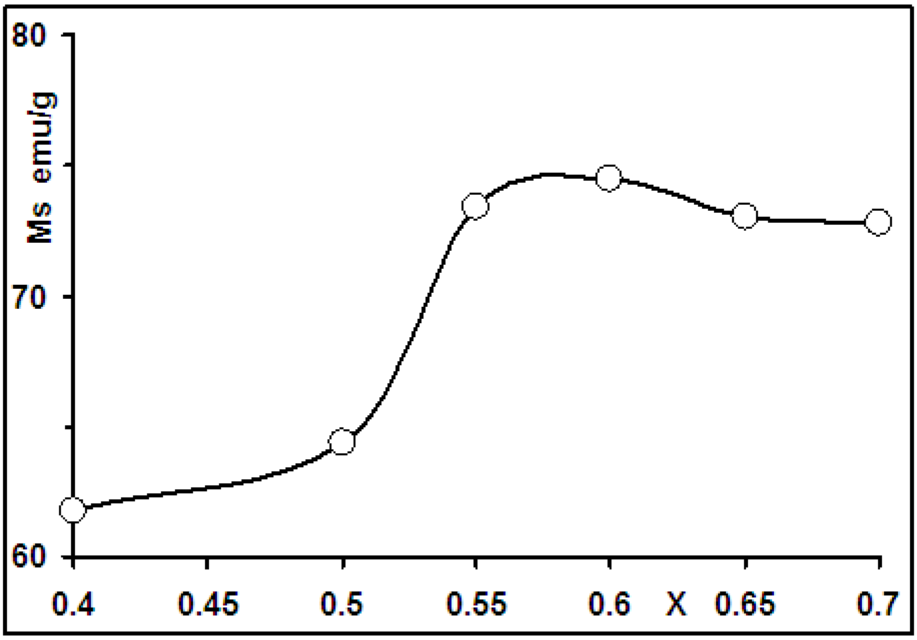

Fig. 5.5 Variation of saturation magnetization of nano $Ni_xZn_{1-x}Fe_2O_4$ samples with Ni content.

Table 5.1 Saturation magnetization (M_s), magneton number (n_B) (theoretical and observed) and Yeffet Kittel angles (Θ_{YK}) of nano $Ni_xZn_{1-x}Fe_2O_4$ samples.

Ni (x)	Zn (1-x)	Ms emu/g	Obs. n_B in u_B	Theor. n_B in u_B	n_B in u_B [23]	ϴYK °		
						Present work	Co-ppt [23]	Standard ceramic [23]
0.40	0.60	61.74	2.636	6.8	2.55	58° 21’	59° 27’	------
0.50	0.50	64.39	2.742	6	2.78	52°32’	52° 57’	24°54’
0.55	0.45	73.44	3.123	5.6	-------	45°30’	-----	-------
0.60	0.40	74.47	3.162	5.2	3.23	41° 28’	45° 36’	21°31’
0.65	0.35	73.06	3.098	4.8	-----	38° 35’	------	------
0.70	0.30	72.83	3.084	4.4	2.99	33° 55’	35°12’	18°25’

samples. For samples with x≤ 0.60 this decremental effect is compensated by increasing A-B exchange interaction due to addition of Ni ions replacing Zn ions. Similar results are reported by Jadhav et al. [23] and Kakatkar *et al* [24]. The maximum $\mathbf{M_s}$ of 74.47 emu/g was observed for Ni=0.60 and a minimum of

61.74 emu/g was obtained for Ni=0.40. The values of **M_s**, magneton number (theoretical and observed) are given in Table 5.1.

Fig. 5.6 shows the differences in variation of observed and theoretically calculated magneton number of nano samples at room temperature as a function Zn content (1-x). It can be seen that observed and theoretically calculated magneton number (saturation magnetisation per formula unit) differs from each other. This discrepancy indicates that, there is a significant amount of spin canting at B site. This confirms, the variation of magnetic moment with Zn content is not governed by a two sublattice model (Neels model). It can be seen that, theoretical magneton number increases linearly as a function of Zn content. However, observed magneton moment is seen to increase up to Zn≤0.40 and decreases for Zn>0.4 due to non-collinear spin arrangements in the octahedral cations [14].

The Y-K angles of nano samples in the present work and that of Ni-Zn ferrite samples prepared from standard ceramic and wet chemical methods [23] are given for the sake of comparison in Table 5.1.

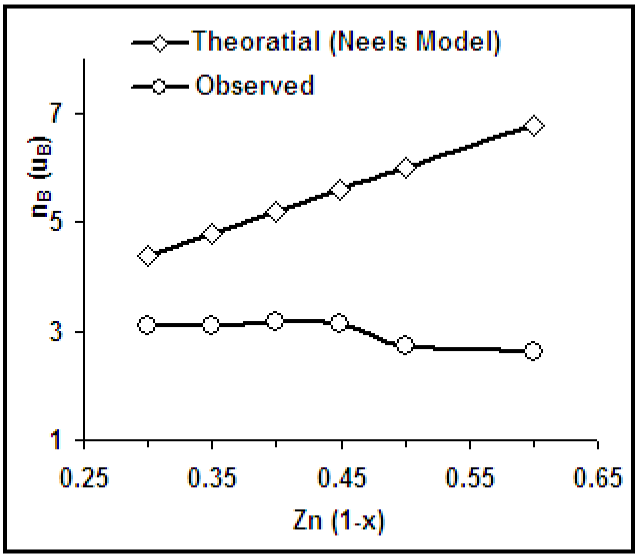

Fig. 5.6 Variation of observed and theoretically calculated magneton number of nano $Ni_xZn_{1-x}Fe_2O_4$ samples as a function Zn content.

It can be noticed that Y-K angles increases with Zn content in all three cases. The values of Y-K angles for nano samples synthesize in present work were greater than that for samples synthesize via known ceramic method and lower than for samples prepared via co-precipitaion method [23]. Thus, we may conclude that Y-K angle depends on method of preparation.

5.12.2 Coercive field (H_c) and retentivity (M_r) of nano samples

The M-H loops of nano samples in the low magnetic field region are reproduced in Fig. 5.7 to obtain $\mathbf{H_c}$ and $\mathbf{M_r}$ of the samples. The variation of $\mathbf{H_c}$ and $\mathbf{M_r}$ of nano samples with the composition is shown in Fig. 5.8. The $\mathbf{H_c}$ decreases with initial increase in Ni concentration up to 0.50 and then increases continuously. This decrease may be is mainly due to decrease in crystal anisotropy [25]. The lowest $\mathbf{H_c}$ for Ni=0.50, may be attributed to its appreciably larger crystallite size (range of 30 nm to 45 nm as per TEM results) compared to Ni=0.40 and 0.70, which are showing maximum $\mathbf{H_c}$ and their crystallite sizes varies in the range of 20 nm to 30 nm and 25 nm to 30 nm respectively. It is reported [26] that $\mathbf{H_c}$ of the assembly increases with the decrease in diameter of the particles. The observed $\mathbf{H_c}$ in present work is one to two orders higher than that of bulk nickel zinc ferrites [26]. This can be attributed to nano size of the Ni-Zn ferrite particles in the present work [27, 28]. From Fig. 5.8 it can be seen that, $\mathbf{M_r}$ also shows similar trend as that of $\mathbf{H_c}$ except for minor decrease at Ni=0.70. The values of $\mathbf{H_c}$ and $\mathbf{M_r}$ vary in the range of 70 Oe to 92.5 Oe and 6.5 emu/g to 8.5 emu/g respectively. This indicates that the samples under investigation are soft ferrites [14].

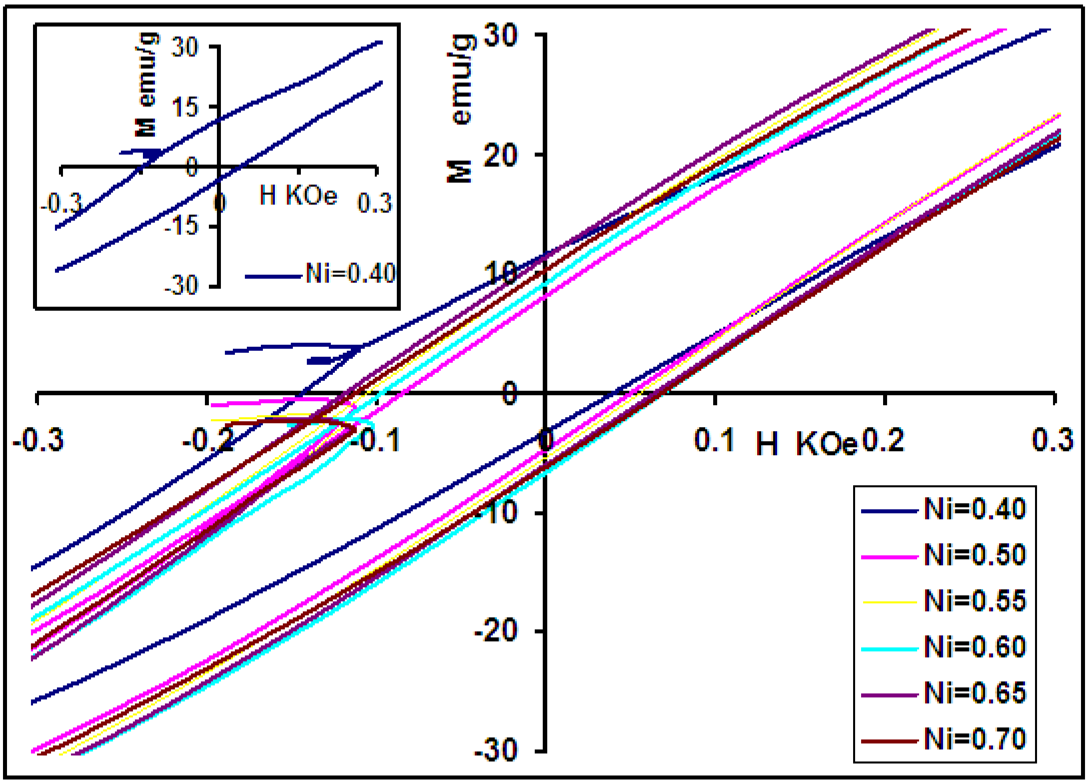

Fig. 5.7 Hysteresis curve at low magnetic field range of nano $Ni_xZn_{1-x}Fe_2O_4$ samples. (Inset shows loop for Ni=0.40).

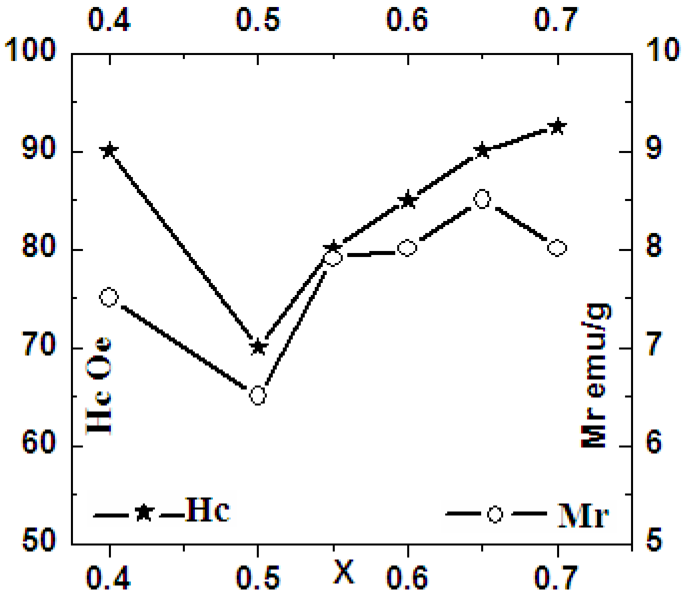

Fig. 5.8 Variation of coercivity (Hc) and retentivity (Mr) of nano $Ni_xZn_{1-x}Fe_2O_4$ samples with Ni content.

5.12.3 M-H loop analysis of nano samples at low temperatures

Variation of magnetization with the static applied field (up to 2 Tesla) at various temperatures (5K, 10K, 50K, 100K, 200K and 300K) for nano samples are shown in Fig. 5.9.

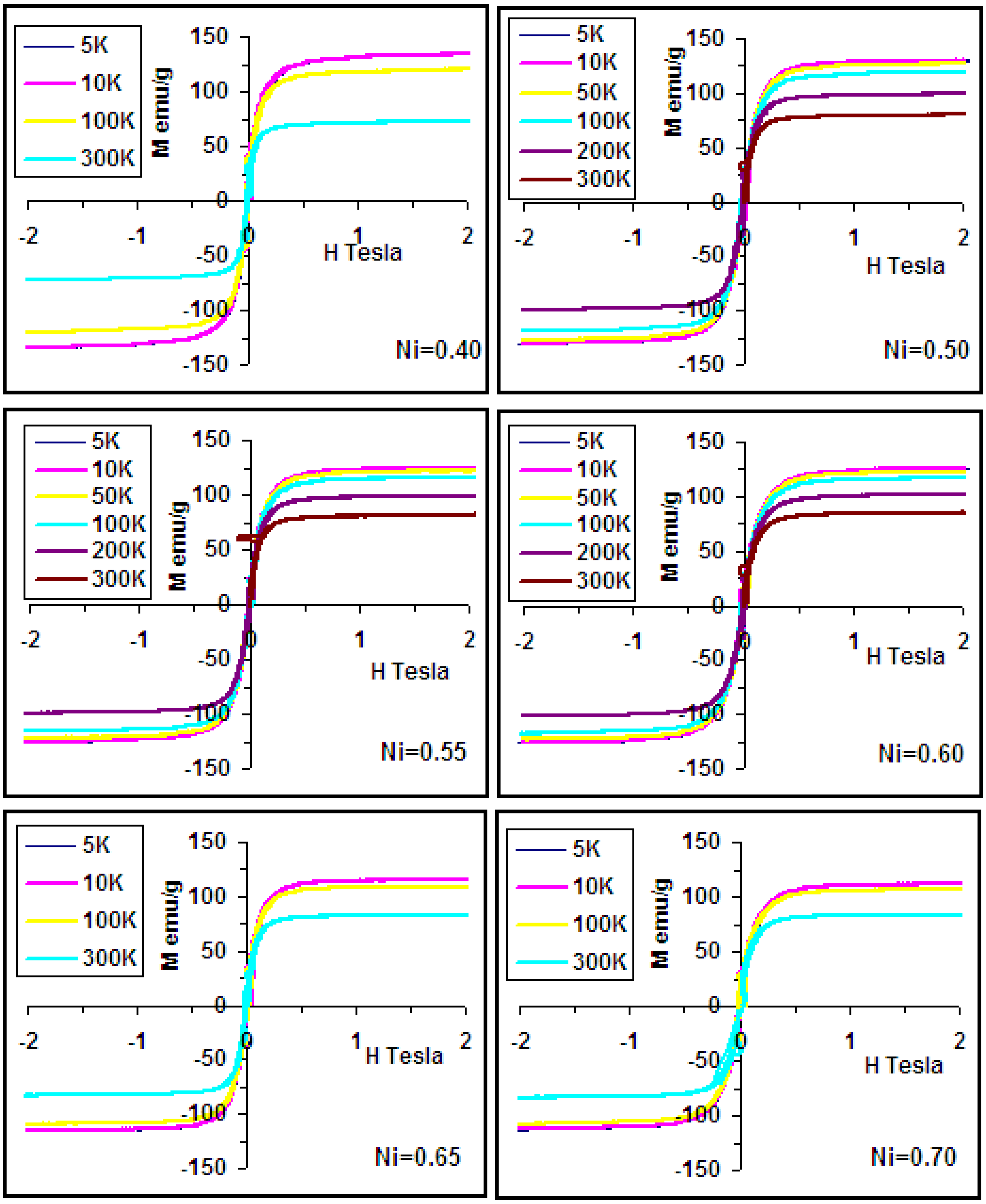

Fig. 5.9 The M-H loops of nano $Ni_xZn_{1-x}Fe_2O_4$ samples measured at various temperatures (5K, 10K, 50K, 100K, 200K and 300K).

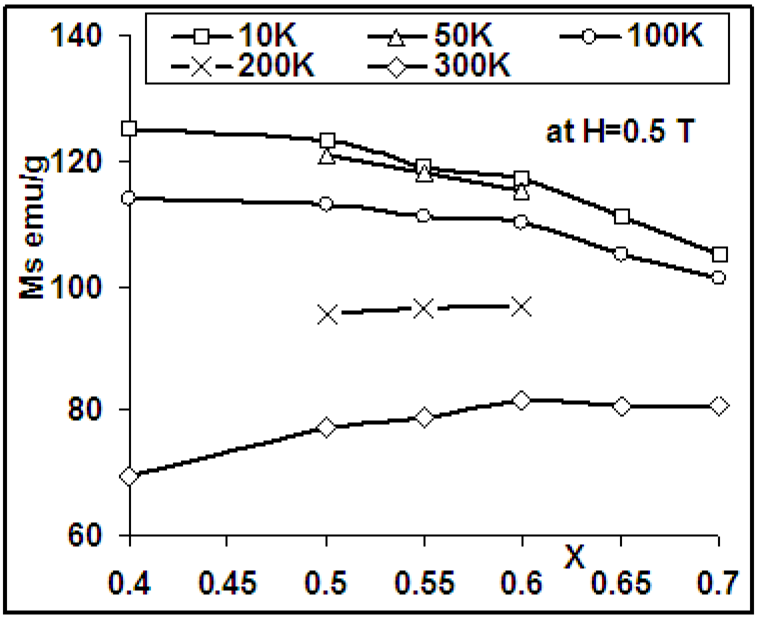

Fig. 5.10 Variation of saturation magnetization of nano $Ni_xZn_{1-x}Fe_2O_4$ samples with Ni content at temperature of 10K, 50K, 100K, 200K and 300K.

From Fig. 5.9 it can be seen that all the samples showed normal narrow hysteresis loops. It was found that magnetization increases with increase in applied field, and attains its saturation value for all the samples at fields higher than 0.50 Tesla. It can be also observed that magnetic moment of the samples increases as measuring temperature is lowered, which can be attributed to less spin canting and spin fluctuations due to lower thermal energy [29]. From Fig. 5.10, it can be seen that, $\mathbf{M}_s$ decreases with increase in Ni content at temperatures of 10K, 50K and 100K, whereas increases at 200 K (recorded only for Ni=0.50, 0.55 and 0.60). At 300K, $\mathbf{M}_s$ increases up to x= 0.60 with a marginal decrease for higher values of Ni. This means below 200 K the samples show collinear magnetic structure as predicted by Neels model and above 200K, samples exhibit nearly non collinear magnetic structure with significant canting effect. Thus effect of spin canting and spin fluctuations due to thermal energy is negligible below 200 K (for field of 0.5 Tesla) for all the samples.

5.12.4 SQUID measurements of nano samples

ZFC and FC performance of the nano samples with Ni=0.40, 0.65 and 0.70 were monitored on Squid setup. The samples were cooled down from 300 K to 5 K under zero fields and magnetizations were recorded with increasing temperature by switching on fixed magnetic field to get ZFC curves. For FC measurements the materials were cooled down from 300 K to 5 K in presence of magnetic field and the corresponding data was recorded. ZFC and FC curves of nano samples are presented in Fig. 5.11.

It can be seen that the magnetization in the ZFC and FC curve decreases continuously with increasing temperature. However in case of FC the magnetization always remains higher at lower temperatures and merges with ZFC values near and above blocking temperature $\mathbf{T_B}$. It may be seen that the ZFC curve shows a curvature leading to a broad peak in the temperature range of 5 K to 40 K. The width of this peak is normally attributed to the particle size distribution in the sample. A wider peak observed for Ni=0.65 and 0.70 compared to Ni=0.40 indicates their bigger particle size or a wider particle size distribution compared to Ni=0.40 sample [29]. It can be seen that, the temperature range at which FC and ZFC splits (as one traverse from high temperature to lower temperature) also varies with Ni content for a fixed applied field. The $\mathbf{T_B}$ was found to be 30 K (±10 K), 35 K (±10 K) and 50 K (±10 K) for Ni=0.40, 0.65 and 0.70 respectively. Above $\mathbf{T_B}$ all the particles are in the superparamagnetic state. The $\mathbf{T_B}$ increases with increasing particle size due to the known volume dependence of the magnetic particle with the $\mathbf{T_B}$ of a superparamagnetic system. The lowest $\mathbf{T_B}$ and lesser peak broadening in ZFC curve

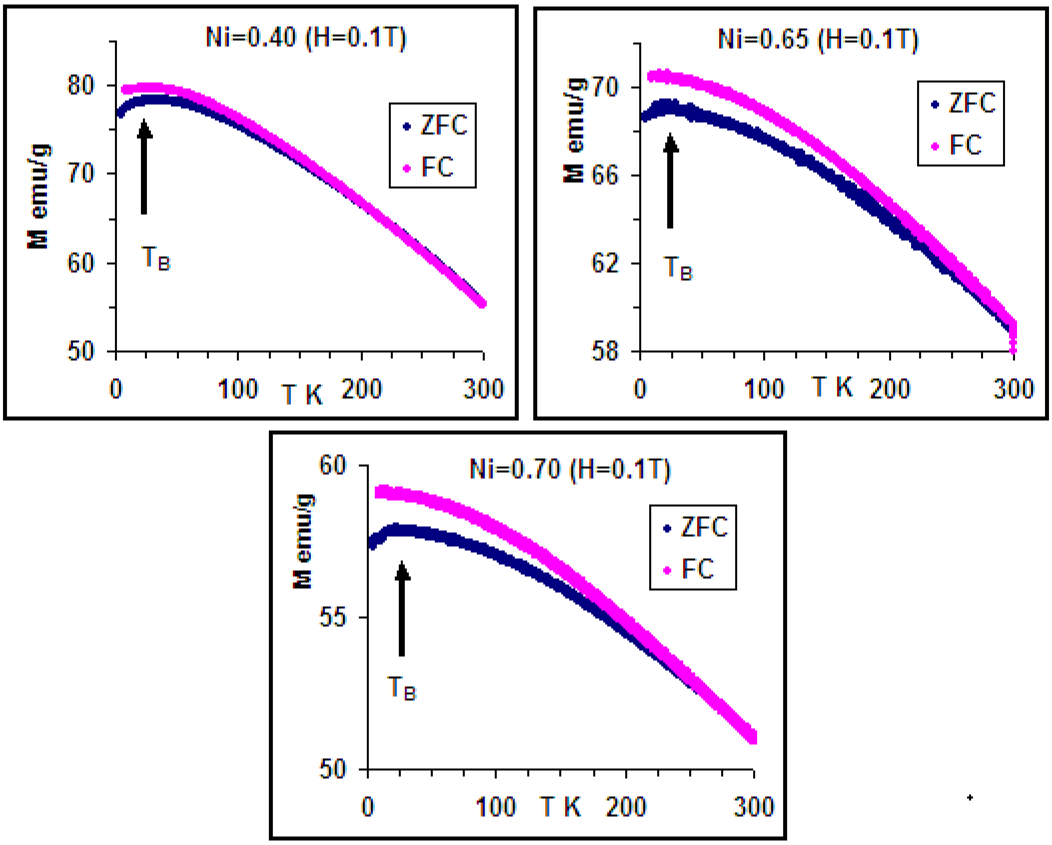

Fig. 5.11 Temperature dependence of magnetization (ZFC and FC curves) of nano $Ni_xZn_{1-x}Fe_2O_4$ samples.

(in lower temperature region) observed for Ni=0.40 was attributed to its smaller particle size or narrow size distribution [30].

5.12.5 Parameters of hysteresis loop of bulk samples

The effect of sintering temperature on the magnetic properties such as coercivity, retentivity and saturation magnetization of bulk $Ni_xZn_{1-x}Fe_2O_4$ samples are discussed in this Section.

5.12.5.1 Saturation magnetization (M_s) of bulk samples

Fig. 5.12 shows M-H loops of nano and bulk samples with Ni=0.50 and 0.60 depicting their variation in magnetization with the applied field. The shifting of

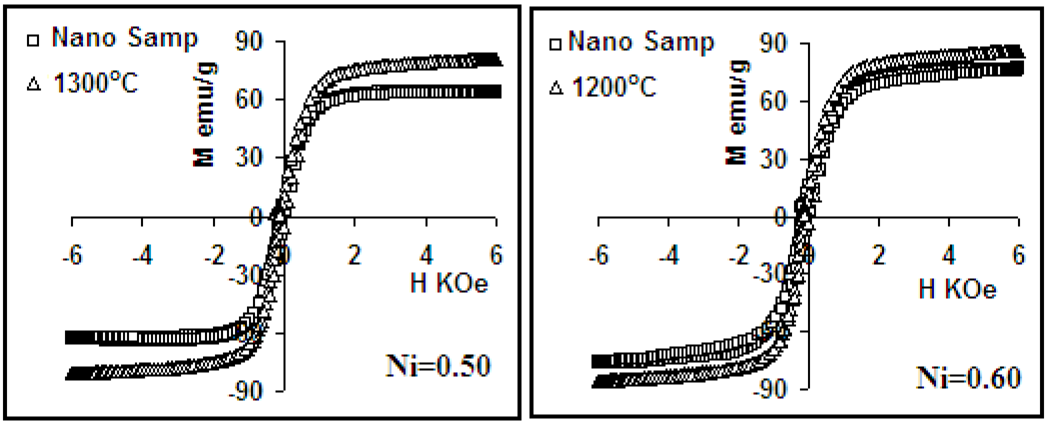

Fig. 5.12 M-H loops of nano and bulk $Ni_xZn_{1-x}Fe_2O_4$ samples.

magnetization curve of bulk samples towards upper side compared to that of nano samples shows that $\mathbf{M_s}$ of the bulk samples are higher compared to their respective nano samples. Similar results were found for all the bulk samples.

Variation of $\mathbf{M_s}$ of bulk samples with sintering temperature is presented in Fig. 5.13. It can be noticed that, $\mathbf{M_s}$ of all the samples in general increases with the sintering temperature. This increase can be attributed to increase in grain size, higher crystalline quality and decreasing porosity with the increasing sintering temperature. The increase may be also attributed to improved densification obtained on sintering [31]. Nevertheless samples also lose their SD nature on sintering, a vital cause for high $\mathbf{M_s}$.

For Ni=0.40 and Ni=0.55, the $\mathbf{M_s}$ increases with increase in sintering temperature till 1300^{o}C. The general trend of $\mathbf{M_s}$ for Ni=0.50, 0.60 and 0.65, is similar, however, the first two samples show an increase in $\mathbf{M_s}$ till 1100^{o}C and the later shows increase till 1200^{o}C followed by a decrease at higher sintering temperatures. In case of Ni=0.7, $\mathbf{M_s}$ show rise, but oscillatory in nature. Marginal decrease of $\mathbf{M_s}$ at 1300°C in case of samples with Ni=0.60 and 0.65 may be

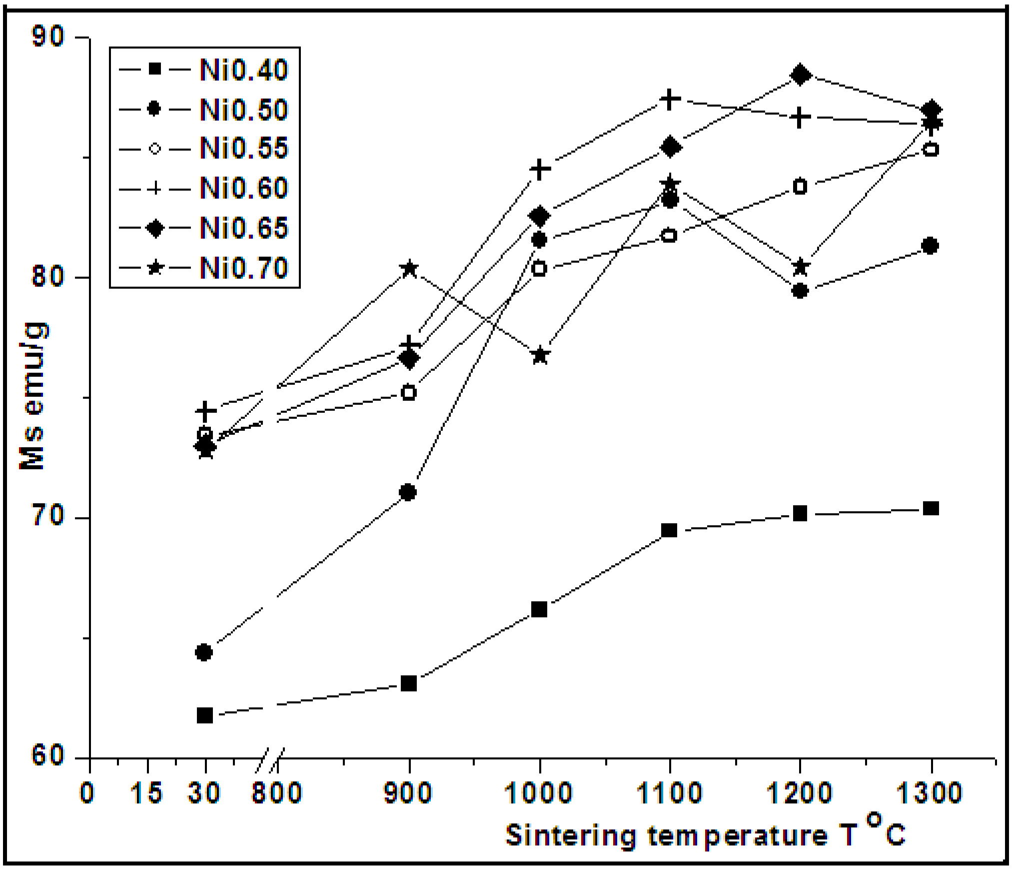

Fig. 5.13 Variation of saturation magnetization of bulk $Ni_xZn_{1-x}Fe_2O_4$ samples with sintering temperature (value of M_s of nano sample is plotted in the graph for comparison).

attributed to evaporation of zinc from the surface of the particles, which also depends on the microstructure of the material. This can cause non-stoichiometric balance in the reaction formulas of the sample that leads to reformation of cation vacancies near the surface [32]. Among all the bulk samples the highest $\mathbf{M_s}$ of 88.47 emu/g was obtained for Ni=0.65 at 1200°C.

5.12.5.2 Coercivity (H_c) of bulk samples

Fig. 5.14 represents variation of coercivity of bulk samples with sintering temperature. Sample with Ni=0.40, show decrease in $\mathbf{H_c}$ with increase in sintering temperature along with a peak at 1200°C. In case of Ni=0.60 and 70, $\mathbf{H_c}$ show peak at 1000°C followed by a decrease till sintering temperature of 1200°C. The major

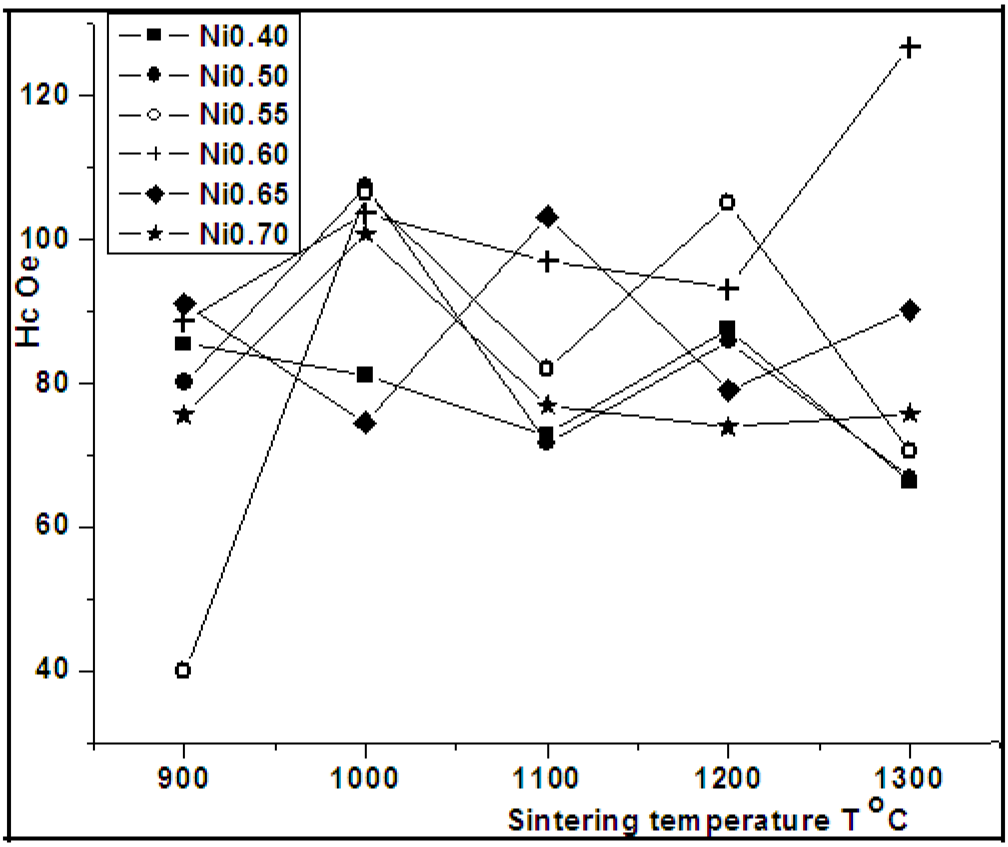

Fig. 5.14 Variation of coercivity of bulk $Ni_xZn_{1-x}Fe_2O_4$ samples with sintering temperature.

increase in $\mathbf{H_c}$ at 1300°C was seen for Ni=0.60 and minor increase for Ni=0.70. The $\mathbf{H_c}$ of bulk samples, with Ni=0.50, 0.55 and 0.65, has shown unusual random variation with increasing sintering temperature.

The inconsistency showing unusual random variation in $\mathbf{H_c}$ at different sintering temperatures for different compositions calls for systematic study of the individual bulk sample. The development of microstructure of the bulk samples with sintering temperature may be largely responsible for such variation in coercivity. Since, coercivity is a micro-structural property it also depends upon defects, strains, non-magnetic atoms, evaporation of zinc at higher temperature etc. Thus extrinsic effect associated with a non favorable microstructure of the sample formed at individual sintering temperature in each case is also important to

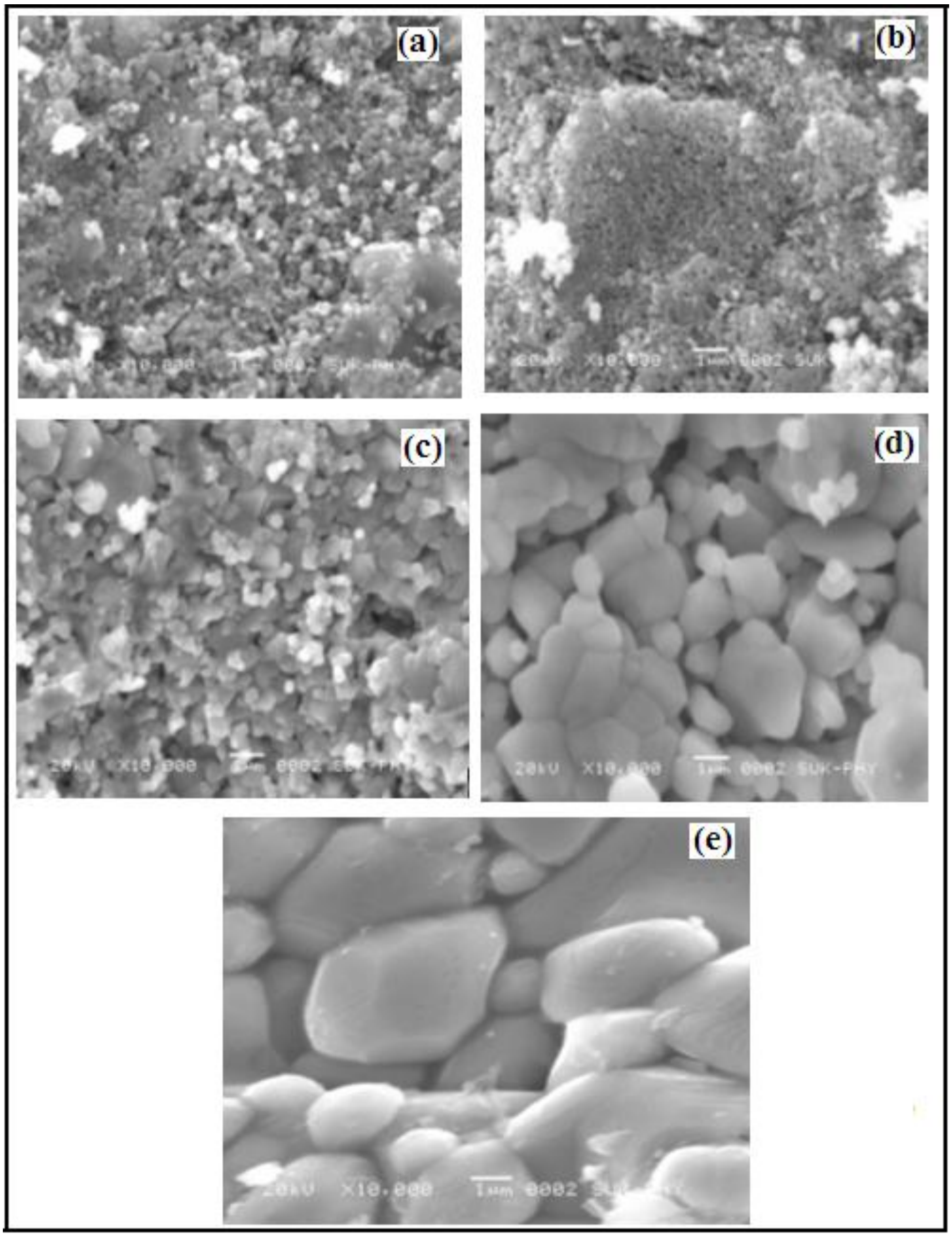

Fig. 5.15 SEM images of bulk $Ni_{0.50}Zn_{0.50}Fe_2O_4$ samples at sintering temperature of (a) 900°C, (b) 1000°C, (c) 1100°C, (d) 1200°C, and (e) 1300°C.

know [33]. This extrinsic effect was well supported by SEM images that have shown composition dependence of grain growth at 1300°C as reported in Section 4.3.8.1.

Fig. 5.15 shows micrographs of bulk sample with Ni=0.50 at sintering temperature of 900°C, 1000°C, 1100°C, 1200°C and 1300°C. The SEM images clearly show the development in grain shape and grain size with increasing sintering temperature. The grains and grain boundaries could not be resolved clearly at lower sintering temperature of ≤1000°C (Fig. 5.15 (a) and (b)). Whereas, compact microstructure with well crystallites having bigger size and less pores can be observed clearly for sample sintered at 1200°C and 1300°C (Fig. 5.15 (d) and (e) respectively). At higher sintering temperature the shape anisotropy diminished due to the well developed grains [34, 35] and may be negligible and instead, magneto-crystalline and strain-induced (porosity-induced) anisotropy influences the $\mathbf{H_c}$. The minimum $\mathbf{H_c}$ of 66.32Oe was observed for Ni=0.40 at 1300°C.

On an average, $\mathbf{H_c}$ of bulk samples were decreased with increasing sintering temperature, which may be attributed to increase in grain size and decrease in porosity of the samples. It is expected that samples are likely MD in nature at higher sintering temperature, which contain more number of domain walls that require lower energy for magnetization and demagnetization due to domain wall movement leading to low $\mathbf{H_c}$, compared to that of domain rotation in case of SD samples [33, 34].

5.12.5.3 Retentivity ($\mathbf{M_r}$) of bulk samples

Fig. 5.16 represents variation of $\mathbf{M_r}$ of bulk samples with sintering temperature. In case of samples with Ni=0.40 and 0.70, $\mathbf{M_r}$ decreases with the increase in sintering temperature along with a peak at 1200°C and 1000°C respectively. For Ni=0.50, two peaks were observed at sintering temperature of 1000°C and 1200°C. Single peak was also observed for Ni=0.55 and 0.60 at 1100°C and 1000°C respectively. In case of Ni=0.65, $\mathbf{M_r}$ increases with sintering temperature and attains a peak at 1100°C. On an average, $\mathbf{M_r}$ of the bulk samples

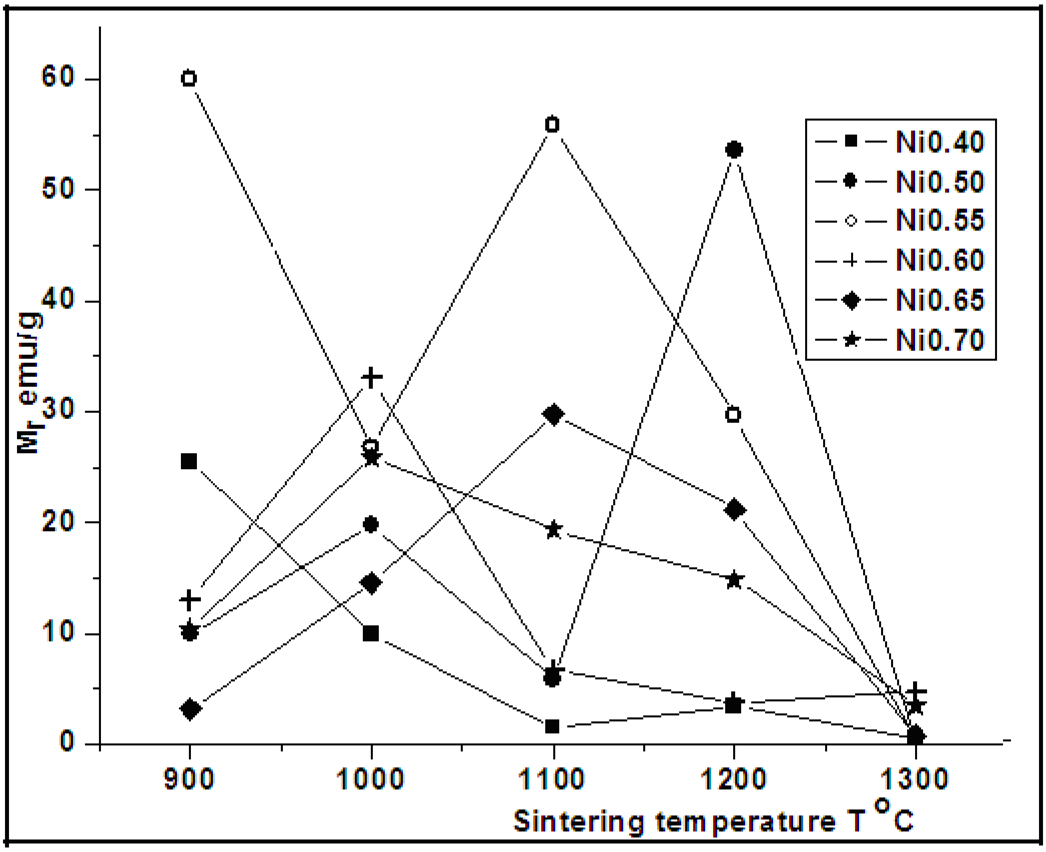

Fig. 5.16 Variation of retentivity of bulk $Ni_xZn_{1-x}Fe_2O_4$ samples with sintering temperature.

shows a peak at different sintering temperatures followed by a fall. It is very interesting to note that, for all the compositions $\mathbf{M_r}$ show minimum at 1300°C and the lowest being 0.27 emu/g for Ni=0.50. Thus we may conclude that bulk samples investigated in the present work show properties of soft ferrite.

5.12.6 AC Susceptibility measurements

The measurements of normalized susceptibility of nano and bulk samples were carried out to analyze variation of Curie temperature and domain structure of the samples as a function of composition and sintering temperature.

5.12.6.1 Normalized AC susceptibility and T_c of nano samples

Fig. 5.17 (a) shows variation in normalized AC susceptibility of nano samples with temperature. Domain structures and $\mathbf{T_c}$ were estimated from these curves. The normalized susceptibility variation indicates that all the samples exhibit typical ferrimagnetic behavior [23]. The ferrimagnetic ordering is seen to increase with increase in Ni content, which is also supported by Mossbauer analysis. The curves also show that, all the samples have mixture of single domain (SD) and multi domain (MD) structures [36]. However, Ni=0.40 has higher volume of SD particles compared to other samples. This can be deduced from the observed peak in the curve before susceptibility drops suddenly near $\mathbf{T_c}$ for Ni=0.40. This may be attributed to their small particle size distribution, and same was also well supported by SQUID and Mossbauer analysis for this sample.

The normalized AC susceptibility of nano samples show broadening of the ferromagnetic transition near $\mathbf{T_c}$, which may be explained as follows. The surface properties such as, surface atoms, variations in the exchange coupling of surface atoms, particle shapes and lattice fluctuations should be considered while studying $\mathbf{T_c}$ of nanoparticles [37, 38]. The particle shape of the grain also provides information on surface atoms whose reduced coordination number affects the exchange energy locally. The increasing lattice fluctuations with increase in temperature will also have an impact on the Heisenberg exchange. It is also known that, as temperature increases, smaller particles might be expecting large thermally induced lattice fluctuations. Obviously, as the size of the system is reduced to values close to the correlation length, it becomes more difficult for the system to achieve zero net magnetization, at least until the correlations are completely destroyed at temperature much greater than **T$_c$** of the main phase [37]. This effect leads to a broadening of the ferrimagnetic transition, which becomes more pronounced as the particle size decreases [39]. The size effect or strong exchange interaction is enough to induce short-range correlations of the magnetic moments even at temperatures >**T$_c$** of the main core contribution. The observed residual magnetization is not an indication of any impurity phase, as this fact was well supported by XRD analysis. Thus it can be related to size effect and surface phenomenon. However, C. Rath et al. [40] also reported such broadening or cusp

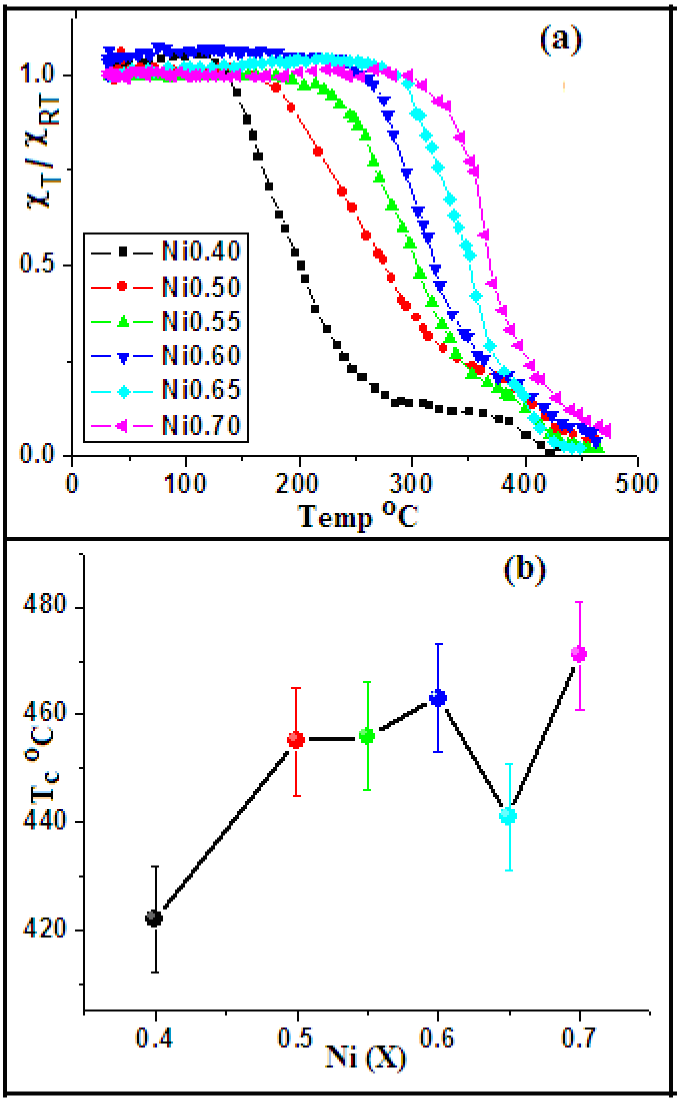

Fig. 5.17 (a) The thermal variation of normalized susceptibility and (b) Variation of Curie temperature, of nano $Ni_xZn_{1-x}Fe_2O_4$ samples with Ni content.

Table 5.2 The Curie temperatures of nano $Ni_xZn_{1-x}Fe_2O_4$ samples in the present work along with reported values for comparison.

Ni (x)	T_c °C ±10°C	T_c °C (Co-ppt) [2]	T_c °C (ceramic) [2]
0.40	422	399	330
0.50	455	461	339
0.55	456	-	-
0.60	463	523	350
0.65	441	-	-
0.70	471	547	489

before $\mathbf{T_c}$, and are explained in terms of transformation from one ferrimagnetic phase to another (metastable state to a stable state). Since, any additional mix phase in the samples with less than 5% amount is hardly detected in XRD, the possibility of some metastable ferrimagnetic phase as reported by C. Rath et al. also can not be ruled out completely in case of samples in the present work.

The variation of $\mathbf{T_c}$ with Ni content is shown in Fig. 5.17(b). It can be seen that, $\mathbf{T_c}$ increases with increasing Ni content in the sample. This is attributed to strengthening of A-B interaction [41, 42]. According to Neel's model, A-B interaction is most dominant in ferrites and $\mathbf{T_c}$ is determined from the overall strength of A-B interaction. The strength of A-B interaction is a function of the number of FeA^{3+}--O^{2}---FeB^{3+} linkages, which, in turn, depends upon the number of Fe^{3+}ions in the formula unit and their distribution amongst tetrahedral (A) and octahedral [B] sites. In the present system, as Ni increases, non magnetic Zn^{2+} (0 μ_B) ions are replaced by magnetic Ni^{2+} (2μ_B) ions. This increases A-B interaction and correspondingly increases $\mathbf{T_c}$. However, for Ni=0.65, $\mathbf{T_c}$ gets decreased. This decrease in $\mathbf{T_c}$ can be attributed to its larger particle size, less broadening of ferromagnetic transition and low lattice fluctuations in this composition compared to others. The $\mathbf{T_c}$ of the nano samples in the present work and reported [2] for standard ceramic and co precipitation method is also provided for comparison in Table 5.2. The **T_c**'s of samples in the present work were found to be higher than the reported **T_c**'s. The nano samples in present work showed highest **T_c** of 471°C ±10°C for Ni=0.70 and lowest of 422°C ±10°C for Ni=0.40.

5.12.6.2 Normalized AC susceptibility and T_c of bulk samples

Fig. 5.18 shows thermal variation of normalized susceptibility of bulk samples at different sintering temperature and corresponding variation in **T_c**. It can be seen that, normalized susceptibility of bulk samples decreases sharply with increase in temperature compared to their respective nano samples (see Fig. 5.17 (a)). The sharpness also increases with increase in sintering temperature, which is a characteristic of better crystal growth. Samples at 1300°C show rapid fall in susceptibility. Minor broadening of ferrimagnetic transition was observed at 1100°C for Ni=0.40 and negligibly small for Ni=0.50 and 0.60. Such broadening is attributed to their smaller grain size and lower crystal growth at this sintering temperature, which was also observed from SEM micrographs.

The **T_c** decreases linearly with increasing sintering temperature for Ni=0.50. This was attributed to increase in grain size as expected. However, in case of Ni=0.40 and 0.60, the decrease in **T_c** was observed till 1200°C, and it increases for 1300°C. This increase in **T_c** may be attributed to evaporation of zinc at higher sintering temperature leading to increase in Fe/Ni ratio [14]. This could also be attributed to observed lattice contraction from XRD analysis at 1300°C for the sample.

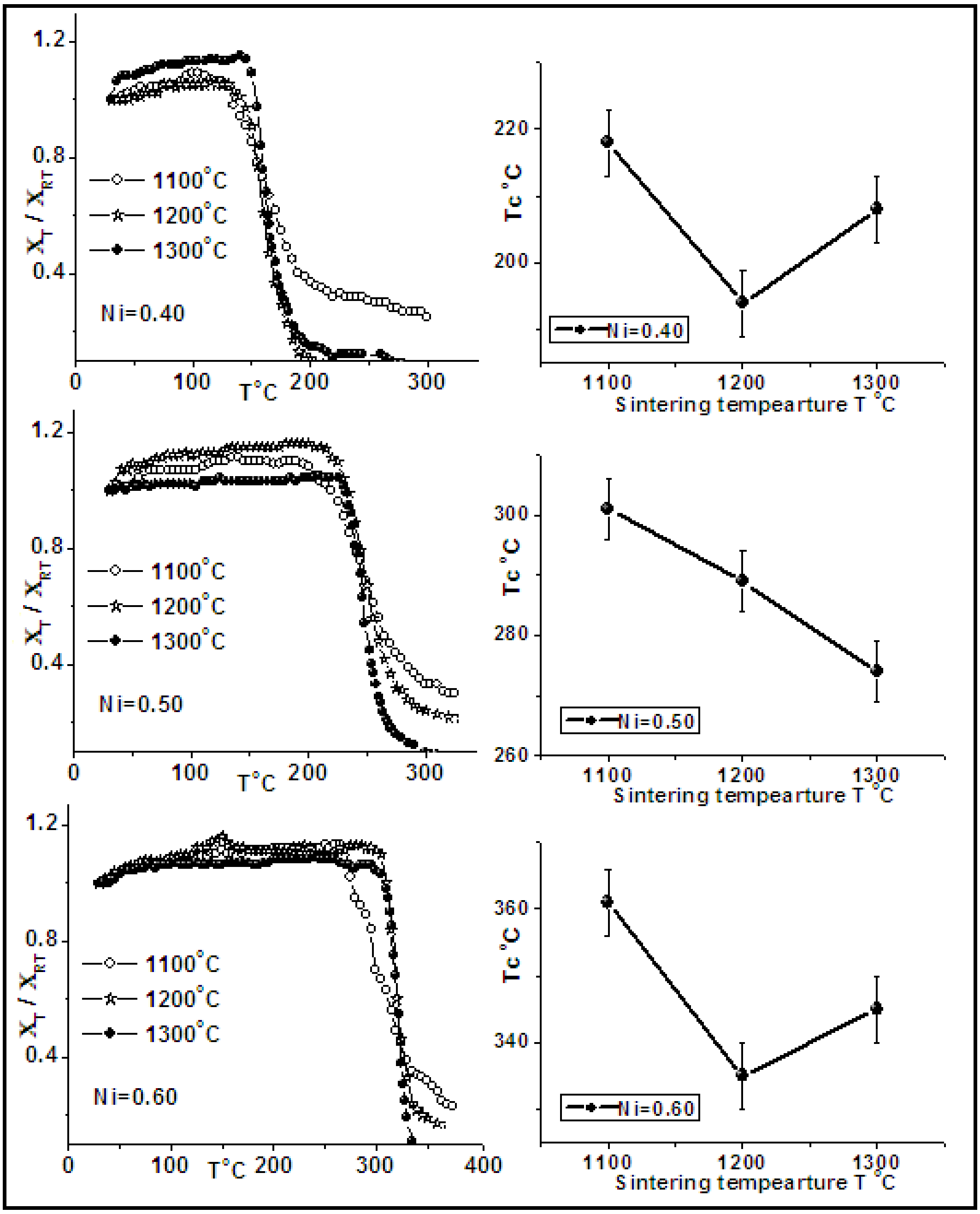

Fig. 5.18 (LHS) Thermal variation of normalized susceptibility of bulk $Ni_xZn_{1-x}Fe_2O_4$ samples at sintering temperature of 1100°C, 1200°C and 1300°C and (RHS) variation in corresponding Curie temperature with sintering temperature.

The lowering of lattice parameter will decrease the distance between magnetic moments of A and B sites, and increases A-B interaction due to increase in overlapping of orbital of Fe_A^{3+}--O^{2-}--Fe_B^{3+} linkages and hence increase in $\mathbf{T_c}$ [2].

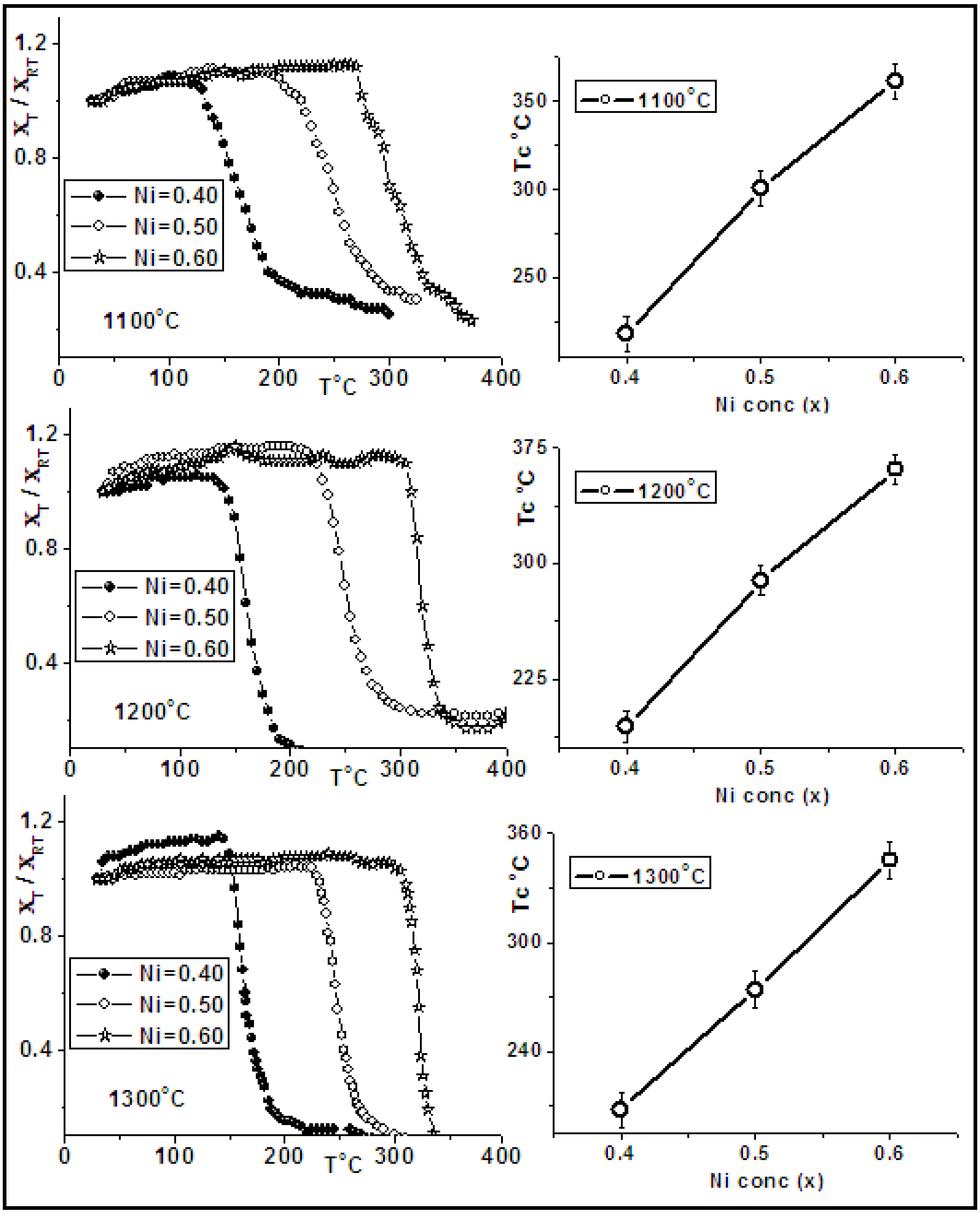

Fig. 5.19 (LHS) Thermal variation of normalized susceptibility of bulk $Ni_xZn_{1-x}Fe_2O_4$ samples at sintering temperature of 1100°C, 1200°C and 1300°C and (RHS) corresponding variation in Curie temperature as a function of Ni content.

Fig. 5.19 Shows thermal variation of normalized susceptibility of bulk samples and variation in **T_c** as a function of Ni content. It can be seen that, all the samples showed typical normalized susceptibility curves with increasing ferrimagnetic order with the increase in Ni content and also, expected increase in $\mathbf{T_c}$ at all the sintering temperatures.

5.12.7 Initial permeability (μ_i) and magnetic loss tangent (tanδ)

Detailed observations on the measurements of initial permeability and magnetic loss tangent as a function of frequency, temperature and composition of the toroids sintered at 900°C, 1000°C, 1100°C, 1200°C and 1300°C are discussed in this Section.

5.12.7.1 Variation of μ_i with frequency

Fig. 5.20 shows that $\boldsymbol{\mu_i}$ decreases sharply at lower frequencies for all the bulk samples. After certain higher frequency, the $\boldsymbol{\mu_i}$ remains almost constant over a large band of frequency and increases abruptly at resonance frequency ($\mathbf{F_r}$). This feature is well known as the ferromagnetic resonance or self driven resonance [43, 44]. The onset of the resonance frequency determines the upper limit of the operational frequency for which magnetic material can be used in any device. It is well known that permeability of polycrystalline ferrite is related to two different magnetizing mechanisms; domain wall motion and spin rotation [14] which can be described by Equation 5.11 to 5.13.

It is found that the domain wall permeability is dominant in lower frequency region and large value of $\boldsymbol{\mu_i}$ observed at lower frequencies, are attributed to reversible displacement of the domain walls [45]. The decrease in contributions of domain walls at higher frequencies is responsible for observed constant value of $\boldsymbol{\mu_i}$ in the large band of higher frequency range before resonance. At higher frequencies the spin rotation plays a relatively more important role when the domain wall motion reduces. Also, at higher frequencies, nonmagnetic impurities between grains and intra-granular pores act as pinning points and increasingly hinder the motion of domain walls and spin rotation thereby decreasing their contribution to permeability [46].

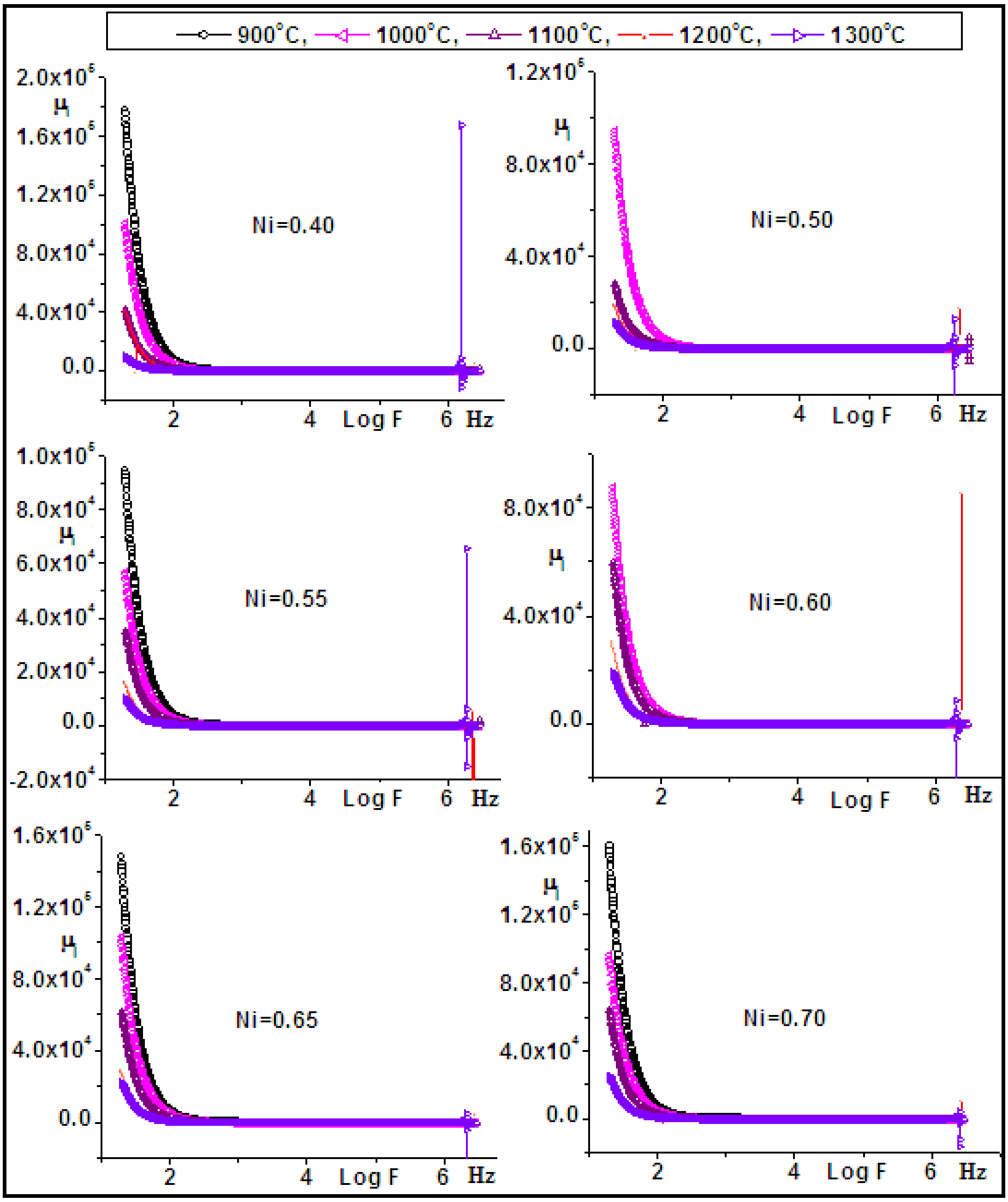

Fig. 5.20 Frequency dependence of initial permeability of bulk $Ni_xZn_{1-x}Fe_2O_4$ samples.

Normally, two resonance peaks are observed in ferrites: one at lower frequency ~ 10-100 MHz, which is due to the domain wall oscillations and the other at higher frequencies ~ few GHz due to Larmour precession of electron spins [47]. The observed resonance peak in the present work is indicative of domain wall oscillations or resonance. From Fig. 5.20, the resonance can be clearly seen for bulk samples at sintering temperature of 1200^oC and 1300^oC. Whereas, the resonance at sintering temperature of 900^oC, 1000^oC and 1100^oC can not be seen, which may be existing beyond 3 MHz (3 MHz is the measuring limit of higher frequency in present study).

The $\mathbf{F_r}$ of all the bulk samples and corresponding values of $\boldsymbol{\mu_i}$ at sintering temperature of 1200^oC and 1300^oC are given in Table 5.3. It can be deduced that, all the samples have $\mathbf{F_r}$ higher than 3 MHz at sintering temperature of 900^oC, 1000^oC and 1100^oC except for Ni=0.50 at 1100^oC. The $\mathbf{F_r}$ of the samples at 1200^oC and 1300^oC lies below 3 MHz. From Table 5.3 and Fig. 5.21 it is seen that as sintering temperature increases from 1200^oC to 1300^oC, the $\mathbf{F_r}$ decreases on the other hand $\boldsymbol{\mu_i}$ increases as predicted by Snoeke's law [17]. This means there is an effective limit to the product of $\mathbf{F_r}$ and $\boldsymbol{\mu_i}$, such that high permeability and high operating frequencies are mutually incompatible. Hence, some times, some grades of Ni-Zn samples are deliberately sintered at low temperature to improve operating frequency.

It was also found that $\mathbf{F_r}$ increases with Ni content at sintering temperature of 1300^oC, whereas, overall increase in $\mathbf{F_r}$ with Ni content can be observed at 1200^oC, with exceptions for Ni=0.40 and Ni=0.70. Similarly, overall decrease in $\boldsymbol{\mu_i}$ with increase in Ni content is observed at both the sintering temperature with exception

Table 5.3 Initial permeability (**μ_i**) and resonance frequency (**F_r**) of bulk $Ni_xZn_{1-x}Fe_2O_4$ samples.

Ni conc. (x)	Resonance frequency (**F_r**) and [Initial permeability (**μ_i**)] at various sintering temperatures				
	900°C	1000°C	1100°C	1200°C	1300°C
0.40	>3 MHz	>3 MHz	>3 MHz	2.51 MHz [6369]	1.57 MHz [167621]
0.50	>3 MHz	>3 MHz	2.91 MHz	2.16 MHz [18740]	1.75 MHz [23064]
0.55	>3 MHz	>3 MHz	>3 MHz	2.34 MHz [6334]	1.90 MHz [65524]
0.60	>3 MHz	>3 MHz	>3 MHz	2.41 MHz [4901]	2.01 MHz [25947]
0.65	>3 MHz	>3 MHz	>3 MHz	2.91 MHz [5310]	2.12 MHz [37935]
0.70	>3 MHz	>3 MHz	>3 MHz	2.77 MHz [11745]	2.51 MHz [16017]

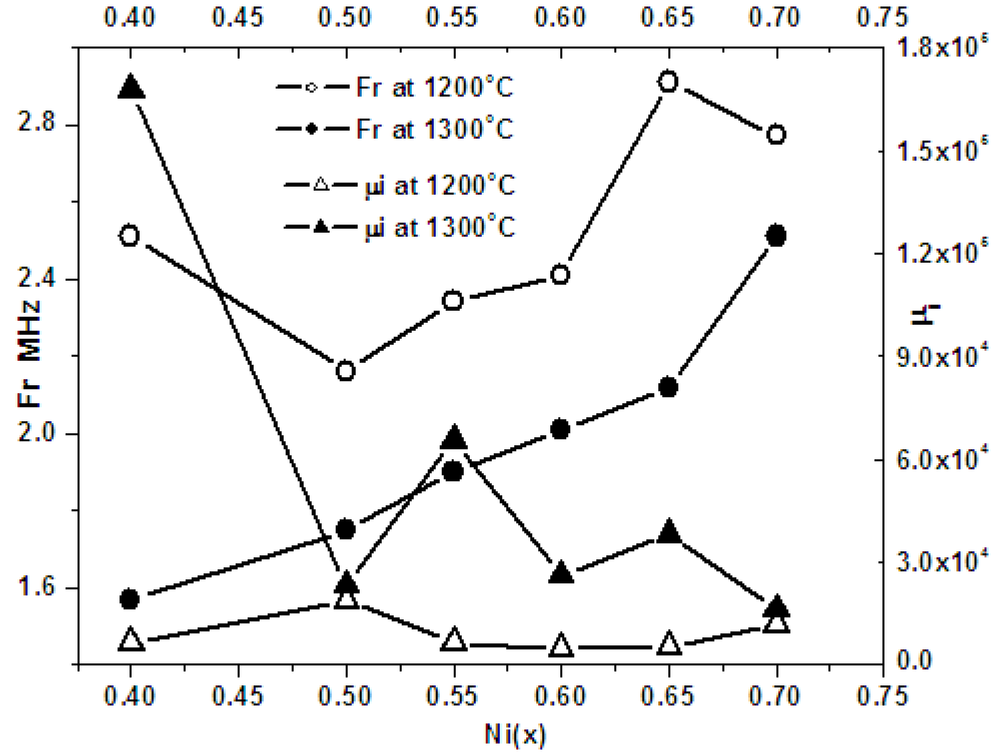

Fig. 5.21 Variation of resonance frequency (left scale) and initial permeability at resonance (right scale) of bulk $Ni_xZn_{1-x}Fe_2O_4$ samples with Ni content at sintering temperature of 1200°C and 1300°C.

for Ni=0.40 and Ni=070 at 1200^{o}C, and Ni=0.50 and Ni=0.60 at 1300^{o}C. The uneven and some exceptional changes in the $\mathbf{F_r}$ and μ_i for the above compositions can be attributed to uneven changes in their properties such as density, nature of porosity, rate of crystal growth, grain sizes, lattice strain, microstructure etc. and which in turn produces changes in anisotropy and domain wall moment. The dependence of grain growth and microstructure on composition was observed from SEM micrographs in the present work. Similar findings have been reported by A. K. M. Hossain and others [14].

5.12.7.2 Effect of sintering temperature and composition on μ_i

The flat portions (frequency range 1 KHz to 1 MHz) of the graphs from Fig. 5.20 are reproduced in Fig. 5.22 to study the effect of sintering temperature and composition on μ_i in detail. It can be seen clearly that μ_i curves are shifted upward for all the composition as sintering temperature increases from 900^{o}C to 1300^{o}C. For sample with Ni=0.40 and Ni=0.65, the μ_i values increases very slowly as sintering temperature increases from 900^{o}C to 1000^{o}C and this can be observed from closeness of their μ_i curves at these sintering temperature.

Fig. 5.23 shows the variation of μ_i (at 1 MHz) of bulk samples with sintering temperature. It is seen that, μ_i increases with sintering temperature for all the compositions. This is attributed to increase in grain size, increase in density and decrease in porosity with increase in sintering temperature. The permeability variation is largely controlled by microstucture which in turn depends on sintering temperature and processing conditions. According to non magnetic grain boundary model by Johnson [16], μ_i has almost linear dependence on grain size (given by

Equation 5.15). Besides, as per Globus model μ_i increases with saturation magnetization and grain diameter (given by Equation 5.14). Globus assumed that the permeability due to the wall motion is likely to be linearly dependent on the grain size, while the permeability contribution due to spin rotation was assumed to be independent of grain size [44].

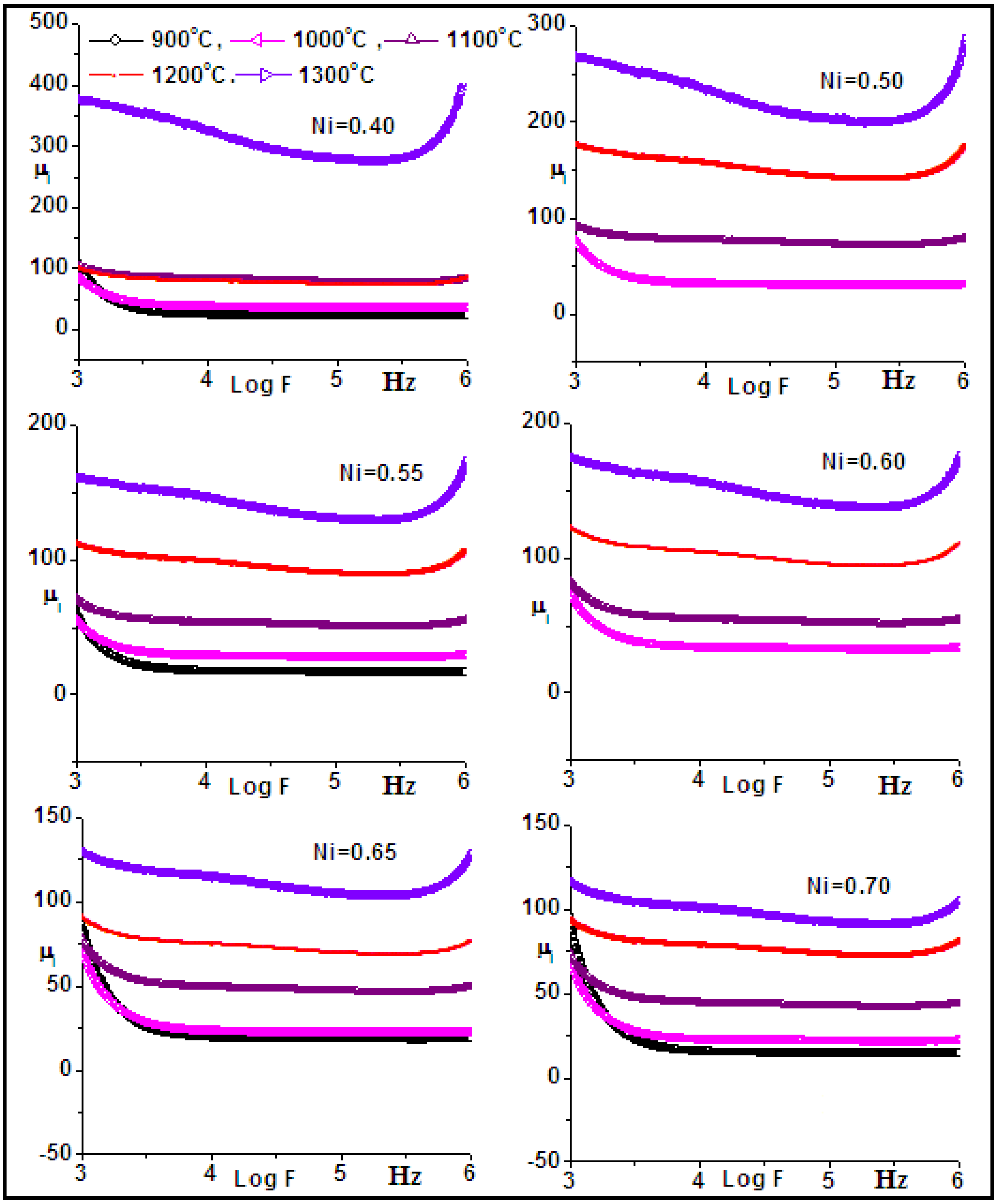

Fig. 5.22 Variation of initial permeability of bulk $Ni_xZn_{1-x}Fe_2O_4$ samples as a function of frequency (between 1 KHz to 1 MHz).

Bigger grains tend to contain more number of domain walls and μ_i being a result of the easy reversal of domain wall displacement in the direction of the applied magnetic field, the greater the number of domain walls, the higher is the μ_i [44]. The increase in sintering temperature leads to growth of crystalline phase and higher density, causing a decrease in the magnetic anisotropy through decreasing internal stresses and crystal anisotropy, which reduces the hindrance to the movement of the domain walls resulting in the increased value of μ_i [48].

An increase in the density of ferrites not only results in the reduction of the demagnetizing field due to the presence of pores but also raises the spin rotational contributions, which, in turn increases the μ_i [44]. Domain wall motion will be more

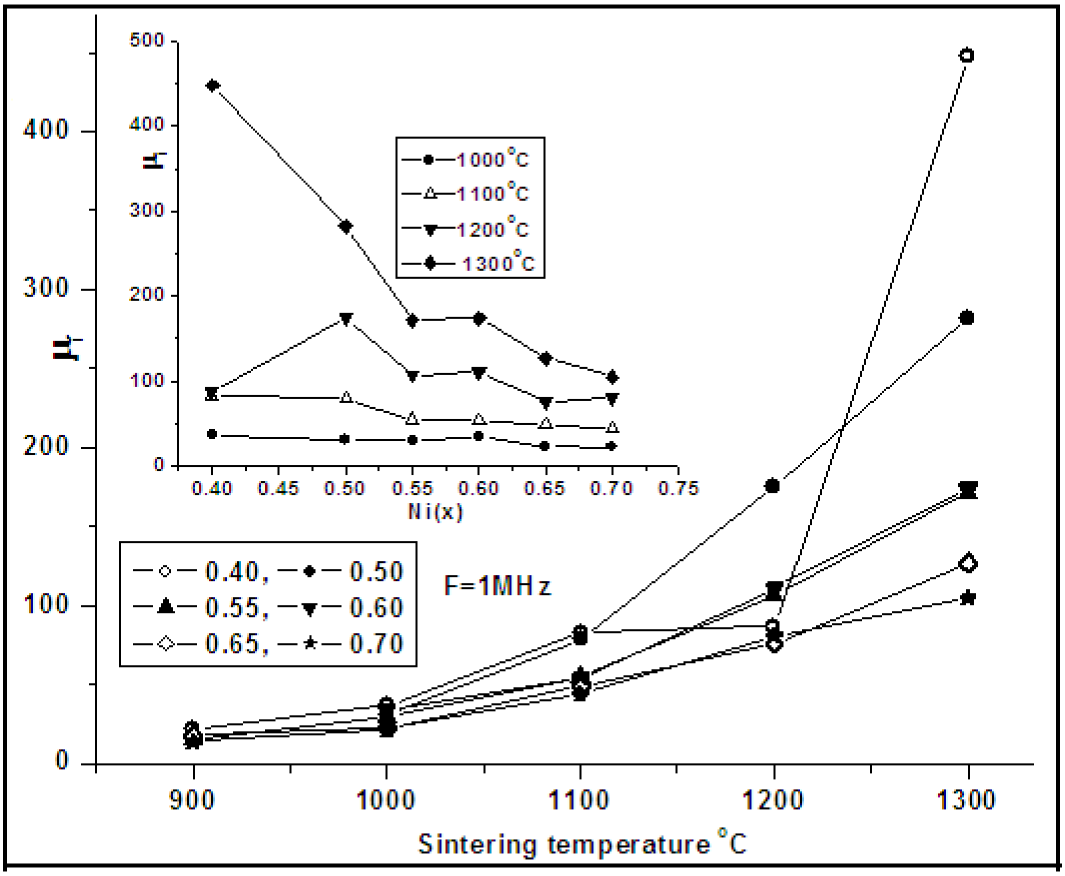

Fig. 5.23 Variation of initial permeability of bulk $Ni_xZn_{1-x}Fe_2O_4$ samples (at 1 MHz) with sintering temperature. Inset show variation of initial permeability (at 1 MHz) with Ni content at sintering temperature of 1000°C, 1100°C, 1200°C and 1300°C.

for samples with higher density. The decreasing porosity also increases μ_i. The pores in the samples act as pinning centers for the domain wall movement. Consequently, domain wall movement is restricted and this limits the rate of growth of μ_i [49]. Inset of Fig. 5.23 shows variation of μ_i (at 1 MHz) with Ni content at sintering temperature of 1000^{o}C, 1100^{o}C, 1200^{o}C and 1300^{o}C. From inset, it can be seen that μ_i decreases with increase in Ni content for 1000^{o}C, 1100^{o}C and 1300^{o}C. The marginal increase was observed for Ni=0.60 at 1000^{o}C compared to Ni=0.55, which may be attributed to its higher bulk density (4.69 g/cm^3 for Ni=0.60 and 4.49 g/cm^3 for Ni=0.55). However, the alternate increase and decrease in μ_i with Ni content was observed for 1200^{o}C. Similar trend was also found in their density variations. Such variations may be attributed to uneven micro-structural changes. The μ_i at 1 MHz in the present work vary in the range of 14 to 448. The obtained value of μ_i of 448 and 282 for Ni=0.40 and Ni=0.50 (at 1 MHz) at sintering temperature of 1300^{o}C in the present work, is higher than the reported value of 236 by V. L. O Brito et al. for Ni-Zn ferrite of same composition at 1 MHz [50].

5.12.7.3 Variation of tanδ with frequency

The magnetic loss tangent (tanδ) determines the efficiency of a ferrite core to suppress the electromagnetic interference at a particular frequency. The loss in the ferrite sample is due to the lag of motion of domain walls with respect to the applied alternating magnetic field and is attributed to imperfections in the lattice.

Fig. 5.24 shows the variation of tanδ with frequency of bulk samples with Ni=0.40 and 0.50. It is seen that, tanδ decreases sharply at lower frequency, and remains constant over a large band of higher frequency and then increases abruptly

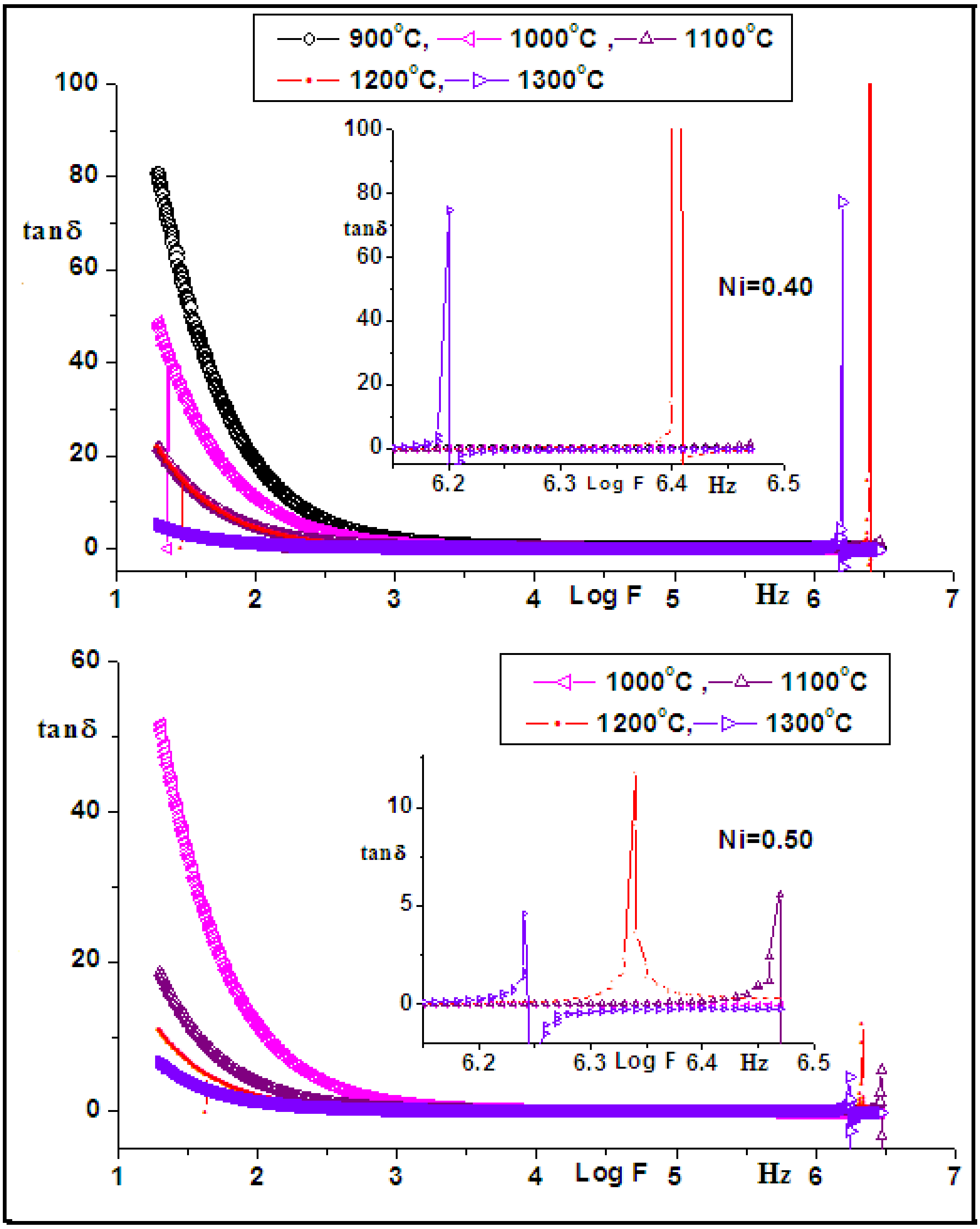

Fig. 5.24 Frequency dependence of loss tangent of bulk $Ni_xZn_{1-x}Fe_2O_4$ samples (x=0.40 and 0.50). Inset show loss tangent variations near resonance frequency.

at resonance frequency. This behavior is similar to that of initial permeability. The sharp increase in the tanδ near resonance frequency for Ni=40 and Ni=0.50 is shown in the inset of Fig. 5.24. The resonance peaks are the results of the absorption of energy due to matching of the oscillation frequency of the magnetic dipoles and the applied frequency. At resonance, maximum energy is transferred from applied field to the lattice, resulting in rapid increase in tanδ [43].

5.12.7.4 Effect of sintering temperature and composition on tanδ

Fig. 5.25 shows variation of tanδ of bulk samples (at 1 MHz) with sintering temperature. It can be seen that, tanδ increases with sintering temperature for all the samples except minor decrease for Ni=0.70 at 1300°C. Although the grain size of the samples is increased with sintering temperature, the reason behind increase in loss with sintering temperature may be due to the formation of trapped pores within the grains and/or grain boundaries. If these pores act as domain wall pinning factor, the domain wall movement would be obstructed and loss will increase. SEM micrograph shows increase in the grain size with increasing sintering temperature up to 1300°C. Thus, a better microstructure and crystal growth can be expected to give lower loss for higher sintering temperatures beyond 1300°C. The loss will be reduced at higher sintering temperatures as pores can be suppressed or transferred at the grain boundaries rather than closed inside the grains [44].

The inset of Fig. 5.25 shows variation of loss tangent of bulk samples (at 1 MHz) with Ni content. It can be seen that, tanδ decreases with increase in Ni content for all the bulk series except, minor increase for Ni=0.55 at 1000°C, 1100°C and Ni=0.70 at 1000°C and 1200°C. This minor increase may be attributed to the differences in their microstructures. The smooth decreasing loss with Ni content at 1300°C indicates formation of more uniform microstructure at this sintering temperature. The overall tanδ in the present work at 1 MHz was in the range of 0.016 to 0.095. The tanδ at 1 MHz varies in the range of 0.0178 to 0.0370 at

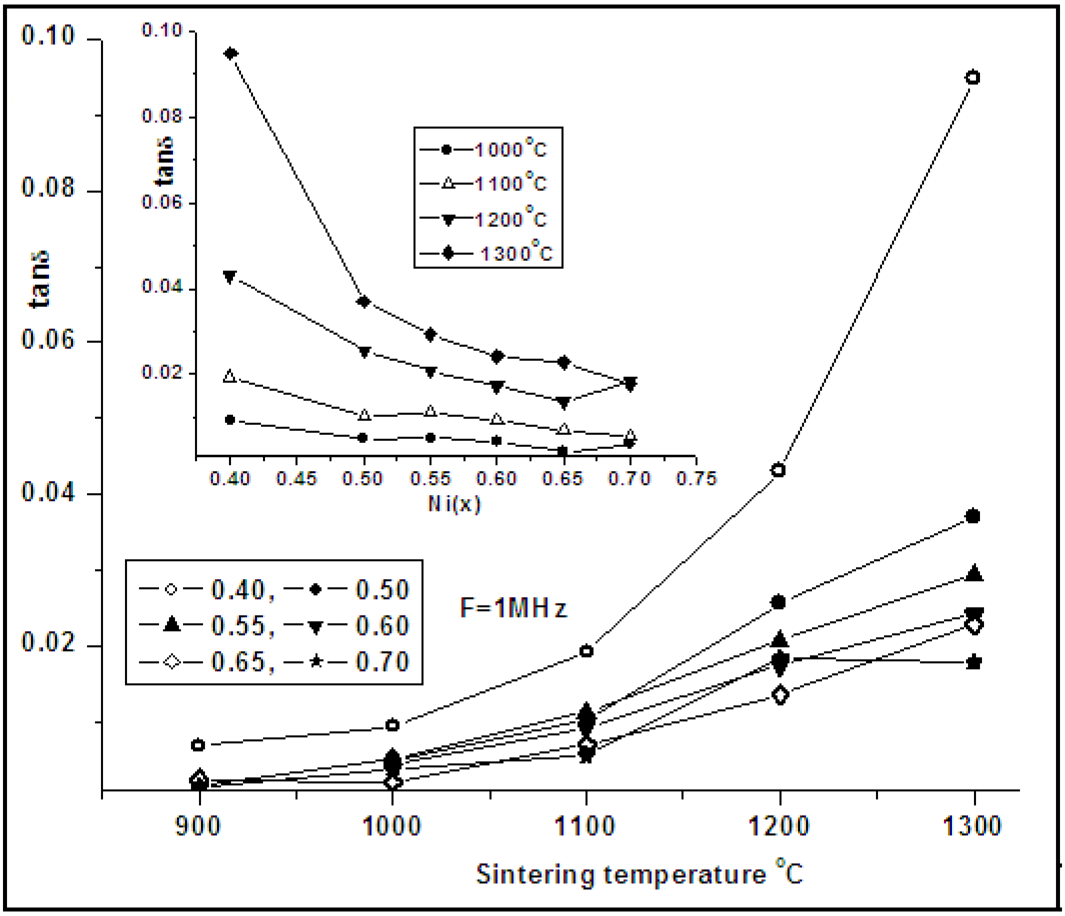

Fig. 5.25 Variation of loss tangent of bulk $Ni_xZn_{1-x}Fe_2O_4$ samples (at 1 MHz) with sintering temperature. Inset show variation of loss tangent (at 1 MHz) with Ni content at sintering temperature of 1000°C, 1100°C, 1200°C and 1300°C.

sintering temperature of 1300°C, which was lower than the reported value of 0.054 by V. L. O Brito et al. for Ni-Zn ferrite under similar condition [50].

5.12.7.5 Thermal variation of μ_i

Since, the μ_i is directly related to the magnetization and microstructure, the thermal spectra of μ_i can be taken as a symbolic test of Curie temperature and the homogeneity of the samples [47]. Fig. 5.26 shows thermal variation of μ_i of bulk samples at various frequencies for Ni=0.40 and 0.60 at sintering temperature of 1100°C. It can be seen that, μ_i increases slowly with temperature especially at frequency of 10 KHz whereas, remains almost constant at other frequencies. The μ_i

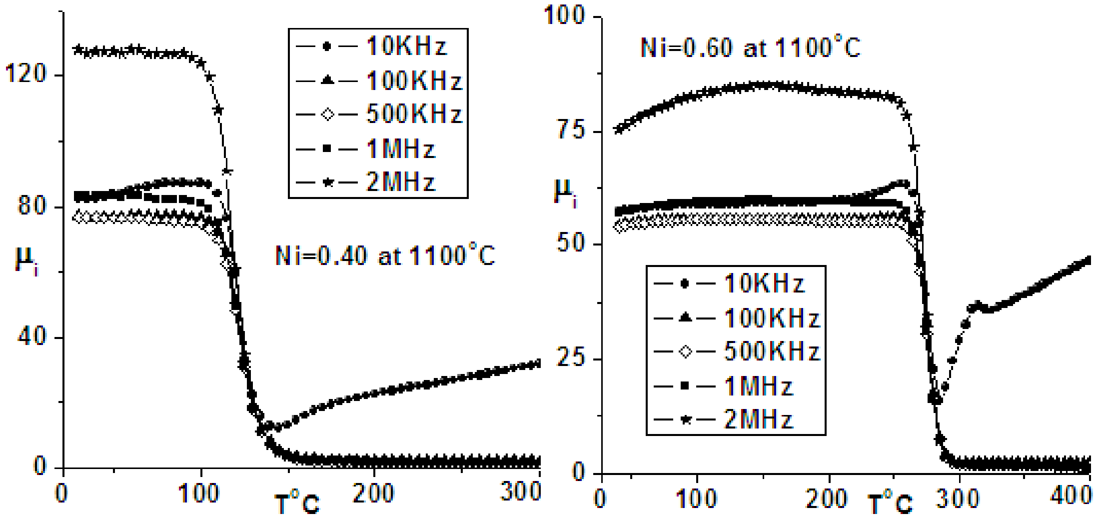

Fig. 5.26 Thermal variation of initial permeability of bulk $Ni_xZn_{1-x}Fe_2O_4$ samples at 1100°C.

drops sharply for all the frequencies at $\mathbf{T_c}$, where the magnetic state of the ferrite samples changes from ferrimagnetic to paramagnetic. The increase in $\boldsymbol{\mu_i}$ with the temperature for Ni=0.60 at 2 MHz can also seen. The peak near $\mathbf{T_c}$ observed for this sample particularly for 10 KHz is known as “Hopkinsons” peak [14].

The variation of $\boldsymbol{\mu_i}$ with temperature can be explained as follows: the anisotropy constant (**K**) and saturation magnetization ($\mathbf{M_S}$) usually decreases with increase in temperature. However, decrease in **K** with temperature is faster than thedecrease in $\mathbf{M_S}$. When the **K** reaches zero, $\boldsymbol{\mu_i}$ attains its maximum value and then drops off to the minimum value near the Curie point [47]. Initially **K** has negative value at room temperature and it increases with temperature and becomes zero at $\mathbf{T_c}$.

5.12.7.6 Effect of sintering temperature on thermal variation of $\boldsymbol{\mu_i}$

Fig. 5.27 show thermal variation of $\boldsymbol{\mu_i}$ of bulk samples at 1 MHz at various sintering temperature. It can be seen that $\boldsymbol{\mu_i}$ remained almost constant or show feeble

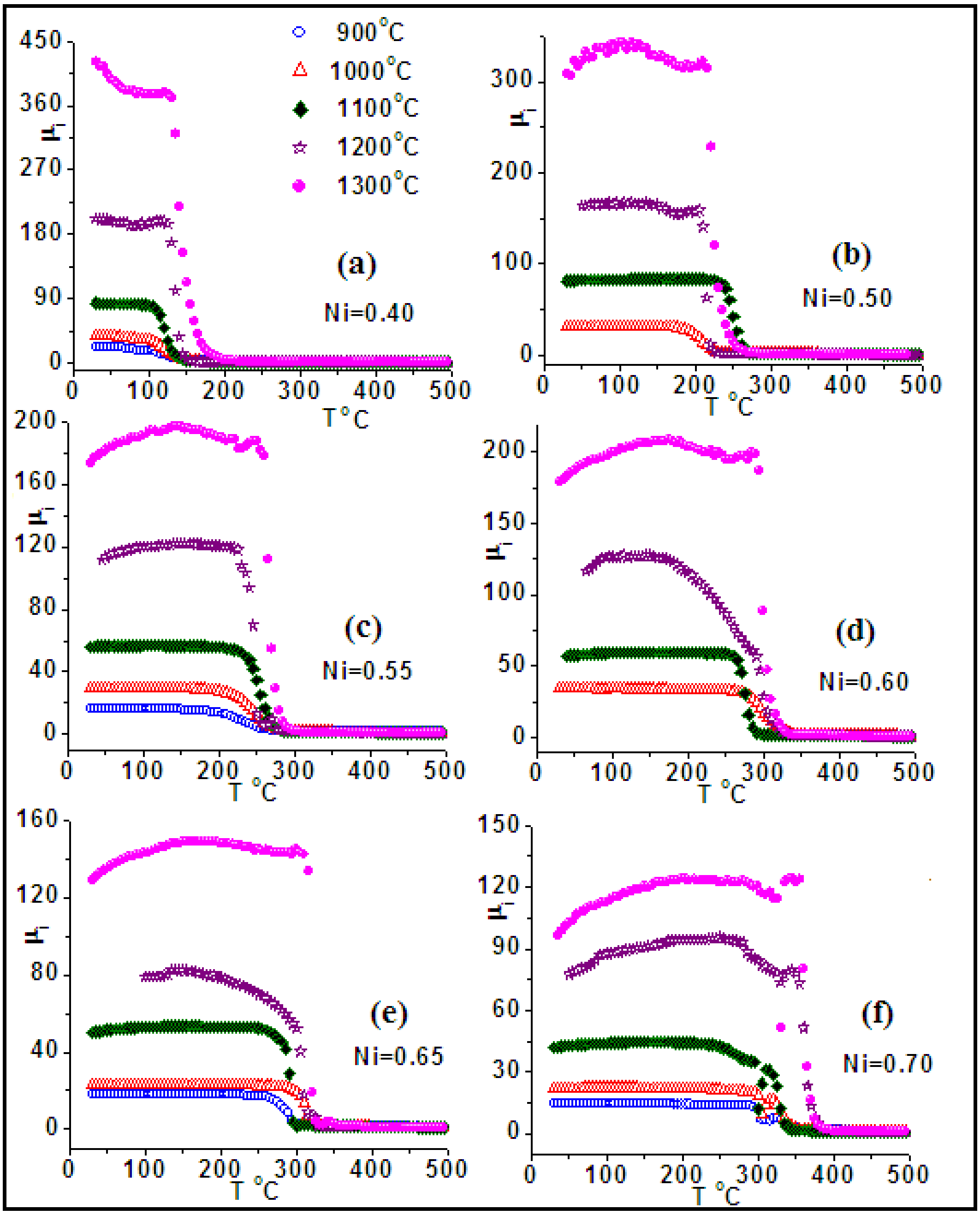

Fig. 5.27 Thermal variation of initial permeability of bulk $Ni_xZn_{1-x}Fe_2O_4$ samples (at 1 MHz), (a) x=0.40, (b) x=0.50, (c) x=0.55, (d) x=0.60, (e) x=0.65 and (f) x=0.70.

increase with increasing temperature for the samples at sintering temperature of 900°C, 1000°C and 1100°C, whereas it increases at 1200°C and 1300°C. The feeble peaking or constant nature of μ_i with increase in temperature at 900°C, 1000°C and 1100°C may be attributed to slower rate of decrease in anisotropy compared to bulk samples obtained at sintering temperatures of 1200^{o}C and 1300^{o}C. Also, as we know that the contribution to permeability from domain rotation is slow and temperature independent process whereas, the contribution due to domain wall motion is relatively quicker and temperature dependent process. This supports the observed initial increase in $\mathbf{\mu_i}$ with temperature for samples at 1200^{o}C and 1300^{o}C, as the grain size is more at these sintering temperatures which in turn increases domain wall contribution to permeability [44].

From Fig. 5.27 it can be seen that, the sharpness of the fall in $\mathbf{\mu_i}$ increases with increase in sintering temperature. This is attributed to improvement in degree of homogeneity of the sample with increasing sintering temperature [14]. The maximum sharpness was observed at 1300^{o}C, reflecting maximum homogeneity in the samples which is also supported by SEM images. The shifting of $\mathbf{\mu_i}$ curves to higher side with the increase in sintering temperature due to increase in grain size can be clearly seen for all the samples.

Fig. 5.28 shows variation of $\mathbf{T_c}$ of bulk samples with sintering temperature. It can be seen that $\mathbf{T_c}$ for Ni=0.40 decreases with increasing sintering temperature up to 1100^{o}C and then increases for and above 1200^{o}C. The initial decrease in $\mathbf{T_c}$ is expected due to increase in grain size. The increase at 1200^{o}C and 1300^{o}C may be attributed to increase in A- B exchange interaction due to lattice contraction and redistribution of cations at A and B sites, as evident from XRD data and Mossbauer spectroscopy respectively. This increase in $\mathbf{T_c}$ may also be attributed to zinc volatilization at higher sintering temperature leading to increase of Fe:Ni ratio in the samples. In case of Ni=0.55, $\mathbf{T_c}$ decreases till 1200^{o}C and increases for 1300^{o}C. For Ni=0.50 and Ni=0.70, an alternate increase and decrease in $\mathbf{T_c}$ with increasing

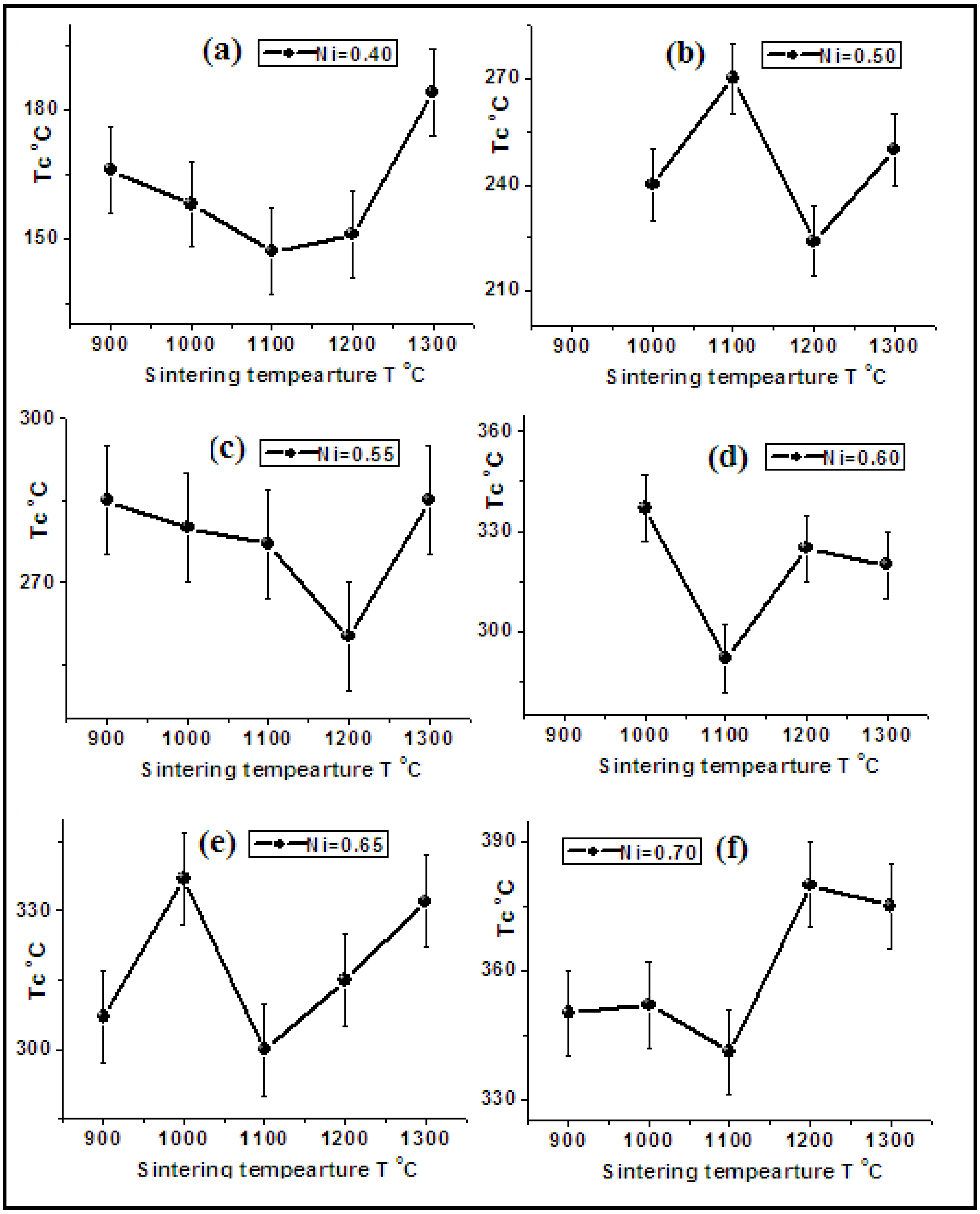

Fig. 5.28 Variation of Curie temperature of bulk $Ni_xZn_{1-x}Fe_2O_4$ samples obtained from curves of thermal variation of initial permeability at 1 MHz with sintering temperature, (a) x=0.40, (b) x=0.50, (c) x=0.55, (d) x=0.60, (e) x=0.65 and (f) x=0.70.

sintering temperature was observed. For Ni=0.65 and 70, $\mathbf{T_c}$ at 900°C is higher than at 1000°C, this may be attributed to change in cation distribution due to sintering. The linear increase in $\mathbf{T_c}$ from 1100°C to 1300°C was observed for Ni=0.65, this is mainly due to lattice contraction, change in cation distribution and zinc volatilization on sintering. However, for Ni=0.60 and 0.70, **T_c** decreases marginally after 1200°C, and hence, in these samples, effect of increase in the size due to sintering temperature may be dominating over other effect such as zinc volatilization or lattice contraction that are responsible for increase in **T_c**.

5.12.7.7 Effect of composition on thermal variation of μ_i

The thermal variation of **μ_i** of bulk samples at 1 MHz at various sintering temperature as a function of Ni content are shown in Fig. 5.29. It can be observed that the **μ_i** curves are shifting towards right side with increase in Ni content for all the bulk samples which is attributed to increase in ferrimagnetic ordering.

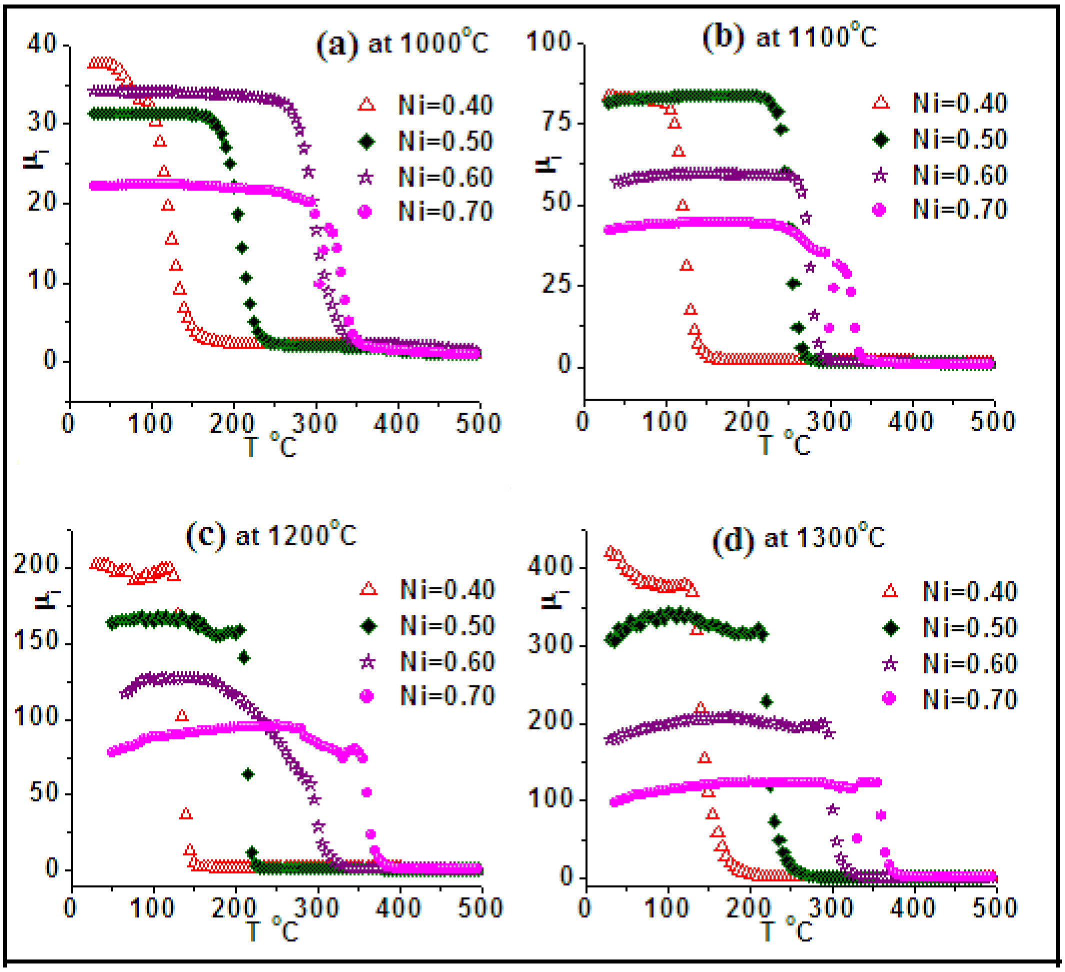

Fig. 5.29 Thermal variation of initial permeability of bulk $Ni_xZn_{1-x}Fe_2O_4$ samples at 1 MHz at sintering temperature of (a) 1000°C, (b) 1100°C, (c) 1200°C and (d) 1300°C.

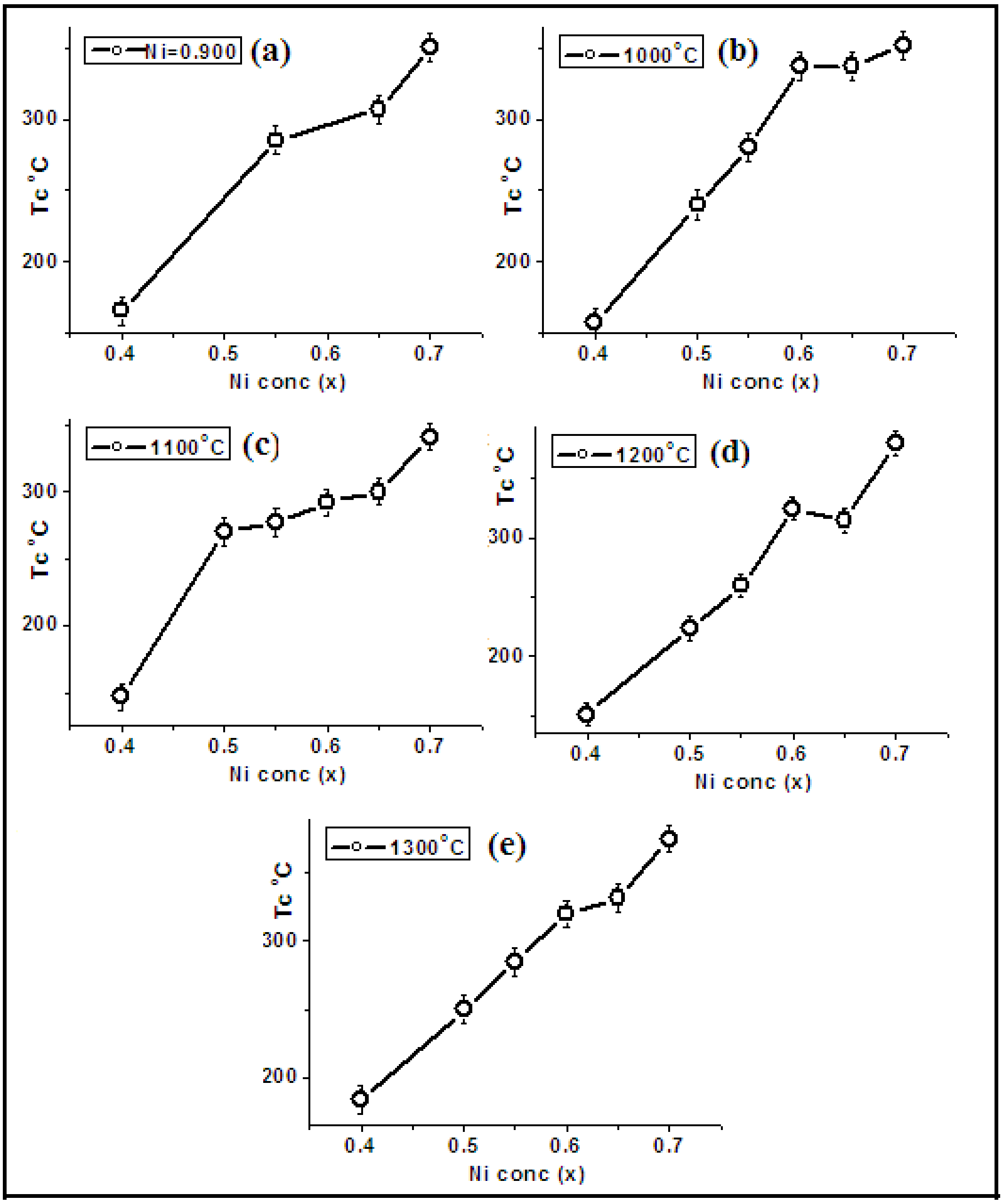

Fig. 5.30 Variation of Curie temperature of bulk $Ni_xZn_{1-x}Fe_2O_4$ samples obtained from curves of thermal variation of initial permeability at 1 MHz with Ni content, at (a) 900°C, (b) 1000°C, (c) 1100°C, (d) 1200°C and (e) 1300°C.

Fig. 5.30 show the variation of $\mathbf{T_c}$ of bulk samples obtained from curves of thermal variation of $\boldsymbol{\mu_i}$ at 1 MHz with Ni content. It is seen that there is overall increase in $\mathbf{T_c}$ with increase in Ni content in the samples at all the sintering temperatures. This may be attributed to increase in ferrimagnetic state and increasing Fe:Ni ratio in the samples. The minor decrease in $\mathbf{T_c}$ was observed for

Ni=0.65 in comparison with Ni=0.60 at sintering temperature of 1000^{o}C and 1200^{o}C. This may be attributed to change in cation distributions. The smooth increase in $\mathbf{T_c}$ with Ni content at 1300^{o}C may be attributed to better homogeneity and more uniformity in grain sizes for the samples at 1300^{o}C which was also observed from SEM micrographs.

By comparing Fig. 5.28 and Fig. 5.30, we may conclude that the variation in $\mathbf{T_c}$ of bulk samples is more uniform with change in Ni content in the samples compared to the change in the sintering temperature.

5.12.8 Mössbauer spectroscopy

The Mössbauer spectra of nano and bulk $Ni_xZn_{1-x}Fe_2O_4$ samples were recorded at room temperature to monitor the local environment around Fe cations in these samples. The variation in Mossbauer hyperfine parameters of nano and bulk samples as a function of composition and sintering temperatures were studied.

5.12.8.1 Mössbauer spectra of nano samples

The Mössbauer spectra of nano samples were recorded at room temperature to monitor the local environment around Fe cations in the samples and are shown in the Fig. 5.31. The solid line in the Fig. represents the simulated curves whereas solid circles represent the experimental data points. Each spectrum was fitted with the three magnetic sextets which are arising due to Zeeman splitting. The two major sextets are corresponding to Fe ions residing at the A site (inner sextet) and B site (outer sextet) of the lattices. This is an indication of ferrimagnetic behavior of the samples [51]. The observed six-line magnetic patterns in the spectra are attributed to super exchange interaction between the magnetic ions at A and B sub-lattices.

The third and broad featureless absorption sextet C, characterized by a significant reduction of the magnetic hyperfine field is associated with relaxation effect. The Fe ions corresponding to broad sextet with much smaller hyperfine field than that of major sextet may be associated with the atoms near the surface of the nano particles experiencing disordered spins [52]. This relaxation effect may also be due to the presence of strong inter-particle interactions and nano sizes of the particles of the samples [53]. The area associated with this broad sextet is maximum for Ni=40.

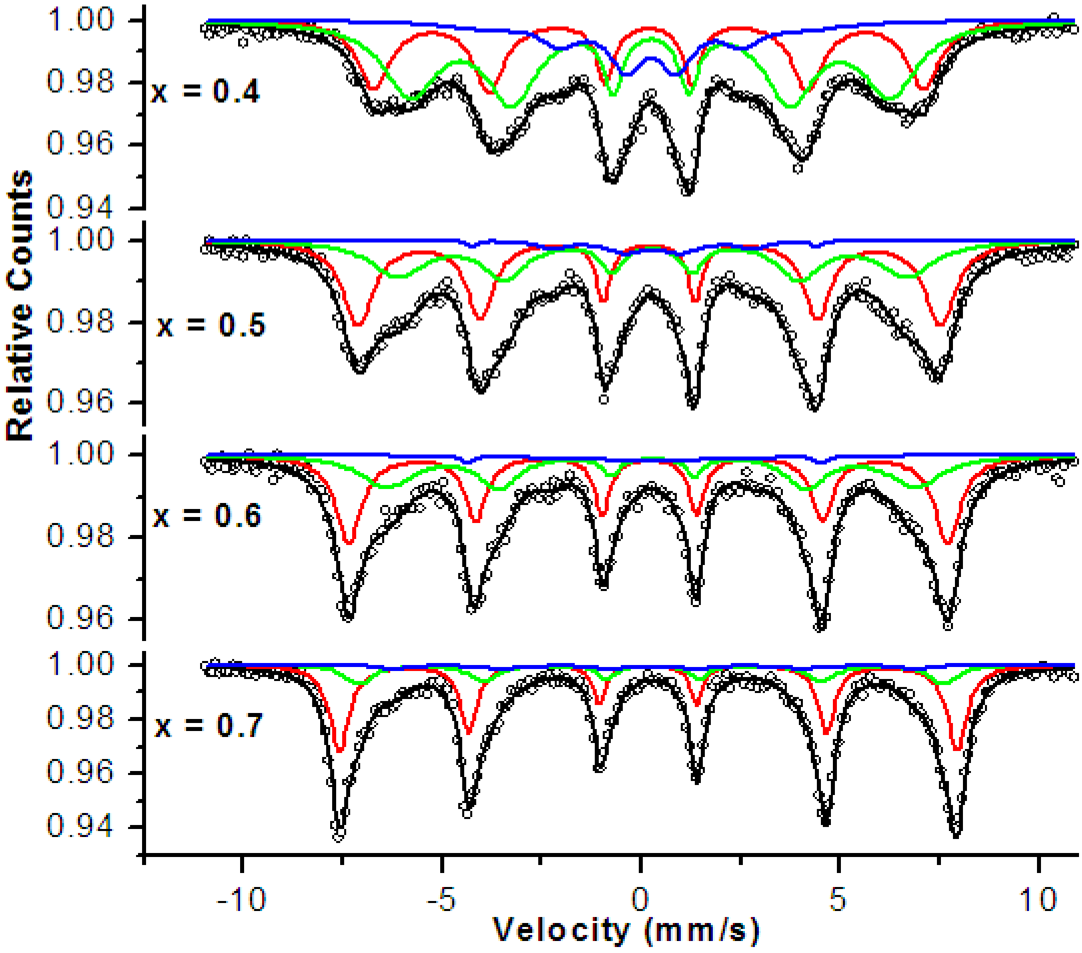

Fig. 5.31 Room temperature Mössbauer spectra of nano $Ni_xZn_{1-x}Fe_2O_4$ samples.

This indicates the presence of larger amount of smaller nano particles in this sample, compared to that of other compositions. This was well supported by observed lower **T_B** for Ni=0.40 (obtained from SQUID measurement) compared to that of other compositions.

The various Mössbauer parameters obtained for nano samples are given in Table 5.4. The results of the isomer shift vary in the range of 0.15 mm/s to 0.47 mm/s. This shows that, Fe ions are in the trivalent state for all the samples. The quadrupole shift (Δ) values were found to be low and is indicating that the local symmetry of the magnetic phase of A sites is close to cubic, while that of B site is close to trigonal [54, 55]. The hyperfine field (H) values at both A and B sites are increasing with increasing Ni content in the sample. This indicates that the samples are more magnetically ordered at higher concentration of Ni.

Table 5.4 The isomer shift (δ), quadrupole splitting (Δ), hyperfine Field values (H), outer line width (T) and areas in percentage of tetrahedral (A) and octahedral (B) sites occupied by Fe^{3+} ions of nano $Ni_xZn_{1-x}Fe_2O_4$ samples derived from Mössbauer spectra recorded at room temperature. [Isomer shift values are relative to α-Fe (0.00 mm/s) foil]

Ni (x)	Iron site	Isomer Shift (δ) mm/s	Quadrupole Splitting Δ (mm/s)	Hyperfine Field H (T)	Outer Line width T (mm/s)	Area %
0.40	A	0.329	-0.006	38.52	1.528	36.0
	B	0.284	0.003	43.16	0.710	11.5
	C	0.354	0.007	24.17	4.182	52.5
0.50	A	0.329	-0.012	38.53	1.777	46.5
	B	0.284	-0.006	45.64	0.710	21.9
	C	0.410	-0.026	29.63	8.384	31.6
0.60	A	0.381	0.020	42.12	1.52	38.2
	B	0.281	0.000	46.76	0.71	41.8
	C	0.474	-0.144	31.24	10.02	20.0
0.70	A	0.455	0.005	43.70	1.538	30.3
	B	0.274	-0.006	47.82	0.710	59.1
	C	0.145	0.903	334.9	9.374	10.6

5.12.8.2 Mössbauer spectra of bulk samples

The room temperature Mössbauer spectra of bulk $Ni_{0.60}Zn_{0.40}Fe_2O_4$ sample are shown in the Fig. 5.32. These spectra were recorded to investigate the effect of sintering temperature on magnetic phase and amount of Fe at A and B site in the lattice. The spectra were fitted with four magnetic sextets which arises due to Zeeman splitting. The inner sextet (red colour) is corresponding to Fe ions on the A site, and other three sextets are corresponding to Fe ions on the B site. The absence of featureless relaxed sextet in bulk samples indicates coarsening of the nano particles and increase in grain sizes due to sintering effect. The increase in sharpness of the Mössbauer spectra with increasing sintering temperature shows improvement in homogeneity and ferrimagnetic ordering in the samples. This is also evident from the increase in the hyperfine field values of both A and B sites with increasing sintering temperature.

The various Mössbauer parameters of bulk $Ni_{0.60}Zn_{0.40}Fe_2O_4$ samples are given in Table 5.5. The results of isomer shift (0.09-0.27 mm/s) shows that all the components are due to Fe^{+3} ions. The quadrupole splitting (Δ) values are low, indicating cubic symmetry at tetrahedral A sites. However, higher values of quadrupole shift in the range of (0.31 mm/s to 0.38 mm/s) observed for sextet B1 may be attributed to distortion in trigonal symmetry at octahedral B sites [54]. The observed ratio of area of Fe at A site to Fe at B site at 1300°C was found to be 0.47 which is close to 0.43 for ideal bulk sample. This ratio was found to be 0.52 and 0.37 at 1100°C and 1200°C respectively. This deviation in fractions of Fe ions occupying octahedral to tetrahedral sites are responsible for change in cation distributions with sintering temperature.

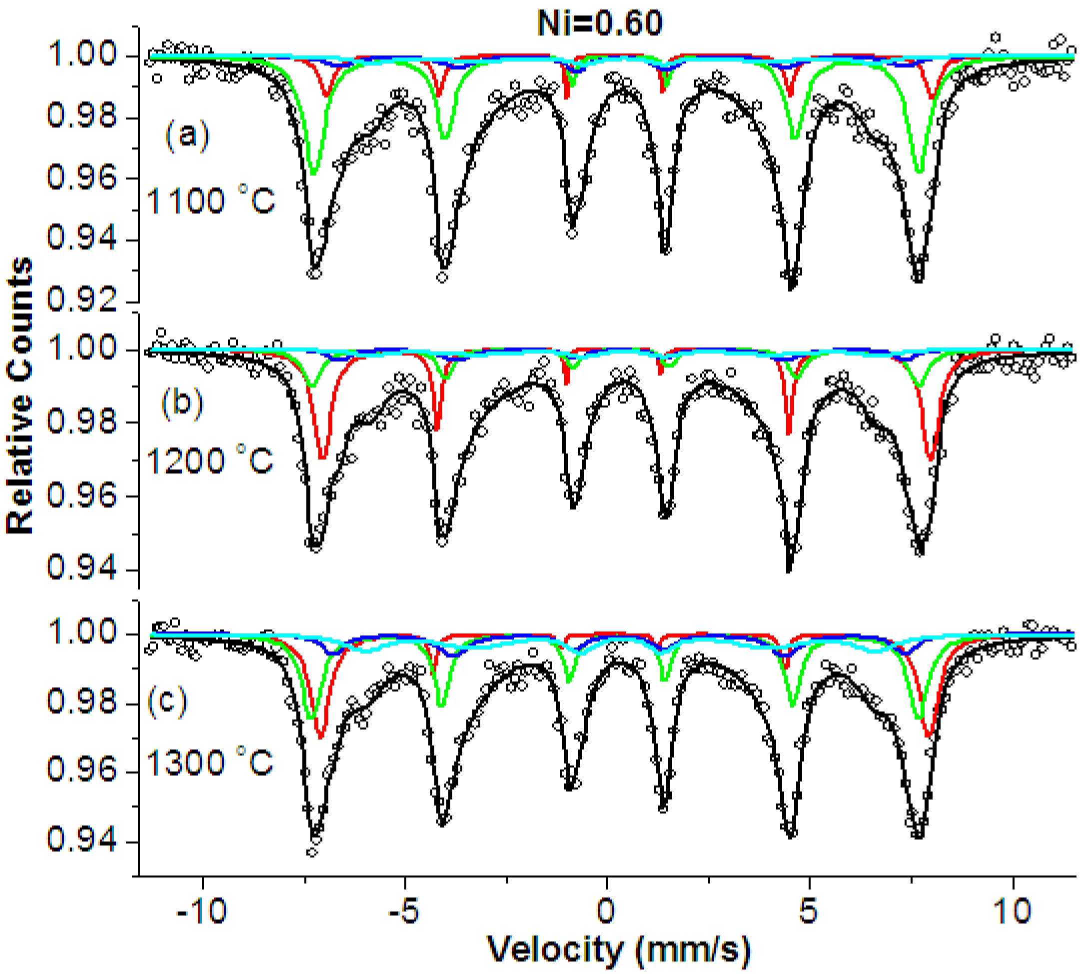

Fig. 5.32 Room temperature Mössbauer spectra of bulk $Ni_{0.60}Zn_{0.40}Fe_2O_4$ sample at sintering temperature of (a) 1100°C, (b) 1200°C and (c) 1300°C.

The room temperature Mössbauer spectra of bulk samples with Ni= 0.40, 0.50 and 0.60 at sintering temperature of 1300°C are shown in Fig. 5.33 and corresponding Mössbauer parameters are given in Table 5.6. It can be seen that the sharpness of the sextets and corresponding hyperfine field at A and B site increases with increasing Ni content in the sample. This is attributed to increase in ferrimagnetic phase in the samples. The observed ratio of area of Fe at A site to Fe at B site was found to be 0.27, 0.37 and 0.47 for Ni=0.40, 0.50 and 0.60 respectively. These ratios were found to be close to that of 0.25, 0.33 and 0.43 for ideal bulk sample with Ni=0.40, 0.50 and 0.60 respectively.

Table 5.5 The isomer shift (*δ*), quadrupole splitting (Δ), hyperfine Field values (H*)*, outer line width (T) and areas in percentage of tetrahedral (A) and octahedral (B) sites occupied by Fe^{3+} ions of bulk $Ni_{0.60}Zn_{0.40}Fe_2O_4$ sample derived from Mössbauer spectra recorded at room temperature. [Isomer shift values are relative to α-Fe (0.00 mm/s) foil]

Sintering Temp. °C	Iron site	Isomer Shift (δ) mm/s	Quadrupole Splitting Δ (mm/s)	Hyperfine Field H (T)	Outer Line width T (mm/s)	Area %
1100	A	0.151	-0.090	46.38	0.158	34.1
	B1	0.239	0.358	46.46	0.112	6.2
	B2	0.226	0.010	43.29	0.593	28.1
	B3	0.245	-0.030	38.47	0.733	31.6
1200	A	0.151	-0.14	46.50	0.345	26.8
	B1	0.189	0.317	46.60	0.084	13.8
	B2	0.216	0.036	43.40	0.508	20.1
	B3	0.269	-0.010	38.96	0.820	39.3
1300	A	0.097	0.064	46.54	0.343	31.9
	B1	0.111	0.385	46.67	0.132	8.3
	B2	0.164	0.004	43.87	0.627	23.7
	B3	0.207	-0.030	39.13	0.690	36.1

Table 5.6 The isomer shift (*δ*), quadrupole splitting (Δ), hyperfine Field values (H*)*, outer line width (T) and areas in percentage of tetrahedral (A) and octahedral (B) sites occupied by Fe^{3+} ions of bulk $Ni_xZn_{1-x}Fe_2O_4$ samples at sintering temperature of 1300°C derived from Mössbauer spectra recorded at room temperature. [Isomer shift values are relative to α-Fe (0.00 mm/s) foil]

Ni (x)	Iron site	Isomer Shift (δ) mm/s	Quadrupole Splitting Δ (mm/s)	Hyperfine Field H (T)	Outer Line width T (mm/s)	Area %
0.4	A	0.193	0.005	36.84	0.492	21.5
	B1	0.156	0.034	40.75	0.523	18.5
	B2	0.237	-0.062	32.49	1.045	23.5
	B3	0.232	0.011	23.69	0.928	36.5
0.5	A	0.198	-0.012	42.29	0.514	26.9
	B1	0.159	0.046	44.95	0.443	24.6
	B2	0.252	0.000	37.23	0.609	28.1
	B3	0.264	0.087	26.52	0.968	20.4
0.6	A	0.097	0.064	46.54	0.343	31.9
	B1	0.111	0.385	46.67	0.132	8.3
	B2	0.164	0.004	43.87	0.627	23.7
	B3	0.207	-0.030	39.13	0.690	36.1

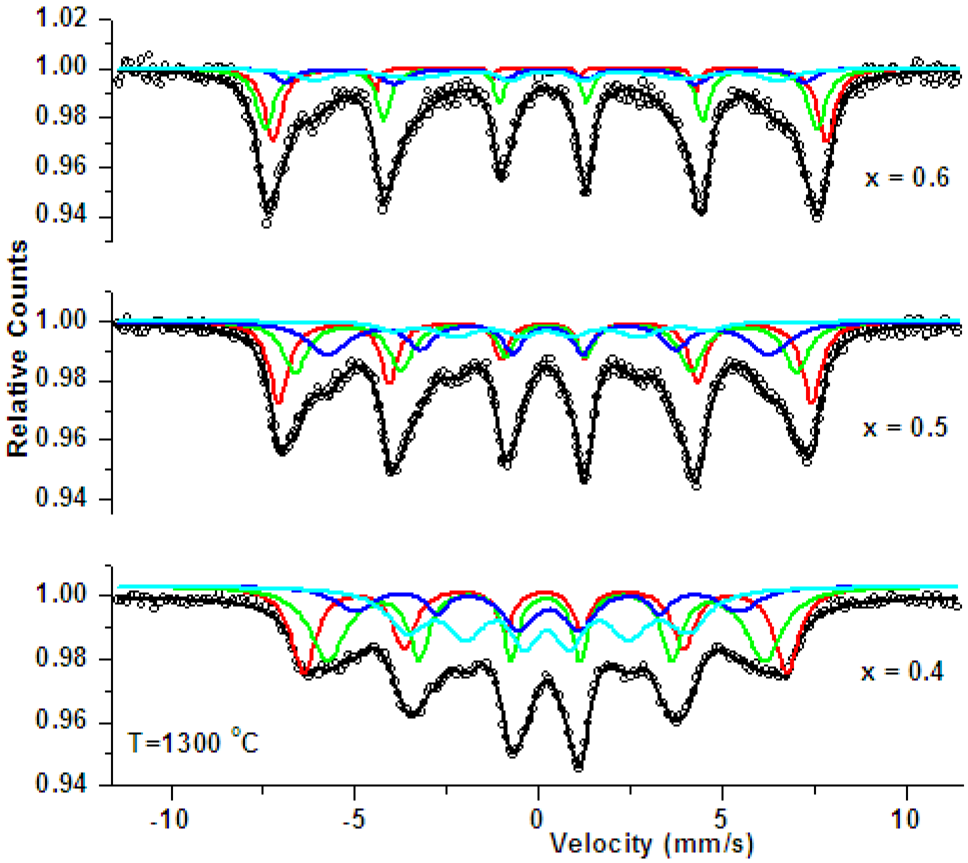

Fig. 5.33 Room temperature Mössbauer spectra of bulk $Ni_xZn_{1-x}Fe_2O_4$ samples (x = 0.40, 0.50 and 0.60) at sintering temperature of 1300°C.

References

1. K. Konds, T. Chiba, E. Otsuki and S. Yamada, Proc. ICF-8, (2000), 396-399.
2. A.C.F.M. Costa, E. Tortella, M. R. Morelli and R.H.G.A. Kiminami, J. Magn.Magn.Mater, 256, (2003), 174-182.
3. H. Ehrhardt, S. J. Campbell, and M. Hofmann, Scr. Mater., 48, (2003), 1141-1145.
4. Y. G. Ma, M. Z. Jin, M. L. Liu, G. Chen, Y. Sui, Y. Tian, G. J. Zhang, and Y. Q. Jia, Mater. Chem. Phys., 65, (2000), 79-82.
5. M. A. E. Hiti, J. Magn. Magn Mater, 164, (1996), 187-196.
6. M. Pardavi and Horvath, J. Magn. Magn Mater, 215, (2000), 171-183.
7. W. Fu, H. Yang, H. Bala, S. Liu, M. Li and G. Zou, Mater. Lett., 60, (2006), 1728-1732.
8. T. Abraham, Am.Ceram.Soc.Bull.,73, (1994), 62-67.
9. D. J. Dunlop, Science, 41, (1972), 176-179.
10. L. Neel , Ann Geophys, 5, (1949), 99-136.
11. N. R. Jana, L. Gearheart and C. J. Murphy C. J, Chem. Mater., 13, (2001), 2313-2315.
12. A. Goldman, Modem Ferrite Technology, Springer Science Business Media Inc. USA, 2nd Ed, (2006), 38-39.
13. A. P. Guimaraes, I. S. Oliveira, Magnetism and magnetic resonance in solids, A Jhon Wiley & Sons Inc. 2ndEd, (2006), 12-15.
14. A. K. M. Akther Hossaina, S. T Mahmuda, M. Seki, T. Kawai and H. Tabata, J. Magn. Magn Mater, 312, (2007), 210-219.
15. A. Globus, J. Physique Coll., (1963), C-1.1-C1.15.

16. M. T. Johnson and E. G. Vissar, IEEE Trans. Magn., MAG-26, (1990), 1987.

17. O. Acher, S. Dubourg, Phys. Rev. B, 77, (2008), 1-22.

18. J. Jankovskis, V. Yurshevich, V. Scavinskis, Electronika IR Electrotechnika, 5, (2005), 5-8.

19. E. De Grave, R. E. Vandenberghe and C. Dauwe, ILEEMS, 161, (1-4), (2005), 147-160.

20. M. D. Dyar, D. G. Agresti, M. Schaefer, C. A. Grant and E. C Sklute, Annual Reviews of Earth and Planetary Science, 34, (2006), 83-125.

21. S. D. Likhite, C. Radhakrihnamurthy and P. W. Sahastrabudhe, Rev.Sci.Inst., 25, (1965), 302-306.

22. S. D. Likhite and C. Radhakrihnamurthy, Curr.Sci., (1966), 534-536.

23. S. S. Jadhav, S. E. Shirsath, B. G. Toksha, S. J. Shukla and K. M. Jadhav, Chinese journal of chemical physics, 21, (2008), 381-386.

24. S. V. Kakatkar, S. S. Kakatkar, R. S. Patil, A. M. Sankpal, S. S. Suryawanshi, D. Bhosale, and S. R. Sawant, Phys. Stat. Sol.(b), 198, (1996), 853-856.

25. N. Gupta, A. Verma, C. Subhash, Kashyap and D.C Dube, J. Magn. & Magn. Mate., 308, (2007), 137-143.

26. P. Mathur, A. Thakur and M. Singh, J. Magn. & Magn. Mate., 320, (2008), 1364-1369.

27. C. Caizer and Stefanescu, J.Phy.D: Appl. Phys., 35, (2002), 3035-3040.

28. K. Velmurugan, V. K. S Venkatachalapathy and S. Sendhilnathan, Materials research, 12, (2009), 529-534.

29. H. M. I. Abduallah, J. Z. Msomi, T. Moyo and A. Lancok, J Supercond. Nov. Magn. 25, (2012), 2619-2623.

30. J. A. Lopez, M. A. Lopez, J. Mira, J. Rivas and S. W. Charles, J. Phys. Chem. B,

101, 41, (1997), 8045-8047.

31. A. Goldman, “Recent Advances in Ferrite Materials Technology,” in Modern Ferrite Technology, Van Nostrand Reinhold, New York, (1990).
32. I. Ismail, M. Hashim, K. Amin Matori and R. J. Hassan, J Supercond Nov Magn, 25, (2012), 71-77.
33. J. F. Wang, C. B. Ponton, R. Grossinge and, I. R. Harris, J. All. Compds., 369, (2004), 170-175.
34. R. V. Mangalaraja, S. Ananthakumar, P. Manohar and F. D. Gnanam, Materials Letters, 57, (2003), 2666-2669.

35 N. Kumar, A. Kumar, R. Jha, A. Dogra, R. Pasricha, R. K. Kotnala, H. Kishan and V. P. S Awana, J. Supercond. Nov. Magn., 23, (2010), 423-426.

36. R.V. Upadhaya, G. J. Baldha and R. G. Kulkarni, Mater. Res. Bull., 21, (1986), 10-15.
37. R. Evansa, U. Nowak, F. Dorfbauer, T. Shrefle, O. Mryasov, R.W. Chantrell, and G. Grochola, J. Appl. Phys., 99, (2006), 701-704.
38. R. Ayer, R. Desai and R. V. Upadhay, Indian J. Pure Appl. Phys., 47, (2009),180-185.
39. A. G. Bhosale and Chowgule, Mater. Chem. and Phys., 97, (2006), 273-276.
40. C. Rath, S. Anand, R. P. Das, K. K. Sahu, S. D. Kulkarni , S. K. Date and N. C. Mishra, Indian J. Appl. Phys., 91-4, (2002), 2211-2215.
41. M. J. Iqbal, Z. Ahmad, T. Meydan and Y. Melikhov, J. Appl. Phys. 111, (2012), 339061-339067.
42. M. U. Rana, M. Islam and T. Abbas, Solid State Communications, 126, (2003), 129- 133.
43. M. M. Haque, M. Huq and M. A. Hakim, J. Magn. Magn Mater, 320, (2008),

2792-2799.

44. D. N. Bhosale, S. R. Sawant, S. A. Gangal, R. R. Mahajan and P. P. Bakare, Materials Science and Engineering, B-65, (1999), 79-89.
45. T. Tsutaoka, T. Nakamura and K. Hatakeyama, J. Appl. Phys., 82, (1997), 3067-3071.
46. A. K. M. Akther Hossain and M. L. Rahman, J. Magn. Magn Mater, 323, (2011), 1954-1962.
47. A. K. Singh, T. C. Goel, R. G. Mendiratta, O. P. Thakur and C. Prakash, J. Appl. Phys., 92(7), (2002), 3872-3876
48. I. Ismail and M. Hashim, J Supercond Nov Magn, 25, (2012), 1551-1561.
49. S. S. Bellad and B. K. Chougule, Materials Chemistry and Physics, 66, (2000), 58-63.
50. V. L. O. Brito and A. C. C. Migliano L. V. Lemos F. C. L. Melo, Progress in electromagnetic research, PIER 91, (2009), 303-318.
51. R. L. Dhiman, S. P. Taneja and V.R. Reddy, Ad.Cond. Matt. Phys., (2008), 1-7.
52. L. H. Singh, R. Govindaraj, G. Amarendra and C.S. Sundar, AIP Conf. Proc. 1447, doi: 10.1063/1.4710071, (2012), 445-446.
53. A. S. Albuquerque, J. D. Ardisson, A. A. M. Waldemar and M. Alves, J. Appl. Phys., 87, (2000), 4352-4357.
54. S. M. Attia, Egypt. J. Solids, 29(2), (2006), 329-339.
55. J. Blasko and J. Garcia, Phys. Rev. B. 83, (2011), 104-105.

CHAPTER 6

ELECTRICAL PROPERTIES

6.1 Introduction

Spinel ferrites have potential for applications in electrical components, memory devices and microwave devices over a wide range of frequencies because of their high resistivity and low loss behavior [1]. Ferrites are also used in the tone generating circuitry of push button telephones and as load coils in transmission lines to reduce signal loss over long distances. A particular composition of initial ingredients makes the material suitable to operate in one particular range of frequency and therefore, to cover the large range of frequency (i.e. 1-100 GHz), different ferrites with different compositions have been tried by researchers over the world [2]. Electrical transport properties of ferrites are widely used in the interpretation of the conduction mechanism in ferrites that provide information on suitability of these materials for specific application [3]. The electrical properties of ferrites are very sensitive to preparative conditions, compositions, sintering temperature, rate of sintering and sintering atmosphere [4].

Ni-Zn ferrites among other ferrites are the most versatile having many technological applications in the high frequency and pulse field applications due to its high resistivity and low eddy current loss [5, 6]. Such ferrites are widely used in broadband ferrite devices, such as offset devices, distribution devices, amplifiers, inductance devices, broadband transformers, user terminals and other electromagnetic interference (EMI) and electromagnetic compatibility (EMC) applications [7, 8, 9].

Present Chapter contains detailed investigation of the important electrical properties such as dc resistivity, thermoelectric power, dielectric constant and dielectric loss tangent of nano and bulk Ni-Zn ferrite samples. The basics of electrical parameters and few models explaining the electrical properties are described in brief at the beginning of this Chapter.

6.2 Resistivity

The resistivity is one of the most important characteristics of the material and is temperature dependent. The resistivity of a metal increases with the rise of temperature and decreases in case of semiconductors and insulators. The resistance to flow of conduction electron is mainly due to two factors (i) the lattice vibrations that are temperature dependent (thermal resistivity) and (ii) imperfections and dislocations in a crystal lattice (which is less significant compared to lattice vibrations). The resistivity is defined as the resistance of unit length of a substance with a uniform unit cross-section. It is measured in ohm-cm. The resistivity of the ferrite samples can be calculated using Equation 6.1 and 6.2.

$$\rho = \frac{RA}{L} \tag{6.1}$$

$$R = \frac{V}{I} \tag{6.2}$$

Where R is resistance of the material at a specific temperature, A is the cross-sectional area of the pallet, L is the height or thickness of the pallet, V is the voltage across the pallet and I is the current flowing through pallet.

The variation in dc electrical resistivity of the ferrites can be explained on the basis of Verwey hopping mechanism [8]. According to it, the electrical conduction in ferrites is due to the hopping of electrons between the ions of same element but of different valence states present at the octahedral sites. The conduction in ferrites is the result of hopping of electrons between Fe^{3+} and Fe^{2+} ions present at octahedral sites. Beside this, the presence of Ni^{3+} ions, if any, at the octahedral sites may also make a small contribution to the conductivity. The occurrence of small percentage of Fe^{2+} and Ni^{3+} ions in the Ni-Zn ferrites may result either due to sintering or the electron exchange between Fe^{3+} and Ni^{2+} [10]. As both Fe^{2+} and Ni^{3+} ions have a strong preference for occupying the octahedral sites, therefore, they favors conduction process and hence the resistivity decreases with the increase in their concentration in the samples.

For ferrites, resistivity varies from 10^{-2} ohm-cm to 10^{11} ohm-cm at room temperature depending on chemical composition of the material [11]. Generally, the electrical resistivity of ferrites decreases with the increase of temperature, which shows that ferrites have semiconductor like behavior. Their resistivity varies with temperature according to Arrhenius Equation [7] given by Equation 6.3.

$$\rho = \rho_o e^{(\frac{\Delta E}{KT})} \qquad 6.3$$

Where, ρ is the resistivity at a particular temperature, ρ_o is temperature dependent constant of the material, T is the absolute temperature, K is the Boltzmann constant and ΔE is activation energy. It is the energy needed to release an electron from an ion to jump to the neighboring ion, giving rise to the electrical conductivity.

In general, increase in temperature of the sample, increases the mobility of the carriers which gives rise to the hopping of charge carriers between the equivalent lattice sites and hence the resistivity decreases. Sometimes, especially in nanoparticles, a change in slope or peak or cusp in Arrhenius plot is noticed and is attributed to different conduction mechanisms [5]. The dc resistivity of the sintered samples decreases with the increase in sintering temperature and sintering time and, is attributed to increased Fe^{2+} ions that are produced during sintering process. The increasing value of density and average grain size with the increase in sintering temperature also lowers the resistivity [8]. The evaporation of zinc with the increase in sintering temperature and time is also another factor that increases the presence of Fe^{2+} contents, which decreases the resistivity [12].

The temperature dependent mobility affects the conductivity in ferrites whereas the carrier concentration is almost unaffected by the temperature variation. In ferrites, the cations are surrounded by close pack oxygen anions and at first approximation can be treated as isolated from each other. The direct overlap of the 3d wave function between the neighboring metal ions is relatively small [10] and hence the isolated electron model is more appropriate for ferrites than the collective electron band model. The few models that have been suggested to account for the electrical properties of ferrites are given below.

6.2.1 Hopping model of electrons

G.H. Jonker [13] has observed in cobalt ferrite that the transport properties differ considerably from those of normal semiconductors, as charge carriers are not free to move through the crystal lattice but jump from ion to ion. It was also noted that in this type of material the possibility exists of changing the valency of a considerable fraction of metal ions and especially that of iron ions. Assuming the number of contributing electrons to be equal to the number of Fe^{2+} ions and the number of holes to be equal to the number of Co^{3+} ions, Jonker has calculated from the resistivity data, extremely low values of mobilities $\mu_1=10^{-4}cm^2/V$ sec for electrons and $\mu_2=10^{-8}cm^2/V$ sec for holes. Further, even for samples with large concentration of Fe^{2+} and Co^{3+} ions, a fairly strong exponential dependence of resistivity on temperature was found. It was found that the temperature dependence of conductivity arises, only due to mobility and not due to number of charge carriers in the sample.

6.2.2 Small polaron model

A small polaron is created when an electron carrier becomes trapped at a given site due to the displacement of adjacent atoms or ions. The entire defect (carrier + distortion) then migrates by an activated hopping mechanism. Small polaron formation can take place in materials whose conduction electrons belong to incomplete inner (d or f) shell, which tends to form extremely narrow bands due to small electron overlap. The migration of small polaron requires hopping of both the electron and the polarized atomic configuration from one site to an adjacent one. If the hopping electron becomes localized due to interaction with phonon, then a small polaron is formed and the conduction is due to hopping motion of small polaron [13].

6.2.3 Phonon induced tunneling

Electrical properties of ferrites have been explained on the basis of tunneling of electrons amongst Fe^{2+} and Fe^{3+} atoms on B site. It has been assumed that the electrons which participate in the $Fe^{2+} \leftrightarrow Fe^{3+}$ + e exchange process are strongly coupled to the lattice and tunnel from one site to other due to a phonon induced transfer mechanism [13].

6.3 Thermoelectric Power

If temperature gradient between two ends of a semiconducting material is maintained, it gives rise to an e.m.f known as thermo e.m.f. It is also called as Seeback voltage. It is developed due to the diffusion of electrons or holes from hotter surface towards the colder surface [10]. It has been observed that the thermo e.m.f is proportional to absolute temperature difference between two surfaces of the sample and is given by Equation 6.4.

$$Vs = Q(T_2 - T_1) \tag{6.4}$$

$$Q = Vs/(T_2 - T_1) \tag{6.5}$$

Where, V_s is Seeback voltage, Q is called as Seeback coefficient or thermoelectric power, T_2 and T_1 are the temperatures of hot and cold surfaces respectively.

The Hall Effect and thermoelectric power studies are widely used in the interpretation of the conduction mechanism in semiconductors. However, in the case of low mobility semiconductors such as ferrites, it is sometimes difficult to measure the Hall Effect, in such cases the thermoelectric measurement is the only alternative [14]. Thermoelectric power depends upon the method of preparation, chemical composition, substitution of foreign ions, and distribution of cations among tetrahedral (A) and octahedral (B) sites [3]. In case of n-type semiconductor material the hot surface becomes positively charged, as it looses some of its electrons. The cold surface becomes negatively charged. Conversely in a p-type semiconductor, the hot surface becomes negative and the cold one positive. Thus type of conduction in a given semiconducting material can be readily determined from the sign of the thermo e.m.f.

6.4 Dielectric Constant (ε) and Dielectric Loss Tangent (tanδ)

The property dielectric constant determines the electrostatic energy stored per unit volume for unit potential gradient. It tells the degree to which a medium can resist the flow of charge. It describes a material’s ability to store charge when used as a capacitor dielectric. It is also defined as the ratio of the charge that would be stored with free space as the dielectric to that stored with the material in question as the dielectric [2]. In present study capacitances of the pellets were determined from the LCRQ meter and dielectric constant can be calculated using Equation 6.6.

$$\varepsilon = \frac{C \times t}{\varepsilon_o A} \qquad 6.6$$

Where C is the capacitance of the pellet in farad, t is the thickness of the pellet in meters, A is the cross-sectional area of the flat surface of the pellet and ε_o is permittivity for free space ($8.85 \mathrm{x} 10^{-12}$ F m^{-1}).

The angle (δ) between the vector for the amplitude of the total current and that for the amplitude of charging current is called the loss angle and is less than 90^o. The tangent of this angle is the loss tangent or dissipation factor or dielectric loss tangent, which is used as a measure of dielectric loss factor. The relation between the dielectric constant and dielectric loss factor is given by Equation 6.7.

$$\tan\delta = \frac{\varepsilon''}{\varepsilon'} \tag{6.7}$$

Where, ε' is the measured dielectric constant of the dielectric material in the capacitor and it is a real part of complex permittivity and ε'' is the loss factor being the imaginary part of complex permeability.

The value of dielectric constant depends upon the polarization produced in the material. The polarization is defined as the induced dipole moment per unit volume. There are four types polarization observed in dielectric material.

A dielectric consists of a large number of atoms. If a dielectric material consists of only one atom, its nucleus is at the center while the electrons are revolving around the nucleus. On the application of the external electric field, its nucleus moves away from the field while the electrons move towards the field. As a result, a displacement is produced between the nucleus and the electrons. This displacement creates induced dipole moment and hence polarization. The polarization produced due to the displacement of electrons is known as electronic Polarization ($\mathbf{P_e}$).

When an electric field is applied to an ionic crystal, the polarization produced in it is due to the displacement of negative ions towards the field while the positive ions moving away from the field. This kind of polarization is known as atomic or ionic polarization ($\mathbf{P_i}$).

On the application of an electric field to a polar molecule, the dipoles experience a torque and try to align parallel to the applied field, which results to the rotation of the dipoles and produces dipolar or oriental polarization ($\mathbf{P_o}$).

If a dielectric medium is placed between two electrodes, in the absence of electric field, the positive and negative charges are not separated. On the application of an external electric field, the charges are separated. As a result, the positive charges are gathered near the negative electrode and give rise to a dipole moment. This induced dipole moment per unit volume is known as interfacial polarization or space charge polarization ($\mathbf{P_s}$) [15].

The space charge polarization occurs at very low frequencies less than 10^2 Hz. It refers to the diffusion of metal ions over several inter-atomic spacing. It also appears in machines having frequencies between 50 to 60 Hz. It is one of the slowest processes as compared to other types of polarizations. It is very small and is negligible as compared to other types of polarizations. The orientation polarization appears in the polar molecules under the application of ac field. Its mechanism is faster than space charge polarization but slower than the ionic and electronic polarizations. Its frequency range is less than 10^7 Hz. The ionic polarization exists in ionic molecules having frequency less than 10^{13} Hz. Ionic polarization cannot appear in optical frequencies ($\sim 10^{15}$ Hz) as the ionic molecules require time of about 100 times greater than the frequency of the applied field. Ionic polarization is faster than space charge and orientation polarization but slower than the electronic polarization. Electronic polarization is the fastest polarization and appears immediately after the supply is switched on. It occurs even at optical frequencies [15].

The dielectric properties of ferrites are dependent upon the several factors including the method of preparation, chemical composition, grain size, grain structure, sintering conditions etc [2]. Dielectric properties of ferrites are extensively studied for different compositions, its variation with frequency of external applied ac electric field and at different measuring temperatures. The variation of dielectric constant can be explained using Maxwell and Wagner two layers model [5].

6.4.1 Maxwell-Wagner two layer model and Koop’s Theory

The variation of dielectric constant depends upon the variation of polarization with the change in frequency. The value of **ε** is very high at lower frequencies. It decreases with the increase in frequency. At very high frequency, its value is so small that it becomes independent of frequency. This variation in dielectric constant can be explained on the basis of Koop’s two layer model and Maxwell - Wagner polarization theory [16, 17, 18]. According to this model, space charge polarization is produced due to the inhomogeneous structure of the dielectric material i.e dielectric material is made of higher conductivity phases (grains) in the insulating matrix (grain boundaries). An externally applied ac electric field produces localized accumulation of charge at the boundary of the grains. If the resistivity of the grain boundary is high enough, the electrons are piled up at the grain boundaries and produces polarization. The assembly of space charge carriers in a dielectric takes a finite time to line up their axes parallel to an alternating electric field. If the frequency of the field reversal increases, very small number of charge carriers can reach the grain boundary, as a result charge carriers cannot keep up with the field and the alternation of their direction lags behind that of the field [5]. This decrease in charge carriers at the grain boundaries results in the reduction of polarization at grain boundaries and hence the decrease in dielectric constant of the material. As the frequency of the field continue to increase, at some stage the space charge carriers will start to move before the field reverses, with no contribution to the polarization of the dielectric.

I. T. Rabinkin et al. [19] pointed out that polarization in ferrites is a process similar to that of conduction. The electron exchange between $Fe^{2+} \leftrightarrow Fe^{3+}$ resulting in the local displacement of electrons in the direction of the applied field, determines the polarization. Polarization decreases with the increase in frequency and then reaches a constant value. It is due to the fact that beyond a certain frequency of external field, the electron exchange $Fe^{2+} \leftrightarrow Fe^{3+}$cannot follow the alternating field. The dielectric constant has large value at lower frequency. It is because of the predominance of species like Fe^{2+} ions, oxygen vacancies, grain boundary defects, interfacial dislocation pile ups, voids etc [18]. The decreasing trend in dielectric constant with the increase in frequency is natural due to the fact that any species contributing to polarizability keeps lagging behind the applied field at higher frequencies [20].

6.5 Sample Preparation and Experimental Work

The sample preparation carried out to measure the dc resistivity, thermoelectric power, dielectric constant and dielectric loss tangent, and various parameters selected to measure these electrical properties in the present work is given below.

6.5.1 DC resistivity measurements

The pallets of nano and bulk samples were coated on both sides with silver paste to provide good electrical contacts with the electrodes. The dc resistivity measurements were done using standard two probe (two electrodes) method. A constant voltage of 2 volts was maintained across the electrodes containing the pallet with current measured using Keithley electrometer. The readings were recorded in step of 5^{o}C in the range of room temperature to 500^{o}C. The resistivity of the sample was calculated using Equation 6.1 and 6.2.

6.5.2 Thermoelectric power measurements

Similar pallets were used in the thermoelectric power measurements. The thermoelectric power measurements are done using standard set up. The temperature of both the faces of the sample was measured using thermocouple equipped with temperature sensor. The thermo e.m.f across the pallet was measured in step of 5^{o}C in the range of room temperature to 350^{o}C. The thermoelectric power of the samples was calculated using Equation 6.4.

6.5.3 Dielectric measurements

All the dielectric measurements were carried out using LCRQ meter (Wayne Kerr 6440B precision component analyzer setup) by inserting silver coated pallet of the sample between a disc and pointer shape sample holder. The values of capacitance and loss factor at room were recorded for all the samples in the frequency range of 20 Hz to 3 MHz. Similarly, the values of capacitance and loss factor as a function of temperature were recorded in step of 5^{o}C in the range of range of 30^{o}C to 495^{o}C for few selected frequencies out of F=20 Hz, 100 Hz, 500 Hz, 1 KHz, 10 KHz,100 KHz, 500 KHz, 1 MHz, 2 MHz and 3 MHz. The dielectric constant was calculated using Equation 6.6.

6.6 Results and Discussion

6.6.1 DC resistivity of nano $Ni_xZn_{1-x}Fe_2O_4$ samples

The plots of log ρ vs. 1000/T of nano $Ni_xZn_{1-x}Fe_2O_4$ samples are shown in Fig. 6.1. It can be seen that the resistivity for all the samples decreases with increasing temperature according to the Equation 6.3. All the samples are showing semiconductor like behavior. However the band theory, which explains the conduction in semiconductors, is not suited for ferrite. The conduction in ferrites is explained on the basis of polaron hopping mechanism [10].

The variation in resistivity curve can be divided in to three temperature regions. Region (I) is in the relatively lower temperature range up to 400K (~125°C). In this region resistivity does not exhibit much variation with temperature, but minor increase in resistivity with temperature is noted. In present work noticeable maxima

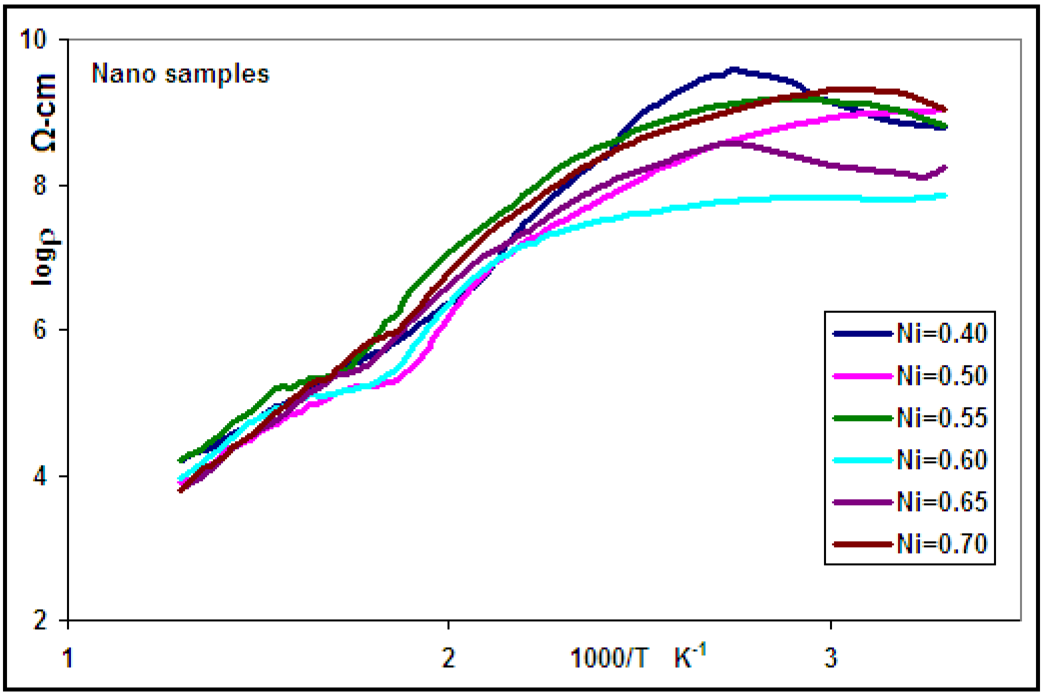

Fig. 6.1 Plot of logρ versus 1000/T of nano $Ni_xZn_{1-x}Fe_2O_4$ samples.

or peak in this region can be seen for Ni=0.40 and Ni=0.65. The other composition showed comparatively less increase in resistivity. This increase is associated with the impurity scattering [21]. The conduction phenomenon in this region is mostly attributed to scattering of charge carriers by lattice vibrations, impurities in the sample, presence of lattice defects (defects are having smaller mobility), voids and high resistive grain boundaries or existence of resonant phonon modes [7]. This may be partially attributed due to moister or water absorption as reported by B. Baruwati et al. [24]. Javed Iqbal et al. also reported that the cause of the observed metallic type behavior at low temperatures is due residing of absorbed water vapor in the inter-granular pores of the samples [6].

The region (II) was observed in the temperature range around 400K to 675K (125^{o}C to 400^{o}C). In this region resistivity decreases with increase in temperature and the conduction phenomenon is attributed to the thermally activated mobility of the charge carriers. The change in slope of the curve was also found in this region. The small dip or cusps in the curves causing change in the slope can be clearly seen in Fig. 6.1. This change is related to the magnetic transition from ferrimagnetic to paramagnetic state and corresponding temperature to the Curie point ($\mathbf{T_c}$) of the sample. The magnified view of the cusps in the resistivity curves observed for nanoparticle samples are shown in Fig. 6.2 and corresponding $\mathbf{T_c}$ is given in Table 6.1. The obtained $\mathbf{T_c}$ is in good agreement with the results from Ac susceptibility measurements. Similar T_c measurements were reported by Shrinivasan et al. [23] and A. D. Sheikh et al. [24] in Ni-Zn ferrites and Rezlescu et al. [25] in Li-Zn ferrites.

In region (III) for temperature range T>673K (400^{o}C), the resistivity decreases rapidly with temperature (above **T$_c$**). This decrease in resistivity is mainly associated to the increase in thermally activated drift mobility of the charge carriers in accordance with the hopping conduction model [10]. The higher temperature region above **T$_c$** is corresponding to a paramagnetic disordered region with comparatively high activation energy [10].

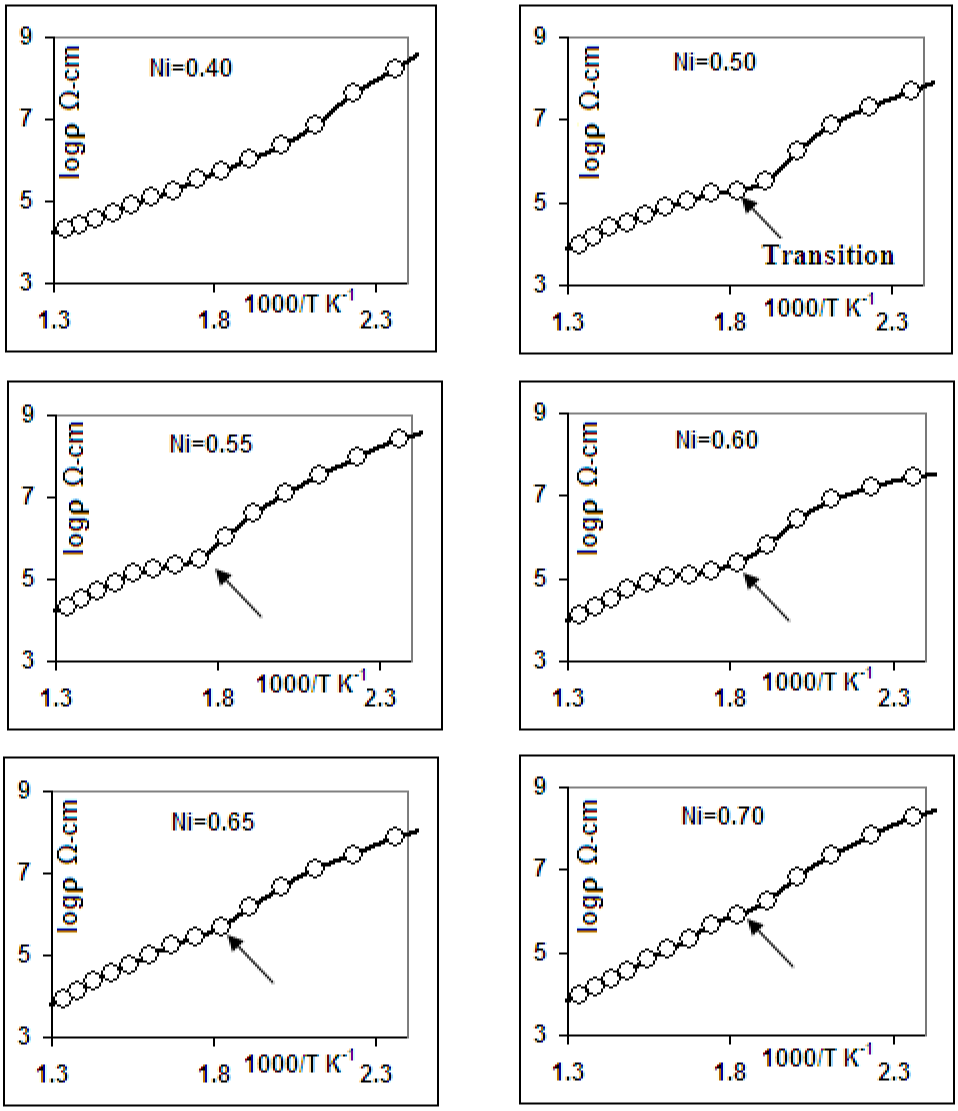

Fig. 6.2 Magnified view (near cusps) of the logρ versus 1000/T curves of nano $Ni_xZn_{1-x}Fe_2O_4$ samples.

Table 6.1 Curie temperatures (**T_c**) of nano $Ni_xZn_{1-x}Fe_2O_4$ samples obtained from dc resistivity curves.

Ni (x)	T_c (in ^oC)
0.40	265
0.50	305
0.55	365
0.60	370
0.65	330
0.70	335

The conduction process in Ni-Zn ferrites can be explained by the Verwey-de-Boer mechanism, in which, electron exchange is taking place between the ions of the same element present in more than one valence state [7]. We have found from thermoelectric power measurements, that all the samples in the present work shows n-type behavior in lower temperature region and p-type behavior in higher temperature region. Thus both types of charge carriers i.e. electrons and holes are taking part in the conduction process. The conduction mechanism for Ni-Zn ferrite in the present work may lead to the following hopping mechanism [10] $Ni^{2+} + Fe^{3+} \Leftrightarrow Ni^{3+} + Fe^{2+}$. In the case of n-type conduction, the hopping of electron takes place from Fe^{2+} to Fe^{3+}ions i.e $Fe^{3+} + e \Leftrightarrow Fe^{2+}$. In case of p-type conduction the transfer of hole from Ni^{3+} to Ni^{2+}ions is taking place i.e $Ni^{2+} + h \Leftrightarrow Ni^{3+}$.

From Fig. 6.3 it can be seen that room temperature resistivity increases with increase in Ni content up to 0.50 and also from Ni=0.60 to 0.70. This increase in resistivity with increase in Ni content can be explained on the basis of site occupation of different ions. It is reported that Zn ions prefer the occupation of tetrahedral (A) sites, Ni ions prefer the occupation of octahedral (B) sites while Fe ions partially occupy the A and B sites. As Ni concentration increases, Ni content at B sites increases, the Zn ion concentration (at A sites) will decrease. This will lead

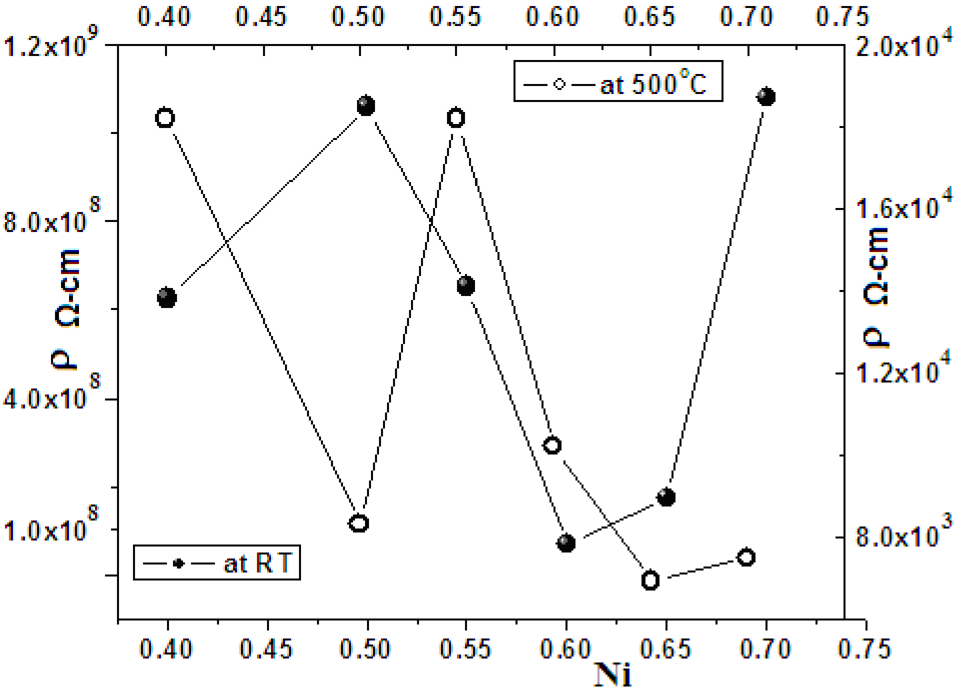

Fig. 6.3 Varition of resistivity at room temperature (LHS scale) and at 500°C (RHS scale) of nano $Ni_xZn_{1-x}Fe_2O_4$ samples.

to the migration of some Fe^{3+} ions from B to A sites to substitute the increase in Ni ion concentration at B sites. As a result, the number of $Fe^{2+}$and Fe^{3+}ions at B sites (which is responsible for electric conduction in ferrites) decreases. Consequently, resistivity increases with increasing Ni content [8, 26, 27].

However, the observed decrease in resistivity as Ni increases from 0.50 to 0.60 may be attributed to the higher influence of their porosity on resistivity compared to that of Ni content in samples. As the porosity decreases, the number of pores or vacancies, and consequently the scattering centers for charge carriers, decreases, and therefore the electrical resistivity decreases [28]. It was found that porosity decreases from 26% for Ni=0.50 to 22% for Ni=0.55 and same was increases from 25% for Ni=0.60 to 30% for Ni=0.70. Hence, intermediate decrease in resistivity is attributed to decrease in porosity of the samples. The lowering of resistivity from Ni=0.50 to 0.60 may also be explained on the basis of the decrease in the lattice strain because of the lower ionic radius of Ni compared to that of Zn ion [29].

It can be seen that, resistivity at 500°C deceases as Ni content increases up to 0.50, increases for 0.55 and follows decrease for 0.55 to 0.65 with marginal increase again at 0.70. The variation in resistivity at 500°C with Ni content can be explained on the similar lines as above. It is well known that the resistivity of ferrites depends upon the ratio of Fe^{3+}/Fe^{2+}. Since this ratio decreases with the increase of Ni content, then the resistivity should exhibit a continuous increase with increasing Ni content. However, such a continuous increase in resistivity at both room temperature and 500°C was not observed for the samples. Therefore, other factors such as porosity and grain sizes of each sample have to be considered individually [21].

The room temperature resistivity of nano samples varies in the range of $6.85x10^7$ ohm-cm (for Ni=0.60) to $1.08x10^9$ ohm-cm (for Ni=0.70). The observed room temperature resistivity is three orders higher than the resisitivity of order of 10^6 ohm-cm reported by Parvatheeswara Rao et al. [30], Naik and Powar [31], Jain et al. [32] and Rezlescu et al. [33] for Ni–Zn ferrites prepared by conventional ceramic method. The room temperature resistivity in present study is also one order higher than reported by A. Verma et al [8] for Ni-Zn ferrite prepared by citrate precursor method. This high resistivity in the present samples is attributed to the nano size and method of preparation of the samples. It has been found that resistivity of polycrystalline material in general increases with decreasing grain size. Smaller grains imply larger number of insulating grain boundaries, which act as barriers to the flow of electrons. Also smaller grains imply smaller surface contact area between adjacent grains and hence there is a reduced electron flow and leads to increase in resistivity.

The significantly higher values of resistivity obtained in the present investigation compared to those obtained for Ni-Zn ferrites prepared by the conventional ceramic method and citrate precursor method are attributed to the reduction in Fe^{+2} content of the ferrite and obtaining more uniform structures and compositions [8]. This shows that the method employed in present investigation shows promising results for preparing high performance ferrites suitable for high frequency applications where eddy current losses are of paramount concern. The higher values of resistivity suggest that Ni-Zn ferrites processed by nitrilotriaccetate route could be used at frequencies much higher than at which the conventionally prepared ferrites could be used.

6.6.2 DC resistivity of bulk $Ni_xZn_{1-x}Fe_2O_4$ samples

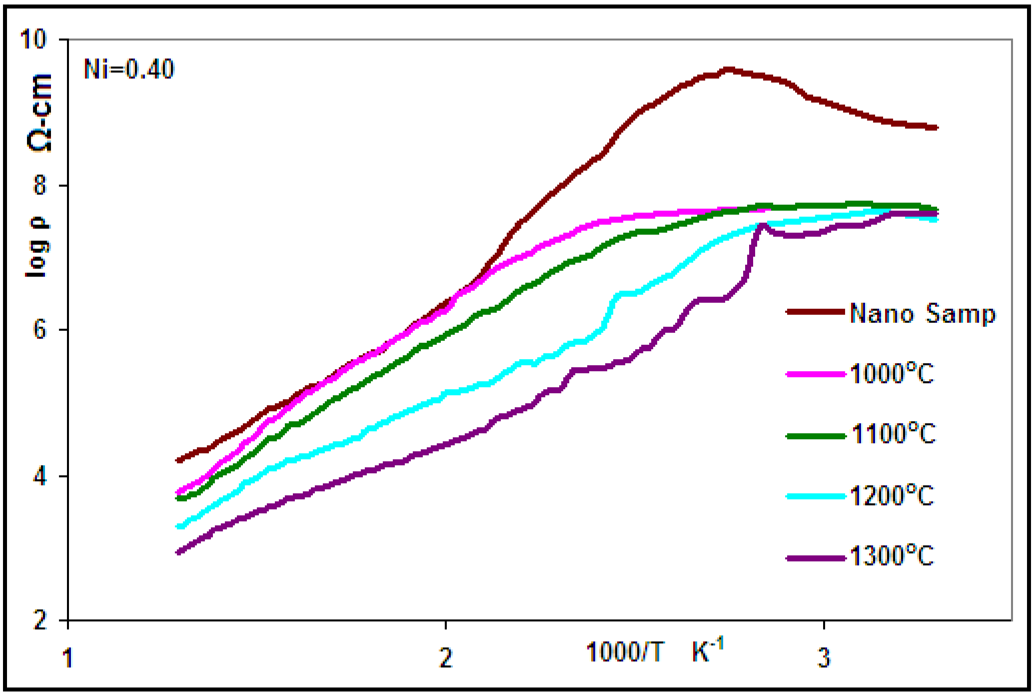

Fig. 6.4 Plot of logρ versus 1000/T of nano and bulk $Ni_{0.40}Zn_{0.60}Fe_2O_4$ samples.

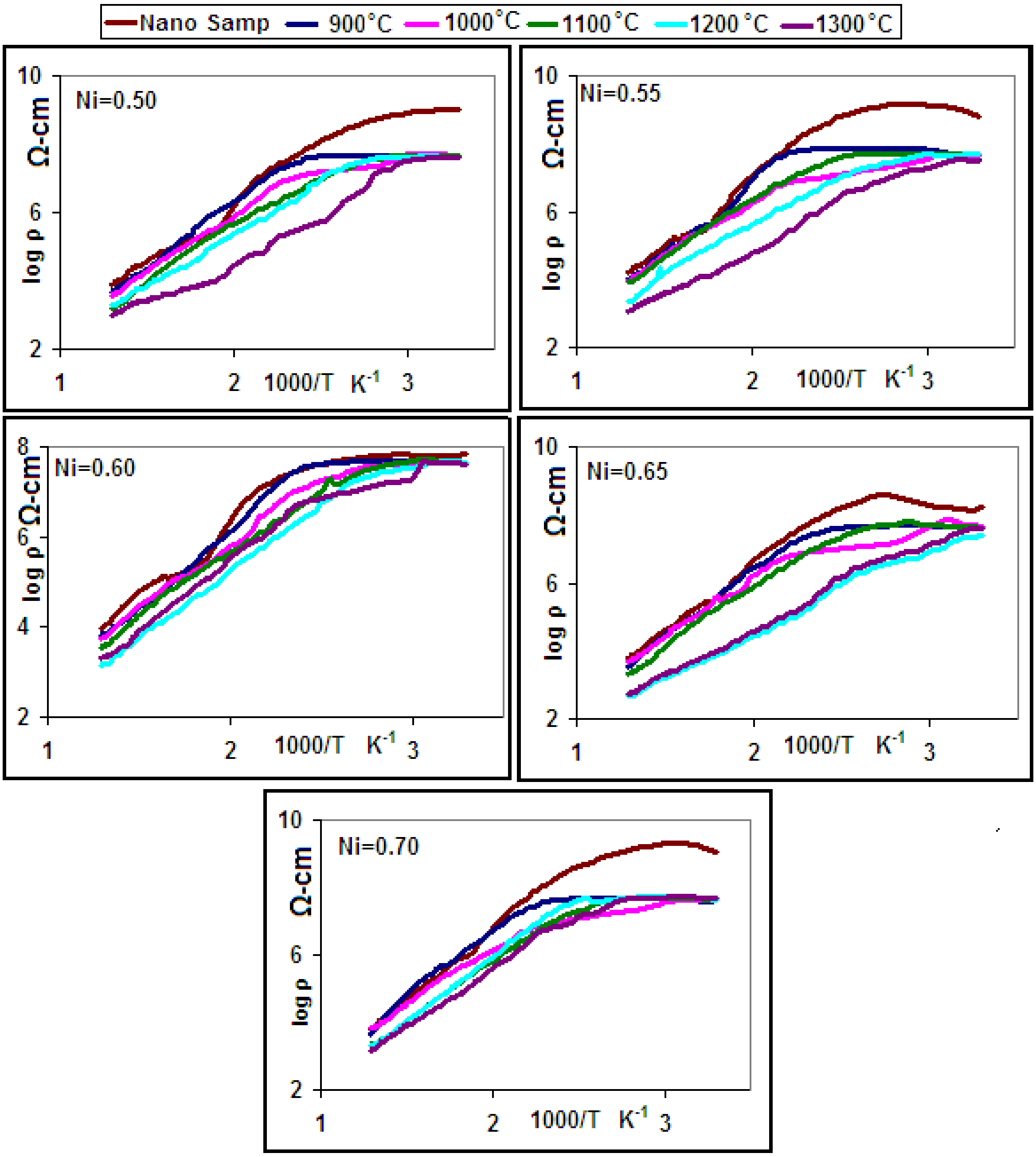

Fig. 6.5 Plot of logρ versus 1000/T of nano and bulk $Ni_xZn_{1-x}Fe_2O_4$ samples.

Fig. 6.4 and 6.5 show variation of logρ with 1000/T of nano and bulk $Ni_xZn_{1-x}Fe_2O_4$ samples. It can be noted that, like nano samples, the resistivity of all the bulk samples decreases with increasing temperature and are showing semiconductor like behavior. However, the resistivities of the bulk samples are lower by one or two orders than that of nano samples. This decrease in resistivity of bulk samples may be explained as follows. Normally, grain size increases with increase in sintering temperature which increases the probability of Fe^{2+} formation and hence increases hopping between Fe^{2+} and Fe^{3+} ions resulting into decrease in resistivity [12]. The formation of Fe^{2+} ions may be expected owing to the evaporation of Zn ions during the sintering process. Also, Ni^{3+} ions are formed when ferrites are cooled from the sintering temperature, due to absorption of oxygen.

R.V. Mangalaraja et al. [12] reported that resistivity is inversely proportional to grain size. As sintering temperature increases, due to the reduced porosity, the individual grains come closer and an effective area of grain-to-grain contact increases. Hence conduction mechanism is enhanced and resistivity of the samples is reduced. In general the values of density, grain diameter and weight percentage of Fe^{2+} concentration are found to increase with increase of sintering temperature.

A cusp or kink or dip or change in slope was also observed in the resistivity curves of bulk samples, however, they were not significantly noticeable as in nano samples. The T_c obtained from the change of slope or cusps observed in the resistivity curves of the bulk samples are given in Table 6.2. Some of the results are in good agreement with the T_c obtained from Ac susceptibility and permeability measurements.

Table 6.2 Curie temperatures (**T_c**) of bulk $Ni_xZn_{1-x}Fe_2O_4$ samples obtained from dc resistivity curves.

Ni	Curie temperatures T_c (in ^oC) at various sintering temperatures			
	1000^{o}C	1100^{o}C	1200^{o}C	1300^{o}C
0.40	335	300	200	165
0.50	340	230	265	235
0.55	330	270	225	205
0.60	330	265	170	200
0.65	300	266	166	164
0.70	305	265	200	205

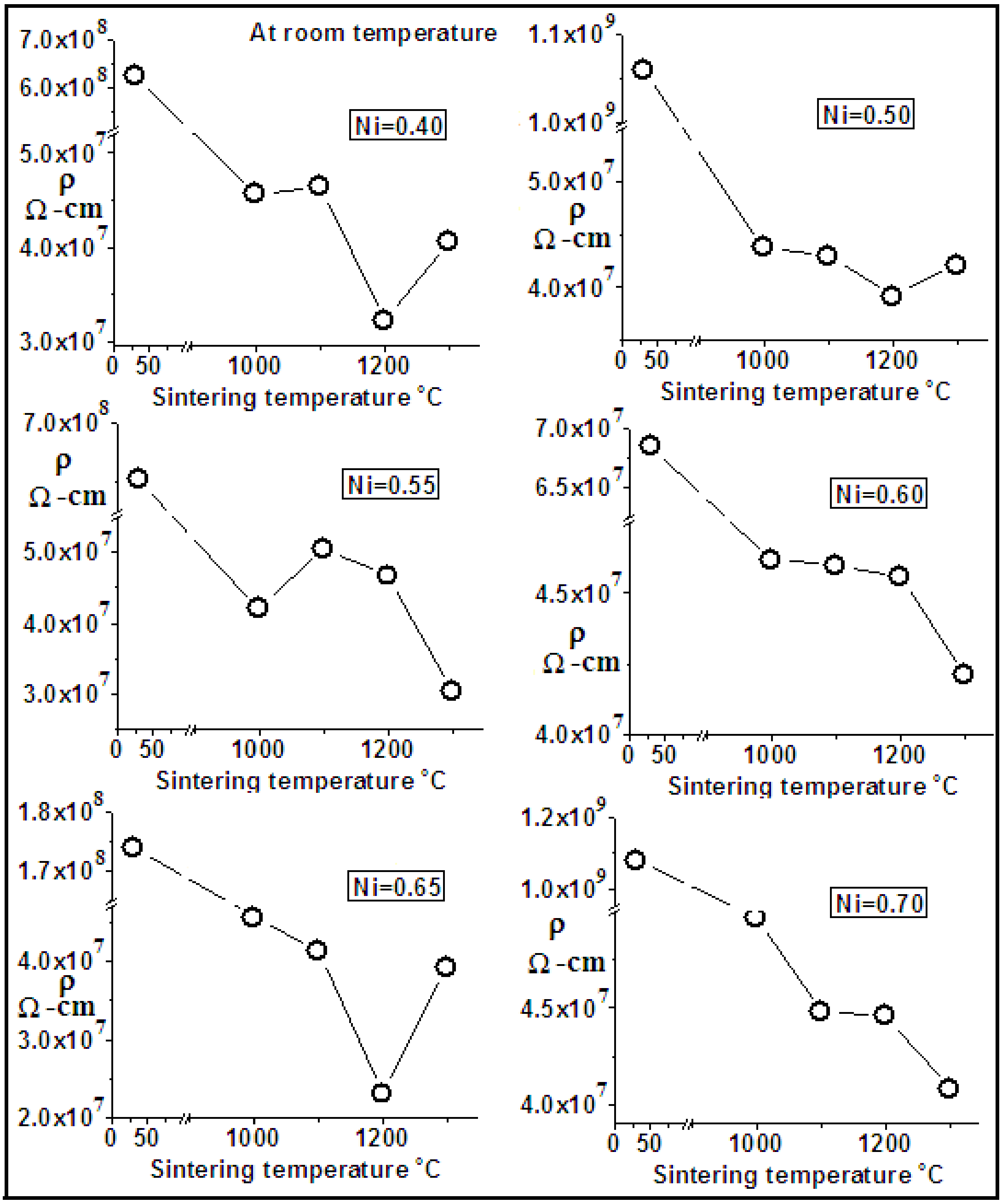

Fig. 6.6 Variation of room temperature resistivity of bulk $Ni_xZn_{1-x}Fe_2O_4$ samples with sintering temperature. (Resistivity of nano samples are provided for comparison).

The variations of room temperature resistivity of bulk samples with sintering temperature, along with resistivity of nano samples for comparison are shown in Fig. 6.6. Apart from the normal decease in resistivity with increasing sintering temperature for most of the bulk samples, we found few exceptional cases categorized on the basis of Ni content in the samples. For Ni=0.40, resistivity at

1100^{o}C is more than at 1000^{o}C as well as resistivity at 1300^{o}C is more than at 1200^{o}C. For Ni=0.50 resistivity at 1300^{o}C is more than at 1200^{o}C and in case of Ni=0.55 resistivity at 1100^{o}C and 1200^{o}C is more than at 1000^{o}C. For Ni=0.65 resistivity at 1300^{o}C is more than at 1200^{o}C and for Ni=0.70 resistivity at 1200^{o}C is more than at 1100^{o}C. This reverse trend of having higher resistivity at higher sintering temperature observed in the above compositions indicates that the influence of micro structure is more significant than that of the anticipated effect of the grain size [8]. A similar trend in resistivity was reported by Van Uitert [34], explaining such variations in terms of increased homogeneity and structural perfection with increase in sintering temperature. In present work the exceptional cases may be attributed to the possibility of having more uniform crystal structures with reduced imperfections at higher sintering temperatures thereby increasing the sample resistivity [8].

If grain growth is small for a given sample at any sintering temperature, there is a possibility of re-oxidation of Fe^{+2} to Fe^{+3} during cooling after sintering process, as the diffusion of oxygen advances more rapidly in small grains than in the larger ones. This re-conversion of Fe^{+2} to Fe^{3+} improves ferrite stoichiometry and consequently increases the resistivity [12, 35, 8]. So exceptions observed in the resistivity in present work can also be related to re-conversion of Fe^{+2} to Fe^{3+} during cooling process.

The variations in resistivity at 500^{o}C of the bulk samples with sintering temperature, along with resistivity of nano samples for comparison are shown in Fig. 6.7. Normal decease in resistivity with increasing sintering temperature was observed apart from few exceptional cases as follows. For Ni=0.50 resistivity at

1200°C is higher than at 1100°C similarly in case of Ni=0.60 resistivity at 1300°C is higher than its value at 1200°C, whereas, for Ni=0.65 resistivity at 1300°C is higher than its value at 1200°C. This reverse trend may be attributed to the significant influence of micro-structure and porosity compared to that of the anticipated effect of the grain size [8].

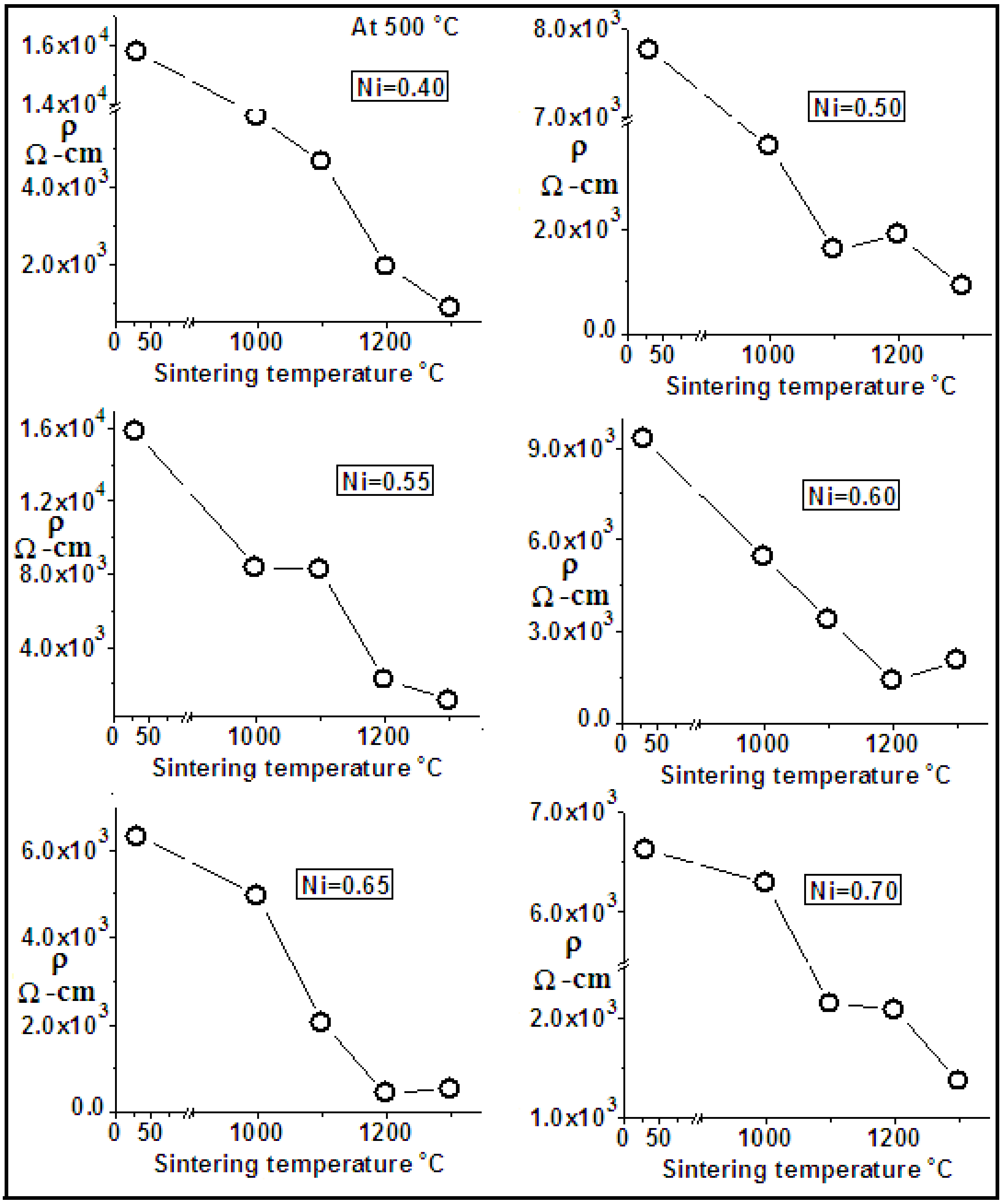

Fig. 6.7 Variation of resistivity at 500°C of bulk $Ni_xZn_{1-x}Fe_2O_4$ samples with sintering temperature. (Resistivity of nano samples are provided for comparison).

At sintering temperature of 1000^oC, the bulk sample with Ni=0.40 showed maximum resistivity, whereas, at 1100^oC, the maximum resistivity was observed for Ni=0.50. At sintering temperature of 1200^oC and 1300^oC the maximum resistivity was observed for Ni=0.70. For comparison, $Ni_{0.3}Zn_{0.70}Fe_2O_4$ sample prepared via standard ceramic method and sol gel method, sintered at 1250^oC for 4h in air shows resistivity of $1.8x10^4$ ohm-cm and $4.5x10^5$ohm-cm respectively [12]. Whereas, in present work the highest resistivity of $4.8x10^7$ ohm-cm (sintered at 1200^oC for 4 hr in air) was found for $Ni_{0.55}Zn_{0.45}Fe_20_4$. The two orders higher value of resistivity in present study can be attributed to the method of sample preparation.

6.6.3 Thermoelectric power

The thermoelectric power or Seeback coefficient of all the $Ni_xZn_{1-x}Fe_2O_4$ samples (nano and bulk) was measured in the temperature range of room temperature to 350^oC. Fig. 6.8 shows thermal variation of thermoelectric power of nano $Ni_xZn_{1-x}Fe_2O_4$ samples. It can be seen that all the compositions have negative thermoelectric power at room temperature. The negativity of the thermoelectric power goes on decreasing with increasing temperature and gets converted into positive value at higher temperatures. Similar, nature was also observed for all the bulk samples.

Fig. 6.9 shows thermal variation of thermoelectric power of bulk $Ni_{0.55}Zn_{0.45}Fe_2O_4$ sample at sintering temperature of 1000^oC, 1100^oC, 1200^oC and 1300^oC. It can be seen that, the samples show n-type semiconductor behavior in lower temperature region and p-type semiconductor at higher temperature region.

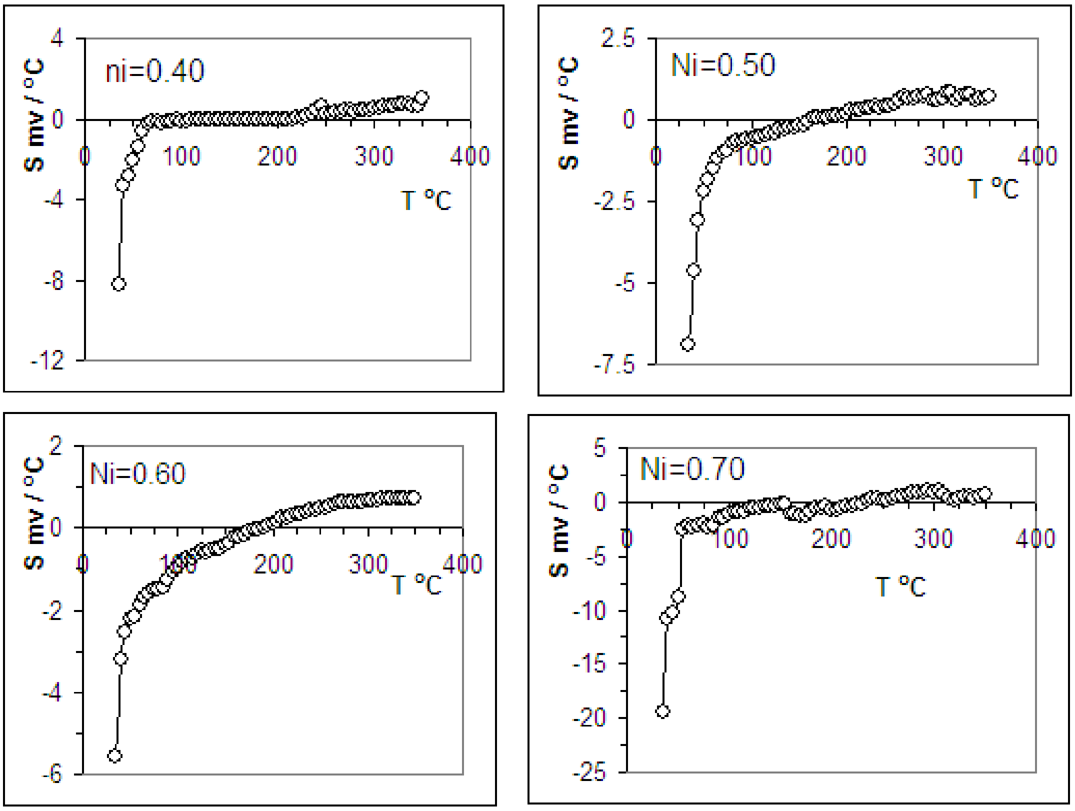

Fig. 6.8 Variation of thermoelectric power with temperature of nano $Ni_xZn_{1-x}Fe_2O_4$ samples.

The conduction mechanism in n-type specimens is predominantly due to hopping of electrons from Fe^{+2} to Fe^{+3} ions and the conduction mechanism in p-type semiconductor is due to transfer of hole from Ni^{+3} to Ni^{+2} ions [10]. The occurrence of n to p transition supports the changes in concentration of Fe^{2+} or oxygen ions in the samples and further predicts the conduction is due to hopping mechanism [14].

The nano sample with Ni=0.40 in Fig. 6.8 and bulk sample with Ni=0.55 at sintering temperature of 1200°C and 1300°C in Fig. 6.9, shows that thermoelectric power at higher temperature remains independent of temperature. This is attributed to degenerate semiconductor behavior of these samples at higher temperature (intrinsic range) and non-degenerate semiconductor behavior at lower temperature (extrinsic range) [36]. The minor cusp can be noticed at relatively low temperature

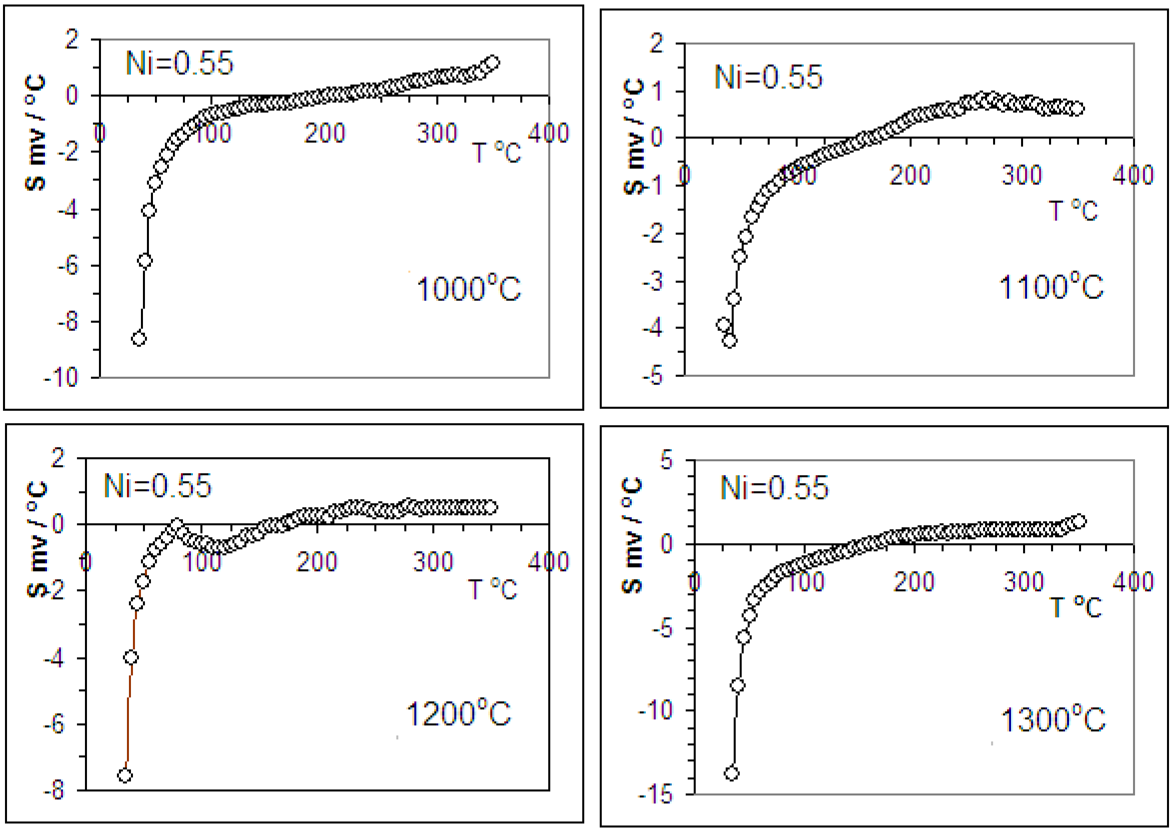

Fig. 6.9 Variation of thermoelectric power with temperature of bulk $Ni_{0.55}Zn_{0.45}Fe_2O_4$ samples.

Table 6.3 Transition temperatures $\mathbf{T_{(n-p)}}$ of nano and bulk $Ni_xZn_{1-x}Fe_2O_4$ samples.

Ni=x	Transition temperature $T_{(n-p)}$ at various sintering temperatures				
	Nano Samples	1000 °C	1100 °C	1200 °C	1300 °C
0.40	220	240	100	165	245
0.50	150	165	130	159	270
0.55	190	205	165	172	265
0.60	200	155	155	115	185
0.65	145	290	180	165	210
0.70	210	200	185	170	175

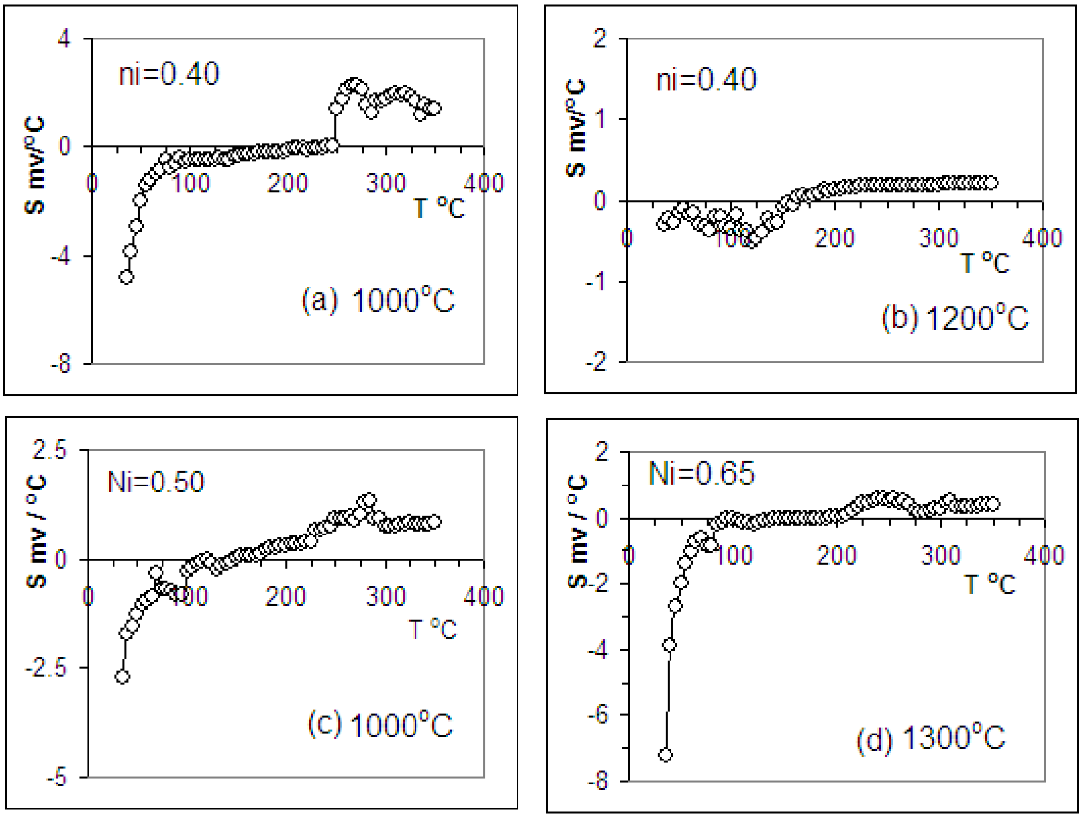

Fig. 6.10 Variation of thermoelectric power with temperature of bulk $Ni_xZn_{1-x}Fe_2O_4$ samples (a) Ni=40 at 1000^{o}C, (b) Ni=40 at 1200^{o}C (c) Ni=0.50 at 1000^{o}C and (d) Ni=0.65 at 1300^{o}C.

<80^{o}C, for nano samples (Ni=0.60 and Ni=0.70) in Fig. 6.8. These cusps are associated with the impurity scattering or electron–phonon scattering and its effect was also noticed in the dc resistivity measurements [21, 37]. Table 6.3 provides the transition temperature $T_{(n-p)}$ of each sample at which the thermoelectric power changes from negative to positive. The temperature $T_{(n-p)}$ varies in the range of 100^{o}C (for Ni=0.40 sintered at 1100^{o}C) to 290^{o}C (for Ni=0.65 sintered at 1000^{o}C).

The thermal variations of thermoelectric power of bulk sample (a) Ni=40 sintered at 1000^{o}C, (b) Ni=40 sintered at 1200^{o}C (c) Ni=0.50 sintered at 1000^{o}C and (d) Ni=0.65 sintered at 1300^{o}C are shown in Fig. 6.10. These bulk samples (a), (b), (c) and (d) showed peaks at 300^{o}C, 130^{o}C, 285^{o}C and 250^{o}C respectively. Such peaks are also reported by D. Ravinder et al. [38] for Ni-Zn ferrite and S. A. Mazen et al. [21] for copper ferrite. These peaks are attributed to magnetic transition from ferrimagnetic to paramagnetic state and the corresponding temperature can be related to Curie temperature of the samples [21]. Also in Fig. 6.10, minor cusp at relatively lower temperature ~80°C to 90°C due to impurity scattering or electron-phonon scattering can be seen for bulk sample (c) Ni=0.50 at 1000°C and (d) Ni=0.65 at 1300°C.

6.6.4 Dielectric properties

The variation of dielectric constant and dielectric loss of nano and bulk $Ni_xZn_{1-x}Fe_2O_4$ samples as a function of frequency, composition and temperature are studied in the present work.

6.6.4.1 Frequency dependence of dielectric constant (ε) of nano samples

The variations of dielectric constant (ε) with frequency of nano $Ni_xZn_{1-x}Fe_2O_4$ samples are shown in Fig. 6.11. It can be seen that ε decreases with the increase in frequency and ultimately attains a constant value at higher frequency for all the compositions. The value of ε is much higher at lower frequencies compared to at high frequencies. The variation of ε with frequency can be explained using Maxwell-Wagner two layers model of interfacial polarization [16, 17] along with Koop's phenomenological theory [18]. According to these models, ferrites are formed by large number of well conducting grains separated by thin poorly conducting intermediate grain boundaries that produces localized accumulation of charge under the influence of an electric field [39]. Such space charge carriers in a dielectric take a finite time to line up their axes parallel to an alternating electric

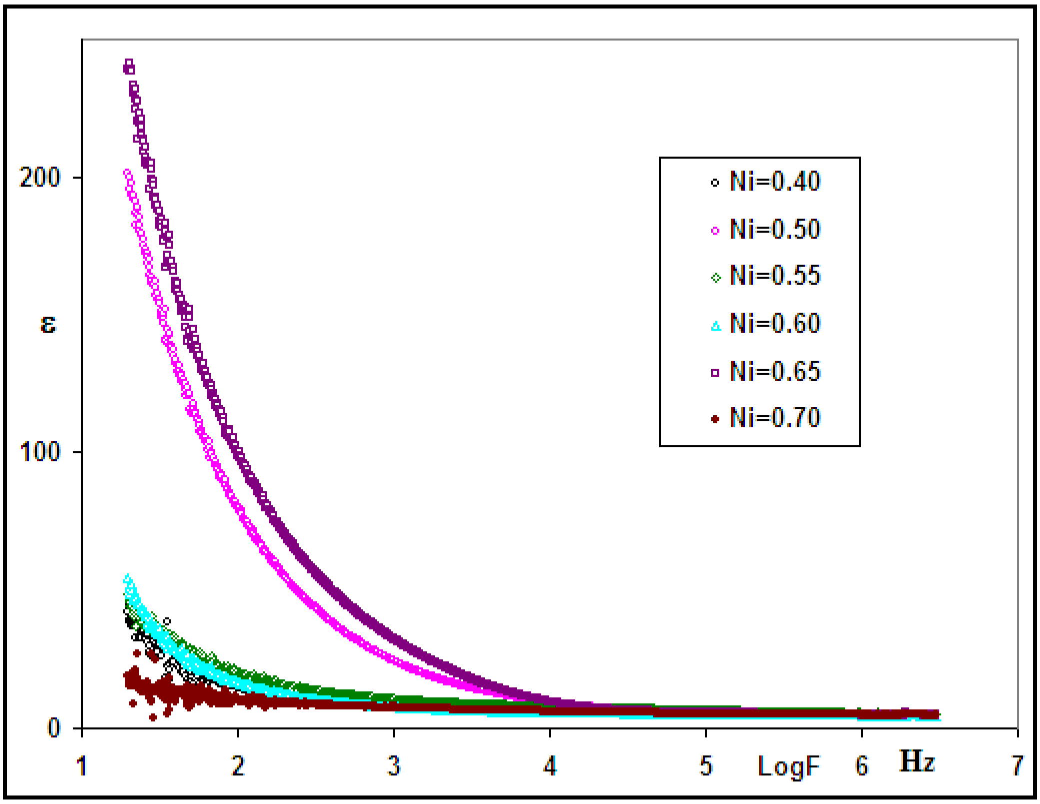

Fig. 6.11 Variation of dielectric constant (ε) with frequency of nano $Ni_xZn_{1-x}Fe_2O_4$ samples.

field. If the frequency of the field reversal increases, a point is reached where the space charge carriers cannot keep up with the field and the alternation of their direction lags behind that of the field. This results in a reduction of **ε** of the material at higher frequencies. Similar kind of variation in **ε** with the frequency is reported by Quin Chen et al. [40], A. D. Shaikh et al. [24], A. M. Shaikh et al. [41] and G. Sathishkumar et al. [42].

Rabinkin and Novikova [19] pointed out that the polarization in ferrites is a similar process to that of conduction. The electron exchange between $Fe^{2+} \leftrightarrow Fe^{3+}$ results in the local displacement of electrons in the direction of applied field and that in turn determines the polarization. Polarization decreases rapidly with the increase in value of frequency and then reaches a constant value due to the fact that beyond a certain frequency of external field, the electron exchange $Fe^{2+} \leftrightarrow Fe^{3+}$ cannot follow the alternating field. The large value of ε at lower frequency is attributed to the predominance of species like Fe^{2+} ions, oxygen vacancies, grain boundary defects, interfacial dislocation pile ups, voids etc [17, 20, 43]. In present work, the maximum ε of 239 (at 50 Hz) was obtained for sample with Ni=0.65, whereas, the minimum ε of 19 (at 50 Hz) was obtained for Ni=0.70.

6.6.4.2 Composition dependence of dielectric constant (ε) of nano samples

Fig. 6.12 shows variation of ε with composition of nano samples at frequency of 100 KHz and 1 MHz. It can be seen that ε increases as Ni concentration increases and attains peak at Ni=0.55 for both the frequencies. The ε also show second minor peak at Ni=0.65.

As we know in Ni-Zn ferrites, Zn ions prefer the occupation of tetrahedral (A) sites and Ni ions prefer the occupation of octahedral (B) sites, while Fe ions partially occupy the A and B sites. On increasing Ni content, its concentration at B site increases, this will lead to migration of some Fe ions from B sites to A sites to substitute the increase in Ni ions concentration at B sites. As a result, the number of ferrous and ferric ions at the B sites decreases so also, hopping between Fe^{3+} and Fe^{2+} ions decreases and hence the resistance of grains increases. This decreases the probability of electrons to reach the grain boundary. Consequently, polarization and ε both decreases [5]. Thus decrease in ε as Ni increases from Ni=0.55 to Ni=60 is well supported by the above theory. However, it can be seen that ε increases as Ni increases from 0.40 to 0.55. This reverse trend may be attributed to other factors such as level of porosity, density, voids and particle size distribution of individual

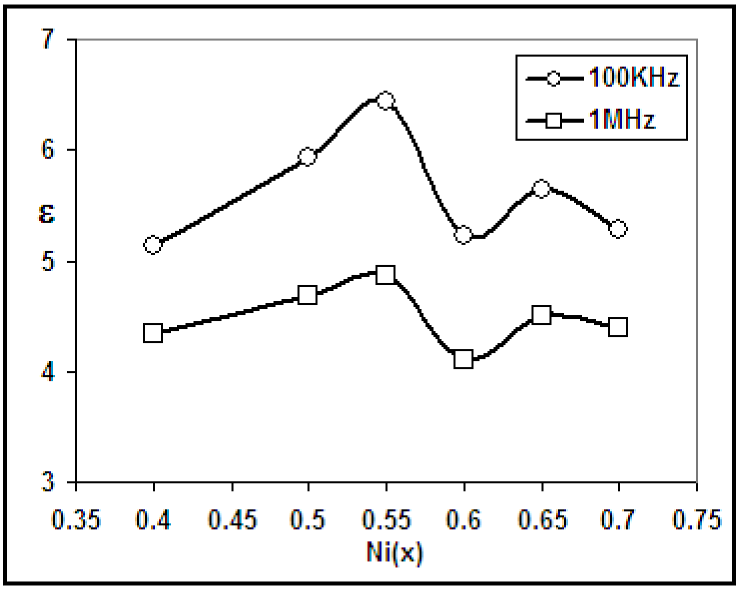

Fig. 6.12 Variation of dielectric constant with composition of nano $Ni_xZn_{1-x}Fe_2O_4$ samples at frequency of 100 KHz and 1 MHz.

nano samples [44]. It is reported that ε of ferrites also depend on the method of preparation [45].

It was found that density increases from 3.87 gm/cm^3 to 4.16 gm/cm^3 as Ni increases from Ni=0.40 to 0.50 and then decreases to 4.02 gm/cm^3 for Ni=0.60. At the same time porosity decrease from 27% to 22% as Ni increases from Ni=0.40 to 0.50 and then increases to 25% at Ni=0.60. Also XRD analysis shows micro strain decreases from 5.9x10^{-4} to 3x10^{-4} as Ni increases from Ni=0.40 to 0.50 and than increases to 5.9x10^{-4} for Ni=0.60. The TEM grain size distribution showed that particle size distribution of Ni=0.40 varies in the range of 30 nm to 40 nm. Whereas in case of sample with Ni=0.55, the particle size distribution varies in the range of 10 nm to 60 nm. Thus particle sizes of sample with Ni=0.55 were found to be higher than of Ni=0.40. Also, particle size distribution of the sample with Ni=0.60 varies in the range of 15 nm to 25 nm which in turn lower than that of Ni=0.55. Thus particle size distribution also supports the observed increase in ε with the increase in Ni from

0.40 to 0.55 (as seen in Fig. 6.12) and also observed minimum value of **ε** for Ni=0.60.

Similarly, increase in **ε** for Ni>0.60 can be attributed to their bigger particle sizes as confirmed from TEM analysis (average particle sizes varies in the range of 15 nm to 40 nm for Ni=0.65 and 25 nm to 30 nm for Ni=0.70) and corresponding lower micro strain of 3.23×10^{-4} and 3.03×10^{-4} for Ni=0.65 and 0.70 respectively (compared to $5.9 \times 10^{-4}$for Ni=0.60). The observed decrease in dielectric constant for Ni=0.70 is attributed to its lower density of 3.73 gm/cm^3, and high porosity of 30% compared to high density of 3.93 gm/cm^3 and lower porosity of 26% for Ni=0.65. Thus we may conclude that, effect of density, particle size distribution, strain and porosity predominates over composition on variation of dielectric constant of nano samples.

6.6.4.3 Frequency dependence of dielectric loss tangent of nano samples

The frequency dependence of dielectric loss tangent (tanδ) of nano $Ni_xZn_{1-x}Fe_2O_4$ samples are shown in Fig. 6.13. It can be seen that, tanδ decreases with the increasing frequency and attains almost constant value at higher frequency for all the compositions. In present investigation the lowest value of tanδ was found to be 0.2 (at 3 MHz) for nano sample with Ni=0.40. The values of tan δ depend on a number of factors such as stoichiometry, Fe^{2+} content and structural homogeneity of the samples, which in turn depends on the composition and method of preparation [46].

The main cause of the loss has been identified as the impurities and imperfections in the crystal lattice [47]. The structural defects give rise to trapping centers, also known as correlated states for the electrons. The response time of the electrons in the trapping centers is higher than the time taken for hopping between the sites of charged particles and hence, lag of polarization gives rise to the dielectric loss [48].

The initial decrease in tan δ with the increase in frequency can be explained on the basis of Koops' phenomenological model [18]. None of the samples exhibit the loss peak. The peaking nature occurs when the jumping frequency of the electrons between Fe^{2+} and Fe^{3+} is equal to the frequency of the applied field. All the nano samples show dispersion in tanδ at lower frequencies. The frequency corresponding to loss peak for the nano Ni-Zn ferrite samples in the present work may be present beyond the measuring limit frequency of 3 MHz.

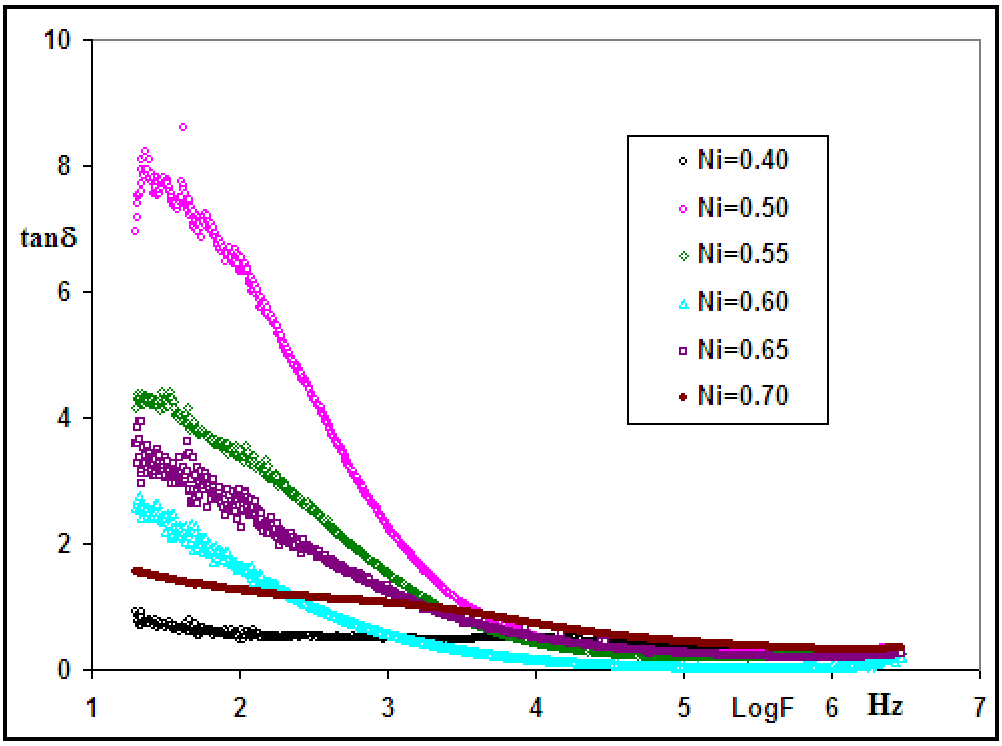

Fig. 6.13 Variation of dielectric loss tangent (tanδ) with frequency of nano $Ni_xZn_{1-x}Fe_2O_4$ samples.

6.6.4.4 Frequency dependence of dielectric constant (ε) of bulk samples

The frequency dependence of ε of bulk $Ni_xZn_{1-x}Fe_2O_4$ samples at 900°C, 1000°C, 1100°C, 1200°C and 1300°C are shown in Fig. 6.14. It was found that ε decreases with the increasing frequency and ultimately, it reaches a constant value.

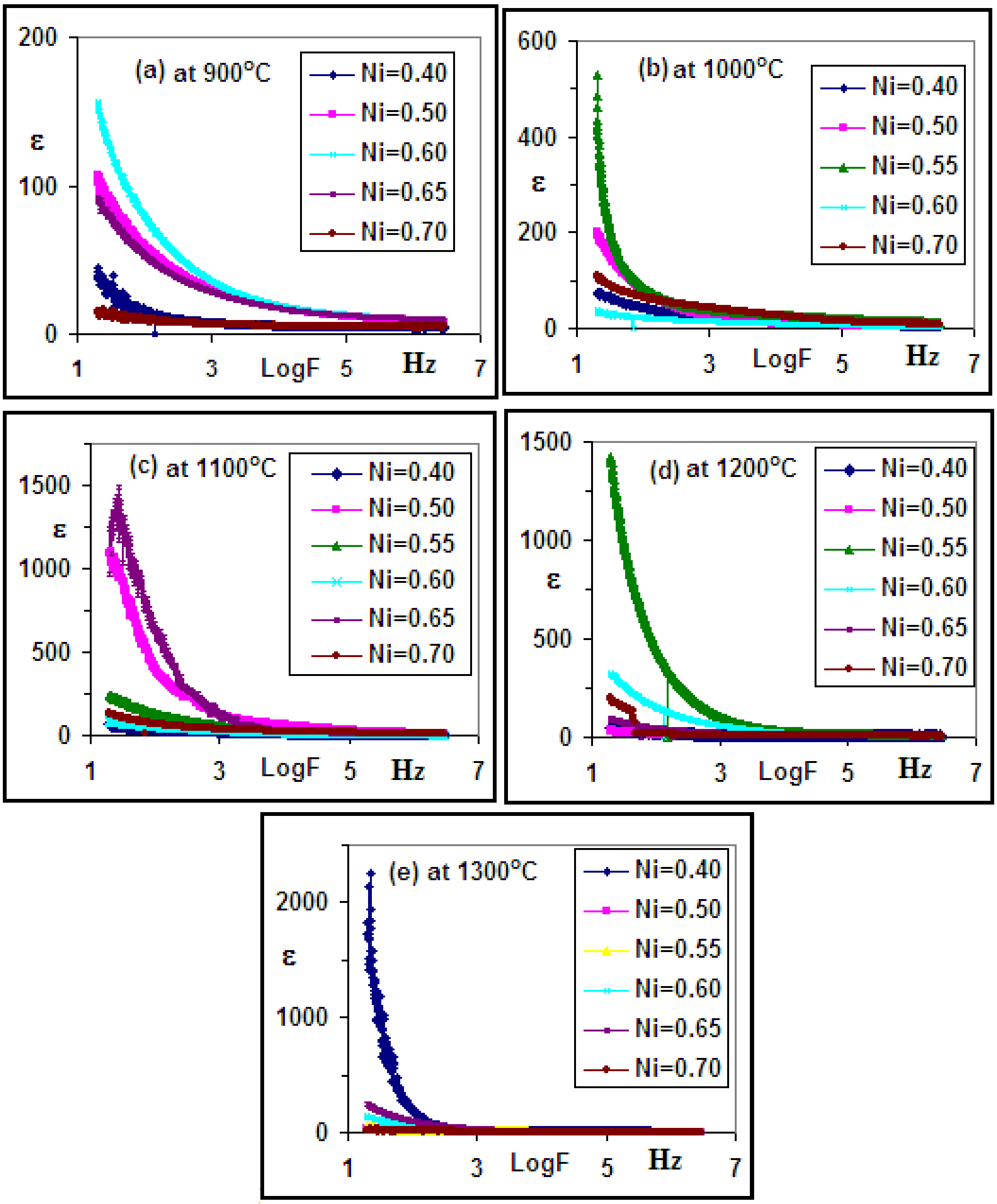

Fig. 6.14 Variation of dielectric constant with frequency for bulk $Ni_xZn_{1-x}Fe_2O_4$ ferrite samples.

This nature was seen for all the bulk samples. This nature of variation of ε is due to the fact that beyond a certain frequency of external field, the electron exchange can not follow the alternating field. The large value of ε at lower frequency is due the predominance of species like Fe^{2+} ions, oxygen vacancies, grain boundary defects, interfacial dislocation pile ups, voids etc. The variation of ε with frequency can be explained by Maxwell-Wagner two layers model of interfacial polarization with Koop's phenomenological theory as explained in Section 6.6.4.1.

The ε of bulk samples measured at frequency of 50 Hz at sintering temperature of 900°C varies in the range of 1.57×10^2 (for Ni=0.60) to 13 (for Ni=0.70) and 5.30×10^2 (for Ni=0.55) to 38 (for Ni=0.60) at 1000°C. Incase of 1100°C, ε varies in the range of 1.09×10^3 (for Ni=0.50) to 62 (for Ni=0.40) and 1.42×10^3 (for Ni=0.55) to 33 (for Ni=0.50) at 1200°C. For sintering temperature of 1300°C ε varies in the range of 1.73×10^3 (for Ni=0.40) to 40 (for Ni=0.70).

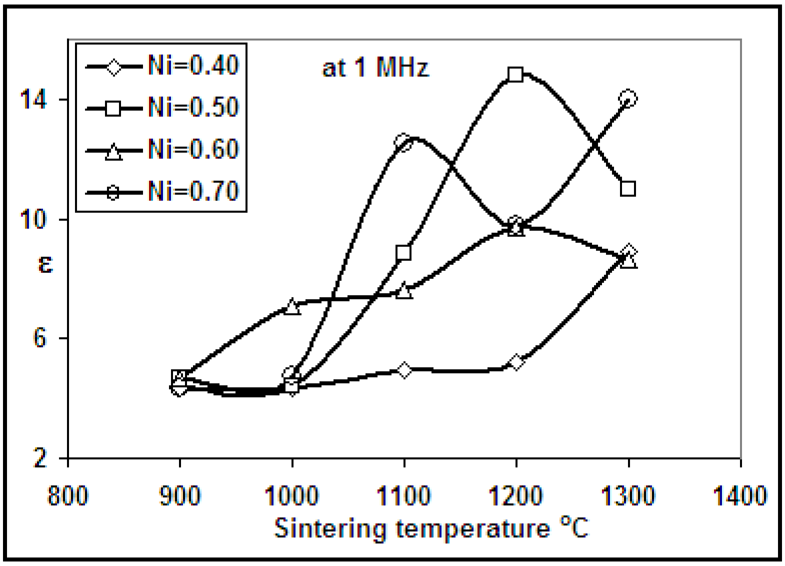

Fig. 6.15 Variation of dielectric constant (at 1 MHz) with sintering temperature of bulk $Ni_xZn_{1-x}Fe_2O_4$ samples.

From Fig. 6.15 it can be seen that ε increases with increase in sintering temperature for all the samples. In case of Ni=0.40, ε increases continuously from sintering temperature of 900°C to 1300°C, and maximum increase was found in the temperature region of 1200°C to 1300°C. In case of Ni=0.50 and Ni=0.60, ε increases with sintering temperature and showed peak at 1200°C. The maximum increase was found in the region of 1100°C to 1200°C. However, in the case of Ni=0.70, ε showed peak at 1100°C. The increase in ε as sintering temperature increases from 1200°C to 1300°C was also seen for Ni=0.70.

The observed increase in ε with sintering temperatures for bulk samples can be explained on the basis of the assumption that the mechanism of dielectric polarization is similar as that of conduction [19]. The electronic exchange between Fe^{2+} and Fe^{3+} is due to the local displacement of electrons in the direction of electric field that determines the polarization in ferrites. As we know, the increase in sintering temperature brings an increase in grain size as well as increase in Fe^{2+} concentration [49] and is responsible for the increase in ε. The probability of evaporation of Zn from the samples increases with increase in sintering temperatures or sintering time [50]. As a result, associated oxygen bonds become unsaturated which are responsible to convert Fe^{3+}ions to Fe^{2+} ions leading to increase in Fe^{2+} concentration which are easily polarized as compared to Fe^{3+} ions [20]. Thus higher value of dielectric constant is expected for the sample sintered at 1300°C as the number of Fe^{2+}ions available for the polarization is greater. In present work, Ni=0.40 and 0.70 showed maximum dielectric constant at 1300°C as expected. R. G Kharabe et al. [20] also reported such increase in dielectric constant with the increase in sintering temperature. However, for Ni=0.50 and 0.60 the favorable sintering temperature for maximum dielectric constant was found to be 1200^{o}C.

6.6.4.5 Frequency dependence of dielectric loss tangent of bulk samples

Frequency dependence of tanδ of bulk samples are shown in Fig. 6.16. It can be seen that all the samples show dispersion in tanδ at lower frequencies. The initial decrease of tan δ with an increase in frequency can be explained on the basis of Koops' phenomenological theory [18]. The bulk samples at sintering temperature of 900^{o}C did not show any resonance peaks up to 3 MHz. The minor peaking nature was observed for the samples with Ni=0.55 and 0.40 at 1000^{o}C. The clear peaking can be seen for sample with Ni=0.65 and minor peak for Ni=0.40 and 0.60 at 1100^{o}C. The noticeable peaking also can be seen for Ni=0.55 and 0.60 at 1200^{o}C. However, very clear high resonance peak can be seen for sample with Ni=0.50, 0.55 and 0.70 at sintering temperature of 1300^{o}C.

The peaking nature occurs when the jump frequency of the electrons between Fe^{2+} and Fe^{3+} is equal to the frequency of the applied field. Resonance peak appearance can be explained as follows. If an ion has two equilibrium positions A and B of equal potential energies separated by a potential barrier. The ion has same probability of jumping from A to B and from B to A. The frequency with which the ion exchanges its position between these two states is called the natural frequency of jump between these two states. When an external alternating electric field of natural frequency is applied, maximum electrical energy is transferred to the oscillating ions causing higher power loss, resulting in resonance. In present work, sample with Ni=0.70 has minimum loss at 50 Hz at all the sintering temperature except at

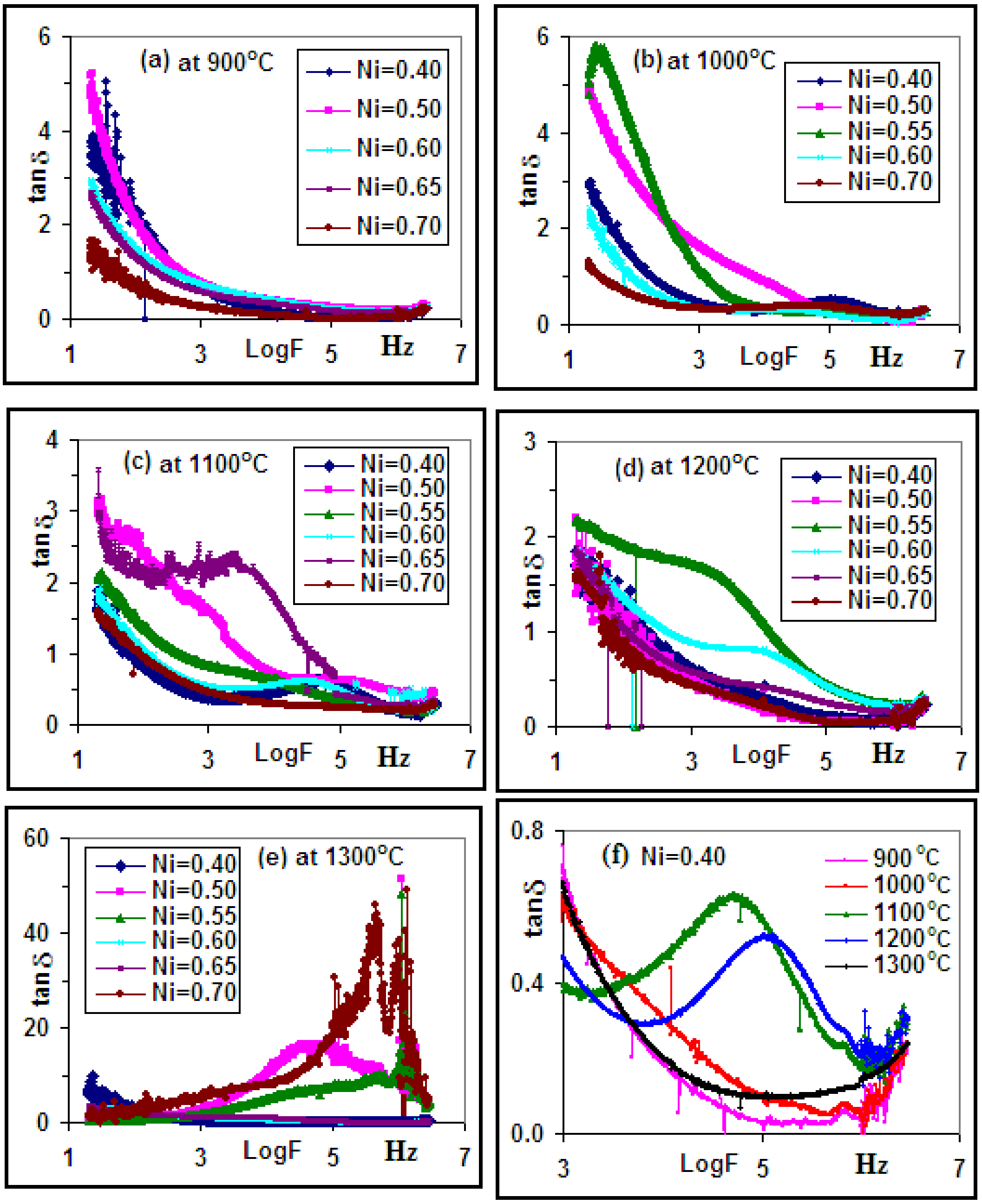

Fig. 6.16 Variation of dielectric loss tangent with frequency of bulk $Ni_xZn_{1-x}Fe_2O_4$ samples.

1300°C. The minimum values of tanδ at 3 MHz varies in the range of 0.21 (for Ni=0.70 at 900°C) to 0.27 (for Ni=0.60 at 1100°C).

The clear and high resonance peak for Ni=0.40 at 1100°C and 1200°C can be seen from the Fig. 6.16 (f). It can be seen that the peak position at 1200°C was shifted to higher frequency compared to that at 1100°C. This may be attributed to the extra Fe^{2+} ions created at sintering temperature of 1200°C that would increase the probability of jumps between the polaron sites. The shifting of peak value towards the higher frequency for Ni-Zn ferrite system was also reported by J. J. Thomas et al. [51]. The tanδ at high frequency was ascribed predominantly to increase in electrical conductivity [52] whereas, the resonance peak observed for Ni=0.55 at 1000°C at very low frequency has been attributed to the resonance of correlated states with an applied field [52]. A similar behavior was also observed by P. Rao et al. [53] in Ni-Zn ferrite and Latha et al. [54] in Mn-Zn ferrites.

6.6.4.6 Temperature dependence of dielectric constant of nano samples

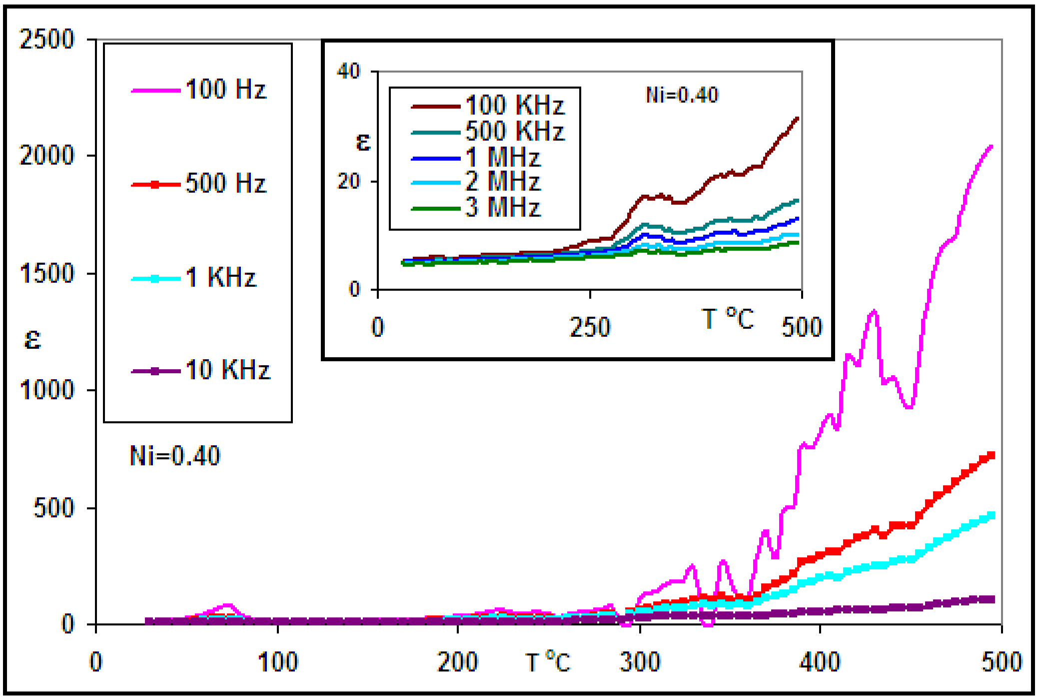

Fig. 6.17 Variation of dielectric constant with temperature of nano $Ni_{0.40}Zn_{0.60}Fe_2O_4$ sample at fixed frequencies. (Inset shows variation at higher frequencies of 100 KHz, 500 KHz, 1 MHz, 2 MHz and 3 MHz).

Fig. 6.17 shows thermal variation of dielectric constant (ε) of nano $Ni_{0.40}Zn_{0.60}Fe_2O_4$ sample at fixed frequencies. It can be seen that ε increases with increase in temperature for all the frequencies. This increase is attributed to the increase in thermally activated drift mobility of charge carriers resulting in the larger dielectric polarization and larger value of ε [55]. The increase in ε was negligible at the initial stage up to 190°C to 200°C, that means the local carriers are immobile i.e thermal activation is negligible. This can also be attributed to high chemical homogeneity and fine grain distribution in the given sample [56]. The expected decrease in ε with the increase in frequency at any fixed temperature can be seen. At lower frequencies (~1 KHz), the increase in ε is large with the increase in temperature, while at higher frequencies (~500 KHz as seen from inset of Fig. 6.17) the increase in ε with increase in temperature is very small.

The ε of a material depends upon four kinds of polarizations i.e dipolar, interfacial, electronic and ionic. The dipolar and interfacial polarizations are important at lower frequencies and both the polarizations are highly temperature sensitive [57]. The interfacial polarization increases with the increase in temperature and dipolar polarization decreases with the increase in temperature. The rapid increase in ε for the sample with the rise in temperature at lower frequencies shows that the effect of temperature is more pronounced on the interfacial polarization than on the dipolar polarization. At higher frequencies, electronic and ionic polarizations are the main contributors compared to interfacial and dipolar polarization, and they are less sensitive to variation in temperature. The slow increase in ε at higher temperature for high frequencies is therefore understandable.

The inset of the Fig. 6.17 shows broad peak in the temperature range of 330°C to 375°C for 100 KHz, 500 KHz, 1 MHz, 2 MHz and 3 MHz. Similar peaks were attributed to collective contribution of two types of charge carriers n and p to the polarization process by A. N. Patil et al [58] for Cu ferrite and N. Ponpandian et al. for $ZnFe_2O_4$ [59].

The variations of **ε** with temperature of nano $Ni_xZn_{1-x}Fe_2O_4$ samples at fixed frequencies of 500 KHz, 1 MHz, 2 MHz and 3 MHz are shown in Fig. 6.18. It can be seen that for Ni=0.60, the **ε** increases continuously with increase in temperature without any major peak. Two peaks were observed in **ε** verses temperature curve at temperature around 290°C and 440°C for Ni=0.50, whereas at temperature around 350°C and 415°C for Ni=0.70. The increase in **ε** with increase in temperature even after peak was observed for Ni=0.70. Incase of Ni=0.55, very broad relaxed peak is observed followed by a continuous increase in **ε** with the increasing temperature.

The appearance of two peaks in the **ε** verses temperature curve may be attributed to statistical fluctuations in the chemical composition at different regions of the sample resulting into different Curie temperatures at different regions of the samples [60]. The broad maximum in the curve may be attributed to diffused phase transition [58, 60, 61]. A. M Bhavakatti [62] attributed the second peak of **ε** at the higher temperature to depletion of space charge peak at a particular temperature for the given composition of ferrite sample. The anomalous behavior of increase in dielectric constant with temperature even after passing through peak was reported by M. Kaise et.al for NiCuZn ferrite [64]. This abnormal dielectric behavior was attributed to collective contribution of two types of carrier n and p to the polarization

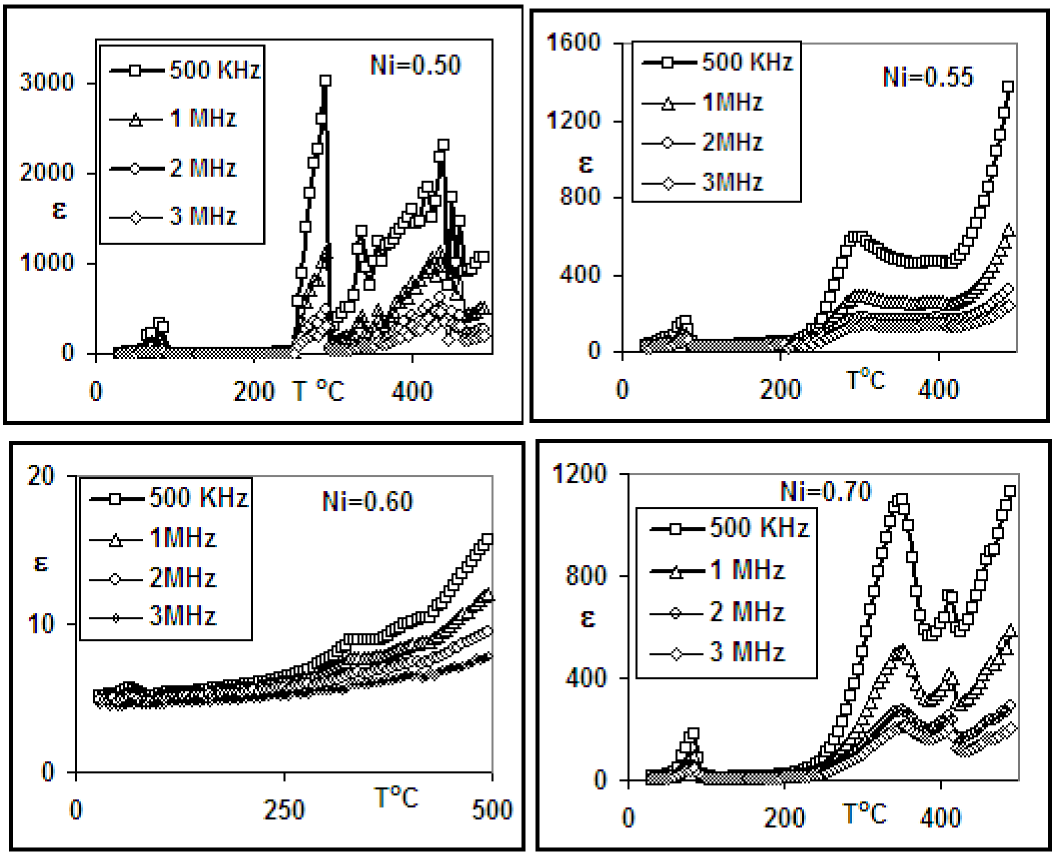

Fig. 6.18 Variation of dielectric constant with temperature of nano $Ni_xZn_{1-x}Fe_2O_4$ samples at fixed frequencies.

[58, 64]. The thermoelectric power results of the ferrite samples in present work have also shown that, both n-type and p-type carries are participating in conduction mechanism. The increase in ε after a peak value was also attributed to the participation of other types of polarization, such as Maxwell-Wagner [63, 65]. This type of polarization plays an important role at higher temperature by increasing the conduction of the samples in the region separating the grains to increases the ε □due to the increasing polarizability.

The minor peak at around 80°C to 100°C can be seen for all the samples and is more pronounced at lower frequencies. This peak is attributed to moisture or water absorption. It should be noted that dipolar polarization is produced only in polar molecules such as H_2O, HCl, nitrobenzene etc. On the application of an electric field to a polar molecule, the dipoles experience a torque and try to align parallel to the applied field, which results to the rotation of the dipoles and produces polarization to give rise in ε [15]. Note that the dipolar polarization decreases with the rise in temperature [66].

6.6.4.7 Temperature dependence of dielectric loss tangent of nano samples

The thermal variations of dielectric loss tangent of nano $Ni_{0.40}Zn_{0.60}Fe_2O_4$ sample at fixed frequencies are shown in Fig. 6.19. It was observed, that at lower frequencies the tanδ increases initially very slowly with the increase in temperature, attains broad maxima and then increases marginally at higher temperatures. In case

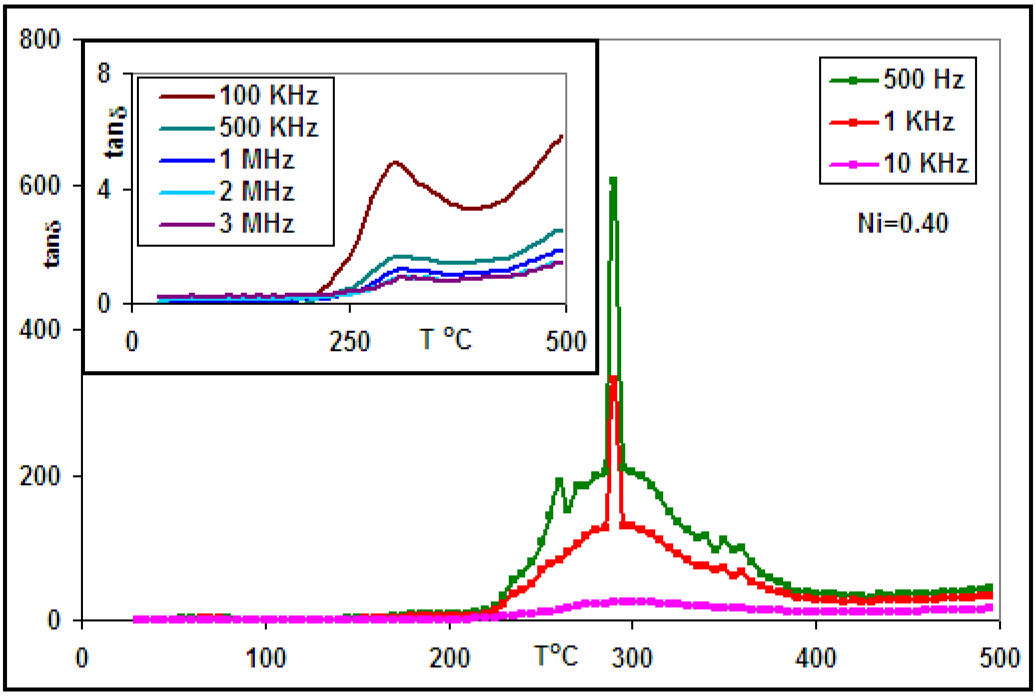

Fig. 6.19 Variation of dielectric loss tangent with temperature of nano $Ni_{0.40}Zn_{0.60}Fe_2O_4$ sample at fixed frequencies. (Inset shows variation at higher frequencies 100 KHz, 500 KHz, 1 MHz, 2 MHz and 3 MHz).

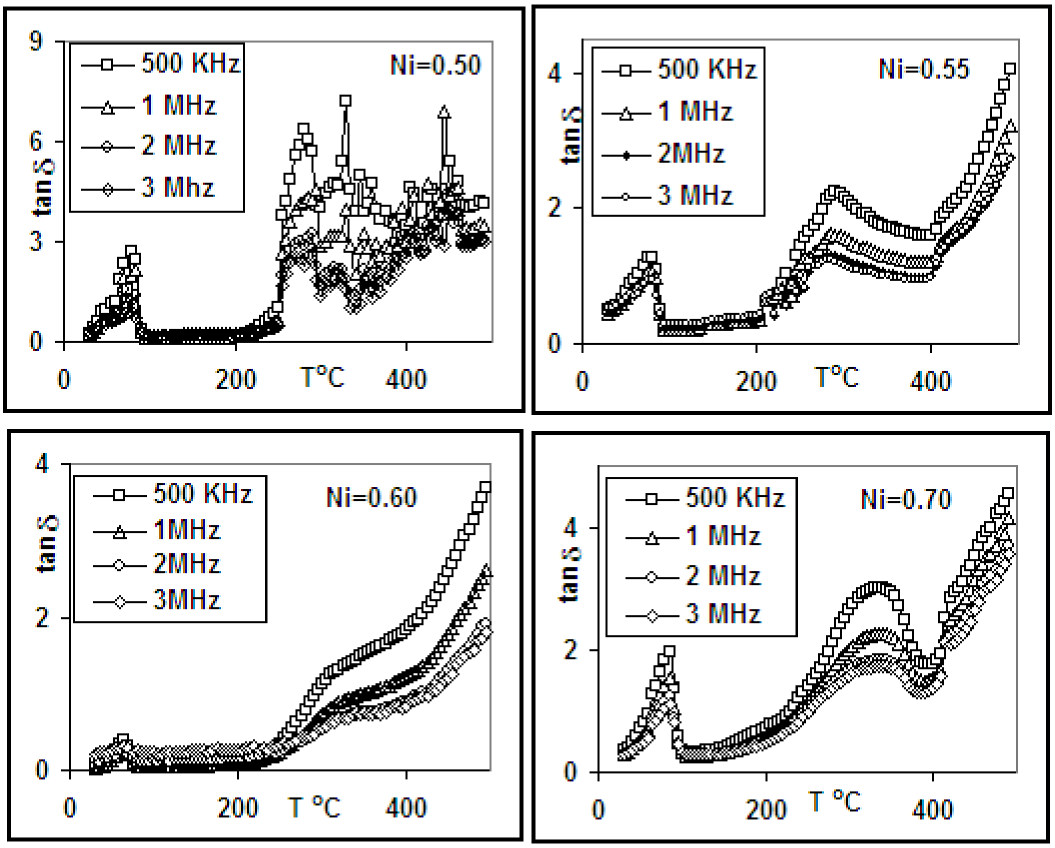

Fig. 6.20 Variation of dielectric loss tangent with temperature of nano $Ni_xZn_{1-x}Fe_2O_4$ samples at fixed frequencies of 500 KHz, 1 MHz, 2 MHz and 3 MHz.

of higher frequencies (inset of Fig. 6.19) the increase in tanδ with temperature even after the broad peak can be seen clearly. The broadness of the peak was found to be increasing with the frequency.

Fig. 6.20 shows variation of tanδ with temperature for nano $Ni_xZn_{1-x}Fe_2O_4$ samples (x=0.50, 0.55, 0.60 and 0.70) at frequencies of 500 KHz, 1 MHz, 2 MHz and 3 MHz. It can be seen that, for Ni=0.60, the tanδ increases continuously with increase in temperature at all the frequencies. For Ni=0.55 and Ni=0.70 broad peaks can be seen at 295°C and 335°C respectively followed by further increase in tanδ with increase in temperature. In case of Ni=0.50, two peaks at the temperature of 280°C and 440°C was observed. The increase in tanδ with increase in temperature can be attributed to the thermal activation of charge carriers and increase in hopping conduction mechanism [55]. The observed maxima in the loss curve may be attributed to increase in space charge polarization effect and rotation direction polarization effect which may be present at higher temperature [45].

6.6.4.8 Temperature dependence of dielectric constant (ε) of bulk samples

The variations of dielectric constant with temperature of bulk $Ni_xZn_{1-x}Fe_2O_4$ samples (x=0.40, 0.50, 0.60 and 0.70) obtained at sintering temperature of 1000°C 1100°C, 1200°C and 1300°C are shown in Fig. 6.21. The measurement was carried out at fixed frequency of 500 KHz.

It can be seen that, the bulk sample with Ni=0.40 shows continuous increase in **ε** with the increase in temperature along with two minor peaks at temperature around 300°C and 400°C at sintering temperature of 1000°C. It shows continuous increase in **ε** with increase in temperature at sintering temperature of 1100°C and 1300°C. However, at sintering temperature of 1200°C, it shows a sharp fall in **ε** at temperature of 400°C.

The bulk sample with Ni=0.50, show initial increase in **ε** with the increase in temperature at all the sintering temperatures. The sharp peaks were observed in this bulk samples at the temperature of around 285°C, 475°C, 355°C and 405°C at sintering temperature of 1000°C, 1100°C, 1200°C and 1300°C respectively.

In case of bulk sample with Ni=0.60, the **ε** show continuous increase with increase in temperature along with a minor peaks at the temperature around 420°C, 415°C and 340°C at sintering temperature of 1000°C, 1200°C and 1300°C respectively. However, at sintering temperature of 1100°C the **ε** shows a broad peak in the temperature range of 320°C to 410°C.

The bulk sample with Ni=0.70 show continuous increase in the **ε** with increase in temperature at sintering temperature of 1000°C and 1300°C. The sample shows a sharp peak in **ε** at temperature of around 320°C at sintering temperature of 1200°C. However, at sintering temperature of 1100°C, the **ε** shows broad peak in the temperature range of 325°C to 400°C.

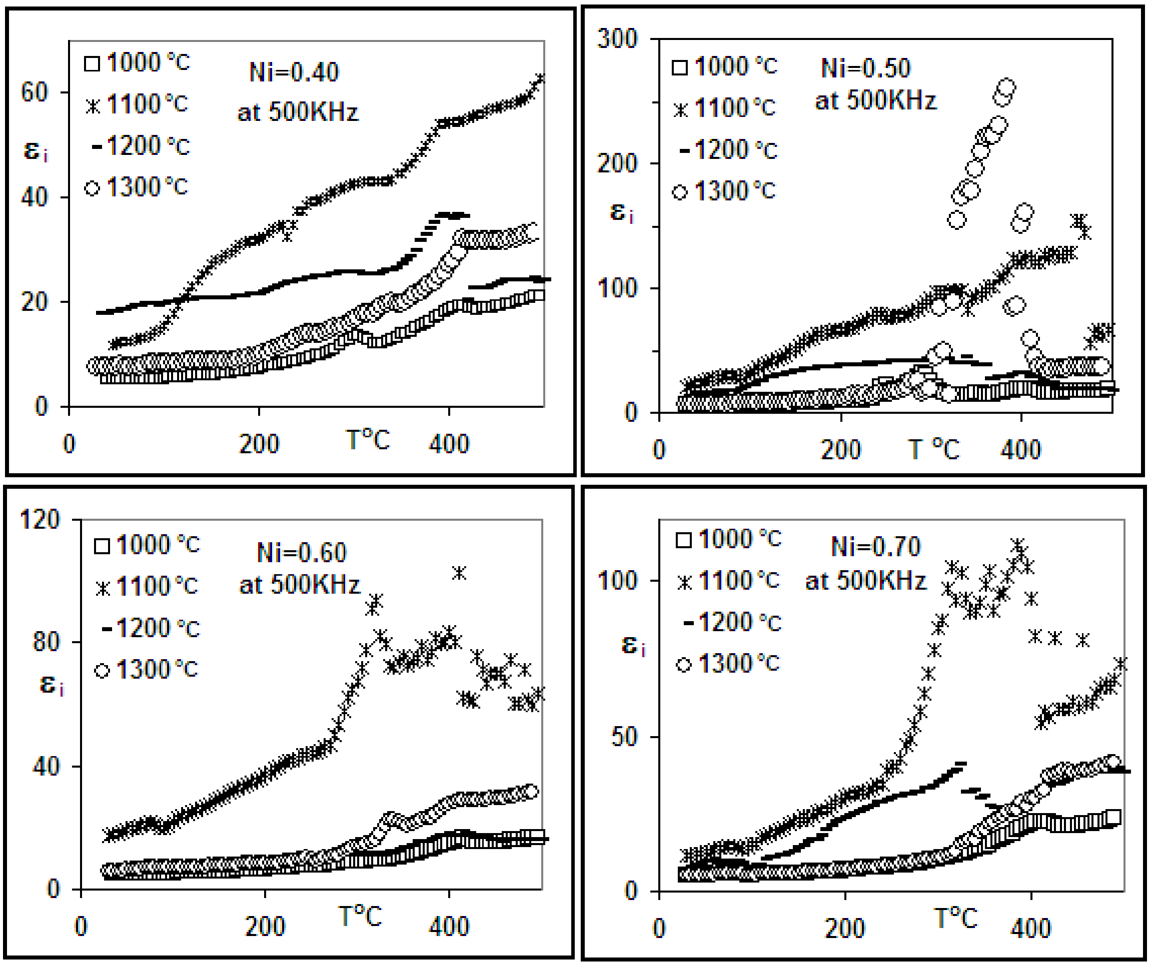

Fig. 6.21 Variation of dielectric constant with temperature of bulk $Ni_xZn_{1-x}Fe_2O_4$ samples at frequency of 500 KHz.

The observed increase in **ε** with the increase in temperature in the bulk samples can be attributed to the increase in thermally activated drift mobility of electric charge carriers. The different peaks may also be attributed to presence of two types of charge carries as reported by Rezlescu [67]. However, shifting in peak position with the sintering temperatures for a given bulk sample may be attributed to the existence of phase transitions which occur during the crystal formation process while sintering them [57].

6.6.4.9 Temperature dependence of dielectric loss tangent of bulk samples

Fig. 6.22 shows the variation of dielectric loss tangent with temperature of bulk $Ni_xZn_{1-x}Fe_2O_4$ samples (x=0.40, 0.50, 0.60 and 0.70) obtained at sintering temperature of 1000^{o}C 1100^{o}C, 1200^{o}C and 1300^{o}C. The measurement was carried out at fixed frequency of 500 KHz.

It can be seen that, the bulk sample with Ni=0.40, show continuous increase in tanδ with increase in temperature at sintering temperature 1000^{o}C, 1100^{o}C and 1200^{o}C. However, the sample showed a peak in tanδ at temperature around 350^{o}C at sintering temperature of 1300^{o}C.

For bulk sample with Ni=0.50, tanδ increases continuously with increase in temperature at sintering temperature of 1200^{o}C. The sample shows a minor peak in loss curve at temperature around 300^{o}C and 315^{o}C at sintering temperature of 1000^{o}C and 1100^{o}C respectively. The broad peak in loss curve was seen in the temperature range of 300^{o}C to 430^{o}C at sintering temperature of 1300^{o}C.

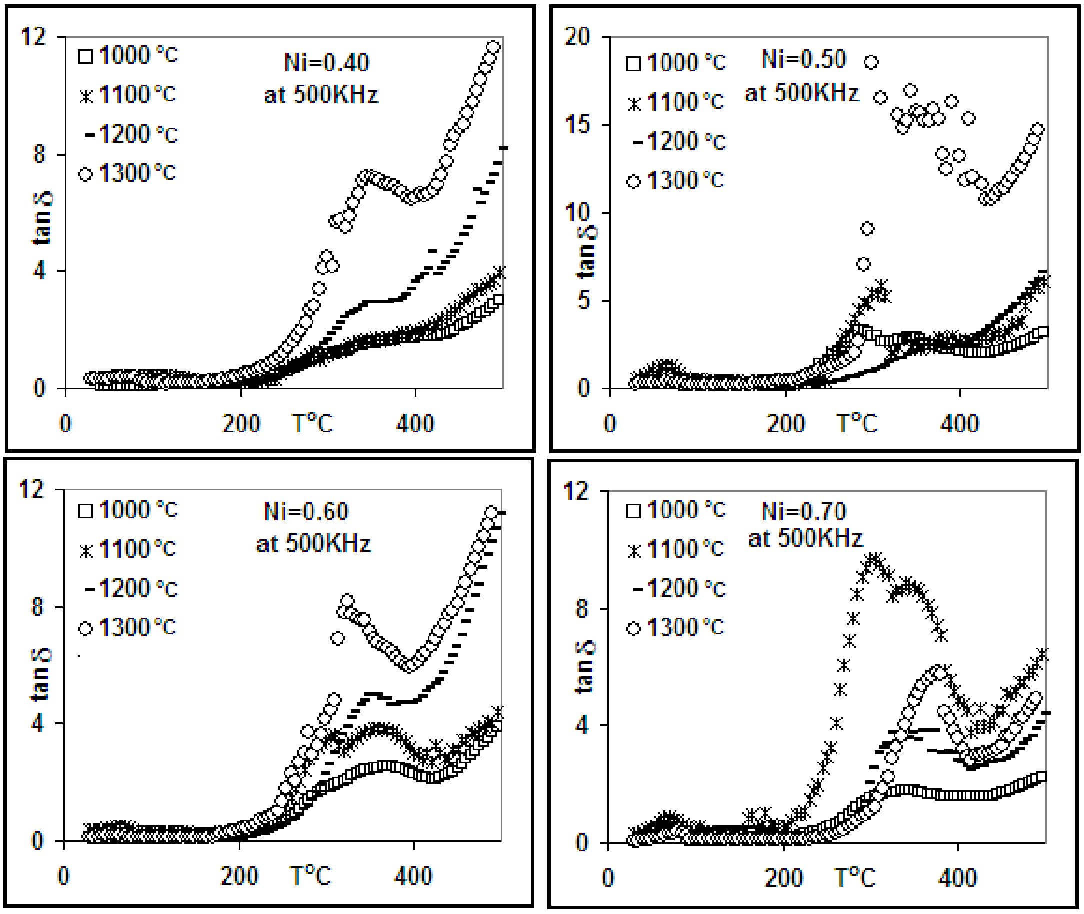

Fig. 6.22 Variation of dielectric loss tangent with temperature of bulk $Ni_xZn_{1-x}Fe_2O_4$ samples at frequency of 500 KHz.

In case of bulk sample with Ni=0.60, the tanδ showed a broad peak in the temperature range of 290^{o}C to 400^{o}C at all the sintering temperatures. The subsequent increase in tanδ at higher temperatures beyond the peaks was also found for this sample at all the sintering temperatures.

The bulk sample with Ni=0.70 show continuous increase in tanδ with increase in temperature at sintering temperature of 1000^{o}C. A broad peak in tanδ for the sample was observed in the temperature range of 290^{o}C to 420^{o}C at sintering temperature of 1100°C, whereas, similar broad peak in the temperature range of around 300°C to 410°C and 330°C to 415°C was observed at sintering temperature of 1200°C and 1300°C respectively.

The increase in tanδ with increase in temperature for bulk samples can be attributed to the thermal activation of charge carriers and increase in hopping conduction mechanism, and maxima in the loss curve may be attributed to increase in space charge polarization effect and rotation direction polarization effect.

References

1. S. C. Watawe, U. A. Bamne, S. P. Gonbare and R. B. Tangsali, Materials Chemistry and Physics, 103, (2007), 323-328.

2. S. S. Bellad and B. K. Chougule, Mater Chem and Phys., 66, (2000), 58-63.

3. H. M. Zaki, Physica B, (2009), 1-7.

4. M. A. Ahmed, E. Ateia, L. M. Salah, and A. A. El-Gamal, phys. stat. sol., (a) 201-13, (2004), 3010-3022.

5. A. K. Singh, T. C. Goel, R. G. Mendiratta, O. P. Thakur and C. Prakash, Appl. Phys., 91-10, (2002), 6626-6631.

6. M. J. Iqbal, Z. Ahmad, T. Meydan and Y. Melikhov, J. Appl. Phys. 111, (2012), 0339061-0339067.

7. A. M. El-Sayed, Materials Chemistry and Physics, 82, (2003), 583-587.

8. A. Verma, T. C. Goel, R. G. Mendiratta and R. G. Gupta, J. Magn.Magn.Mater, 192, (1999), 271-276.

9. P. Laokul, P. Thongbai, T. Yamwong and S. Maensiri, J Supercond Nov Magn, 25, (2012), 1195-1201.

10. A. G Bhosale and B. K. Chougule Materials Letters 60, (2006), 3912-3915.

11. M. G. Patil, V. C. Mahajan, A. K. Ghatage, S. A. Patil, Indian J. Pure App. Phys., 34, (1996), 166-170.

12. R. V. Mangalaraja, S. Ananthakumar, P. Manohar and F. D. Gnanam, Materials Letters, 57, (2003), 2662-2665.

13. B. Vishwanathan and V. R. K Murthy, Ferrrite Materials Sience and Technology, Narosa Publishing House, (1990), 26-32.

14. D. Ravinder, P. Vijaya and B. Reddy, J. Magn.Magn.Mater, 263, (2003), 127-133.

15. V. Rajendran and A. Marikani, Materials Science, Tata Mc-Graw-Hill Publishing Company Limited, New Delhi, (2004).
16. J. C. Maxwell, Electricity and Magnetism, Vol-1 Oxford, Oxford University Press, (1929), section 328.
17. K. W. Wagner, Ann. Phys. 40, (1913), 817.
18. C. G. Koops, Phys. Rev. 83, (1951), 121.
19. I. T. Rabinkin and Z. I. Novikova, Ferrites, Izv Acad. Nauk USSR Minsk, (1960).
20. R. G. Kharabe, R. S. Devan, C. M. Kanamadi and B. K. Chougule, Smart Mater. Struct. 15, (2006), N36.
21. S. A. Mazen and H. M. Zaki, J. Magn.Magn.Mater, 248, (2002), 200-215.
22. B. Baruwati, R. Rana, and S. Manorama, J. Appl. Phys.,101, (2007), 14302(1-7).
23. T. T. Srinivasan, P. Ravindranathan, L. E. Cross, R. Roy, R. E. Newman, S. G. Sankar and K. C. Patil, J. Appl. Phys., 63, (1988), 3789-94.
24. A. D. Sheikh and V. L. Mathe, J. Mater Sci., 43, (2008), 2018-2025.
25. N. Rezlescu, D. Condurache, P. Petrariu and E. Luca, J. Amer. Ceram. Soc., 57, (1974), 40-45.
26. A. K. M. Akther Hossain, S. T. Mahmud, M. Seki, T. Kawai and H. Tabata, J. Magn.Magn.Mater, 312, (2007), 210-219.
27. V. D. Kapsea, S. A. Ghosha, F. C. Raghuwanshi, S. D. Kapse and U. S. Khandekar, Talanta, 78, (2009), 19-25.
28. I. H. Gul, A. Z. Abbasi, F. Amin, M. Anis-ur-Rehman and A. Maqsood, J. Magn.Magn.Mater, 311, (2007), 494-499.
29. K. Vijaya Kumar and D. Ravinder, International Journal of Inorganic Materials, 3, (2001), 661-666.

30. B. Parvatheeswara Rao and K. H. Rao, J. Mater. Sci., 32, (1997), 6049-6055.

31. A. B. Naik and J. I. Powar, Ind. J. Pure Appl. Phys., 23, (1985), 436-440

32. G. C. Jain, B. K. Das, R. B. Tripathi and R. Narayan, IEEE Trans. Magn., 18, (1982), 776-782.

33. E. Rezlescu, L. Sachelarie, P. D. Popa and N. Reslezcu, IEEE Trans. Magn., 36, (6), (2000), 3962-3968.

34. L. G. Van Uitert, J. Chem. Phys., 23, (10), (1955), 1883-1889.

35. P. Mathur, A. Thakur and M. Singh, Indian J. Eng. Mater. Sci., 15, (2008), 55-60.

36. A. D. P. Rao, B. Ramesh, P. R. M. Rao and S. B. Raju, Journal of Material Sci., 34, (1999), 621-623.

37. B. P. Ladgaonkar, P. N. Vasambekar and A. S. Vaingankar, Bull. Mater. Sci., 23, (2000), 87-90

38. D. Ravinder and G. R. Mohan, Materials Letters, 44, (2000), 139-143.

39. M. Chanda, Science of engineering materials, Vol. 3. The Mach-millan Company of India Ltd, New Delhi, (1980).

40. Q. Chen, P. Du, W. Huang, Lu Jin, W. Weng, and G. Han, Applied Physics Letters, 90, (2007), 132907-(1-3).

41. A. M. Shaikh, S. S. Bellad and B. K. Chougule, J. Magn. Magn. Mater. 195, (1999), 384-389.

42. G. Sathishkumar, C. Venkatarajua and K. Sivakumar, Materials Sciences and Applications, 1, (2010), 19-24.

43. J. C. Maxwell, Electricity and Magnetism, Vol 2, New York, Oxford University Press, (1973).

44. M. A. Ahmed and E. H. El-Khawas, Indian. J. Phys., 74A, (2000), 497-501.

45. S. S. Bellad, S. C. Watawe and B. K. Chougule, Mat. Res. Bull., 34, (1999), 1099-1103.

46. A. Verma, T. C. Goel, R. G. Mendiratta and P. Kishan, J. Magn. Magn. Mater., 208, (2000), 13-17.

47. A. K. Singh, T. C. Goel, R. G. Mendiratta and M. I. Alam, Materials Science and Engineering , 60, (1999), 156-162.

48. K. L. Ngai and C. T White, Physical Review, 20, (1979), 2475-2486.

49. J. Smit and H. P. J. Wijn, Ferrites, Philips Technical Library (1959), 242.

50. K. Iwauchi, Jpn. J. Appl. Phys., 10, (1971), 1520-1523.

51. J. Job Thomas, S. Krishnan and N. Kalarikkalr, Proceeding of ICNM - 2009 1st International Conference on Nanostructured Materials,Nanocomposites, Applied Science Innovations Private Limited, India., (2009), 169-175.

52. S. F. Mansour, Egypt. J. Solids, 28(2), (2005), 263-273.

53. B. Parvatheeswara Rao, P. S. V. Subba Rao and K. H. Rao, J. Mater.Sci. Lett., 15, (1996), 781-786.

54. K. Latha, K. Satyamohan and D. Ravinder, Phys. Status Solidi, A-142, (1994), K103.

55. V. R. K. Murthy. and Shobhandri, J. Phys. Stat. Sol., (1980), a-36, K-133.

56. V. A. Hiremeth and A. Venkataraman, Bull. Mater. Sci., 26, (2003), 391-396.

57. B. M. Tareev, N. V. Korotkova, V. M. Petrov and A. A. Preobrazhensky, “Electrical and Radio Engineering Materials”, MIR Publishers, Moscow, (1980).

58. A. N. Patil, M. G. Patil, K. K. Patankar, V. L. Mathe, R. P. Mahajan and S. A. Patil, Bull. Mater. Sci., 23, (2000), 447-452.

59. N. Ponpandian and A. Narayanasarny, J. Appl. Phys., 92, (2002), 2770-72.

60. S. Upadhyay, D. Kumar and O. Parkash, Bull. Mater. Sci., 19, (1996), 513-517.

61. L. E. Cross, “Relaxor ferroelectrics,” Ferroelectrics, 76-1, (1987), 241-267,

62. A. M. Bhavakatti, IJST, 3, (2011), 687-695.

63. M. Kaiser, S. S. Ata-Allah, Materials Research Bulletin, 44, (2009), 1249-1255.

64. S. S. Shinde and K. M. Jadhav, Mat. Lett., 37, (1998), 63-68.

65. E. Ateia, Egypt.J.Solids, 29-2, (2006), 317-327.

66. M. Chimei, Z. Lide and W Guozhong, Nanostructured Materials, 6, (1995) 823-830.

67. N. Rezlescu and E. Rezlescu, Physics.Status Solidi, A23, (1974) 575-579.

CHAPTER 7

CONCLUSIONS

7.1 Summary

This concluding chapter provides the glimpse of the investigations carried out and scope for the future work on nanoparticle and bulk Ni-Zn ferrite material. The main focus of this study was to prepare, characterize and investigate the magnetic and electrical properties of nanoparticle Ni-Zn ferrite obtained by microwave assisted combustion synthesis and bulk material obtained by sintering nanoparticles.

In the present work nanoparticle $Ni_xZn_{1-x}Fe_2O_4$ samples (x=0.40, 0.50, 0.55, 0.60, 0.65 and 0.70) were successfully synthesized by microwave assisted combustion of nitrilotriacetate based precursor method. This method is a novel route kind to synthesis of nanoparticle $Ni_xZn_{1-x}Fe_2O_4$ samples. The bulk samples were obtained by sintering nano samples at temperatures of 900^{o}C, 1000^{o}C, 1100^{o}C, 1200^{o}C and 1300^{o}C.

The characterizations of the samples were done using standard techniques such as X-ray-diffraction (XRD), Infrared spectroscopy (IR) and Energy Dispersive Spectroscopy (EDS). The XRD spectrum of all the samples are complying with JCPDS file no 8-234 and AMCSD card 99-101-2527 to signature the formation of single phase Ni-Zn ferrite material with cubic spinel structure. The lattice constants '*a*' decreased with increasing Ni concentration in the samples. Lattice constant of all the samples follow Vegard’s Law. The values of ‘*a*’ are in good agreement with reported results.

The EDS spectra of the nano samples show only Ni, Zn, Fe and O peaks revealing no impurities in the samples. The observed compositions were in good agreement (within 5% error) to that of the theoretical stoichiometric calculations evidently indicating that the method of sample preparation employed in the present work preserves the material/samples stoichiometry. The single phase spinel structure with two sub-lattices of the nano samples also revealed from the presence of two absorption bands in IR spectra.

The Scherrer’s formula calculations show average crystallite sizes in the range of 51 nm to 69 nm whereas TEM micrograph analysis show particle sizes in the range of 6 nm to 75 nm. Thus the formation of nano size Ni-Zn ferrite was confirmed by these measurements. The variations of crystallite sizes of the samples are attributed to change in the rate of ferrite formation process or reaction rate due to variation in compositions. The AFM results of grain diameter of samples analyzed using powder deposition method were found to be in good agreement with TEM particle size analysis.

The X-ray densities of nano samples show dependence on Ni content, which was attributed to changes in their lattice parameters and molecular weights. The porosity of the nano samples are found to be in the range of 22% to 30%. The theoretical calculations of cation distributions of nano samples show that zinc atoms prefers to reside only at A site, Ni ions prefers to reside at B site and Fe atoms are distributed over A and B sites. This analysis is well supported by IR spectroscopy and is also in agreement with reported results.

The XRD spectra of the bulk samples show increase in intensities of the peaks with increasing sintering temperature which is a clear indication of improvement in the crystallinity of the samples on sintering. The density of all the bulk samples increased with the increase in sintering temperature on the other hand porosity decreased. The increase in density is attributed to increase in crystallite sizes and improvement in crystallinity. The highest density of 4.99 gm/cm^3 for sample with Ni=0.65 and lowest porosity of 7% for Ni=0.50 and 0.65 were found at sintering temperature of 1300^{o}C.

The microstructure, grain growth and densification process of bulk samples with sintering temperatures were analyzed using SEM micrograph images. The clear grains are seen from SEM images of bulk samples at sintering temperature of 1200^{o}C, and well resolved grains of few micrometer sizes are observed at sintering temperature of 1300^{o}C. The microstructure of the samples shows polycrystalline grains and grain sizes increased with the increasing sintering temperature. The rate of densification is higher compared to rate of grain growth for lower sintering temperatures ~ 900°C to 1000°C. On the other hand, rate of grain growth is higher than rate of densification for higher sintering temperatures of 1200°C and 1300°C. The grain size distributions obtained from SEM images of the bulk samples show composition dependence. Unsaturated grain growths are clearly seen at sintering temperature of 1300^{o}C along with few grains with truncated hexagonal shapes in few samples. This indicates that the sintering temperature of 1300^{o}C is very close to a transitional phase.

The nano and bulks samples in the present work show narrow hysteresis loops which indicate that they are soft magnetic materials. The saturation magnetization (**M_s**) of nano samples vary in the range of 61.74 emu/g to 74.47 emu/g, which are higher than reported values. The magnetic structure was found to be non-collinear leading to significant spin canting at B site. The soft ferrite natures of the prepared samples were also deduced from their values of coercivity and retentivity. The coercivity (**H_c)** and retentivity (**M_r)** values of nano samples vary in the range of 70 Oe to 92.5 Oe and 6.5 emu/g to 8.5 emu/g respectively. The temperature dependence of magnetization of nano samples obtained from ZFC and FC performance on SQUID setup show that the blocking temperature **T_B** varies with Ni content in the samples. The low temperature magnetization study of nano samples showed collinear magnetic structure below 200 K.

The **M_s** of the bulk samples are higher compared to their respective nano samples. This can be attributed to many factors such as increase in grain size, higher crystalline quality, decreasing porosity, improved densification and conversion of SD to MD structure with the increasing sintering temperature. Among all the bulk samples the highest **M_s** of 88.47 emu/g is found for Ni=0.65 at sintering temperature of 1200^{o}C. On an average, **H_c** and **M_r** of the bulk samples show decrease with increasing sintering temperature with few exceptions. The minimum value of **H_c** and **M_r** of the bulk samples are found to be 66.32 Oe (for Ni=0.40) and 0.27 emu/g (Ni=0.50) respectively at sintering temperature of 1300^{o}C.

The variations of normalized AC susceptibility with temperature of nano samples show typical ferrimagnetic curves with mixture of SD and MD structures. The analysis show broadening of the ferrimagnetic transition near T_c which can be attributed to nano sizes of the samples and their transformation from one ferrimagnetic phase to another (metastable state to a stable state). The Curie temperatures $\mathbf{T_c}$ of nano samples increased with increasing Ni content in the sample and highest $\mathbf{T_c}$ of 471^{o}C ±10^{o}C is found for Ni=0.70 whereas lowest of 422^{o}C ±10^{o}C for Ni=0.40.

The normalized AC susceptibility curves of bulk samples show sharp fall with the increasing temperature compared to that of nano samples. This behavior can be attributed to increase in grain size and better crystal growth of bulk samples. The $\mathbf{T_c}$ of bulk samples decreased with the increase in sintering temperatures due to increase in their grain sizes on sintering. The exceptional increase in $\mathbf{T_c}$ of some of the bulk samples (obtained at 1300^{o}C) is found, which are attributed to evaporation of zinc at higher sintering temperature leading to increase in Fe/Ni ratio, and also, attributed to observed lattice contraction of bulk samples leading to increase in overlapping of orbital of Fe_A^{3+}--O^{2-}--Fe_B^{3+} linkages to dominate the size effect.

Initial permeability ($\boldsymbol{\mu_i}$) of the bulk samples decreases sharply at lower frequencies, remains almost constant over a large band of frequency and it then increases abruptly at resonance frequency. These variations in ($\boldsymbol{\mu_i}$) are explained on the basis of magnetizing mechanisms due to domain wall motion and spin rotation. The samples show resonance peak, which are attributed to domain wall resonance. The resonance frequencies ($\mathbf{F_r}$) are higher than 3 MHz for all the bulk samples obtained at sintering temperature of 900^{o}C, 1000^{o}C and 1100^{o}C, whereas same are found to be 3 MHz for samples obtained at sintering temperature of 1200^{o}C and 1300^{o}C. All the bulk samples obey Snoek’s law. The $\boldsymbol{\mu_i}$ show increment with the increase in sintering temperature. This is attributed to increase in grain sizes, increase in density and decrease in porosity of the samples with the increase in sintering temperature. The samples show high permeability and low loss factor compared to values reported by other workers. The thermal spectra of $\boldsymbol{\mu_i}$ for given sample show sharp fall with the increasing sintering temperature revealing the improvement in degree of homogeneity of the sample.

The room temperature Mössbauer spectra of nano samples show two major sextets corresponding to Fe ions residing at the A site and B site of the lattices, and the patterns can be attributed to super exchange interactions between the magnetic ions at A and B sub-lattices. The third and broad featureless absorption sextet, characterized by a significant reduction in the magnetic hyperfine field is attributed to the atoms at the surface of the nano particles. The values of the isomer shifts of the nano samples vary in the range of 0.15 mm/s to 0.47 mm/s, which shows that, Fe ions are in trivalent state.

The featureless relaxed sextet was absent in the Mössbauer spectra of bulk $Ni_{0.60}Zn_{0.40}Fe_2O_4$ sample. This is an indication of coarsening of the nano particles and increase in grain sizes on sintering process. The hyperfine field values of both A and B sites increased with the increase in sintering temperature. These were attributed to improvement in homogeneity and ferrimagnetic ordering in the samples. The ratio of area of Fe at A site to Fe at B site of bulk samples changes with the sintering temperature. This clearly demonstrates the change in cation distributions in the samples on sintering process.

The DC resistivity of nano and bulk samples showed semiconductor behavior. The magnetic transition from ferrimagnetic to paramagnetic state was investigated from small dip or cusps causing changes in the slope of the resistivity curves. The values of $\mathbf{T_c}$'s obtained from such curves are found to be in good agreement with the results obtained from Ac susceptibility measurement. The room temperature resistivity of nano samples vary in the range of 6.85x10^7 ohm-cm (for Ni=0.60) to 1.08x10^9 ohm-cm (for Ni=0.70) and are found to be two to three orders higher than reported values. The resistivities of the bulk samples are found to be one or two orders lower than that of nanoparticle samples. This can be attributed to increase in grain sizes, decrease in porosity and increase in density due to sintering. The highest resistivity value of 4.8x10^7 ohm-cm obtained for bulk sample with Ni=0.55 at sintering temperature of 1200°C is two orders higher than the values reported for bulk samples prepared by ceramic method. The thermoelectric power show that, all the ferrite samples in the present work are behaving as n-type semiconductor in lower temperature region and p-type semiconductor in the higher temperature region. Thus both n-type and p-type carriers, contribute in conduction mechanism.

The dielectric constant (**ε**) of nano and bulk samples decreases with the increasing frequency and ultimately attains a constant value at higher frequency, and these variations are explained using Maxwell-Wagner two layers model of interfacial polarization along with Koop's phenomenological theory. The dielectric constant **(ε)** of bulk samples increased with the increase in sintering temperature. This is attributed to increase in grain sizes leading to increase in polarization of the samples. In present work, sample with Ni=0.40 obtained at sintering temperature of 1300°C showed maximum dielectric constant of 1.73x10^3 at 50 Hz. All the nano samples show dispersion in tanδ at lower frequencies and the curves did not show any peaks within frequency range of 3 MHz, whereas, loss peak was visible in case of bulk samples, for Ni=0.50, 0.55 and 0.70 obtained at sintering temperature of 1300°C. The tanδ of bulk samples varies in the range of 5.12 to 0.21. The samples investigated in present work exhibit high permeability and low loss compared to reported values.

The dielectric constant (ε) of nano and bulk samples increased with increase in temperature at all the frequencies. The peaks obtained in the thermal variation of ε curves are attributed to collective contributions of p-type and n-type charge carriers in the polarization process. The appearance of two peaks in the ε versus temperature curves are attributed to statistical fluctuations in chemical composition and different Curie temperatures, in different regions of the samples. The samples prepared in the present work show higher dielectric constant and low loss compared to reports by other workers for the samples prepared by using conventionally known methods. This suggests that, the samples investigated in the present work exhibit superior dielectric properties.

7.2 Scope for Future Work

Exhaustive research work is going on across the globe on magnetic nano materials including various types of ferrites, essentially due to advancement in nanotechnology giving a boost to new and high performance devices to facilitate higher sciences and man kind. The aim of the electronic industries has been always to miniaturize and enhance efficiencies of the electronic devices. The modern devices are always exclusively in need of soft magnetic materials and Ni-Zn ferrites are adequately one of them at fore front to accomplish their demands.

Following are few areas with ample scope to work in future:

1. Various modifications in the parameters of the sample preparation can be carried out to obtain narrow size distribution of nano samples, and size dependent superparamagnetic properties of these Ni-Zn nano particles could be examined.

2. In general, uniformly packed microstructures must be obtained to achieve reliability and reproducibility in sample processing. Thus, further work of optimizing sintering criteria such as temperature, time, heating rate etc. to obtain desired grain sizes and densification of bulk samples can be taken up.

3. The permeability results in the present work show promising results applicable in the field of wireless heart rate monitors and transponders i.e. devices used to transmit or respond to RF signals in which ferrite core is popularly used for low frequency applications (below 500 KHz). The detailed systematic study can be taken up to learn the usefulness of the prepared samples in the above applications.

4. The higher values of resistivity and permeability reflected in the present work shows that our method of sample preparation is promising to avail high performance ferrites suitable for high-frequency applications where eddy current losses are of paramount concern. A detailed comparative study between commercially available ferrites and ferrites prepared in the present work could be taken up to learn their potential at higher frequencies, wherein samples prepared by conventionally known methods can not be used.

5. Temperature sensitivity of the magnetic permeability of the ferrite can be tested for their application in temperature transducer. The study on working temperature range can be tuned by exploiting heterogeneity of the samples by optimizing

sintering conditions. Thus detail study on temperature variation of permeability of the samples prepared in the present work may show interesting results by selecting optimum sintering temperature conditions based on combination of temperature sensitivity, frequency stability and degree of homogeneity for temperature sensors applications.

6. The bulk samples in the present work show evidences and promising results compared to reported results for the application of pulsed-current sensors. An in-depth study can discover the ability of samples in the present work in the application of pulsed current sensors. The pulsed current sensors require transducers constituted of magnetic materials with high magnetic permeability in a frequency range compatible with the period and the frequency of the current pulse.

7. The changes in magnetic properties of ferrite under compressive stress from the external forces open possibilities of construction of magnetoelastic stress and force sensors. The influence of compressive stresses on hysteresis loop and changes in relative permeability as a function of the compressive stress can be utilized for sensing technique. Thus detailed and independent work in this direction on the samples prepared in the present work may produce fascinating results.

8. A reduction in size and weight of power supplies can be achieved by using switched mode or resonant concepts at increasing frequencies which requires ferrite grades with low magnetic and eddy current losses. The samples in the present work show low loss factor compared to many reported results and hence, detailed comparative study between commercial and prepared samples exclusively on magnetic and electric loss can be taken up.

9. The samples in the present work show promising values of saturation magnetization, high dc resistivity, high permeability, low loss and high dielectric constant, which are essential parameters for electronic and electromagnetic applications. Further detailed investigations on essential magnetic and electrical properties for few short listed specific applications may possibly be undertaken as an extension of the present work.

10. Recently, there has been a growing interest in low-temperature sintered Ni-Zn ferrite for fabrication of multilayer-type chip inductors. The multilayer chip inductors are used as surface mount devices for miniaturized electronic products such as cellular phones, digital cameras, video camera etc. Thus, new bulk samples can be prepared by sintering nano powder at lower sintering temperature and can be explored to investigate the potential of magnetic properties of the samples in the said applications.

11. The use of ferrite-based tunable negative index meta-materials in microwave electronics for phase shifter and electromagnetic interference suppression applications showed great advantage as it allows the use of a ferrite in the negative permeability region near the FMR, where permeability is relatively high and still maintain low losses. The bulk samples sintered at 1100^oC, 1200^oC and 1300^oC in the present work showed very high negative permeability near resonance. Hence, detail study of investigating the meta-materials property of the samples prepared in the present work can be undertaken to learn its potential in the field of ferrite-based tunable negative index meta-materials.

12. In the present investigation the dielectric and permeability studies were limited in the mid frequency range up to 3 MHz. Hence scope exists to carry out further measurements at higher frequencies.

13. The permeability studies of nano Ni-Zn ferrite samples fabricated in a composite form with suitable matrix can be investigated to manipulate and improve operating frequency bandwidth.

14. The development of samples in the form of thin films and study of their electrical and magnetic properties may bring exciting results. It will also interesting to pursue in this directions in coming years, as research and development in the area of thin films is growing rapidly world wide due to their wide range of possible applications.

15. The nano samples of Ni-Zn ferrites are unambiguously promising candidates for various practical applications such as MRI contrast enhancement agents, magnetic probes for bio-molecules and magnetically guided drug delivery etc. However, detailed and in-depth study on related magnetic and electrical parameters in this application will be very exciting.

ANNEXURE 1

Publications:

1. M. M. Kothawale, R. B. Tangsali, G. K. Naik, J. S. Budkuley, Sher Singh Meena and Pramod Bhatt, “**Sintering Effect on Structural and Magnetic Properties of $Ni_{0.6}Zn_{0.4}Fe_2O_4$ Ferrite”,** AIP Conf. Proc. 1512, doi: 10.1063/1.4791460, **(2013),** 1160-1161.

2. Manoj M. Kothawale, R. B. Tangsali, G. K. Naik and J. S. Budkuley, “**Characterization and Magnetic Properties of Nanoparticle $Ni_{1-x}Zn_xFe_2O_4$ Ferrites Prepared using Microwave Assisted Combustion Method**”, J Supercond Nov Magn, 25-6, **(2012)**, 1907-1911.

3. M. M. Kothawale, R. B. Tangsali, G. K. Naik and J. S. Budkuley, S. S. Meena, **“Synthesis of Nanoparticles $Ni_{0.55}Zn_{0.45}Fe_2O_4$ by Novel Precursor Method Showing Enhanced Resistivity”**, American Institute of Physics , AIP Conf. Proc. 1447, doi: 10.1063/1.4710007, **(2012)**, 317-318.

4. M. M. Kothawale, R. B. Tangsali, Jaison Joseph, G. K. Naik, J. S. Budkuley, Sher Singh Meena, S. M. Yusuf and J. V. Yakhmi, **“Characterization and Mössbauer Study of $Ni_{0.45}Zn_{0.55}Fe_2O_4$ Nanoparticles Prepared by Novel Precursor Method”**, American Institute of Physics, AIP Conf. Proc. 1349, doi: 10.1063/1.3606278. **(2011)**, 1165-1166.

5. Manoj M. Kothawale, R.B. Tangsali, G.K. Naik, J.S. Budkuley, “**Effect of Sintering on Magnetic Properties of $Ni_{0.55}Zn_{0.45}Fe_2O_4$”,** J Supercond Nov Magn 26, **(2013),** 3293–3298.

6. Manoj M. Kothawale, R.B. Tangsali, G.K. Naik, J.S. Budkuley, “**Synthesis and Characterization of Nanoparticle $Ni_{0.40}Zn_{0.60}Fe_2O_4$ Showing High DC Resistivity and Saturation Magnetization**” **communicated**.

Papers/posters presented at National /International conferences:

1. “**Sintering Effect on Structural and Magnetic Properties of $Ni_{0.6}Zn_{0.4}Fe_2O_4$ Ferrite”**. (M. M. Kothawale, R. B. Tangsali, G. K. Naik, J. S. Budkuley, S. S. Meena and P. Bhatt). Poster presented at “57th DAE Solid State Physics Symposium 2012” held at IIT Powai- Mumbai, during 3- 7 December 2012.

2. **“Lattice Contraction, Magnetization Enhancement, Resonance Frequency Variation and Microstructure Evolution on Heating Nanoparticle $Ni_{0.55}Zn_{0.45}$ Ferrite”.** (M. M. Kothawale, R. B. Tangsali, G. K. Naik and J. S. Budkuley). Paper presented at “International conference NANOCON 012, Innovative materials, Processes, Products and Applications” organized by Bharati Vidyapeeth, Deemed University-Pune, during 18-19 October 2012.

3. **“Dielectric Properties of Nanoparticles $Ni_{0.65}Zn_{0.35}Fe_2O_4$ Prepared by Precursor Method”.** (M. M. Kothawale, R. B. Tangsali, G. K. Naik, J. S. Budkuley and S. S. Meena). Paper presented at “International conference on Nanotechnology and functional materials” organized by SNIST and UNISA-Gahatkesar, Hyderabad, during 4-7 January, 2012.

4. “**Synthesis of Nanoparticles $Ni_{0.55}Zn_{0.45}Fe_2O_4$ by Novel Precursor Method Showing Enhanced Resistivity”.** (M. M. Kothawale, R. B. Tangsali, G. K. Naik, J. S. Budkuley and S. S. Meena). Presented poster at “56th DAE Solid State Physics symposim” held at SRM University-Kattankulathur, Tamilnadu, during 19-23 December, 2011.

5. “**Characterization and Mössbauer Study of $Ni_{0.45}Zn_{0.55}Fe_2O_4$ Nanoparticles Prepared by Novel Precursor Method”.** (M. M. Kothawale, R. B. Tangsali, J. Joseph, G. K. Naik, J. S. Budkuley, S. S. Meena, S. M. Yusuf and J. V. Yakhmi). Presented poster at “55th DAE Solid State Physics Symposium 2010” held at Manipal University-Manipal, during 26-30 December 2010.

6. **“Mossbauer Study of $Ni_XZn_{1-x}Fe_2O_4$ Nanoparticles”.** (S. S. Meena, M. M. Kothawale, J. Joseph, R. B. Tangsali, G. K. Naik, S. M. Yusuf and J. V. Yakhmi). Presented poster at “DAE-BRNS 3rd International symposium on materials chemistry” held at BARC-Mumbai, during 7-11 December 2010.

7. **“Synthesis and Magnetic Properties of Nanoparticle $Ni_{1-X}Zn_xFe_2O_4$ Ferrite Prepared by Precursor Method”.** (M. M. Kothawale, R. B. Tangsali, G. K. Naik and J. S. Budkuley). Presented poster at “International Workshop & Symposium on the Synthesis and Characterization of Glass/Glass-ceramics (IWSSCGGC-2010)” organized by Materials research society of India & Centre for materials for electronics technology-PUNE, during 7-10 July 2010.

8. **“Study of Cation Distribution and its Effect on Magnetic Properties of Nano-size $Ni_{1-x}Zn_xFe_2O_4$ Ferrites Prepared using Novel Method”.** (M. M. Kothawale, R. B. Tangsali, G. K. Naik and J. S. Budkuley). Paper presented at “International conference on Nanomaterials synthesis, characterization and applications” organized by M.G University-Kerala, during 27-29 April 2010.